ISTANBUL TECHNICAL UNIVERSITY ★ GRADUATE SCHOOL

COMPARATIVE NUMERICAL AND EXPERIMENTAL STUDY OF HOMOGENIZED AND FULL-SCALE FE MODELS FOR SANDWICH STRUCTURES WITH RE-ENTRANT AND ANTI-TETRACHIRAL AUXETIC CORES

M.Sc. THESIS

Özgür DEĞİRMENCİ

Department of Mechanical Engineering

Solid Mechanics Programme

OCTOBER 2025

ISTANBUL TECHNICAL UNIVERSITY ★ GRADUATE SCHOOL

COMPARATIVE NUMERICAL AND EXPERIMENTAL STUDY OF HOMOGENIZED AND FULL-SCALE FE MODELS FOR SANDWICH STRUCTURES WITH RE-ENTRANT AND ANTI-TETRACHIRAL AUXETIC CORES

M.Sc. THESIS

Özgür DEĞİRMENCİ

(503141508)

Department of Mechanical Engineering

Solid Mechanics Programme

Thesis Advisor: Prof. Dr. Şafak YILMAZ

Thesis Co-Advisor: Prof. Dr. Halit Süleyman TÜRKMEN

OCTOBER 2025

İSTANBUL TEKNİK ÜNİVERSİTESİ ★ LİSANSÜSTÜ EĞİTİM ENSTİTÜSÜ

RE-ENTRANT VE ANTI-TETRACHIRAL AUXETIC ÇEKİRDEKLİ SANDVİÇ YAPILARIN HOMOJENLEŞTİRİLMİŞ VE TAM ÖLÇEKLİ MODELLERİ ÜZERİNE SAYISAL VE DENEYSEL KARŞILAŞTIRMALI BİR ÇALIŞMA

YÜKSEK LİSANS TEZİ

Özgür DEĞİRMENCİ

(503141508)

Makina Mühendisliği Anabilim Dalı

Katı Cisimlerin Mekaniği Programı

Tez Danışmanı: Prof. Dr. Şafak YILMAZ

Eş Danışman: Prof. Dr. Halit Süleyman TÜRKMEN

EKİM 2025

Özgür Değirmenci, a M.Sc. student of İTU Graduate School student ID 503141508, successfully defended the thesis/dissertation entitled "COMPARATIVE NUMERICAL AND EXPERIMENTAL STUDY OF HOMOGENIZED AND FULL-SCALE FE MODELS FOR SANDWICH STRUCTURES WITH RE-ENTRANT AND ANTI-TETRACHIRAL AUXETIC CORES", which he prepared after fulfilling the requirements specified in the associated legislations, before the jury whose signatures are below.

Thesis Advisor :	**Prof. Dr. Şafak Yılmaz** İstanbul Technical University	....
Co-advisor :	**Prof. Dr. Halit Süleyman Türkmen** İstanbul Technical University	....
Jury Members :	**Doç. Dr. Uğurcan Eroğlu** Istanbul Technical University	....
	Doç. Dr. Bora ŞENER Yıldız Technical University	....
	Dr. Öğr. Üyesi Alperen Acar Yıldız Technical University	....

Date of Submission : 06 October 2025
Date of Defense : 21 October 2025

To my dear family, Evren and Arzu,

FOREWORD

First of all, I would like to express my deepest gratitude to my thesis advisor Prof. Dr. Şafak Yılmaz and my co-advisor Prof. Dr. Halit Süleyman Türkmen for their invaluable guidance, insightful feedback, and flexibility throughout the course of this study. Their expertise and mentorship have been instrumental in shaping the direction and quality of this thesis.

I extend my heartfelt and special thanks to my colleague Kadir Günaydın for his remarkable contributions and continuous support, both technically and morally, which have been crucial to the completion of this thesis. His willingness to assist at every step has been a source of inspiration and motivation.

Finally, I wish to express my sincerest love, admiration, and gratitude to my wife, Arzu, for her unwavering support, endless patience, positivity, and unshakable belief in me throughout this challenging thesis journey. To my beloved son, Evren, who brings immense joy, laughter, and boundless energy into my life, you have been my constant source of happiness and inspiration, and I dedicate my deepest appreciation to you. I am also deeply thankful to my mom, dad, and sister, whose lifelong love, support, and encouragement at every stage of my life have been a constant source of strength. Their wisdom and belief in me have guided me in completing this thesis. Without their endless understanding, patience, and love, this work would not have been possible.

October 2025 Özgür Değirmenci
(Mechanical Engineer)

TABLE OF CONTENTS

Page

ABBREVIATIONS

3D	: Three-Dimensional
AM	: Additive Manufacturing
ASTM	: American Society for Testing and Materials
CAD	: Computer-Aided Design
cm^3	: Cubic Centimeter
DOF	: Degrees of Freedom
FE	: Finite Element
FEA	: Finite Element Analysis
FEM	: Finite Element Method
FRF	: Frequency Response Function
g	: Gram
Hz	: Hertz
HX	: Heat Exchanger
MJM	: Material Jetting Method
MJT	: Material Jetting
MPa	: Megapascal
mJ	: Millijoule
mm	: Millimeter
mm/mm	: Millimeter per millimeter (unit of strain)
N	: Newton
NPR	: Negative Poisson's Ratio
Pa	: Pascal
RVE	: Representative Volume Element
UC	: Unit Cell
VAM	: Variational Asymptotic Method
X-Y-Z	: Cartesian Coordinate Axes

SYMBOLS

E	: Elastic modulus
E1	: Elastic modulus in the X-direction
Ex	: Elastic modulus in the X-direction
E2	: Elastic modulus in the Y-direction
Ey	: Elastic modulus in the Y-direction
E3	: Elastic modulus in the Z-direction
Ez	: Elastic modulus in the Z-direction
G	: Shear modulus
G12	: Shear modulus in the XY plane
Gxy	: Shear modulus in the XY plane
G23	: Shear modulus in the YZ plane
Gyz	: Shear modulus in the XY plane
G31	: Shear modulus in the XZ plane
Gyz	: Shear modulus in the XZ plane
Nu	: Poisson’s ratio
Nu12	: Poisson’s ratio in the XY plane
Nuxy	: Poisson’s ratio in the XY plane
Nu13	: Poisson’s ratio in the XZ plane
Nuxz	: Poisson’s ratio in the XZ plane
Nu23	: Poisson’s ratio in the YZ plane
Nuyz	: Poisson’s ratio in the YZ plane
$\boldsymbol{\rho}$	: Density
$\boldsymbol{\sigma}$	: Stress
$\boldsymbol{\sigma_1}$	**:** Maximum principal stress
$\boldsymbol{\sigma_3}$	**:** Minimum principal stress
$\boldsymbol{\varepsilon}$	: Strain
$\boldsymbol{\varepsilon_1}$	**:** Maximum principal strain
$\boldsymbol{\varepsilon_3}$	**:** Minimum principal strain
Fx	: Force in X-direction
Fy	: Force in Y-direction
Fz	: Force in Z-direction
Ux	: Displacement in X-direction
Uy	: Displacement in Y-direction
Uz	: Displacement in Z-direction

LIST OF TABLES

Page

LIST OF FIGURES

Page

COMPARATIVE NUMERICAL AND EXPERIMENTAL STUDY OF HOMOGENIZED AND FULL-SCALE FE MODELS FOR SANDWICH STRUCTURES WITH RE-ENTRANT AND ANTI-TETRACHIRAL AUXETIC CORES

SUMMARY

Additive manufacturing (AM), widely known as 3D printing, has transformed the field of structural design by enabling the fabrication of complex, lightweight, and highly customized architectures that are often impossible to produce using conventional manufacturing techniques. This technological advancement has unlocked new possibilities for the exploration of architected materials, particularly auxetic structures, which exhibit a negative Poisson's ratio. Auxetic materials, when stretched, expand laterally rather than contracting, and when compressed, they contract inwards rather than bulging. This counterintuitive behavior imparts auxetic structures with remarkable mechanical advantages, including superior energy absorption, enhanced impact resistance, and improved damping performance, making them highly attractive for a wide range of engineering applications. In particular, re-entrant and anti-tetrachiral lattice geometries have emerged as promising auxetic designs due to their tunable mechanical responses, near-isotropic behavior under specific loading conditions, and ability to withstand large deformations while maintaining stability. These features make them well-suited for use in aerospace panels, biomedical implants, and protective systems such as armor panels for defense applications.

Despite the advantages of auxetic designs, their complex lattice architectures, composed of intricate geometrical features and periodic unit cells, present significant challenges in numerical modeling and simulation. Full-scale finite element analysis (FEA), which resolves each geometric detail, provides detailed insight into localized stress distributions, deformation patterns, and failure mechanisms. However, this approach demands substantial computational resources, with the complexity of mesh generation, solver runtimes, and post-processing increasing rapidly as the size of the model grows. For large-scale engineering systems like heat exchangers or energy-absorbing panels, where millions of unit cells may be present, full-scale FEA becomes impractical within typical design workflows. To address these challenges, homogenization techniques have been developed as an alternative strategy. By approximating the periodic lattice as an equivalent orthotropic or anisotropic continuum, homogenization enables significant reductions in model complexity, allowing engineers to analyze large and complex structures more efficiently. Nevertheless, homogenization may struggle to capture localized stress concentrations and detailed deformation behaviors, highlighting the trade-off between accuracy and computational efficiency.

This study undertook a comprehensive investigation of sandwich structures incorporating re-entrant and anti-tetrachiral auxetic cores, comparing the mechanical behavior of full-scale and homogenized finite element models under different loading

conditions. The research also benchmarks these numerical models against experimental tests to provide a robust assessment of their performance. The study begins with the 3D modeling of the two auxetic lattice designs, using Siemens NX 12 software to generate detailed CAD models of both re-entrant and anti-tetrachiral geometries. These designs were selected based on their prevalence in the literature and their contrasting structural characteristics. The full-scale models capture every geometric feature of the lattice, while the homogenized models simplify the complex geometry into an equivalent orthotropic continuum, derived through numerical homogenization techniques.

The physical specimens were fabricated using a Stratasys Objet Connex 1 3D printer via the material jetting method, with VeroBlue RDG840 polymer chosen as the base material due to its suitable mechanical properties and compatibility with high-precision additive manufacturing. To determine the fundamental material properties of VeroBlue RDG840, tensile tests were conducted on printed tensile specimens, establishing key parameters such as Young's modulus, Shear Modulus, Poisson's ratio, and density for use in the numerical simulations. In addition, compression tests were performed to determine the corresponding Young's modulus under compressive loading.

Following fabrication, the experimental phase involved a series of mechanical tests to evaluate the structural response of the lattice specimens. Modal response testing was performed using the roving hammer technique to identify the natural frequencies and mode shapes, providing insights into the dynamic behavior of the structures. Static compression tests were conducted on cube-shaped specimens to assess their load-bearing capacity and stress-strain behavior under uniaxial compression. Three-point bending tests were also performed to evaluate the flexural stiffness and deformation response of the sandwich panels under bending loads. These experimental results provided essential benchmarks for comparing the numerical models and evaluating the applicability of the homogenization approach.

In the numerical phase, finite element models were developed in ANSYS Workbench 2020 R2 for both full-scale and homogenized representations of the re-entrant and anti-tetrachiral structures. The Material Designer module in ANSYS was used to derive the equivalent orthotropic material properties for the homogenized models, based on representative unit cell analyses. Sensitivity studies were conducted to evaluate the effects of mesh density, unit cell selection, and boundary conditions on the accuracy of the homogenized properties. These homogenized models were then used in modal, compression, three-point bending, and tensile FE analyses to assess the global mechanical behavior of the structures under different loading scenarios.

The results indicate that modal analyses yielded the closest and most promising match between numerical predictions and experimental benchmarks, demonstrating a strong positive outcome for the homogenization approach in capturing dynamic behavior, such as natural frequencies and mode shapes. This highlights modal analysis as the most suitable scenario for applying homogenized finite element models in auxetic structures, offering both accuracy and significant computational savings. The compression analyses also showed highly promising results, with homogenized models closely matching full-scale simulations and experimental test data, particularly in predicting global stiffness and load-displacement behavior. In contrast, the three-point bending analyses revealed the largest discrepancies, indicating that homogenized models have limitations in accurately representing detailed local deformation patterns, stress concentrations, and complex failure mechanisms under bending loads. While minor differences were also observed in detailed deformation patterns under tensile loading, these differences were generally within acceptable ranges for engineering applications focusing on global response. Additionally, the study demonstrated that the accuracy of three-point bending simulations strongly depends on the correct definition of material behavior under both tensile and compressive loading. The incorporation of averaged and separately defined Young’s modulus for tension and compression significantly improved the correlation between numerical and experimental results. This highlights the necessity of accurate material calibration in modeling polymer-based auxetic lattices to achieve physically consistent predictions of bending and flexural responses. Overall, these findings confirm that while homogenized models are highly effective for early-stage design, parametric evaluations, and large-scale system analyses, full-scale finite element models remain essential for accurately capturing local stress distributions, failure initiation, and nonlinear deformations in complex auxetic sandwich structures.

This thesis provides a systematic comparison of full-scale and homogenized finite element models for sandwich structures with re-entrant and anti-tetrachiral auxetic cores, highlighting the trade-offs between computational efficiency and accuracy. Homogenization significantly reduces model complexity and solution times while maintaining sufficient accuracy for global analyses, though careful benchmarking against experimental results is essential. The study emphasizes the importance of considering manufacturing imperfections, such as anisotropy and dimensional variability, in modeling strategies. It offers practical insights for engineering applications where homogenized models enable efficient analysis of large-scale systems. Finally, the findings provide a foundation for future work in hybrid modeling strategies that combine homogenized global models with localized full-scale analyses for enhanced design precision.

xxx

RE-ENTRANT VE ANTI-TETRACHIRAL AUXETIC ÇEKİRDEKLİ SANDVİÇ YAPILARIN HOMOJENLEŞTİRİLMİŞ VE TAM ÖLÇEKLİ MODELLERİ ÜZERİNE SAYISAL VE DENEYSEL KARŞILAŞTIRMALI BİR ÇALIŞMA

ÖZET

Katmanlı imalat (additive manufacturing, AM) veya yaygın adıyla üç boyutlu (3D) yazıcı teknolojileri, modern mühendislik alanında devrim yaratmış ve karmaşık, hafif, yüksek özgül mukavemetli ve özelleştirilebilir yapıları üretme imkânı sağlamıştır. Geleneksel imalat yöntemleriyle üretimi zor veya imkânsız olan çok karmaşık geometrilere sahip yapıların tasarımı ve üretimi, özellikle AM teknolojilerinin gelişimiyle mümkün hale gelmiştir. Bu gelişmeler, malzeme mühendisliğinde özellikle yapılandırılmış ve hücresel malzemelere yönelik yeni araştırma alanlarının açılmasına katkıda bulunmuş ve negatif Poisson oranı (auxetic behavior) sergileyen auxetic yapılara olan ilgiyi artırmıştır. Negatif Poisson oranına sahip auxetic malzemeler, çekme yükleri altında genişleyen ve basma yükleri altında içe doğru büzülen, dolayısıyla konvansiyonel malzemelerden farklı bir şekilde davranan malzemelerdir. Bu tersine deformasyon mekanizması sayesinde auxetic yapılar, üstün enerji soğurma kapasitesi, yüksek darbe dayanımı, gelişmiş sönümleme özellikleri ve şekil uyumluluğu gibi avantajlar sunar. Özellikle re-entrant ve anti-tetrachiral geometriye sahip auxetic kafes tasarımları, belirli yükleme koşullarında izotropiye yakın mekanik tepkileri, ayarlanabilir rijitlikleri ve büyük deformasyonlar altında stabilitelerini koruma özellikleriyle dikkat çeker. Bu özellikler, söz konusu yapıları havacılık, biyomedikal implantlar ve savunma sanayiinde zırh sistemleri gibi koruyucu uygulamalar için cazip kılmaktadır.

Ancak, auxetic yapıların bu karmaşık geometrik düzenleri, tekrar eden hücresel desenleri ve detaylı yük aktarım yolları, sayısal modelleme ve simülasyon çalışmaları açısından büyük zorluklar yaratmaktadır. Her bir geometrik detayın tek tek modellenmesi gereken tam ölçekli sonlu elemanlar analizleri (FEA), lokal gerilme dağılımları, deformasyon modları ve potansiyel hasar bölgelerini doğru bir şekilde tespit edebilmek için tercih edilen bir yöntemdir. Ancak, bu yüksek doğruluk düzeyi, önemli ölçüde hesaplama kaynakları gerektirir ve model boyutu büyüdükçe ağ (mesh) oluşturma, çözüm süreleri ve sonuçların işlenmesi gibi süreçlerin karmaşıklığı da katlanarak artar. Milyonlarca tekrar eden hücreden oluşan büyük ölçekli sistemlerde (örneğin, ısı değiştiriciler veya enerji sönümleyici paneller gibi) tam ölçekli FEA uygulamak, endüstriyel tasarım süreçleri için pratik olmaktan çıkar ve hesaplama süreleri ve donanım gereksinimleri açısından aşırı bir yük oluşturur. Bu zorlukları aşmak için geliştirilen homojenleştirme yöntemleri, karmaşık geometrik detayları, eşdeğer ortotropik veya anizotropik bir malzeme modeliyle temsil ederek analizlerde önemli bir sadeleştirme sağlar. Homojenleştirme, karmaşık kafes yapısını bir temsil hücresi üzerinden ortalama enerji eşitliği esasına göre sadeleştirir ve bu sayede daha

düşük ağ yoğunluğu ile global mekanik tepkilerin tahmin edilmesini mümkün kılar. Ancak, bu yöntem lokal gerilme yığılmaları ve detaylı deformasyon modları gibi kritik yerel etkileri tam olarak yakalamakta yetersiz kalabilir.

Bu tez çalışmasında, re-entrant ve anti-tetrachiral auxetic çekirdekli sandviç yapıların mekanik davranışları, tam ölçekli ve homojenleştirilmiş sonlu elemanlar modelleri üzerinden detaylı bir şekilde incelenmiş ve farklı yükleme senaryolarında (modal analizi, statik basma, üç nokta eğme ve statik çekme) karşılaştırmalar yapılmıştır. Çalışmada, sayısal model sonuçları, deneysel test sonuçları ile karşılaştırılarak homojenleştirme yönteminin uygulanabilirliği değerlendirilmiştir. Tezin ilk aşamasında, Siemens NX 12 CAD yazılımı kullanılarak re-entrant ve anti-tetrachiral auxetic geometriye sahip detaylı 3D modeller oluşturulmuştur. Bu geometriler, literatürde yaygın olarak kullanılan standart auxetic hücre tasarımlarına dayandırılmıştır. Detaylı tam ölçekli modeller, her bir geometrik ayrıntıyı içeren yüksek çözünürlüklü kafes yapılarını temsil ederken, homojenleştirilmiş modeller, karmaşık geometrilerin yerine, ANSYS yazılımındaki Material Designer modülü ile hesaplanan eşdeğer ortotropik malzeme özelliklerini kullanan basitleştirilmiş modellerden oluşmaktadır.

Tez çalışmasının deneysel aşamasında, seçilen geometriler Stratasys Objet Connex 1 cihazı ile, malzeme püskürtme (material jetting) yöntemiyle, VeroBlue RDG840 polimer kullanılarak üç boyutlu yazıcıda yazdırılmıştır. Bu malzeme, yüksek boyutsal hassasiyet ve iyi mekanik özellikler sunması nedeniyle tercih edilmiştir. VeroBlue'nun temel mekanik özelliklerini belirlemek için çekme testleri gerçekleştirilmiş ve elastiklik modülü, Poisson oranı, kesme modülü ve yoğunluk gibi kritik parametreler elde edilmiştir. Ayrıca, basma yüklemesi altında karşılık gelen elastisite modülünü belirlemek amacıyla basma testleri de gerçekleştirilmiştir. Deneysel testler arasında, yapıların doğal frekanslarını ve mod şekillerini belirlemek amacıyla modal analiz, kübik numuneler üzerinde basma testleri ve sandviç paneller üzerinde üç nokta eğme testleri uygulanmıştır. Bu deneysel çalışmalar, hem sayısal modellerin doğruluğunu değerlendirmek için bir karşılaştırma temeli sağlamış, hem de homojenleştirme yönteminin performansını gerçek test verileriyle kıyaslamak için kritik bir rol oynamıştır.

Sayısal analiz aşamasında, ANSYS Workbench 2020 R2 yazılımında her iki modelleme yaklaşımı için modal, basma, üç nokta eğme ve çekme analizleri gerçekleştirilmiştir. Homojenleştirme sürecinde, birim hücre analizleri kullanılarak elde edilen eşdeğer elastik sabitler, yoğunluklar ve Poisson oranları, karmaşık kafes yapılarını temsil eden sadeleştirilmiş modellerde uygulanmıştır. Ağ yoğunluğu, birim hücre boyutlandırması ve sınır koşullarının hassasiyet üzerindeki etkileri incelenmiş ve parametrelerin homojenleştirilmiş modellerin doğruluğu üzerindeki etkileri değerlendirilmiştir.

Sonuçlar, modal analizlerin sayısal modellemeler ile deneysel veriler arasındaki en yakın ve en umut verici uyumu sağladığını göstermektedir. Homojenleştirme yaklaşımı, doğal frekanslar ve mod şekilleri gibi dinamik davranışları tahmin etmede güçlü bir başarı sağlamış ve bu yönüyle önemli bir pozitif sonuç sunmuştur. Modal analizler, homojenleştirilmiş sonlu eleman modellerinin auxetik yapıların dinamik davranışlarını doğru şekilde tahmin edebildiği ve aynı zamanda önemli ölçüde hesaplama avantajı sunduğu en uygun analiz senaryosu olarak öne çıkmıştır. Basma analizleri de oldukça olumlu sonuçlar göstermiş; homojenleştirilmiş modeller, özellikle global rijitlik ve yük-deplasman davranışlarını tahmin etmede, hem tam ölçekli simülasyonlar hem de deneysel test verileri ile büyük ölçüde uyum sağlamıştır. Buna karşın, üç nokta eğme analizlerinde en büyük farklılıklar gözlemlenmiş;

homojenleştirilmiş modeller, lokal deformasyon modları, gerilme yığılmaları ve karmaşık hasar mekanizmalarını doğru şekilde tahmin etmede sınırlı kalmıştır. Çekme yüklemelerinde ise detaylı deformasyon desenlerinde bazı küçük farklar bulunmasına rağmen, homojenleştirilmiş modeller genel yük-deplasman tepkilerini tahmin etmede yeterli doğruluğa ulaşmıştır ve mühendislik uygulamaları için kabul edilebilir bir doğruluk düzeyi sağlamıştır. Ayrıca, yapılan analizler üç nokta eğme simülasyonlarının doğruluğunun, malzemenin çekme ve basma altındaki davranışının doğru tanımlanmasına doğrudan bağlı olduğunu göstermiştir. Çekme ve basma testlerinden elde edilen elastisite modüllerinin ortalamasının kullanıldığı ve çekme–basma için ayrı modüllerin tanımlandığı analizlerde, sayısal ve deneysel sonuçlar arasındaki uyum belirgin şekilde artmıştır. Bu durum, auxetic yapılar gibi karmaşık geometrilere sahip polimer esaslı malzemelerin modellenmesinde, doğru malzeme kalibrasyonunun büyük önem taşıdığını ortaya koymuştur. Gerçekçi ve fiziksel olarak tutarlı eğilme ve burkulma tepkilerinin elde edilebilmesi için, hem çekme hem de basma davranışlarının doğru şekilde temsil edilmesi gerektiği sonucuna varılmıştır. Bu bulgu, üç nokta eğme ve genel eğilme analizlerinde malzeme tanımının doğru yapılmasının sonuçların güvenilirliğini doğrudan etkilediğini göstermektedir. Genel olarak bu bulgular, homojenleştirilmiş modellerin erken aşama tasarım çalışmaları, parametrik incelemeler ve büyük ölçekli sistem analizleri için son derece etkili ve pratik bir yaklaşım olduğunu ortaya koymaktadır. Ancak, lokal gerilme dağılımları, hasar başlangıç noktaları ve doğrusal olmayan deformasyon davranışlarının kritik önem taşıdığı senaryolarda, tam ölçekli sonlu eleman modellerinin vazgeçilmez olduğu sonucuna varılmıştır.

Tez çalışması, re-entrant ve anti-tetrachiral auxetic çekirdekli sandviç yapıların tam ölçekli ve homojenleştirilmiş modelleri arasındaki temel farkları ortaya koyarak, her iki yaklaşımın avantaj ve sınırlamalarını kapsamlı bir şekilde ele almıştır. Homojenleştirmenin sağladığı hesaplama verimliliği ve hız avantajları, özellikle geniş ölçekli yapılar için analiz yapılması gereken durumlarda büyük önem taşırken, detaylı gerilme dağılımları ve lokal deformasyonlar için tam ölçekli modellerin gerekliliği vurgulanmıştır. Bu çalışma, auxetic yapıların mühendislik tasarımlarında kullanımına yönelik modelleme stratejilerinin geliştirilmesi ve iyileştirilmesi için sağlam bir temel oluşturmuş ve gelecekte hibrit modelleme yaklaşımlarının (global homojenleştirilmiş modeller ile lokal tam ölçekli modellerin birlikte kullanılması) uygulanabilirliğine dair önemli bir öneri sunmuştur.

1.INTRODUCTION

The field of modern engineering has been significantly influenced by additive manufacturing (AM), or 3D printing, since it enables the production of complex shapes and lightweight designs with tailored properties, capabilities that remain limited in conventional manufacturing processes [1].

This technological advancement has particularly accelerated interest in architected materials, especially auxetic structures, also known as auxetic metamaterials, which exhibit a negative Poisson's ratio (NPR), characterized by lateral contraction under compressive loading and expansion under tensile loading [2]. The unique deformation mechanism associated with this NPR is illustrated in Figure 1.1 [3].

The deformation behaviors of different auxetic metamaterial designs are illustrated in Figure 1.2 [4]. The figure highlights a fundamental distinction between conventional materials, which contract laterally under tensile loading (positive Poisson's ratio), and auxetic materials, which expand in the transverse direction when stretched (negative Poisson's ratio). It also shows how a conventional hexagonal lattice can be transformed into an auxetic bow-tie lattice by rotating rigid elements at nodal points. Further examples include auxetic designs based on rotating rigid squares and triangles, which exhibit lateral expansion and a systematic reduction in solid surface fraction under tensile strain. These examples underscore the unique deformation mechanisms of auxetic lattices, offering advantages in applications requiring enhanced energy absorption and conformability.

This counterintuitive deformation mechanism imparts auxetic materials with exceptional mechanical properties, including enhanced energy absorption, superior impact resistance, and improved shear stiffness [5].

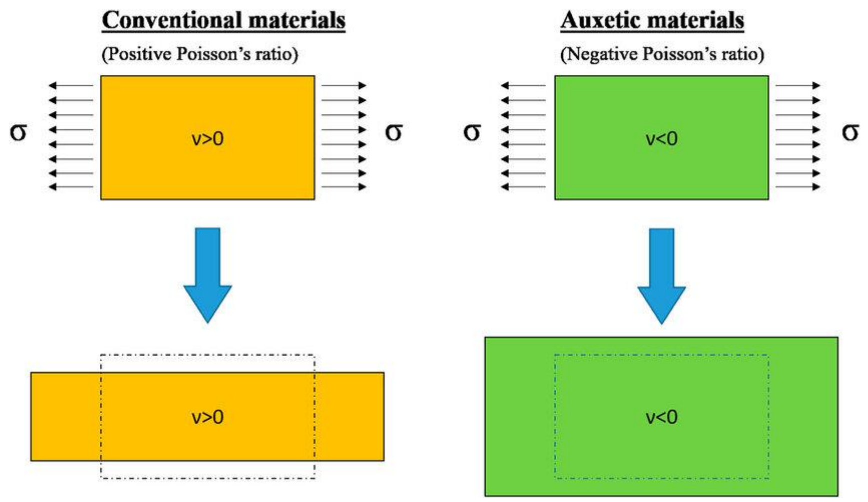

Figure 1.1: Comparison of lateral deformation in conventional and auxetic materials under uniaxial tensile loading [3].

Reproduced from [3] with permission of Taylor & Francis Group.

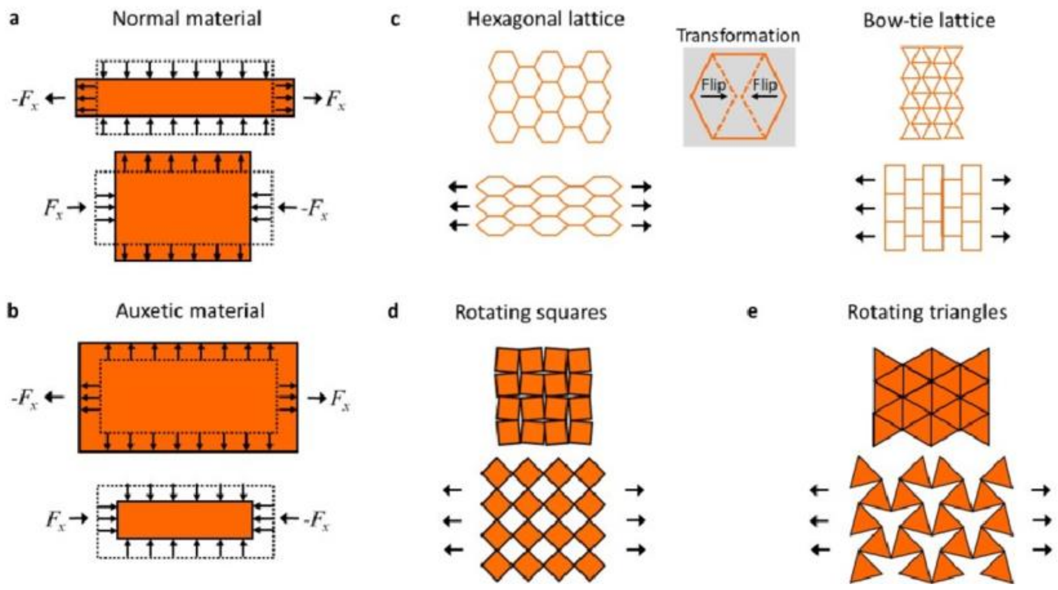

Figure 1.2: Comparison of deformation behavior between normal and auxetic materials [4].

Reproduced from [4] under the Creative Commons Attribution (CC BY 4.0) license.

Among different auxetic lattice geometries, re-entrant and anti-tetrachiral structures are particularly notable for their tunable mechanical properties, near-isotropic performance under certain loading scenarios, and broad applicability in diverse engineering domains, including aerospace, biomedical, and impact-resistant systems [6]. Re-entrant lattice structures achieve auxetic behavior through inward-slanting ligaments that bend or fold under applied loading, resulting in a characteristic NPR behavior. In contrast, anti-tetrachiral architectures generate negative Poisson's ratios by facilitating the coupled rotation of rigid circular nodes, which are interconnected by slender ligaments, thereby enabling efficient in-plane deformation mechanisms [7]. These distinct deformation patterns make auxetic designs highly suitable for diverse applications such as aerospace components for improved energy absorption and impact resistance, biomedical implants and scaffolds that conform to complex anatomical geometries, and lightweight protective systems in defense engineering [8, 9]. An example illustrating the classification of different 2D lattice geometries, including honeycomb, zero-Poisson, and auxetic types, used in aerospace applications is presented in Figure 1.3 [10].

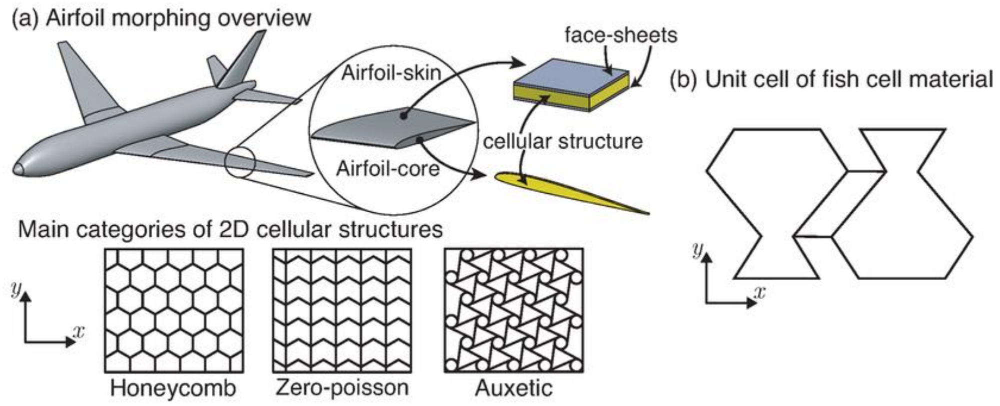

Figure 1.3: Integration of cellular lattice structures into aerospace components [10]. Reproduced from [10] under the Creative Commons Attribution (CC BY 4.0) license.

However, the inherent complexity of these architectures, characterized by intricate geometric features and periodic unit cells, presents significant challenges for accurate numerical modeling and simulation. Full-scale finite element analysis (FEA), which explicitly resolves each geometric details of the lattice, offers a high-fidelity approach capable of capturing localized stress concentrations, deformation patterns, and potential failure mechanisms with precision. Yet, this level of detail comes at a substantial computational cost. The resources required for mesh generation, solver run times, and post-processing increase exponentially with model size and geometric complexity. For large-scale engineering systems such as heat exchangers or energy-absorbing panels, where millions of unit cells may be present, full-scale FEA becomes impractical, often requiring excessive computation times and hardware capabilities beyond typical design workflows [11, 12, 13].

To address these challenges, homogenization techniques have been developed as an efficient alternative. By approximating the periodic lattice as an equivalent orthotropic or anisotropic material, homogenization significantly reduces model complexity while preserving the essential global mechanical responses [12]. The effective stiffness, density, and Poisson’s ratio are extracted from representative unit cell analyses and incorporated into continuum-scale simulations, enabling the modeling of intricate structures without explicitly resolving every geometric detail. A visual and mathematical representation of the homogenization process is presented in Figure 1.4 [13].

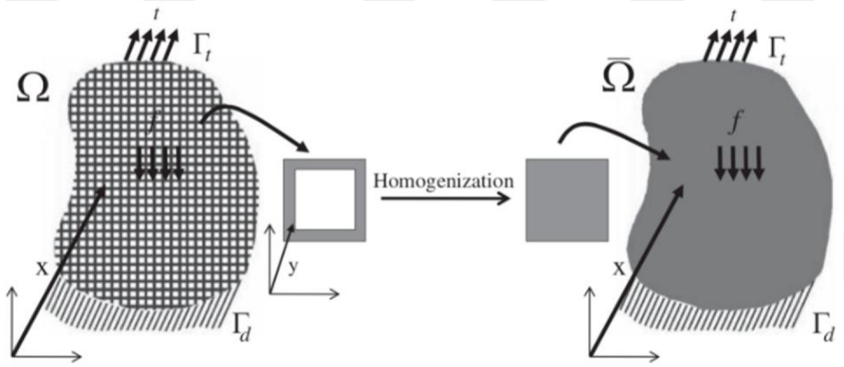

Figure 1.4: Mathematical representation of the homogenization process [13].

While homogenization offers significant computational advantages, it introduces uncertainties in capturing localized phenomena such as stress concentrations and failure initiation sites.

This thesis aims to systematically explore and quantify the trade-offs between full-scale and homogenized FEA models of sandwich structures with re-entrant and anti-tetrachiral auxetic cores. By comparing simulation results across modal, compression, bending, and tensile loading scenarios, and benchmarking them against experimental test data, this study seeks to establish practical guidelines for selecting appropriate modeling strategies based on accuracy requirements, computational efficiency, and specific engineering applications.

1.1.Purpose of Thesis

The primary objective of this thesis is to evaluate the mechanical behavior of sandwich structures incorporating re-entrant and anti-tetrachiral auxetic cores by systematically comparing full-scale and homogenized finite element models. The study investigates differences in predicted global mechanical responses, such as stiffness, natural frequencies, and load-displacement behavior, between the two modeling approaches. It also aims to assess the computational efficiency gained through homogenization by analyzing mesh sizes, solution times, and identifying the trade-offs between accuracy and computational demand.

A critical aspect of this study is identifying the limitations of homogenization methods under different loading scenarios, as these may significantly influence the accuracy of design predictions in engineering practice. To ensure the validity of the findings, simulation results are benchmarked against experimental data, including modal analysis, static compression, and three-point bending tests, thereby establishing a robust basis for comparison. Through this integrated approach, the thesis provides a practical framework for selecting appropriate modeling strategies based on accuracy requirements, available computational resources, and specific design objectives.

A real-world example of this challenge can be seen in plate-fin heat exchangers, where complex, repeating fin structures, effectively repetitive unit cells, are critical for thermal performance. However, conducting full-scale simulations of every geometric detail is computationally impractical. An example of a heat exchanger design incorporating repeating lattice structures is illustrated in Figure 1.5 [14].

The integration of additive manufacturing (AM) techniques further expands the possibilities for fabricating complex auxetic geometries that were previously unachievable [6]. Auxetic materials, characterized by their NPR and typically reduced stiffness compared to conventional materials, exhibit unique deformation mechanisms that enhance performance under various loading conditions. A visual classification of different lattice structures, based on their stiffness characteristics and Poisson's ratio behavior, is presented in Figure 1.6 [10].

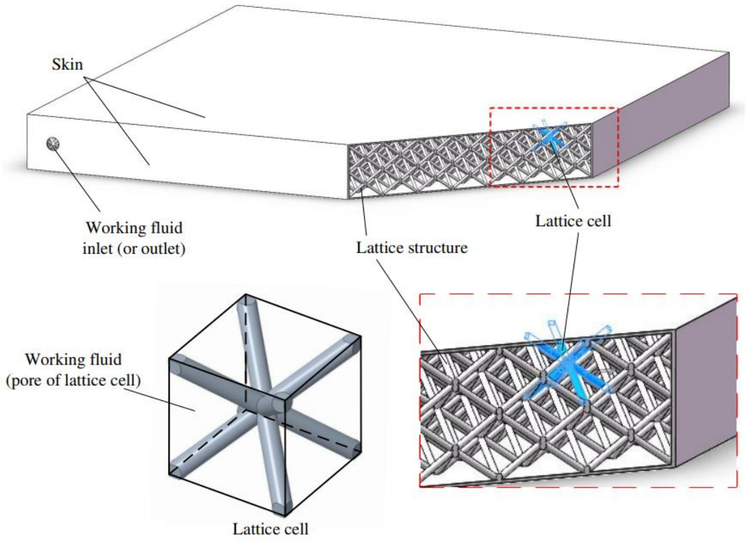

Figure 1.5: Heat exchanger with a lattice structure [14].

Auxetic materials have also demonstrated significant potential in biomedical engineering, particularly in the development of implants and prosthetics that require conformability to complex anatomical geometries and enhanced energy absorption capabilities [6, 15].

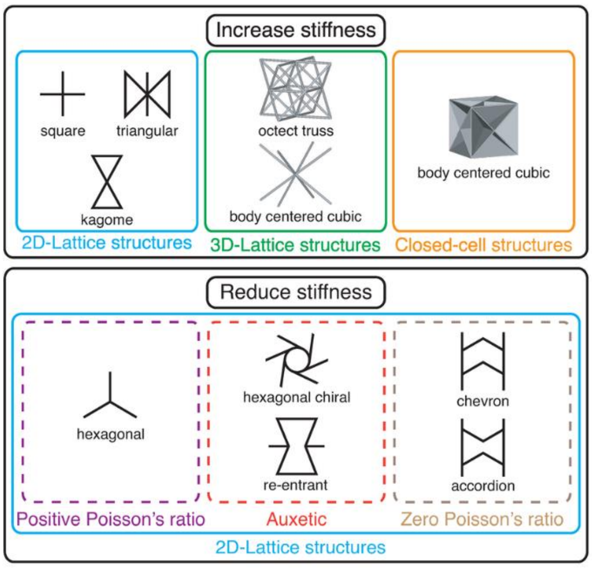

Figure 1.6: Classification of lattice structures by stiffness characteristics and Poisson's ratio behavior [10].

In addition, defense applications have leveraged the unique properties of auxetic structures for improved energy dissipation, enabling the design of lightweight protective panels and armor systems that offer superior resistance to ballistic and fragment impacts [16, 17].

The exploration of hybrid auxetic structures, which combine different geometries or materials, represents a promising research direction for optimizing mechanical behavior in complex design scenarios [5].

Overall, this thesis contributes the broader understanding of auxetic materials and their diverse applications, offering valuable insights that can guide future research and practical design strategies within this rapidly evolving field.

1.2.Literature Review

The introduction of auxetic materials by Lakes in 1987 marked a significant milestone in material design, as it demonstrated the possibility of achieving a NPR in engineered materials [2]. Since then, extensive research has focused on developing and optimizing auxetic geometries to achieve specific mechanical properties, such as enhanced energy absorption and tailored deformation behavior [5]. Among these geometries, re-entrant and anti-tetrachiral lattices have emerged as foundational designs in the field, offering tunable auxetic responses and improved mechanical performance [6].

A wide range of auxetic topologies has been explored, as illustrated in Figure 1.7, which showcases various lattice configurations, including: (a) Re-entrant, (b) Trichiral, (c) Double arrowhead, (d) Missing rib, (e) Missing rib, (f) Hexachiral, (g) Anti-tetrachiral, (h) Anti-trichiral, (i) Trichiral, (j) Star-shaped, (k) Rotational, (l) Perforated, (m) Perforated, (n) Elliptical, and (o) S-shaped designs [18].

Additional examples of auxetic core structures are presented in Figure 1.8, illustrating different core geometries such as: (a) Honeycomb, (b) Re-entrant, (c) Arrowhead, and (d) Anti-tetrachiral [19]. In these sandwich panel configurations, the top and bottom plates are referred to as the face sheets, while the central layer is known as the cellular core.

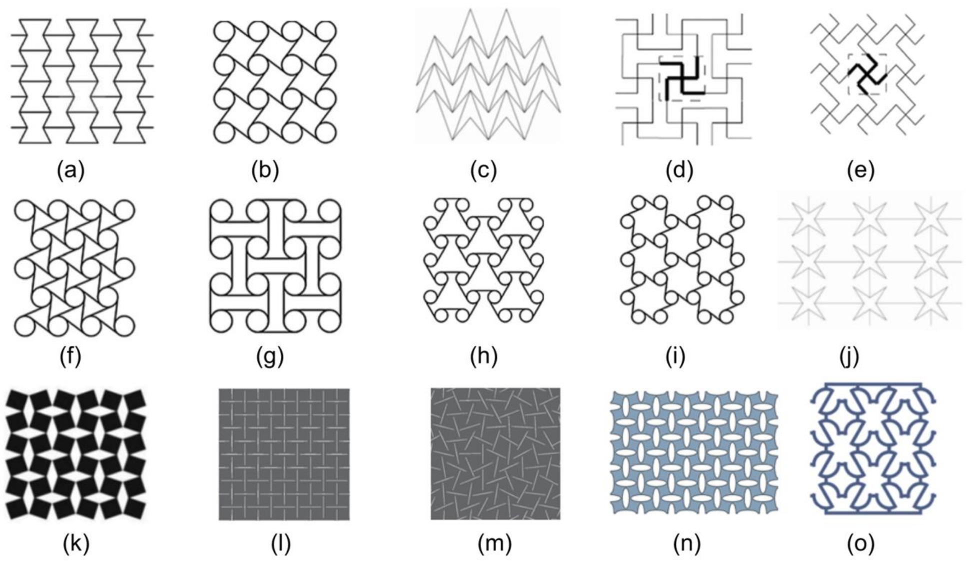

Figure 1.7: Illustration of diverse 2D auxetic and lattice unit cell geometries [18].

Reproduced from [18] under the Creative Commons Attribution (CC BY 4.0) license.

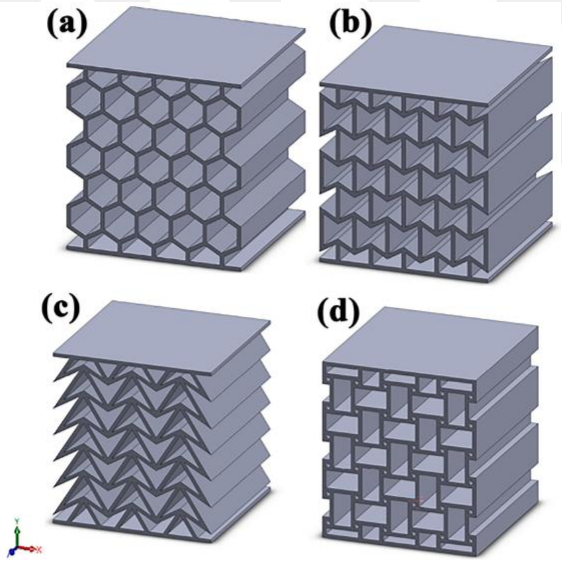

Figure 1.8: Various core geometries in sandwich structures [19].

Reproduced from [19] with permission of Spring Nature.

Auxetic lattices deform differently from conventional materials: re-entrant structures expand laterally under tensile loading, while anti-tetrachiral structures enable isotropic auxetic behavior through the rotation of rigid elements [7].

Additive manufacturing (AM) has played a pivotal role in the realization of complex auxetic architectures, enabling the fabrication of intricate lattice geometries with controlled material properties [1]. However, AM also introduces challenges, including geometric inaccuracies, residual stresses, and anisotropy resulting from the layer-by-layer build process [1]. These imperfections can significantly affect the mechanical response of auxetic structures and must be carefully considered in both experimental and numerical investigations.

Full-scale FEA remains the primary tool for studying the mechanical behavior of auxetic structures. Full-scale models, which explicitly resolve the geometry of each unit cell, provide the highest fidelity and are essential for capturing detailed stress distributions, local deformations, and failure mechanisms. However, the computational demands of such models increase exponentially with system size and mesh density, rendering them impractical for large-scale assemblies or iterative design processes [12].

Homogenization methods offer an attractive alternative by approximating the periodic architecture of auxetic lattices as an equivalent orthotropic continuum. Foundational work by Bensoussan et al. and Terada and Kikuchi established the theoretical basis for computational homogenization, introducing frameworks for multi-scale analysis of periodic structures [20]. Recent advancements, including the strain-based expansion method and the variational asymptotic method (VAM)-based approach, have further enhanced the accuracy and applicability of homogenization techniques for complex lattice designs.

2.MATERIAL AND METHOD

The primary objective of this study is to explore the use of the homogenization method as an effective strategy for modeling complex lattice geometries in a simplified manner, thereby enabling finite element analysis (FEA) with reduced modeling complexity, computational solve time, and associated costs. The study also aims to investigate the capabilities and limitations of the homogenization method by conducting comparative analyses across various numerical models and analysis types. Numerical homogenization involves determining effective material properties by establishing energy equivalence between full-scale (real-case) geometries and homogenized (simplified-case) representations. This approach facilitates the modeling and analysis of complex lattice structures by replacing detailed geometries with simplified continuum models that incorporate homogenized material properties, as opposed to using fully resolved geometries with isotropic material definitions. As a result, this method significantly reduces the meshing requirements and computational effort while maintaining sufficient accuracy for engineering analysis.

This thesis focuses on two specific auxetic structures: the re-entrant lattice design and the anti-tetrachiral lattice design. Both structures belong to the class of auxetic metamaterials, which have gained widespread attention in the field of additive manufacturing due to their unique mechanical properties, particularly their NPR and enhanced energy absorption capabilities. The full-scale geometry of the re-entrant structure is presented in Figure 2.1, with its corresponding 3D CAD model shown in Figure 2.2. Similarly, the full-scale geometry of the anti-tetrachiral structure is presented in Figure 2.3, and its 3D CAD model is shown in Figure 2.4. The simplified-scale 3D CAD geometry, which serves as the homogenized model for both structures, is shown in Figure 2.5.

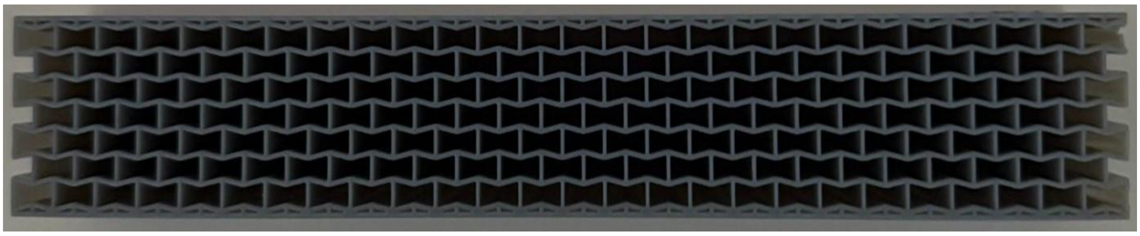

Figure 2.1: Re-entrant lattice structure.

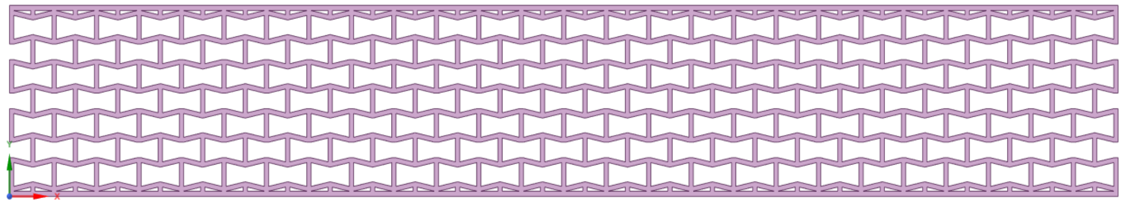

Figure 2.2: Re-entrant lattice structure 3D model.

Figure 2.3: Anti-tetrachiral lattice structure.

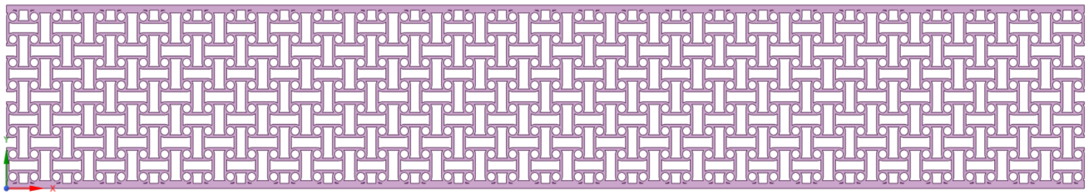

Figure 2.4: Anti-tetrachiral lattice structure 3D model.

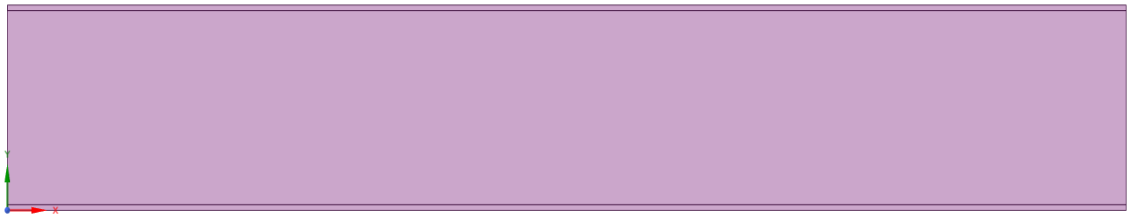

Figure 2.5: Simplified geometry.

The study began with the 3D modeling of two widely studied auxetic lattice designs: the re-entrant and anti-tetrachiral structures. The geometric configurations of both designs were based on standard lattice unit topologies commonly found in the literature. Siemens NX 12 software was used to generate the detailed 3D models of these structures.

The designed geometries were fabricated using additive manufacturing technology, by using a Stratasys Objet Connex 1 3D printer with the material jetting method (MJM). VeroBlue RDG840 polymer was selected as the base material, while solution-soluble SUP706B served as the support material. The parts were printed in high-quality mode with a horizontal build layer thickness of 16 microns, ensuring precise reproduction of the intricate lattice geometries. Following fabrication, support structures were removed from the main parts using a sodium hydroxide solution.

To determine the fundamental material properties of VeroBlue RDG840, tensile test specimens were fabricated and tested according to standard procedures. The tensile tests provided key isotropic material parameters, including Young’s modulus and Poisson’s ratio, while the material density was measured using the same specimens.

The fabricated auxetic structures were then subjected to a series of experimental tests. Modal testing was conducted to determine their natural frequencies and gain insight into their dynamic behavior. Additionally, three-point bending tests were performed on the same parts to evaluate their flexural performance under bending loading. Cube-shaped specimens with matching lattice configurations were also produced and tested under compression loading to assess their load-bearing behavior. The experimental results from modal, three-point bending, and compression tests provided important data for evaluating the accuracy of the finite element models developed in the numerical phase.

Following the experimental studies, numerical modeling was conducted to simulate and analyze the mechanical behavior of both lattice structures. The homogenization method was employed to derive equivalent material properties for the auxetic cores, replacing the complex lattice geometry with a continuum model for simplified analysis. Sensitivity studies were performed during this process to assess the impact of mesh density, unit cell quantity, and boundary conditions on the accuracy of the homogenized properties. The final homogenized material properties, including density, Young’s modulus, shear modulus, and Poisson’s ratios in the X, Y, and Z directions, were determined using the Material Designer module in ANSYS Workbench 2020 R2 software.

Subsequent numerical analyses included modal response analysis, static compression simulations, and three-point bending simulations for both full-scale and homogenized models of the re-entrant and anti-tetrachiral structures. These simulations were performed using ANSYS Workbench 2020 R2, and results from the two numerical models were compared with each other as well as with the experimental data to assess the effectiveness and reliability of the homogenization approach.

Finally, additional numerical analyses were carried out to investigate the tensile behavior of the structures under axial loading in the X and Y directions separately. These tensile simulations were performed solely for numerical comparison, providing further insight into the mechanical response of the auxetic cores under diverse loading conditions.

2.1.Geometry Details

The re-entrant and anti-tetrachiral geometries were chosen for this study based on their extensive use as auxetic lattice structures in additive manufacturing and their proven mechanical performance in diverse engineering applications. The geometries were generated using Siemens NX 12 software. Dimensional specifications for both lattice configurations are presented in the following sections.

2.1.1.Re-entrant structure

The external dimensions of the re-entrant structure are as follows: the width in the X-direction is 232.3 millimeters (mm), the height in the Y-direction is 36.6 mm, as shown in Figure 2.6, and the depth in the Z-direction is 36.0 mm, as illustrated in Figure 2.7. Detailed dimensions of the re-entrant unit cell geometry are presented in Figure 2.8 and Figure 2.9.

The surface area of the front or back face in the X–Y plane is calculated as 2986 mm^2, and the total volume of the part is 107,487 mm^3.

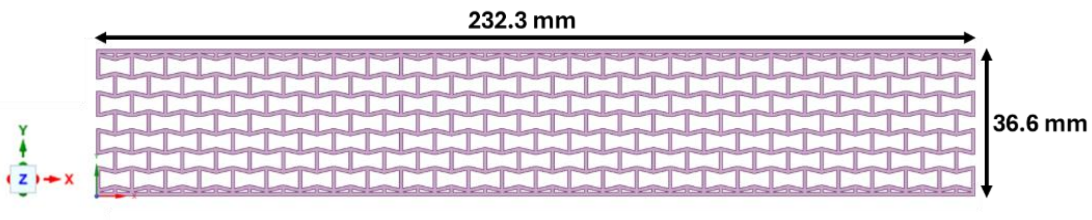

Figure 2.6: Width and Height for Re-entrant structure.

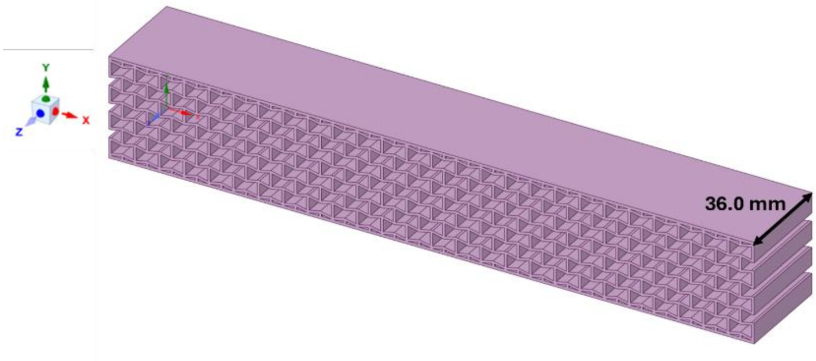

Figure 2.7: Depth for Re-entrant structure.

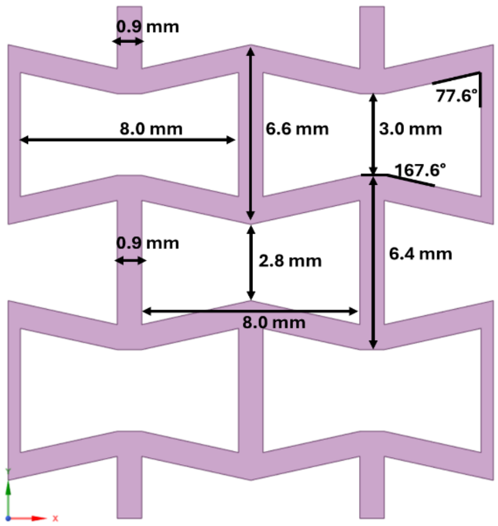

Figure 2.8: Detailed Re-entrant geometry.

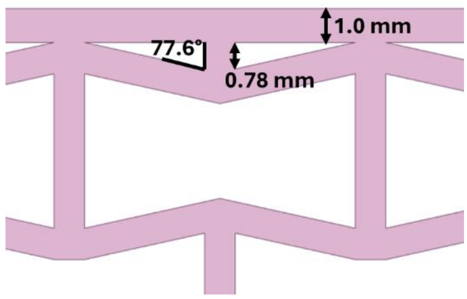

Figure 2.9: Top and Bottom plate dimensions for Re-entrant structure.

2.1.2.Anti-tetrachiral structure

The external dimensions of the anti-tetrachiral structure are as follows: the width in the X-direction is 226.8 millimeters (mm), the height in the Y-direction is 36.6 mm, as shown in Figure 2.10, and the depth in the Z-direction is 36.0 mm, as shown in Figure 2.11. The detailed geometric specifications of the anti-tetrachiral unit cell are provided in Figure 2.12 and Figure 2.13.

The surface area of the front or back face in the X–Y plane is calculated as 3039 mm², and the total volume of the structure is 109,394 mm³.

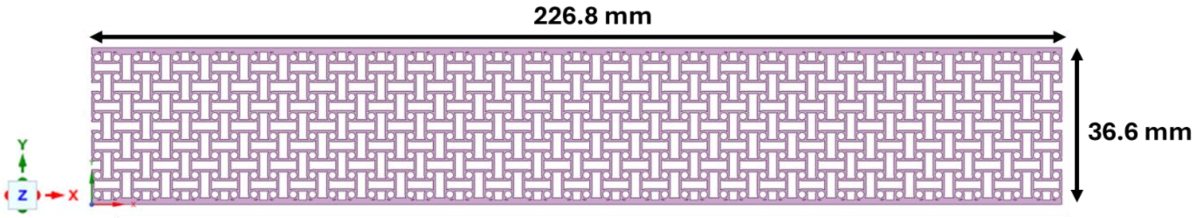

Figure 2.10: Width and Height for Anti-tetrachiral structure.

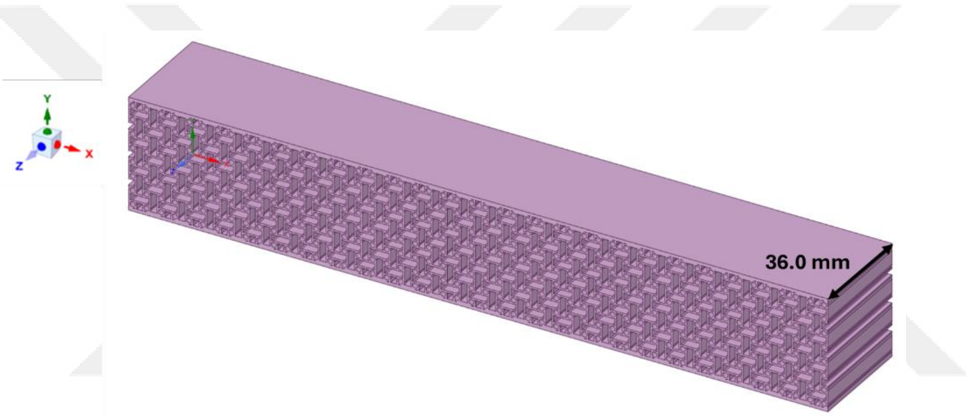

Figure 2.11: Depth for Anti-tetrachiral structure.

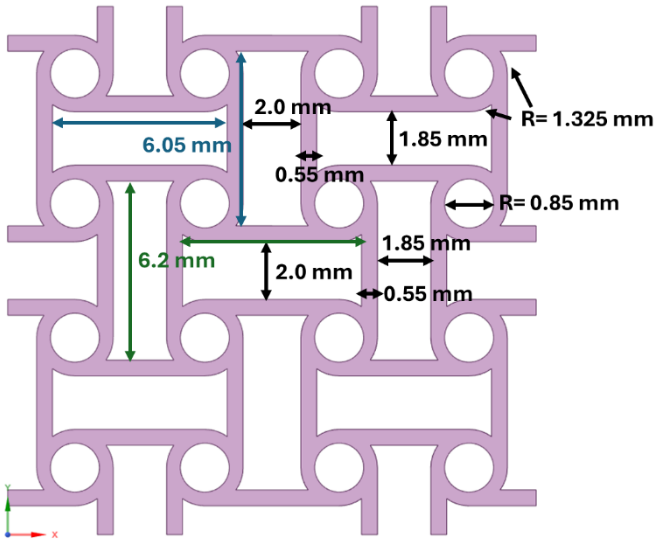

Figure 2.12: Detailed Anti-tetrachiral geometry.

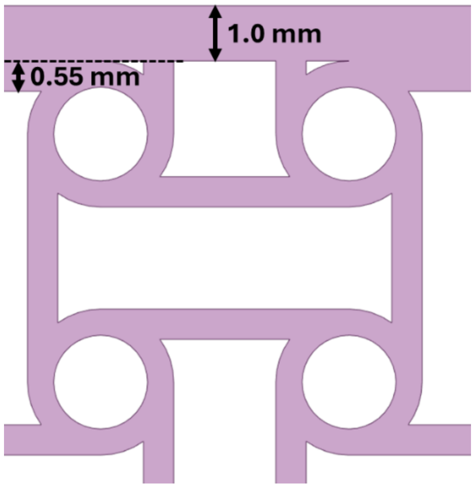

Figure 2.13: Top and Bottom plate dimensions for Anti-tetrachiral structure.

2.2. Extraction of Isotropic Material Properties of Veroblue RDG840

To determine the isotropic material properties of the base material, tensile tests were conducted using an MTS 647 Hydraulic Wedge Grips universal testing, with data acquisition performed through the MTS 793 Series Controller Software. A constant crosshead velocity of 2 mm/min was applied throughout the testing process. To ensure accurate displacement and strain measurements, three strain gauges were placed on the specimens at angles of 0°, 45°, and 90°.

Two tensile test coupons were fabricated for the experiment, each having a cross-sectional area of 78 mm² (13 mm × 6 mm). The detailed geometry of the test specimens is illustrated in Figure 2.14, Figure 2.15, and Figure 2.16.

Following the tensile tests, load–displacement curves were extracted and subsequently converted into stress–strain curves for further analysis. These stress–strain curves were used to determine the isotropic material properties of the specimens, including Young’s modulus and Poisson’s ratio.

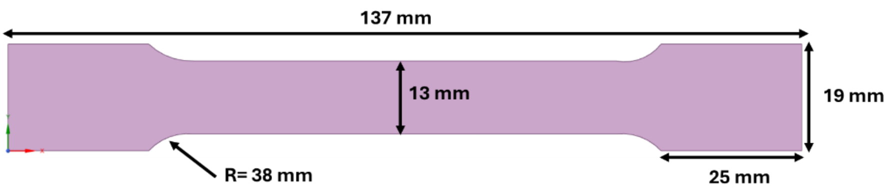

Figure 2.14: Width and Height for tensile test specimen.

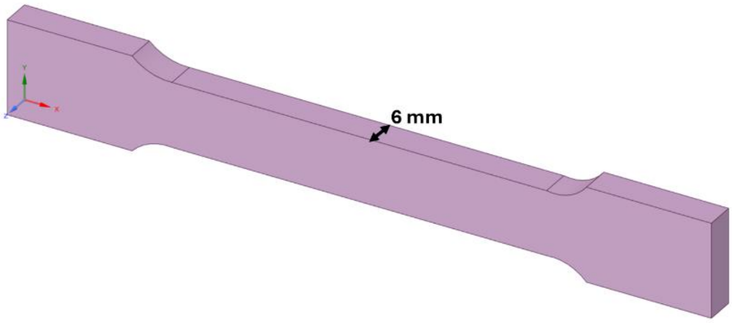

Figure 2.15: Depth for tensile test specimen.

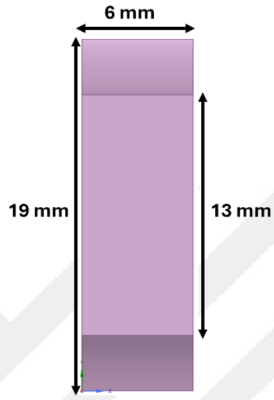

Figure 2.16: Height and Depth for tensile test specimen.

The VeroBlue polymer family, including the VeroBlue RGD840 material, is developed and manufactured by Stratasys, Ltd. According to the technical datasheet provided by Stratasys, the material properties of VeroBlue RGD840 [21] are summarized in Figure 2.17. This polymer exhibits isotropic mechanical behavior, with an elastic modulus ranging from 2000 MPa to 3000 MPa, a flexural modulus between 1900 MPa and 2500 MPa, and a density between 1.18 and 1.19 g/cm³. Additionally, values reported in the literature indicate that the Poisson's ratio for VeroBlue RGD840 ranges from 0.39 to 0.49, and a tensile strength ranging from 50 MPa to 60 MPa.

VeroBlue RGD840 is primarily used as a prototyping material in 3D printing applications due to its favorable mechanical and processing properties. It is classified as a thermoplastic material according to the technical specifications provided in the open literature [22].

Vero PolyJet resins are photopolymer materials designed for high-precision material jetting in additive manufacturing. These materials enable the production of parts with fine feature details and smooth surface finishes, making them well-suited for rapid prototyping applications. [23].

The material jetting process, used in PolyJet 3D printing, involves depositing liquid photopolymer droplets through an array of nozzles onto a build platform, layer by layer. The material jetting process is illustrated in Figure 2.18 [23]. Each layer is immediately cured and solidified using UV light, allowing complex geometrs to be built with fine resolution. Supports are typically printed simultaneously using a dissolvable material and later removed during post-processing [23].

The material properties of VeroBlue RGD840 from open sources are provided in [24, 25, 26].

PolyJet Materials Data Sheet

stratasys

MATERIALS SIMULATING STANDARD PLASTICS

Rigid Opaque Materials

Veroblue RGD840

	ASTM	Units	Value
Tensile strength	D-638-03	MPa (psi)	50-60 (7250-8700)
Elongation at break	D-638-05	% (%)	15-25 (15-25)
Modulus of elasticity	D-638-04	MPa (psi)	2000-3000 (290,000-435,000)
Flexural Strength	D-790-03	MPa (psi)	60-70 (8700-10200)
Flexural Modulus	D-790-04	MPa (psi)	1900-2500 (265,000-365,000)
HDT, oC @ 0.45MPa	D-648-06	°C (°F)	45-50 (113-122)
HDT, oC @ 1.82MPa	D-648-07	°C (°F)	45-50 (113-122)
Izod Notched Impact	D-256-06	J/m (ft lb/inch)	20-30 (0.375-0.562)
Water Absorbtion, %	D-570-98 24hr	% (%)	1.5-2.2 (1.5-2.2)
Tg	DMA, E»	°C (°F)	48-50 (118-122)
Shore Hardness (D)	Scale D	Scale D (Scale D)	83-86 (83-86)
Rockwell Hardness	Scale M	Scale M (Scale M)	73-76 (73-76)
Polymerized density	D792	g/cm3 (---)	1.18-1.19 (---)
Ash content	USP281	% (%)	0.21-0.22 (0.21-0.22)

Figure 2.17: Material properties of VeroBlue RGD840 polymer as provided by Stratasys Company [21].

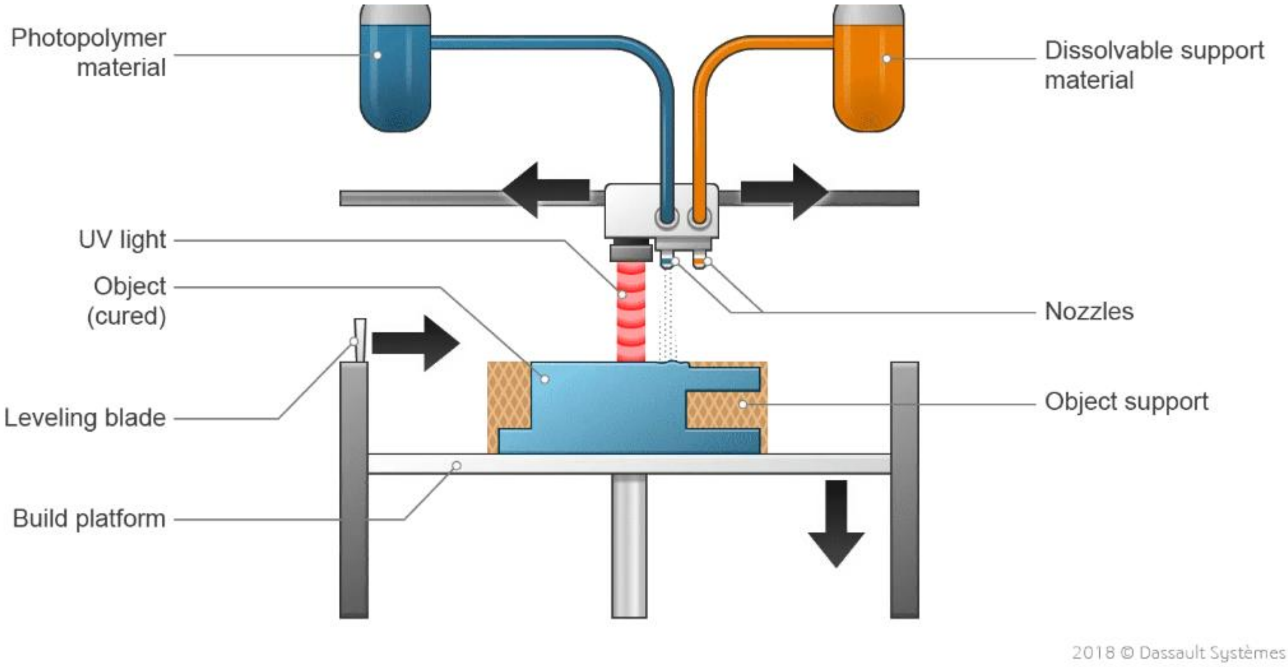

Figure 2.18: Material Jetting 3D printing manufacturing technique [23].

2.2.1.Tensile test result

The tensile test setup is illustrated in Figure 2.19 and Figure 2.20, corresponding to the first and second test specimens, respectively. Tensile tests were conducted using an MTS universal testing machine, equipped with MTS 647 Hydraulic Wedge Grips, while data acquisition was performed through the MTS 793 Series Controller Software. A constant crosshead velocity of 2 mm/min was applied during all tests to ensure consistent loading conditions.

To capture accurate displacement and strain measurements, three strain gauges were affixed to each specimen at orientations of 0°, 45°, and 90°. Two tensile test coupons, each with a cross-sectional area of 78 mm² (13 mm × 6 mm), were prepared for the experiment. The geometric details of the specimens are presented in Figure 2.14, Figure 2.15, and Figure 2.16.

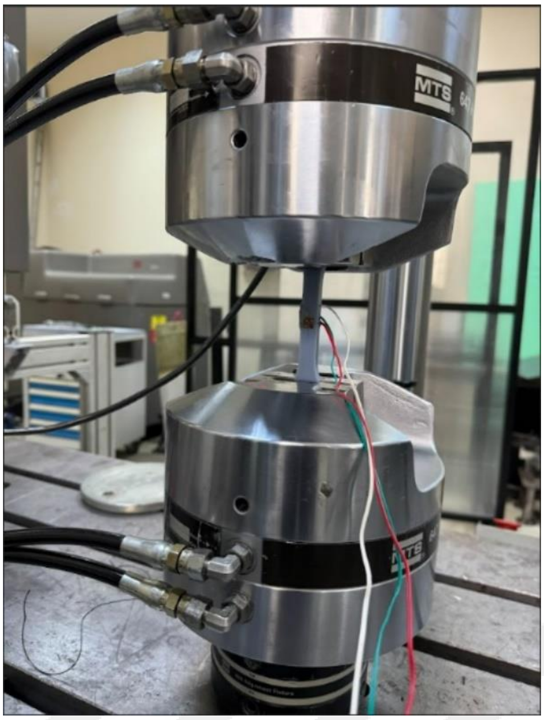

Figure 2.19: Tensile test setup for the first specimen.

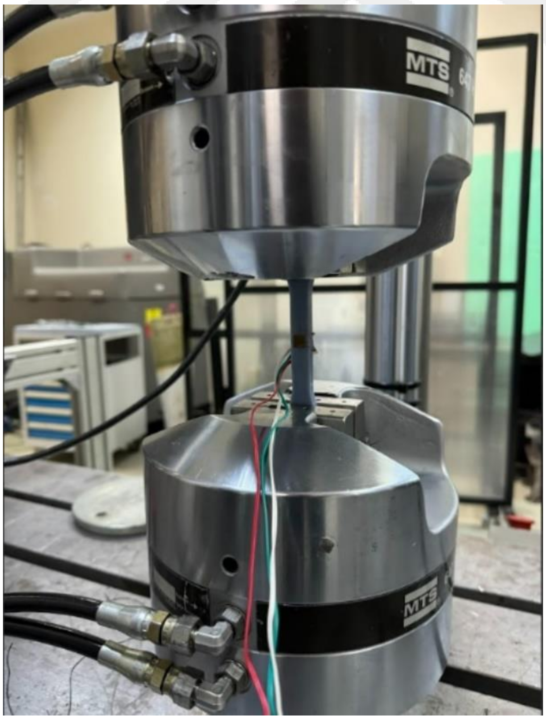

Figure 2.20: Tensile test setup for the second specimen.

Following the tensile tests, the applied load and corresponding displacement curves were extracted. The force and strain versus time graphs, limited to the linear elastic region, are presented in Figure 2.21 and Figure 2.22.

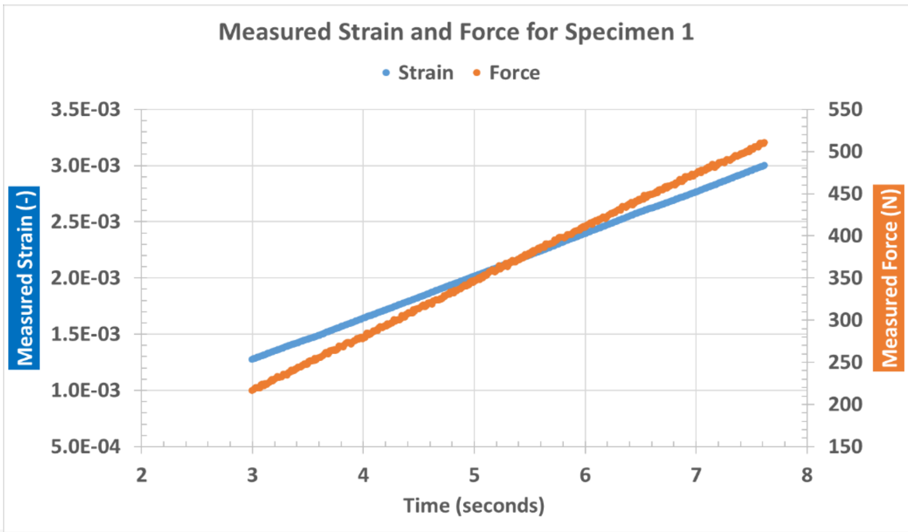

Figure 2.21: Measured strain and force for the first tensile test specimen.

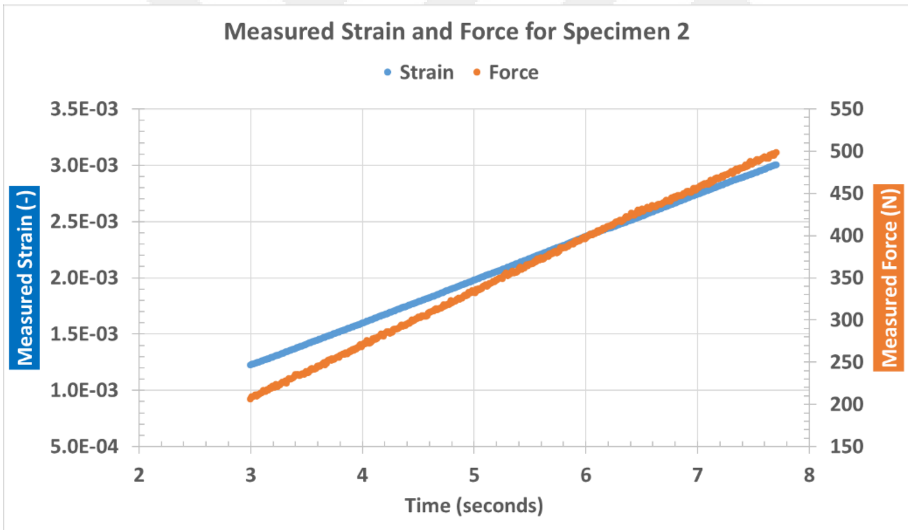

Figure 2.22: Measured strain and force for the second tensile test specimen.

The microstrain data recorded from all three strain gauges is presented in Figure 2.23 and Figure 2.24 for both specimens. The strain gauge connected to the white cable measured longitudinal strain at 0 degrees, the green cable captured shear strain at 45 degrees, and the red cable measured lateral strain at 90 degrees. This multi-directional measurement approach provides a clearer understanding of the material's strain distribution and deformation characteristics under tensile loading.

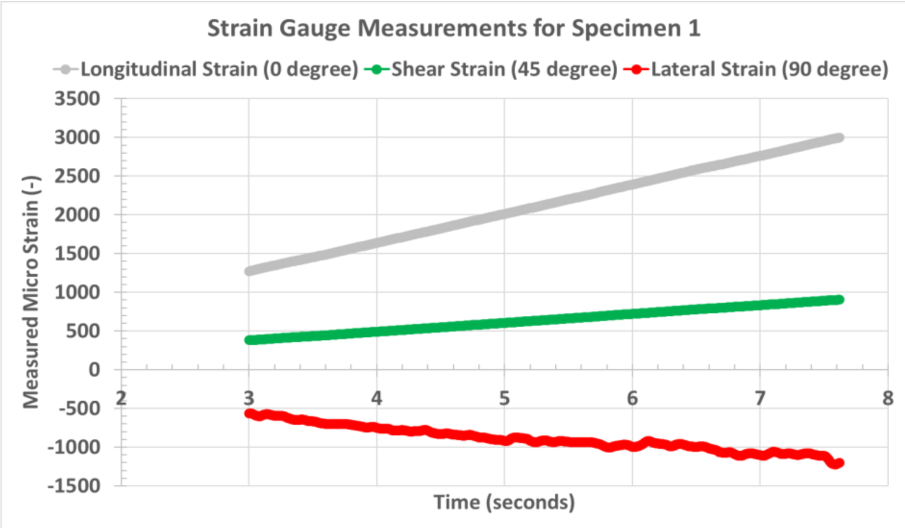

Figure 2.23: Strain gauge data for the first tensile test specimen.

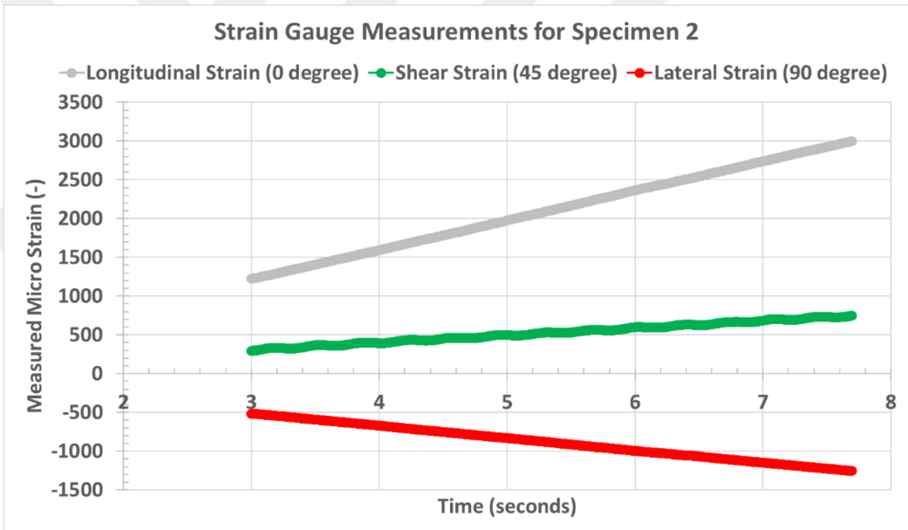

Figure 2.24: Strain gauge data for the second tensile test specimen.

Stress values were calculated using Equation 2.1, based on the measured force and the cross-sectional area of the specimens. The resulting stress–strain curves, derived from the calculated stress and measured strain data, are presented in Figure 2.25 and Figure 2.26.

$$\sigma = F/A \tag{2.1}$$

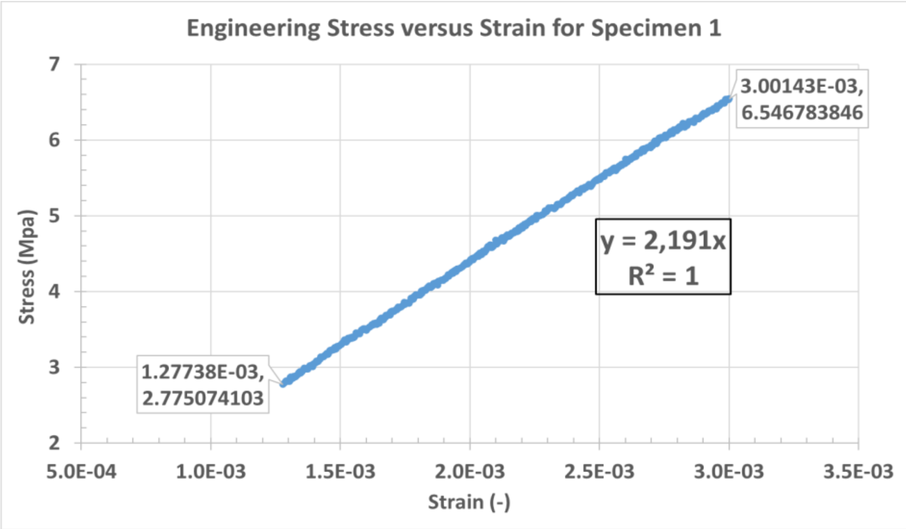

Figure 2.25: Stress vs. strain curve for the first tensile test specimen.

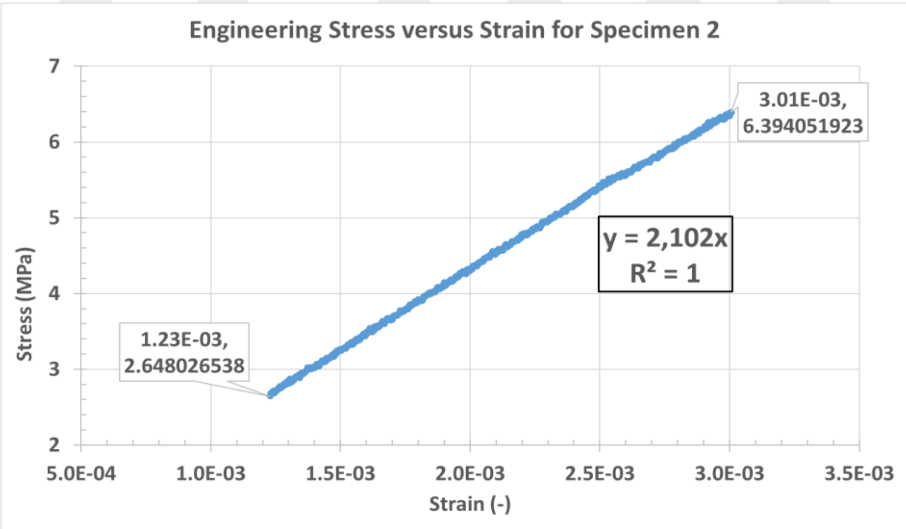

Figure 2.26: Stress vs. strain curve for the second tensile test specimen.

Based on Equation 2.2 and Equation 2.3, the calculated stress and measured strain values were used to determine the modulus of elasticity. The modulus of elasticity versus strain graphs are presented in Figure 2.27 and Figure 2.28, respectively. In both graphs, a linear relationship is observed between stress and strain within the elastic region, allowing the application of a linear trendline with an R^2 value of 1. Furthermore, Equation 2.4 was employed to calculate Young’s modulus, giving values of 2188 MPa and 2104 MPa for specimens 1 and 2, respectively.

For the first specimen, the slope of the trendline indicates a modulus of elasticity of approximately 2191 MPa, while for the second specimen, the value is approximately 2102 MPa. In accordance with ASTM D3039/D3039M (Standard Test Method for Tensile Properties of Polymer Matrix Composite Materials) and ASTM D638 (Standard Test Method for Tensile Properties of Plastics), the data is presented only within the range of 1000 microstrain to 3000 microstrain, to accurately represent the elastic region.

Based on these guidelines, the modulus of elasticity was determined as approximately 2200 MPa for the first specimen (shown in Figure 2.27) and 2150 MPa for the second specimen (shown in Figure 2.28), both within the selected strain range.

$$\sigma = E\,\varepsilon \tag{2.2}$$

$$E = \sigma/\varepsilon \tag{2.3}$$

$$E = (\text{Stress2} - \text{Stress1}) / (\text{Strain2} - \text{Strain1}) \tag{2.4}$$

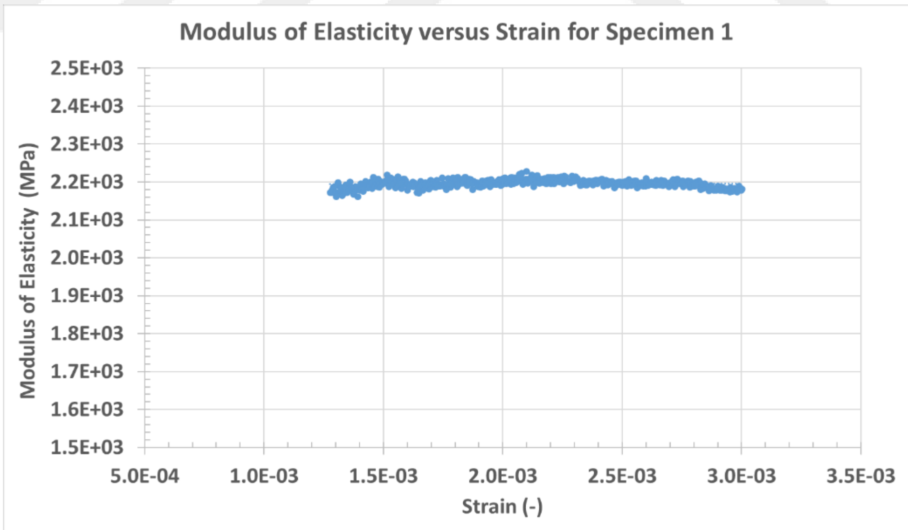

Figure 2.27: Young’s modulus vs. strain curve for the first tensile test specimen.

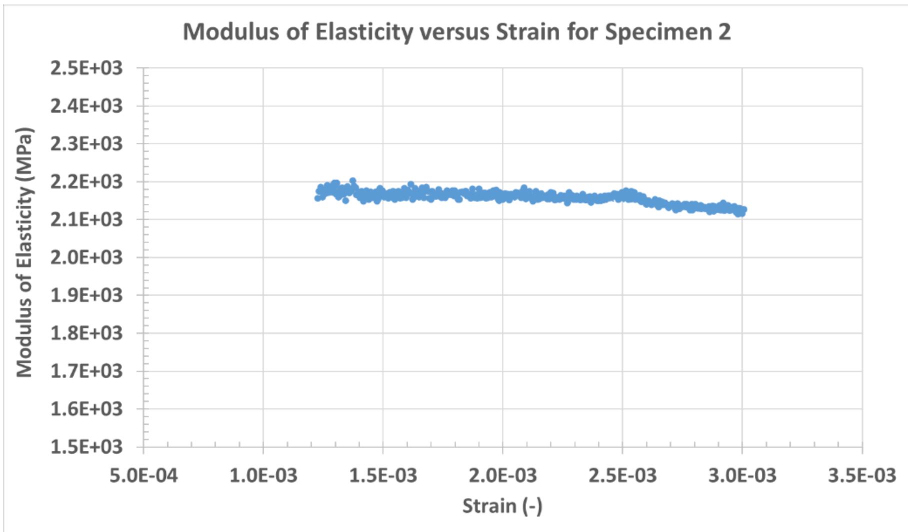

Figure 2.28: Young's modulus vs. strain curve for the second tensile test specimen.

Based on Equation 2.5, the calculated Poisson's ratio versus strain graphs are presented in Figure 2.29 and Figure 2.30, using data limited to the range of 1000 microstrain to 3000 microstrain. For the first specimen, an average Poisson's ratio of approximately 0.422 is observed (shown in Figure 2.29), while the second specimen exhibits an average Poisson's ratio of approximately 0.418 (shown in Figure 2.30).

$$\nu = -\frac{\varepsilon \ lateral}{\varepsilon \ longitudinal} \tag{2.5}$$

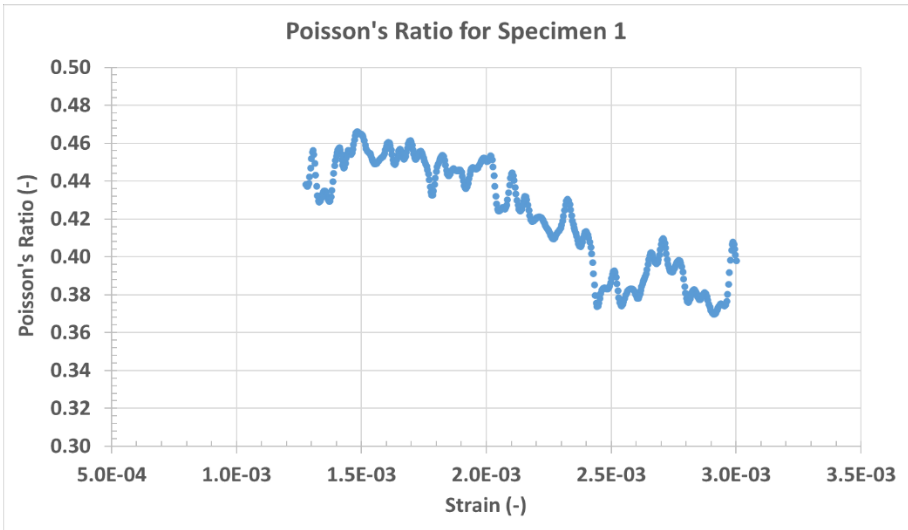

Figure 2.29: Poisson's ratio vs. strain curve for the first tensile test.

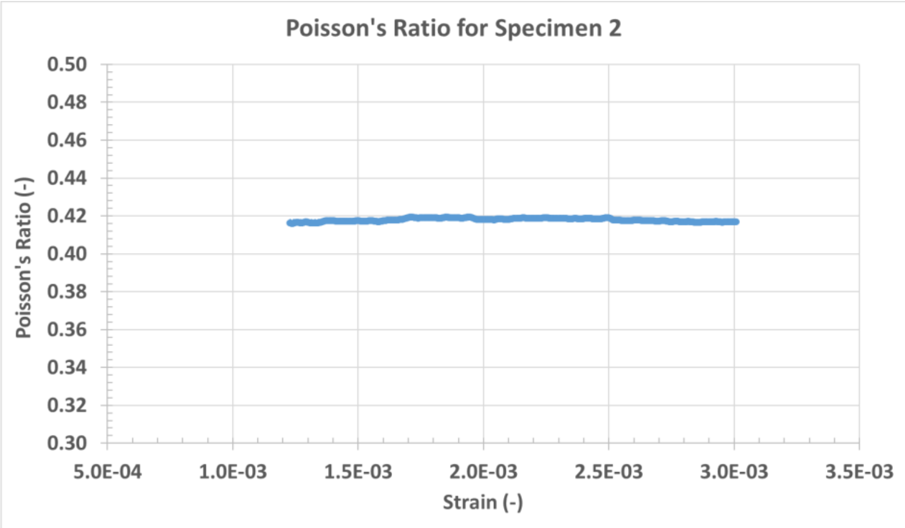

Figure 2.30: Poisson's ratio vs. strain curve for the second tensile test.

The total weight of the re-entrant structure, shown in Figure 2.1, was measured as 127 grams (g) while its total volume was calculated as 107,487 mm^3, resulting in a density of 1.182 grams per cubic centimeter (g/cm^3). Similarly, the total weight of the anti-tetrachiral structure, presented in Figure 2.3, was measured as 130 g, with a calculated volume of 109,394 mm^3, corresponding to a density of 1.188 g/cm^3. Finally, the isotropic material density of the specimens was determined as approximately 1.185 g/cm^3, based on the measured weights and geometrically derived volume.

As a result, by averaging the outcomes of the two test specimens, the isotropic material properties of VeroBlue RDG840 were determined as follows: the modulus of elasticity is 2175 MPa, the Poisson's ratio is 0.42, and the density is 1.185 grams/cm^3. Additionally, the shear modulus was calculated as 766 MPa. All of these material properties are summarized in Table 2.1.

Table 2.1: Isotropic Material Properties of VeroBlue RDG840.

Engineering Constants	Results	Units
E	2.175E+09	Pa
G	7.66E+08	Pa
Nu	0.42	
Density	1.185	g/cm^3

Additionally, the tensile strength of the material was assumed to be 55 MPa, based on the specification sheet provided by Stratasys Company and shown in Figure 2.17.

2.2.2.Compression test result

Compression testing was also carried out in order to characterize the material properties of the part under compressive loads. The compression test setup is illustrated in Figures 2.31 and 2.32, corresponding to the three cubic specimens of the re-entrant structure and the three cubic specimens of the anti-tetrachiral structure, respectively.

Compression tests were conducted using a Shimadzu Autograph AG-IS 50 kN universal testing machine, as shown in Figure 2.33, while data acquisition and control were performed with Shimadzu's Trapezium2 software. A constant crosshead speed of 1 mm/min was applied to specimen 1 for both re-entrant and anti-tetrachiral configurations, with a total stroke of 1 mm. For specimens 2 and 3, a constant speed of 2 mm/min was used, with a total stroke of 2 mm, ensuring consistent loading conditions across all tests. The compression load was applied to the front face in the X–Y plane, while the specimens were fixed at the back face in the same plane, where the auxetic cells are visible, as shown in Figures 2.31 and 2.32.

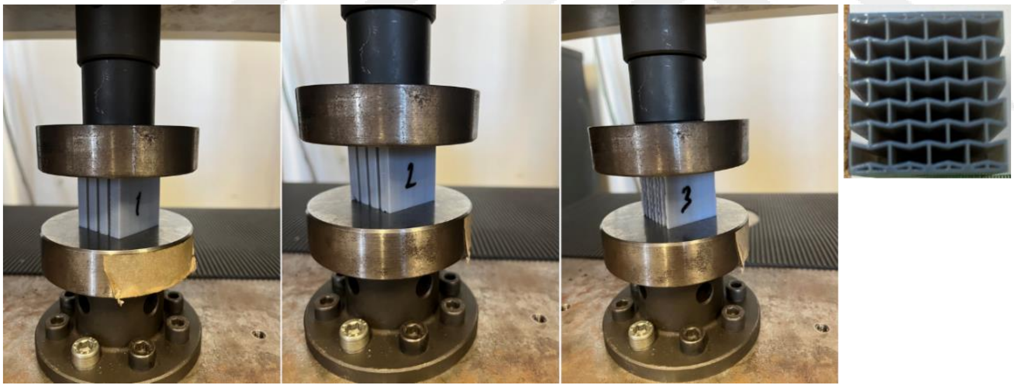

Figure 2.31: Cubic specimens of the re-entrant structure used in the compression test.

Figure 2.32: Cubic specimens of anti-tetrachiral structure used in the compression test.

Figure 2.33: Shimadzu Autograph AG-IS 50 kN universal testing machine.

The geometric details of the compression test specimens are presented in Figure 2.34 for the re-entrant structure and in Figure 2.35 for the anti-tetrachiral structure. The width in the X-direction is reported as the average value of the three cubic specimens, while the height in the Y-direction and the depth in the Z-direction are identical to the dimensions of the individual cubic specimens

For re-entrant specimens, the average width in X-direction is 36.8 mm, the height in Y-direction is 36.6 mm, and the depth in Z-direction is 36.0 mm, as illustrated in Figure 2.34. The corresponding surface area of the front or back face in the X–Y plane is calculated as 511 mm².

For anti-tetrachiral specimens, the average width in X-direction is 37.6 mm, the height in Y-direction is 36.6 mm, and the depth in Z-direction is 36.0 mm, as illustrated in Figure 2.35. The corresponding surface area of the front or back face in the X–Y plane is calculated as 516 mm².

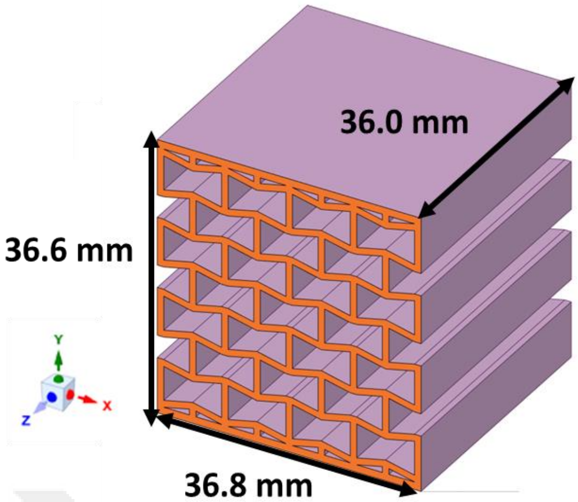

Figure 2.34: Geometric details of re-entrant specimens used in the compression test.

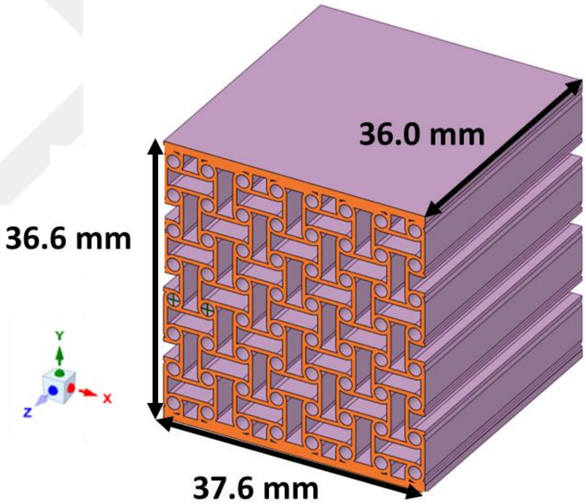

Figure 2.35: Geometric details of anti-tetrachiral specimens used in the compression test.

Following the compression tests, the applied load–displacement curves were extracted. The force–displacement and stress–strain responses over the entire test duration are presented in Figure 2.36, Figure 2.37, and Figure 2.38 for the re-entrant test specimens 1, 2, and 3, respectively. Likewise, Figure 2.39, Figure 2.40, and Figure 2.41 present the corresponding results for the anti-tetrachiral test specimens 1, 2, and 3.

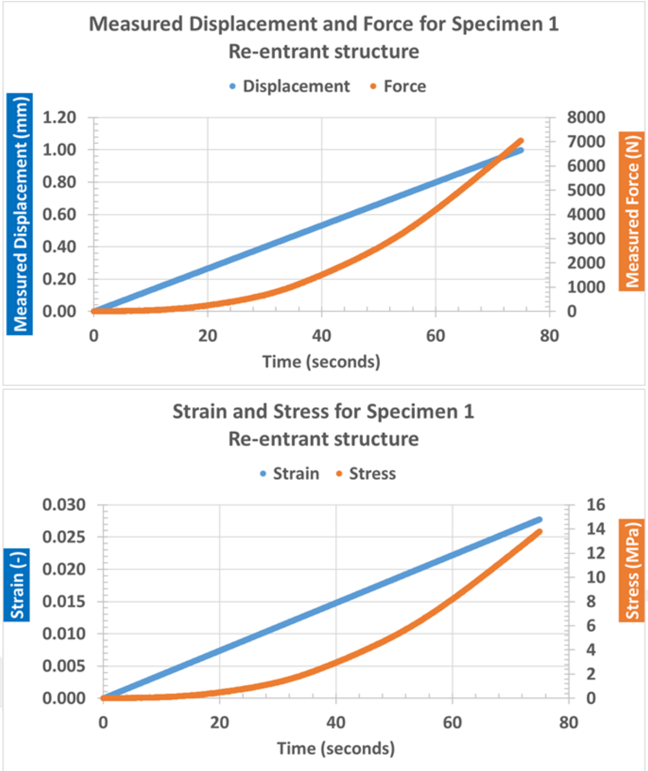

Figure 2.36: Measured load–displacement curve and calculated stress–strain response for the first re-entrant compression test specimen.

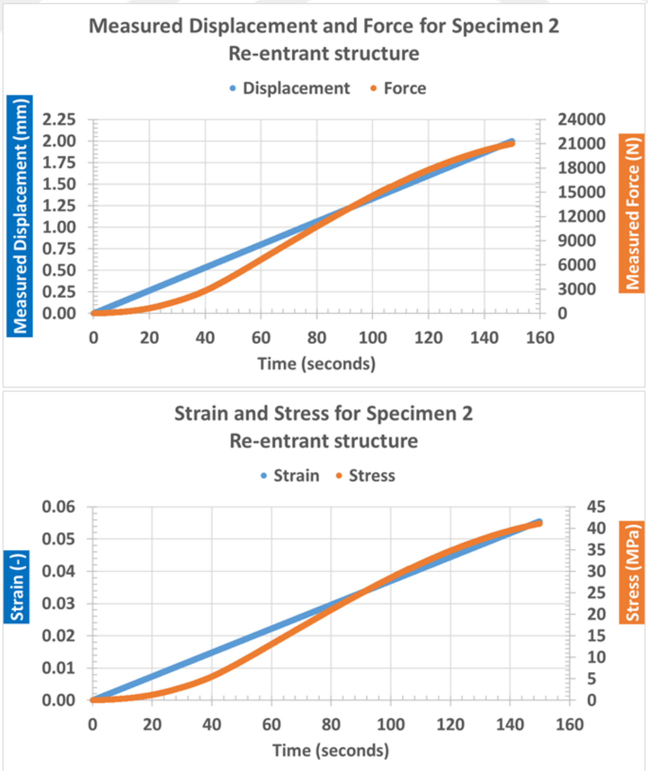

Figure 2.37: Measured load–displacement curve and calculated stress–strain response for the second re-entrant compression test specimen.

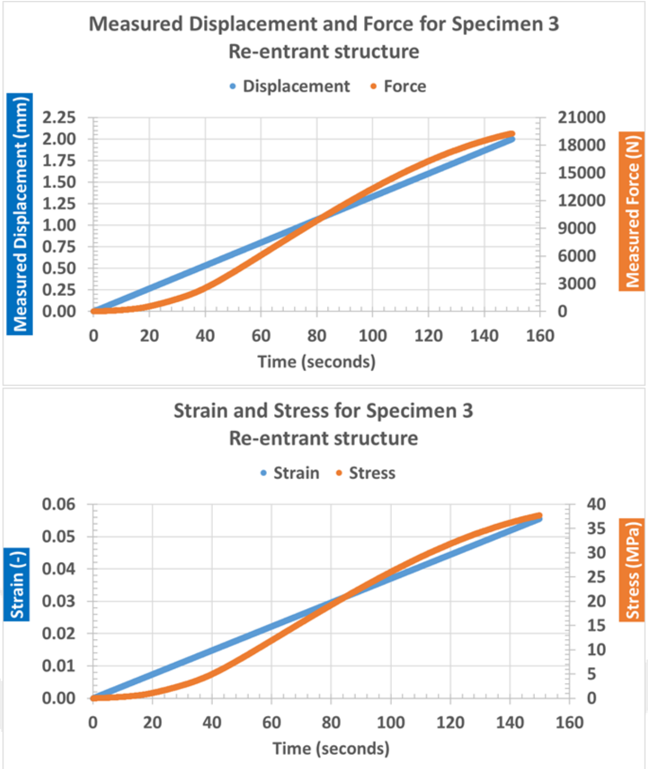

Figure 2.38: Measured load–displacement curve and calculated stress–strain response for the third re-entrant compression test specimen.

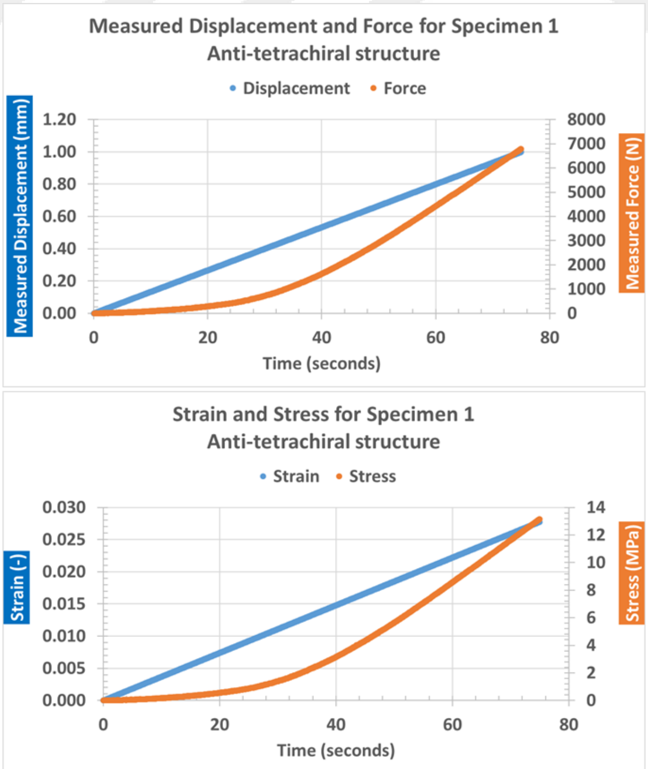

Figure 2.39: Measured load–displacement curve and calculated stress–strain response for the first anti-tetrachiral compression test specimen.

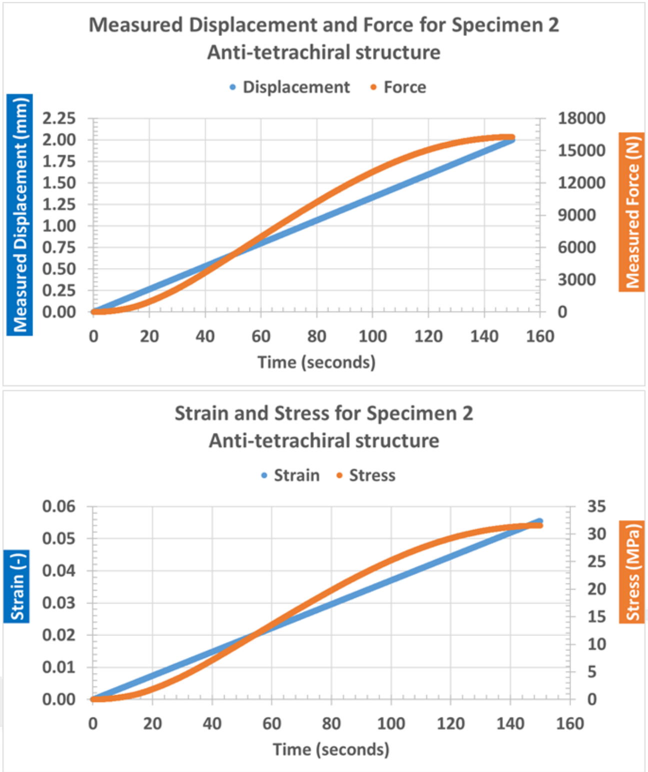

Figure 2.40: Measured load–displacement curve and calculated stress–strain response for the second anti-tetrachiral compression test specimen.

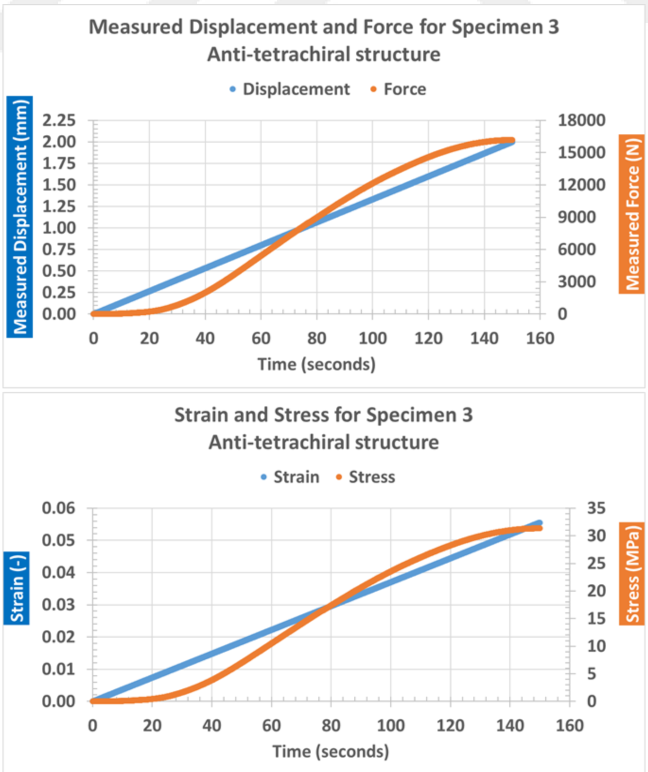

Figure 2.41: Measured load–displacement curve and calculated stress–strain response for the third anti-tetrachiral compression test specimen.

Stress values were calculated using Equation 2.1, based on the measured force and the cross-sectional area of the specimens. The resulting stress–strain curves, derived from the calculated stress and strain data, are presented in Figure 2.42 for the three re-entrant specimens and in Figure 2.43 for the three anti-tetrachiral specimens. The data are shown only within the strain range of 1% to 2% in order to represent the elastic region.

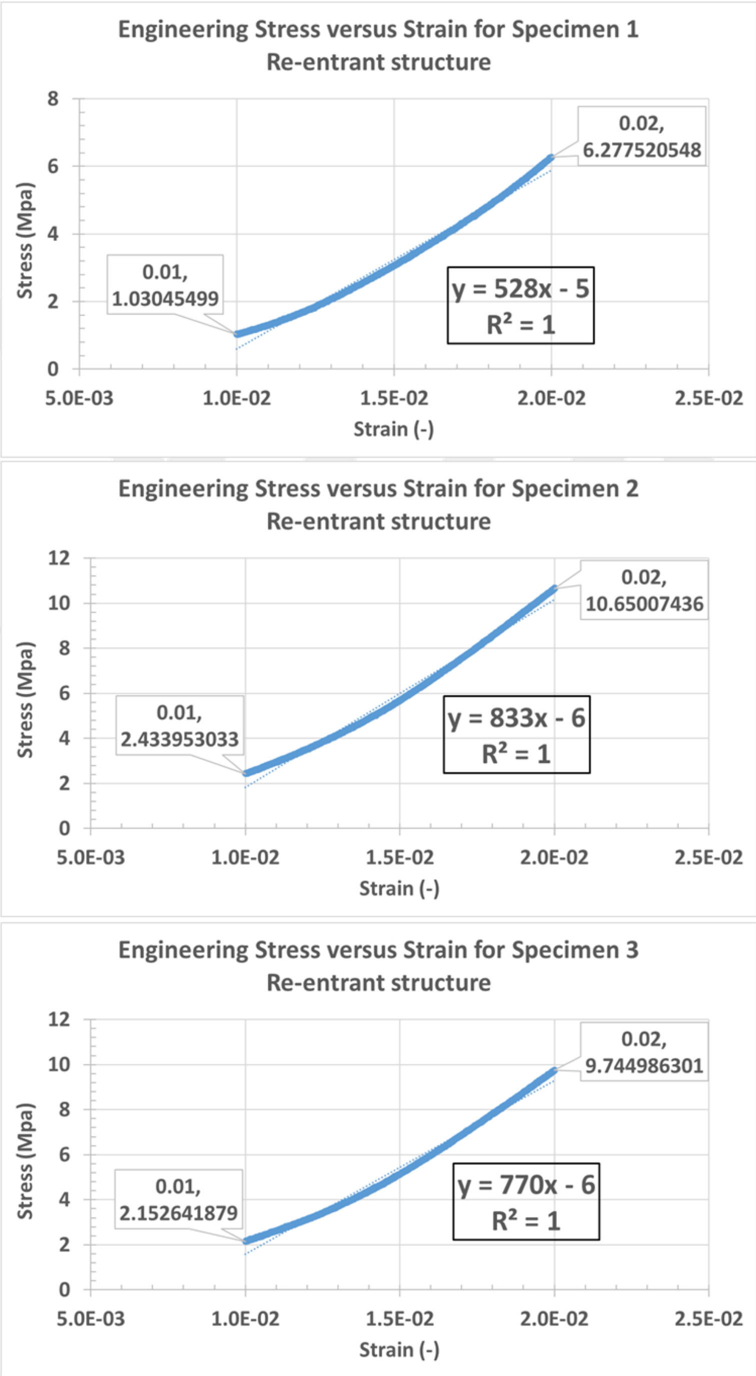

Figure 2.42: Stress vs. strain curves of the re-entrant compression test specimens.

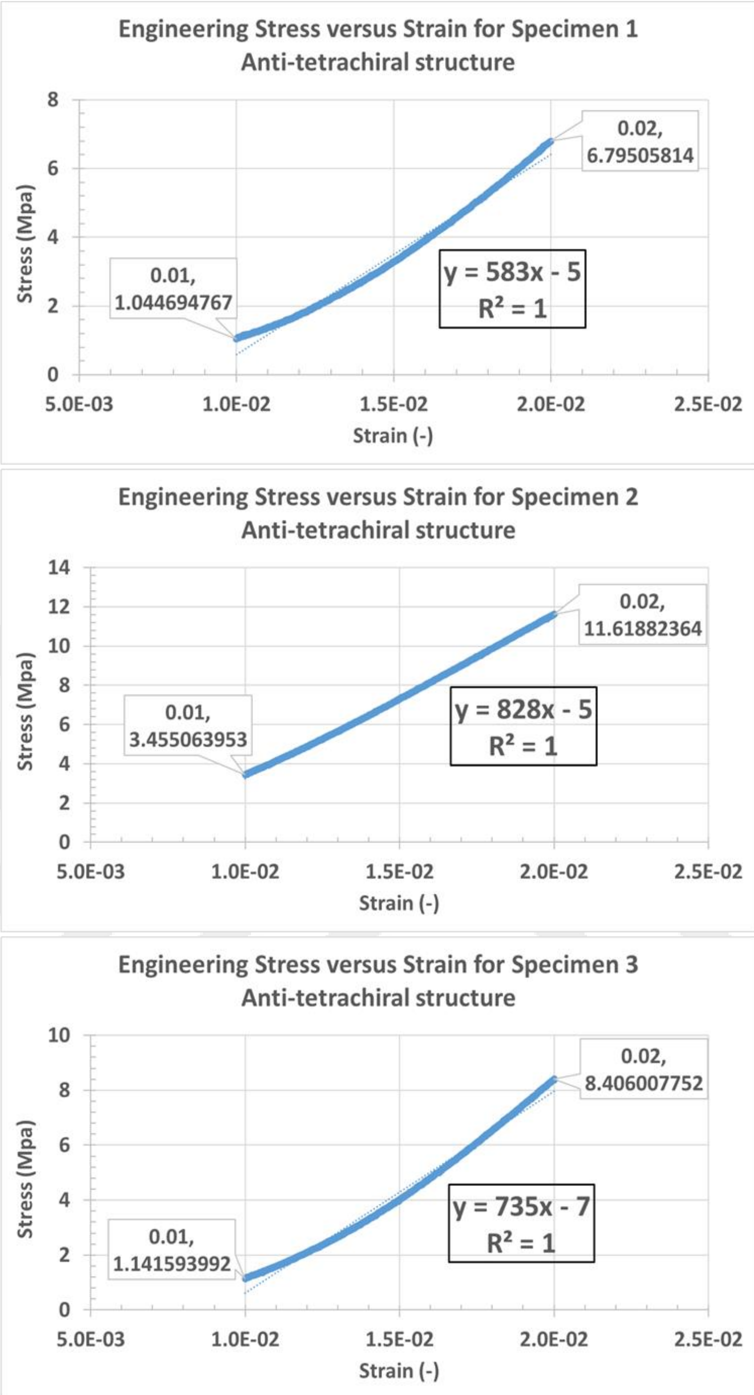

Figure 2.43: Stress vs. strain curves for the anti-tetrachiral compression test specimens.

In all graphs, a linear relationship is observed between stress and strain within the elastic region, allowing the application of a linear trendline with an R^2 value of 1. The modulus of elasticity (E) was calculated using the Equation 2.4.

For the re-entrant specimens, the calculated modulus of elasticity were approximately 525 MPa, 822 MPa, and 759 MPa for specimens 1, 2, and 3, respectively. Since the crosshead speed differed for specimen 1, its result was excluded. Therefore, the modulus of elasticity for the re-entrant structure under compression load was determined to be approximately 790 MPa, calculated as the arithmetic average of specimens 2 and 3.

For the anti-tetrachiral specimens, the calculated modulus of elasticity were approximately 575 MPa, 816 MPa, and 726 MPa for specimens 1, 2, and 3, respectively. Again, the result from specimen 1 was excluded due to the different crosshead speed. Consequently, the modulus of elasticity for the anti-tetrachiral structure under compression load was determined to be approximately 771 MPa, based on the arithmetic average of specimens 2 and 3.

The results of the compression tests showed that the modulus of elasticity of the re-entrant (790 MPa) and anti-tetrachiral (771 MPa) structures with VeroBlue RDG840 base material under compression loading is approximately one-third of the value obtained from tensile testing of the isotropic coupon made from the same material (2175 MPa).

All of these material properties are summarized in Table 2.2 for the re-entrant structure with VeroBlue RGD840 under compression loading, in Table 2.3 for the anti-tetrachiral structure under the same condition, in Table 2.4 for the re-entrant structure based on the average Young's modulus obtained from both tensile and compression tests, and in Table 2.5 for the anti-tetrachiral structure evaluated in the same manner.

Table 2.2: Mechanical properties of the re-entrant structure with VeroBlue RDG840 base material under compression loading.

Engineering Constants	Results	Units
E	7.90E+08	Pa
G	2.78E+08	Pa
Nu	0.42	
Density	1.185	g/cm^3

Table 2.3: Mechanical properties of the anti-tetrachiral structure with VeroBlue RDG840 base material under compression loading.

Engineering Constants	Results	Units
E	7.71E+08	Pa
G	2.72E+08	Pa
Nu	0.42	
Density	1.185	g/cm^3

Table 2.4: Mechanical properties of the re-entrant structure with VeroBlue RDG840, based on the average Young's modulus obtained from tensile and compression tests.

Engineering Constants	Results	Units
E	1.483E+09	Pa
G	5.22E+08	Pa
Nu	0.42	
Density	1.185	g/cm^3

Table 2.5: Mechanical properties of the anti-tetrachiral structure with VeroBlue RDG840, based on the average Young's modulus obtained from tensile and compression tests.

Engineering Constants	Results	Units
E	1.473E+09	Pa
G	5.18E+08	Pa
Nu	0.42	
Density	1.185	g/cm^3

2.3.Homogenization Method Study and Homogenized Material

Analyzing complex geometries with micro-scale features using traditional Finite Element Analysis (FEA) can become computationally challenging and inefficient due to the fine meshing required to capture intricate details. To address these challenges, homogenization techniques are employed as a practical approach to simplify numerical models while maintaining an acceptable level of accuracy. By reducing model size, complexity, and computation time, homogenization enhances productivity and enables efficient analysis of intricate structures that would otherwise be difficult to simulate using full-scale modeling.

Homogenization techniques determine effective material properties by leveraging the principle of energy equivalence between the real-case (full-scale) geometry and its simplified (homogenized) representation. In this approach, explicit unit cells with detailed isotropic material definitions are replaced by equivalent continuum models that exhibit orthotropic or anisotropic behavior, depending on the geometry. This substitution transforms complex, repetitive lattice structures into simpler representations with homogenized properties, thereby reducing computational demands without significantly compromising model fidelity.

One of the key strengths of homogenization lies in its multi-scale capability. This methodology allows material properties derived at the micro-scale, such as stiffness, density, and Poisson's ratio, to be transferred and applied within macro-scale structural analyses. Such hierarchical modeling supports the analysis of complex lattice geometries across different length scales, enabling a balance between computational efficiency and result accuracy.

For homogenization to be meaningful and accurate, the underlying structure must exhibit either strict three-dimensional periodicity or a clear separation of scales across all spatial directions. This principle ensures that the micro-level behavior of a material can be effectively translated into macro-level predictions without compromising model fidelity. The concept of the Representative Volume Element (RVE) is central to this approach, as highlighted by Nemat-Nasser and Hori [27], who define the RVE as the smallest possible volume over which the material's heterogeneity can be averaged to derive its macroscopic properties. The RVE must accurately capture the periodic microstructural behavior so that the homogenized material properties truly reflect the behavior of the entire structure.

Belytschko et al. [28] further emphasize that homogenization is not merely a mathematical convenience but a physical necessity for the efficient simulation of large-scale problems involving complex microstructures. Their work underscores that homogenization, when implemented through unit cell analysis, enables a balanced trade-off between computational efficiency and model fidelity. By applying periodic boundary conditions (PBCs) to the unit cell, artificial edge effects are minimized, allowing the global mechanical behavior of the structure to be reliably predicted from localized analyses. This ensures that the effective material properties derived from homogenization—such as elastic modulus, density, and Poisson's ratio—are valid for use in larger-scale finite element models.

Together, these insights from Nemat-Nasser and Hori [27] and Belytschko et al. [28] highlight the theoretical foundations of homogenization methods and their critical importance in analyzing complex lattice structures such as the auxetic designs studied in this thesis.

At the heart of the homogenization process is the concept of the RVE, which captures the geometric and mechanical characteristics of the repeating structure and serves as the fundamental building block for deriving the effective material properties [27]. These properties, such as density, directional elastic modulus, shear modulus, and Poisson's ratios, are then applied to the simplified finite element models of larger structures. By employing homogenization, the number of elements in the finite element model is drastically reduced, enabling significantly faster solution times while still capturing the essential mechanical response of the complex lattice geometry.

In this study, the homogenization process was conducted in three main phases. First, the representative unit cell was selected, reflecting the basic repeating element based on the geometric characteristics of the re-entrant and anti-tetrachiral lattice designs. Next, a sensitivity analysis was performed to evaluate the influence of geometric parameters, boundary conditions, and mesh convergence on the derived effective properties, ensuring the robustness and reliability of the homogenized material data. Finally, the homogenization analysis was executed using the Material Designer module in ANSYS Workbench 2020 R2. This tool computed the homogenized material properties, including directional elastic modulus, shear modulus, Poisson's ratios, and density, which were subsequently assigned to the simplified-scale models of the auxetic sandwich structures for further FEA simulations.

2.3.1.Unit cell selection

A fundamental element of the homogenization method is the use of a repeating unit cell, commonly referred to as the Representative Volume Element (RVE). The RVE captures the essential geometric and mechanical characteristics of the periodic lattice structure and serves as the foundational building block for deriving effective material properties. By accurately representing the microstructural behavior within this smaller domain, the unit cell enables the use of these properties to the entire structure in a computationally efficient manner.

For this study, the unit cell of the re-entrant auxetic structure was selected based on its geometric features and periodicity, ensuring that it adequately represents the repeating pattern of the full lattice. The geometry of the selected unit cell is illustrated in Figure 2.44, while detailed dimensional information is presented in Figure 2.45.

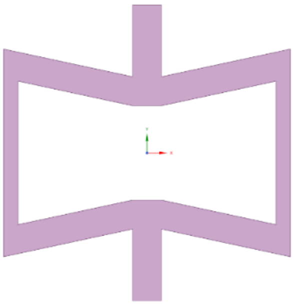

Figure 2.44: Selected unit cell for Re-entrant.

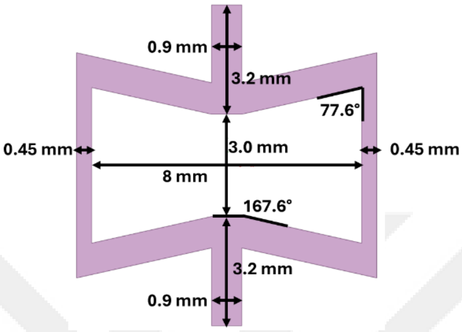

Figure 2.45: Re-entrant unit cell geometry details.

The selected unit cell for the anti-tetrachiral structure is presented in Figure 2.46, with its detailed geometric dimensions illustrated in Figure 2.47.

The selected unit cells for the re-entrant and anti-tetrachiral lattice structures were carefully chosen to represent the periodic geometry and essential mechanical characteristics of each design. By accurately capturing the repeating patterns, these unit cells serve as the foundation for homogenization analyses, enabling the derivation of effective material properties such as elastic modulus, shear modulus, Poisson's ratios, and density. This approach ensures that the simplified models retain the fundamental mechanical behavior of the full-scale structures, while significantly reducing computational complexity in subsequent finite element analyses.

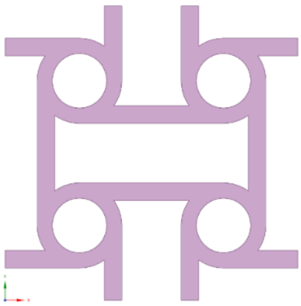

Figure 2.46: Selected unit cell for Anti-tetrachiral.

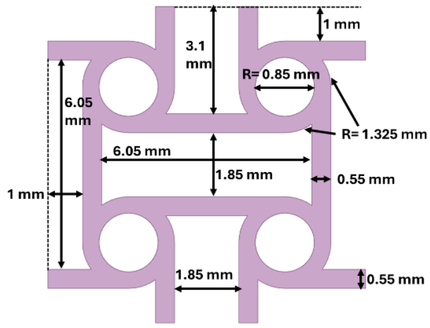

Figure 2.47: Anti-tetrachiral unit cell geometry details.

2.3.2.Homogenization analysis background

To better illustrate the homogenization process works, an example from this thesis study is presented. For the selected unit cells, a 2x2 stack configuration was employed in the X and Y directions, as shown in Figure 2.48 for the re-entrant structure and in Figure 2.49 for the anti-tetrachiral structure.

The homogenization analysis was carried out using the Material Designer module within ANSYS Workbench 2020 R2. This tool performs a series of six static structural simulations on the selected unit cells, each corresponding to a specific loading scenario aligned with the principal material directions. These simulations allow for the extraction of the effective orthotropic material properties that characterize the mechanical behavior of the complex lattice structure. Specifically, the six static analyses involve applying controlled boundary conditions and loads in the X, Y, and Z directions to compute the effective elastic modulus (Ex, Ey, Ez), Poisson's ratios (NUxy, NUxz, NUyz), and shear modulus (Gxy, Gxz, Gyz). By systematically evaluating the response of the unit cell under these loading conditions, the Material Designer generates a complete orthotropic material property set that accurately reflects the behavior of the periodic structure.

This homogenized material definition is then used to assign properties to the simplified-scale models of the re-entrant and anti-tetrachiral structures.

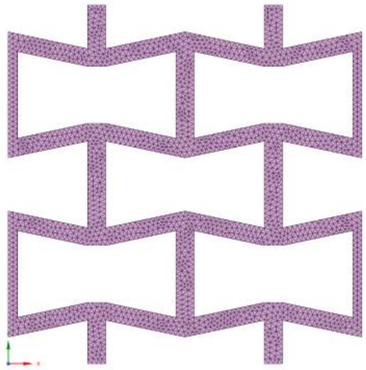

Figure 2.48: 2x2 unit cells for Re-entrant.

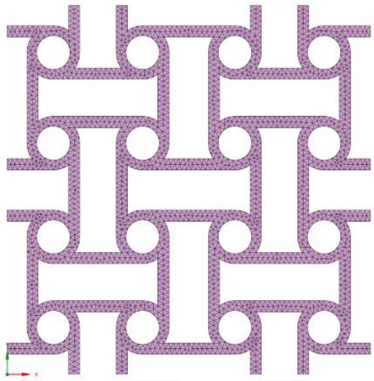

Figure 2.49: 2x2 unit cells for Anti-tetrachiral.

Based on the static X-direction analysis results, with boundary conditions illustrated in Figure 2.50 for the re-entrant structure and Figure 2.51 for the anti-tetrachiral structure, the elastic modulus in the X-direction (Ex) and the Poisson's ratios in the X–Y (NUxy) and X–Z (NUxz) planes were determined.

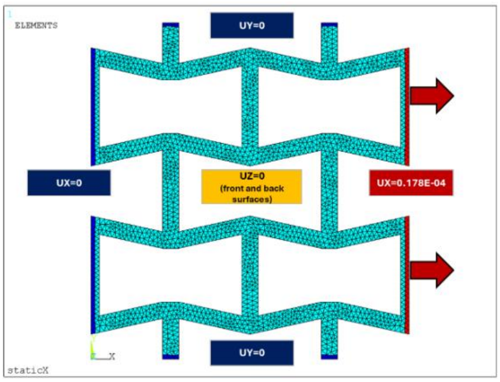

Figure 2.50: Static X analysis for Re-entrant.

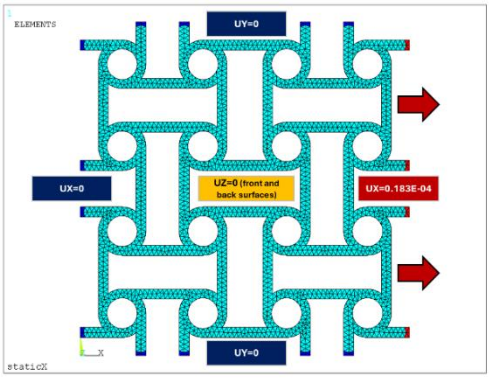

Figure 2.51: Static X analysis for Anti-tetrachiral.

Based on the static Y-direction analysis results, with boundary conditions illustrated in Figure 2.52 for the re-entrant structure and Figure 2.53 for the anti-tetrachiral structure, the elastic modulus in the Y-direction (Ey) and the Poisson's ratios in the X–Y (NUxy) and Y–Z (NUyz) planes were determined.

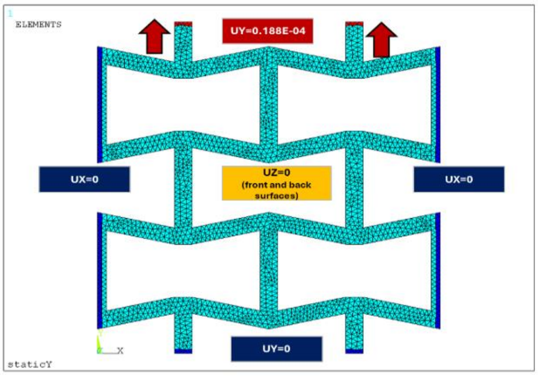

Figure 2.52: Static Y analysis for Re-entrant.

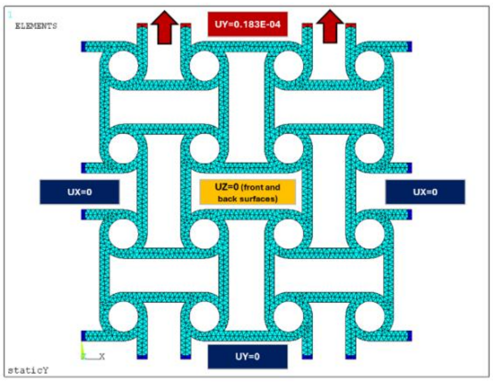

Figure 2.53: Static Y analysis for Anti-tetrachiral.

Based on the static Z-direction analysis results, with boundary conditions illustrated in Figure 2.54 for the re-entrant structure and Figure 2.55 for the anti-tetrachiral structure, the elastic modulus in the Z-direction (Ez) and the Poisson's ratios in the X–Z (NUxz) and Y–Z (NUyz) planes were determined.

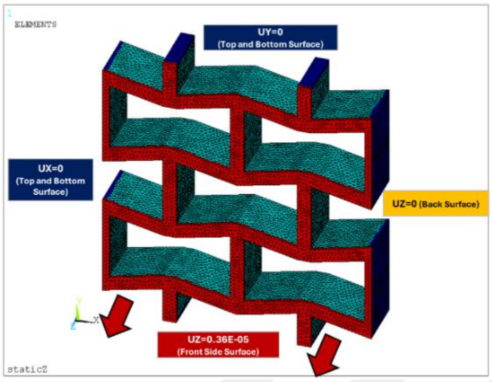

Figure 2.54: Static Z analysis for Re-entrant.

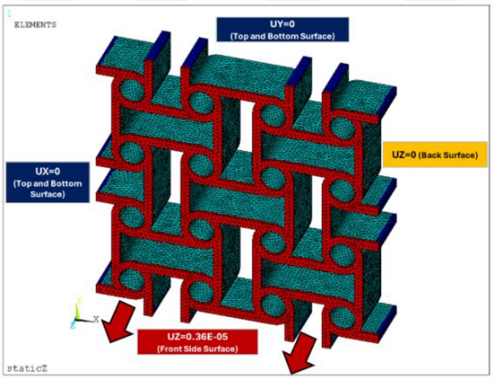

Figure 2.55: Static Z analysis for Anti-tetrachiral.

Based on the static XY-direction analysis results, with boundary conditions shown in Figure 2.56 for the re-entrant structure and Figure 2.57 for the anti-tetrachiral structure, the shear modulus in the X–Y direction (Gxy) was determined.

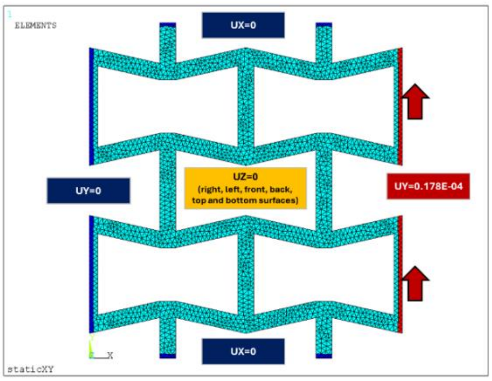

Figure 2.56: Static XY analysis for Re-entrant.

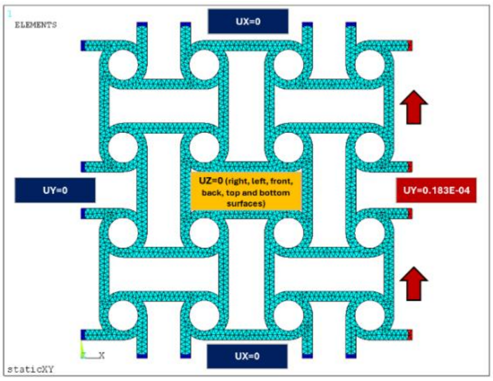

Figure 2.57: Static XY analysis for Anti-tetrachiral.

Based on the static XZ-direction analysis results, with boundary conditions shown in Figure 2.58 for the re-entrant structure and Figure 2.59 for the anti-tetrachiral structure, the shear modulus in the X–Z direction (Gxz) was determined.

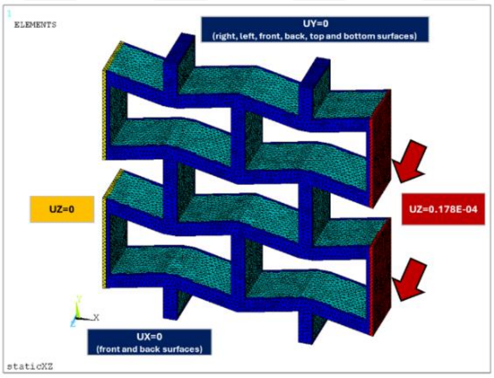

Figure 2.58: Static XZ analysis for Re-entrant.

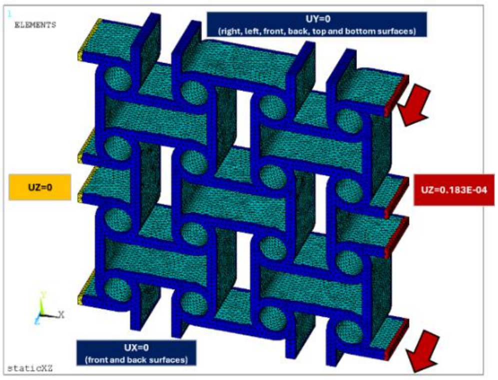

Figure 2.59: Static XZ analysis for Anti-tetrachiral.

Based on the static YZ-direction analysis results, with boundary conditions shown in Figure 2.60 for the re-entrant structure and Figure 2.61 for the anti-tetrachiral structure, the shear modulus in the Y–Z direction (Gyz) was determined.

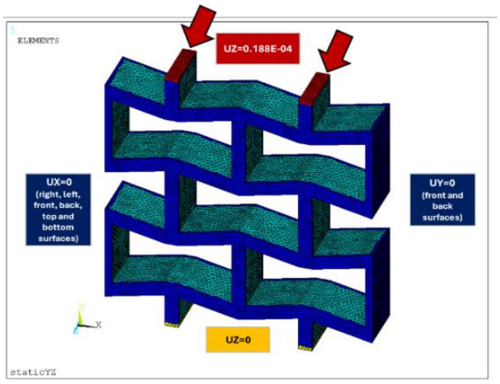

Figure 2.60: Static YZ analysis for Re-entrant.

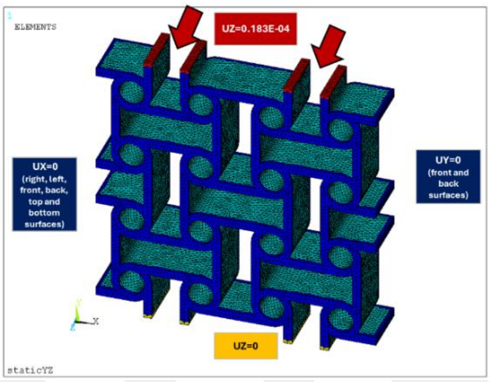

Figure 2.61: Static YZ analysis for Anti-tetrachiral.

In addition to the six static structural analyses, the density of the homogenized material was calculated using the Material Designer tool in ANSYS Workbench 2020 R2.

For the re-entrant structure, the unit cell selected for analysis has a width of 8.9 mm and a height of 9.4 mm, as shown in Figure 2.62. The actual surface area of the unit cell is measured as 24.6 mm^2, whereas the surface area of the full rectangular bounding box enclosing the unit cell is 83.7 mm^2. Therefore, the ratio of the unit cell area to the bounding rectangle is 24.6 mm^2 / 83.7 mm^2 = 0.294. The effective density of the homogenized material is then computed by multiplying the density of the solid isotropic material (1.185 g/cm^3) by this area ratio. Accordingly, the homogenized density for the re-entrant structure is calculated as 0.349 g/cm^3.

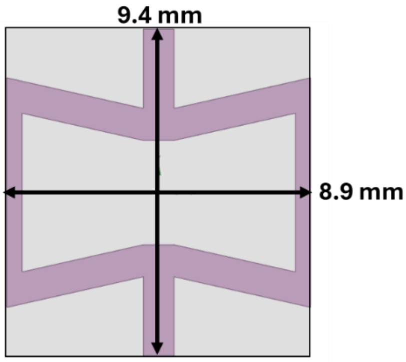

Figure 2.62: Width and height of Re-entrant unit cell.

Similarly, for a 1x1 unit cell of the anti-tetrachiral structure, the width and height are both 9.15 mm, as shown in Figure 2.63. The actual surface area of the unit cell is measured as 26.5 mm², while the surface area of the full rectangular bounding box is 83.7 mm². Therefore, the area ratio of the unit cell to the bounding rectangle is 26.5 mm² / 83.7 mm² = 0.316. The effective density of the homogenized material is computed by multiplying the density of the solid isotropic material (1.185 g/cm³) by this area ratio. As a result, the homogenized density for the anti-tetrachiral structure is calculated as 0.374 g/cm³.

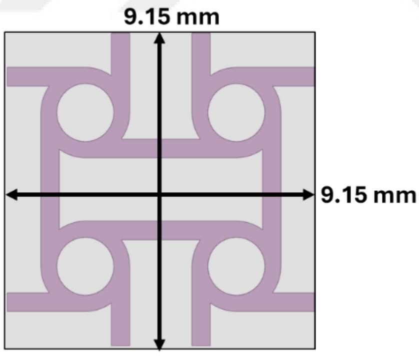

Figure 2.63: Width and height of Anti-tetrachiral unit cell.

2.3.3.Homogenization sensitivity studies

Prior to obtaining the final homogenized material properties, a series of numerical sensitivity studies were performed to evaluate the key parameters that could influence the accuracy and reliability of the results. These investigations were carried out using the Material Designer module in ANSYS Workbench 2020 R2.

The first step involved determining the overall material behavior of the lattice structures, specifically whether they exhibited orthotropic, or fully anisotropic characteristics. This classification was critical for establishing appropriate homogenization assumptions and defining the necessary number of analyses.

Subsequently, the impact of applying a periodic mesh and enforcing periodic boundary conditions (PBCs) was assessed. This analysis ensured that the simulated behavior of the unit cells aligned with the theoretical expectations for a repeating periodic structure, thereby minimizing edge effects and artificial stiffness artifacts.

Another important consideration was the depth of the part in the Z-direction. Sensitivity studies were conducted to examine whether variations in thickness influenced the homogenized material properties, particularly for the re-entrant and anti-tetrachiral geometries.

The influence of the number of unit cells arranged in the X and Y directions was also analyzed. By systematically increasing the number of repeating cells, the study verified the convergence and stability of the computed effective properties, ensuring that the selected RVE size was representative of the global lattice behavior.

Mesh type and quality were further explored by comparing the use of tetrahedral (Tet) and hexahedral (Hex) elements. Lastly, a mesh refinement study was conducted to investigate how the element size and resulting node count affected the computed material properties. This analysis helped establish a trade-off between computational cost and solution accuracy, guiding the mesh density selection for subsequent homogenization and finite element analyses.

These sensitivity studies provided a comprehensive understanding of the factors affecting the homogenization process and ensured that the final material properties were reliable and representative of the actual lattice structures used in this study.

2.3.3.1.Type of anisotropy

The first sensitivity study focused on determining the anisotropic behavior of the auxetic lattice structures. Specifically, the goal was to establish whether the re-entrant and anti-tetrachiral geometries exhibited orthotropic or anisotropic material characteristics when analyzed through homogenization. For this purpose, homogenized material properties were computed under the assumption of full anisotropy.

The meshed finite element model of the re-entrant structure used for this analysis is shown in Figure 2.64, while the corresponding meshed model of the anti-tetrachiral structure is presented in Figure 2.65.

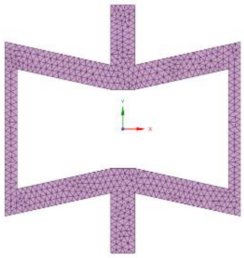

Figure 2.64: Re-entrant FE model for Type of Anisotropy sensitivity study.

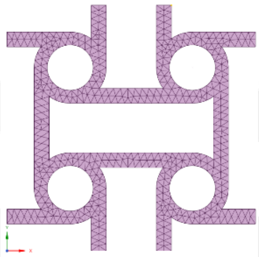

Figure 2.65: Anti-tetrachiral FE model for Type of Anisotropy sensitivity study.

In this analysis, the type of anisotropy was initially defined as anisotropic material, which is the main focus and sensitivity parameter for this study. Both the re-entrant and anti-tetrachiral models shared identical mesh and analysis settings.

The specific analysis settings were configured as follows: the number of unit cells in the X and Y directions was set to 1x1, and the depth in the Z-direction was defined as 9 mm, corresponding to 25% of the total part depth. Tetrahedral elements were used throughout the models, with a maximum element size of 0.25 mm. This meshing configuration resulted in a total of 212,268 nodes for the re-entrant structure model and 217,909 nodes for the anti-tetrachiral structure model.

Based on these finite element model configurations, the homogenized material results, including the stiffness matrix components and density, are presented in Figure 2.66 for the re-entrant structure and in Figure 2.67 for the anti-tetrachiral structure. The analysis results indicated that the stiffness matrix terms D[4,1], D[5,1], D[6,1], D[4,2], D[5,2], D[6,2], D[4,3], D[5,3], D[6,3], D[5,4], D[6,4], and D[6,5], highlighted in blue within the figures, are negligibly small compared to the other matrix components. The remaining significant terms form an orthotropic stiffness matrix, as illustrated in Figure 2.68.

Consequently, orthotropic material behavior was selected for the subsequent homogenization analyses.

Stiffness Matrix (C)		
D[1,1]	4.36E+08	Pa
D[2,1]	-7.66E+07	Pa
D[3,1]	1.51E+08	Pa
D[4,1]	-3.24E+03	Pa
D[5,1]	-6.51E+01	Pa
D[6,1]	-1.64E+02	Pa
D[2,2]	3.74E+07	Pa
D[3,2]	-1.65E+07	Pa
D[4,2]	-2.66E+03	Pa
D[5,2]	-5.56E+01	Pa
D[6,2]	-1.31E+01	Pa
D[3,3]	6.99E+08	Pa
D[4,3]	-2.46E+03	Pa
D[5,3]	-5.54E+01	Pa
D[6,3]	-6.81E+01	Pa
D[4,4]	5.18E+06	Pa
D[5,4]	-2.72E+00	Pa
D[6,4]	-4.33E+01	Pa
D[5,5]	5.30E+07	Pa
D[6,5]	-3.33E+03	Pa
D[6,6]	1.51E+08	Pa
Density		
Density	0.349	g/cm^3

Figure 2.66: Homogenization result for Re-entrant FE model – Anisotropy sensitivity.

Stiffness Matrix (C)		
D[1,1]	7.09E+07	Pa
D[2,1]	-6.04E+07	Pa
D[3,1]	4.40E+06	Pa
D[4,1]	-5.88E+00	Pa
D[5,1]	4.55E+00	Pa
D[6,1]	8.91E+00	Pa
D[2,2]	7.09E+07	Pa
D[3,2]	4.40E+06	Pa
D[4,2]	1.46E-01	Pa
D[5,2]	-2.81E+01	Pa
D[6,2]	2.63E+01	Pa
D[3,3]	6.92E+08	Pa
D[4,3]	8.12E-02	Pa
D[5,3]	-1.06E+01	Pa
D[6,3]	9.54E+00	Pa
D[4,4]	3.97E+06	Pa
D[5,4]	-3.55E+03	Pa
D[6,4]	-1.33E+03	Pa
D[5,5]	9.19E+07	Pa
D[6,5]	-2.87E-02	Pa
D[6,6]	9.19E+07	Pa
Density		
Density	0.374	g/cm^3

Figure 2.67: Homogenization result for Anti-tetrachiral FE model – Anisotropy sensitivity.

$$\begin{Bmatrix} \sigma_{11} \\ \sigma_{22} \\ \sigma_{33} \\ \tau_{23} \\ \tau_{13} \\ \tau_{12} \end{Bmatrix} = \begin{bmatrix} C_{11} & C_{12} & C_{13} & 0 & 0 & 0 \\ C_{12} & C_{22} & C_{23} & 0 & 0 & 0 \\ C_{13} & C_{23} & C_{33} & 0 & 0 & 0 \\ 0 & 0 & 0 & C_{44} & 0 & 0 \\ 0 & 0 & 0 & 0 & C_{55} & 0 \\ 0 & 0 & 0 & 0 & 0 & C_{66} \end{bmatrix} \begin{Bmatrix} \varepsilon_{1} \\ \varepsilon_{2} \\ \varepsilon_{3} \\ \gamma_{23} \\ \gamma_{13} \\ \gamma_{12} \end{Bmatrix}$$

Figure 2.68: Orthotropic material stiffness matrix.

2.3.3.2.Periodic meshing and boundary conditions

The second sensitivity aims to understand how periodic meshing and periodic boundary conditions influence the homogenized material properties results. The meshed finite element (FE) model of the re-entrant structure is shown in Figure 2.69, while the meshed FE model of the anti-tetrachiral structure is presented in Figure 2.70.

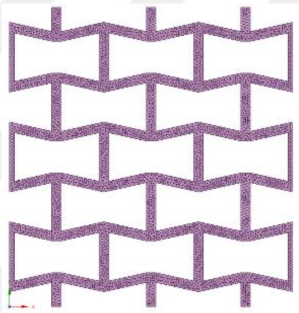

Figure 2.69: Re-entrant FE model – Periodic meshing and boundary conditions.

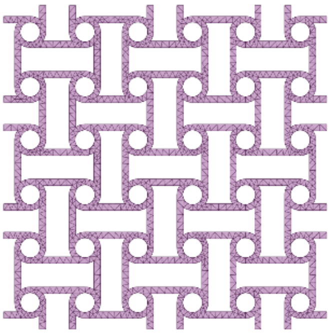

Figure 2.70: Anti-tetrachiral FE model – Periodic meshing and boundary conditions.

In this case, periodic meshing and boundary conditions were applied in Case 1, and not applied in Case 2, making this the main focus and sensitivity parameter of the study. For all other settings, both models share the same mesh and analysis configuration.

Both models shared identical mesh and analysis settings to ensure a fair comparison. The number of unit cells was set to 3x3 in the X and Y directions, the depth in the Z-direction was selected as 3.6 mm, corresponding to 10% of the total part depth, and tetrahedral elements were used throughout, with a maximum element size of 0.25 mm. This configuration resulted in 772,875 nodes for the re-entrant model and 681,703 nodes for the anti-tetrachiral model.

The homogenized material results, including the stiffness matrix components and density, are presented in Figure 2.71 for the re-entrant structure and Figure 2.72 for the anti-tetrachiral structure.

In terms of computational performance, the application of periodic meshing and boundary conditions in Case 1 led to an increase in solve time. Specifically, Case 1 required approximately 2.6 times longer computational time for the re-entrant model and 1.7 times longer for the anti-tetrachiral model compared to Case 2, where periodic settings were not applied.

Engineering Constants		
E1 (Ex)	2.59E+08	Pa
E2 (Ey)	2.38E+07	Pa
E3 (Ez)	6.42E+08	Pa
G12 (Gxy)	5.18E+06	Pa
G23 (Gyz)	5.30E+07	Pa
G31 (Gzx)	1.51E+08	Pa
Nu12 (Nuxy)	-1.972	
Nu13 (Nuxz)	0.169	
Nu23 (Nuyz)	0.015	
Density	0.349	g/cm^3

Figure 2.71: Homogenization result for Re-entrant FE model – Periodic Meshing and Boundary Conditions.

Engineering Constants		
E1 (Ex)	2.01E+07	Pa
E2 (Ey)	2.01E+07	Pa
E3 (Ez)	6.88E+08	Pa
G12 (Gxy)	4.43E+06	Pa
G23 (Gyz)	9.31E+07	Pa
G31 (Gzx)	9.31E+07	Pa
Nu12 (Nuxy)	-0.854	
Nu13 (Nuxz)	0.012	
Nu23 (Nuyz)	0.012	
Density	0.374	g/cm^3

Figure 2.72: Homogenization result for Anti-tetrachiral FE model – Periodic Meshing and Boundary Conditions.

Despite the increased computational effort, the sensitivity analysis revealed that applying periodic meshing and boundary conditions did not result in any meaningful differences in the derived homogenized material properties.

These findings indicate that, for the lattice geometries and analysis objectives considered in this study, periodic meshing and boundary conditions are not strictly necessary for obtaining reliable homogenization results, and their omission can lead to substantial computational savings without compromising the accuracy of the material property predictions.

2.3.3.3.Depth in z direction

The third sensitivity study aimed to investigate how the depth in the Z-direction affects the homogenized material properties of the lattice structures. The meshed finite element models of the re-entrant structure are shown in Figure 2.73, while the meshed models of the anti-tetrachiral structure are presented in Figure 2.74.

Case 1 Depth in Z direction **1.8 mm (5% of total)**	Case 2 Depth in Z direction **3.6 mm (10% of total)**	Case 3 Depth in Z direction **9 mm (25% of total)**	Case 4 Depth in Z direction **18 mm (50% of total)**	Case 5 Depth in Z direction **36 mm (100% of total)**

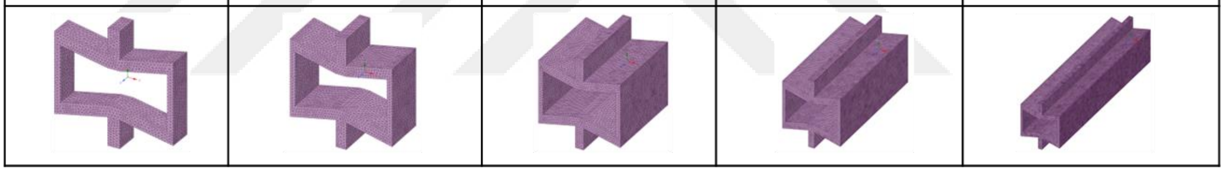

Figure 2.73: Re-entrant FE model – Depth in Z direction study.

Case 1 Depth in Z direction **1.8 mm (5% of total)**	Case 2 Depth in Z direction **3.6 mm (10% of total)**	Case 3 Depth in Z direction **9 mm (25% of total)**	Case 4 Depth in Z direction **18 mm (50% of total)**	Case 5 Depth in Z direction **36 mm (100% of total)**

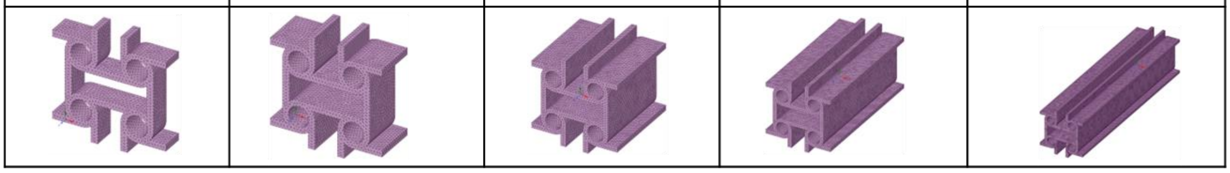

Figure 2.74: Anti-tetrachiral FE model – Depth in Z direction study.

In this analysis, the depth in the Z-direction was systematically varied as the primary sensitivity parameter. Five cases were defined to examine the impact of depth: Case 1 used a depth of 1.8 mm, Case 2 used 3.6 mm, Case 3 used 9 mm, Case 4 used 18 mm, and Case 5 used 36 mm. All other parameters, including mesh settings and boundary conditions, were kept the same to isolate the influence of Z-depth on the homogenized properties.

The shared analysis configuration was as follows: the number of unit cells in the X and Y directions was fixed at 1x1, tetrahedral elements were used throughout the model, and the maximum element size was set to 0.25 mm. For the re-entrant FE models, this resulted in 48,096 nodes for Case 1, 88,574 nodes for Case 2, 211,784 nodes for Case 3, 416,679 nodes for Case 4, and 814,761 nodes for Case 5. For the anti-tetrachiral FE models, the total number of nodes was 45,674 for Case 1, 88,121 for Case 2, 217,937 for Case 3, 431,791 for Case 4, and 863,150 for Case 5.

The homogenized material results, including the stiffness matrix and density, are presented in Figure 2.75 for the re-entrant structure and Figure 2.77 for the anti-tetrachiral structure. Additionally, the sensitivity of key parameters such as the elastic modulus in the X-direction (Ex) and the Poisson's ratio in the X–Y plane (NUxy) is shown in Figure 2.76 for the re-entrant model and Figure 2.78 for the anti-tetrachiral model.

Engineering Constants		
E1 (Ex)	2.59E+08	Pa
E2 (Ey)	2.38E+07	Pa
E3 (Ez)	6.42E+08	Pa
G12 (Gxy)	5.18E+06	Pa
G23 (Gyz)	5.30E+07	Pa
G31 (Gzx)	1.51E+08	Pa
Nu12 (Nuxy)	-1.971	
Nu13 (Nuxz)	0.169	
Nu23 (Nuyz)	0.015	
Density	0.349	g/cm^3

Figure 2.75: Homogenization result for Re-entrant FE model – Depth in Z direction.

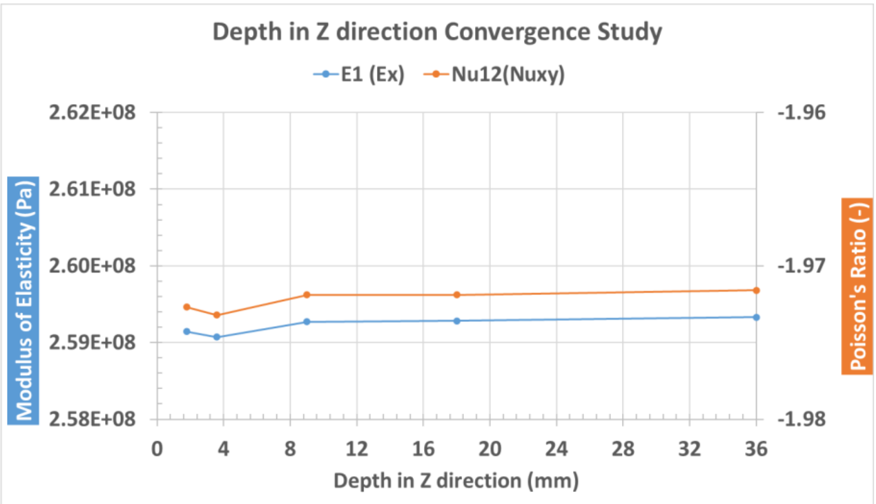

Figure 2.76: Sensitivty result for Re-entrant FE model – Depth in Z direction.

Engineering Constants		
E1 (Ex)	1.93E+07	Pa
E2 (Ey)	1.93E+07	Pa
E3 (Ez)	6.88E+08	Pa
G12 (Gxy)	3.97E+06	Pa
G23 (Gyz)	9.19E+07	Pa
G31 (Gzx)	9.19E+07	Pa
Nu12 (Nuxy)	-0.853	
Nu13 (Nuxz)	0.011	
Nu23 (Nuyz)	0.011	
Density	0.3749	g/cm^3

Figure 2.77: Homogenization result for Anti-tetrachiral FE model – Depth in Z direction.

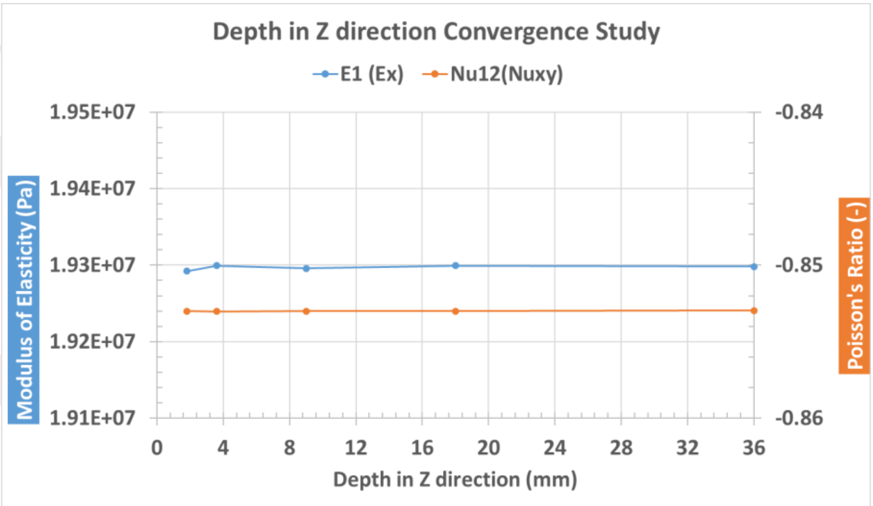

Figure 2.78: Sensitivty result for Anti-tetrachiral FE model – Depth in Z direction.

The results indicated that variations in the Z-depth had a minimal impact on the homogenized material properties across five different cases. In terms of computational performance, the models with greater Z-depth required significantly more computation time. For instance, Case 5 required approximately five times the solution time of Case 1, while Case 4 required about three times, Case 3 required twice, and Case 2 required 1.5 times the solve time.

Based on the findings of this sensitivity analysis, increasing the depth in the Z-direction did not result in a significant change in the homogenized material properties. Therefore, a Z-depth of 3.6 mm, corresponding to 10% of the total part depth, was selected for all subsequent homogenization analyses. This value offers a practical balance between computational efficiency and model accuracy, ensuring that the derived homogenized material properties reliably represent the mechanical behavior of the auxetic structures while minimizing unnecessary computational costs.

2.3.3.4.Number of unit cells in x and y directions

The fourth sensitivity study aimed to investigate how the number of unit cells stacked in the X and Y directions influences the homogenized material properties. The meshed finite element models of the re-entrant structure are shown in Figure 2.79, while the meshed FE models of the anti-tetrachiral structure are presented in Figure 2.80.

In this study, the number of unit cells in the X and Y directions was varied systematically as the primary sensitivity parameter, while all other analysis settings remained consistent across the models.

Eight cases were analyzed, a 1x1 unit cell configuration (Case 1), 2x2 unit cells (Case 2), 3x3 unit cells (Case 3), 4x4 unit cells (Case 4), 5x5 unit cells (Case 5), 6x6 unit cells (Case 6), 7x7 unit cells (Case 7), and 8x8 unit cells (Case 8). The depth in the Z-direction was fixed at 3.6 mm, tetrahedral elements were used throughout, and the maximum element size was set to 0.5 mm.

Case 1 Number of Unit Cells in X and Y **1x1**	Case 2 Number of Unit Cells in X and Y **2x2**	Case 3 Number of Unit Cells in X and Y **3x3**	Case 4 Number of Unit Cells in X and Y **4x4**
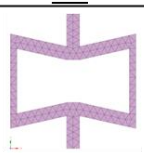	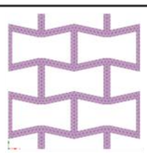		
Case 5 Number of Unit Cells in X and Y **5x5**	Case 6 Number of Unit Cells in X and Y **6x6**	Case 7 Number of Unit Cells in X and Y **7x7**	Case 8 Number of Unit Cells in X and Y **8x8**
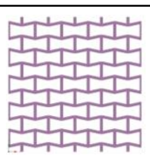		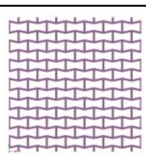	

Figure 2.79: Re-entrant FE model – Number of Unit Cells in X and Y directions.

Case 1 Number of Unit Cells in X and Y **1x1**	Case 2 Number of Unit Cells in X and Y **2x2**	Case 3 Number of Unit Cells in X and Y **3x3**	Case 4 Number of Unit Cells in X and Y **4x4**
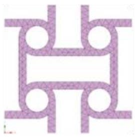	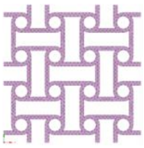		
Case 5 Number of Unit Cells in X and Y **5x5**	Case 6 Number of Unit Cells in X and Y **6x6**	Case 7 Number of Unit Cells in X and Y **7x7**	Case 8 Number of Unit Cells in X and Y **8x8**
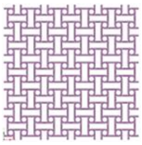	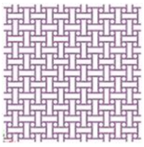	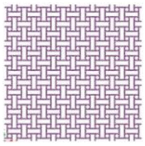	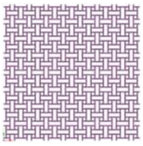

Figure 2.80: Anti-tetrachiral FE model – Number of Unit Cells in X and Y directions.

This meshing configuration resulted in 10,750 nodes for Case 1, 42,277 nodes for Case 2, 94,911 nodes for Case 3, 167,963 nodes for Case 4, 262,537 nodes for Case 5, 376,842 nodes for Case 6, 512,985 nodes for Case 7, and 669,744 nodes for Case 8 in the re-entrant FE models. The anti-tetrachiral FE models yielded 13,451 nodes for Case 1, 63,302 nodes for Case 2, 141,436 nodes for Case 3, 249,165 nodes for Case 4, 383,359 nodes for Case 5, 566,165 nodes for Case 6, 762,101 nodes for Case 7, and 986,554 nodes for Case 8.

The computed homogenized material properties, including the stiffness matrix and density, are presented in Figure 2.81 for the re-entrant structure, with sensitivity results for Ex and NUxy shown in Figure 2.82.

Engineering Constants		
E1 (Ex)	2.65E+08	Pa
E2 (Ey)	2.45E+07	Pa
E3 (Ez)	6.42E+08	Pa
G12 (Gxy)	5.37E+06	Pa
G23 (Gyz)	5.32E+07	Pa
G31 (Gzx)	1.52E+08	Pa
Nu12 (Nuxy)	-1.937	
Nu13 (Nuxz)	0.173	
Nu23 (Nuyz)	0.016	
Density	0.349	g/cm^3

Figure 2.81: Homogenization result for Re-entrant FE model – Number of Unit Cells in X and Y directions.

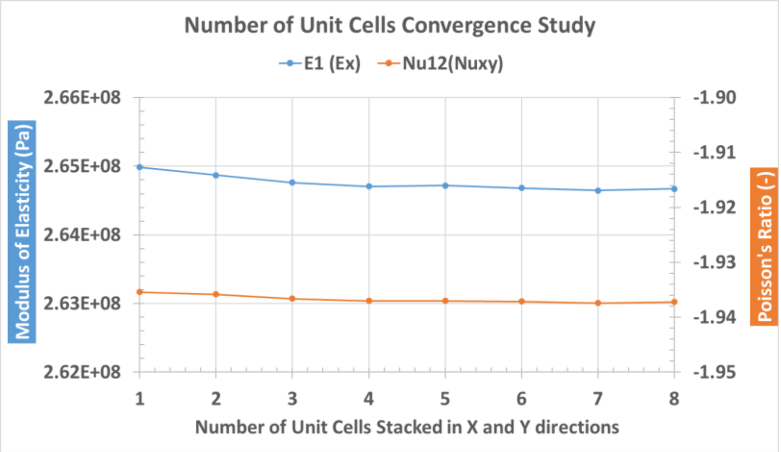

Figure 2.82: Sensitivty result for Re-entrant FE model – Number of Unit Cells in X and Y directions.

For the anti-tetrachiral structure, the homogenized material properties are presented in Figure 2.83, while the sensitivity results for Ex and NUxy are shown in Figure 2.84.

Engineering Constants		
E1 (Ex)	1.98E+07	Pa
E2 (Ey)	1.98E+07	Pa
E3 (Ez)	6.88E+08	Pa
G12 (Gxy)	4.23E+06	Pa
G23 (Gyz)	9.27E+07	Pa
G31 (Gzx)	9.27E+07	Pa
Nu12 (Nuxy)	-0.854	
Nu13 (Nuxz)	0.012	
Nu23 (Nuyz)	0.012	
Density	0.374	g/cm^3

Figure 2.83: Homogenization result for Anti-tetrachiral FE model – Number of Unit Cells in X and Y directions.

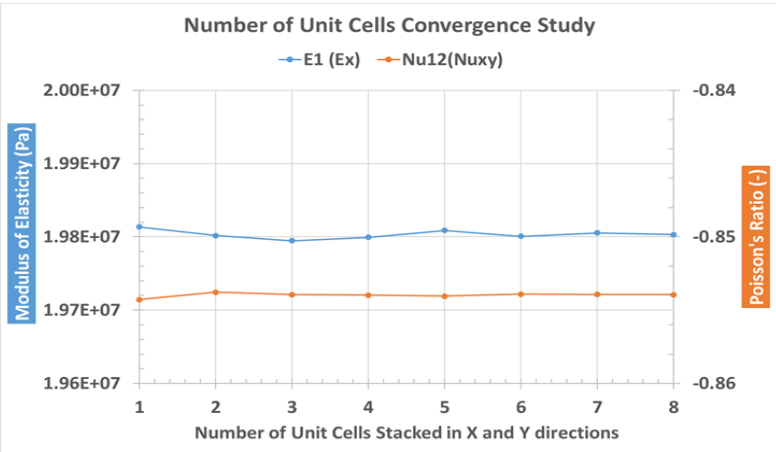

Figure 2.84: Sensitivty result for Anti-tetrachiral FE model – Number of Unit Cells in X and Y directions.

In terms of computational performance, Case 8 required approximately 5 times the solve time of Case 1, while Case 7 required 4.4 times, Case 6 required 3.6 times, Case 5 required 2.5 times, Case 4 required 2 times, Case 3 required 1.5 times, and Case 2 required 1.2 times the solve time.

The sensitivity analysis demonstrated that increasing the number of unit cells in the X and Y directions beyond a certain threshold did not result in significant changes to the homogenized material properties. Therefore, a 2×2 unit cell configuration, consisting of two unit cells along both the X and Y directions, was selected as the optimal configuration. This approach provides a practical balance between computational efficiency and model fidelity, ensuring sufficiently accurate material properties while minimizing computational time.

2.3.3.5.Mesh element type

The fifth sensitivity study aimed to investigate how the mesh element type, specifically tetrahedral versus hexahedral elements, impacts the homogenized material properties. The meshed finite element models of the re-entrant structure are shown in Figure 2.85, while the meshed FE models of the anti-tetrachiral structure are presented in Figure 2.86.

Case 1 Element Type: **Tetrahedral Mesh**	Case 2 Element Type: **Hexahedral Mesh**
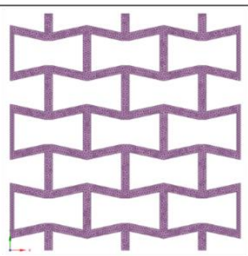	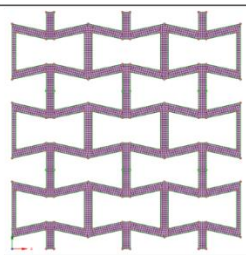

Figure 2.85: Re-entrant FE model – Mesh Element Type.

Case 1 Element Type: **Tetrahedral Mesh**	Case 2 Element Type: **Hexahedral Mesh**
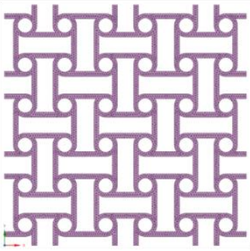	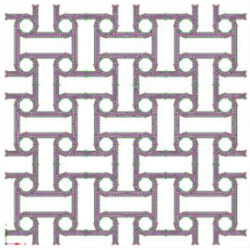

Figure 2.86: Anti-tetrachiral FE model – Mesh Element Type.

In this study, tetrahedral elements were used in Case 1, and hexahedral elements were used in Case 2, making the element type the main sensitivity parameter of the analysis. All other mesh and analysis settings remained identical for both models to ensure consistency.

The analysis configuration was as follows, the number of unit cells in the X and Y directions was set to 3x3, and the depth in the Z-direction was fixed at 3.6 mm, corresponding to 10% of the total part depth. The maximum element size was defined as 0.25 mm. For the re-entrant FE models, the tetrahedral configuration (Case 1) resulted in 681,703 nodes, while the hexahedral configuration (Case 2) yielded 310,719 nodes. For the anti-tetrachiral FE models, the corresponding node counts were 788,650 for Case 1 and 361,114 for Case 2.

The homogenized material properties, including the stiffness matrix and density, derived from these configurations are presented in Figure 2.87 for the re-entrant structure and Figure 2.88 for the anti-tetrachiral structure.

Engineering Constants for Case 1			Engineering Constants for Case 2		
E1 (Ex)	2.59E+08	Pa	E1 (Ex)	2.60E+08	Pa
E2 (Ey)	2.38E+07	Pa	E2 (Ey)	2.39E+07	Pa
E3 (Ez)	6.42E+08	Pa	E3 (Ez)	6.42E+08	Pa
G12 (Gxy)	5.18E+06	Pa	G12 (Gxy)	5.20E+06	Pa
G23 (Gyz)	5.30E+07	Pa	G23 (Gyz)	5.29E+07	Pa
G31 (Gzx)	1.51E+08	Pa	G31 (Gzx)	1.51E+08	Pa
Nu12 (Nuxy)	-1.971		Nu12 (Nuxy)	-1.966	
Nu13 (Nuxz)	0.169		Nu13 (Nuxz)	0.169	
Nu23 (Nuyz)	0.015		Nu23 (Nuyz)	0.015	
Density	0.349	g/cm^3	Density	0.349	g/cm^3

Figure 2.87: Homogenization results for Re-entrant FE models – Mesh Element Type.

Engineering Constants for Case 1		
E1 (Ex)	1.93E+07	Pa
E2 (Ey)	1.93E+07	Pa
E3 (Ez)	6.88E+08	Pa
G12 (Gxy)	3.97E+06	Pa
G23 (Gyz)	9.19E+07	Pa
G31 (Gzx)	9.19E+07	Pa
Nu12 (Nuxy)	-0.853	
Nu13 (Nuxz)	0.011	
Nu23 (Nuyz)	0.011	
Density	0.374	g/cm^3

Engineering Constants for Case 2		
E1 (Ex)	1.94E+07	Pa
E2 (Ey)	1.94E+07	Pa
E3 (Ez)	6.88E+08	Pa
G12 (Gxy)	4.02E+06	Pa
G23 (Gyz)	9.19E+07	Pa
G31 (Gzx)	9.19E+07	Pa
Nu12 (Nuxy)	-0.852	
Nu13 (Nuxz)	0.011	
Nu23 (Nuyz)	0.011	
Density	0.374	g/cm^3

Figure 2.88: Homogenization results for Anti-tetrachiral FE models – Mesh Element Type.

In terms of computational performance, Case 1 (tetrahedral elements) required approximately twice the solve time compared to Case 2 (hexahedral elements) for both models. Despite this difference in computational time, the sensitivity analysis revealed no significant differences in the homogenized material properties when comparing tetrahedral and hexahedral elements.

Given this outcome, and considering that the Material Designer module in ANSYS Workbench uses tetrahedral meshing as the default meshing option, the tetrahedral mesh was selected for all subsequent analyses in this study.

2.3.3.6.Mesh convergence study based on element size

The sixth and final sensitivity study focused on mesh convergence, evaluating how the maximum element size influences the homogenized material properties. The meshed finite element models of the re-entrant structure are shown in Figure 2.89, while the meshed FE models of the anti-tetrachiral structure are presented in Figure 2.90.

In this study, the maximum element size was varied as the main sensitivity parameter. Eight cases were defined: 4 mm (Case 1), 2 mm (Case 2), 1 mm (Case 3), 0.5 mm (Case 4), 0.25 mm (Case 5), 0.20 mm (Case 6), 0.15 mm (Case 7), and 0.10 mm (Case 8). All other parameters were kept constant across models to ensure consistency.

The remaining analysis settings were as follows, the number of unit cells in the X and Y directions was set to 2x2, the depth in the Z-direction was set to 3.6 mm, and tetrahedral elements were used throughout the entire model.

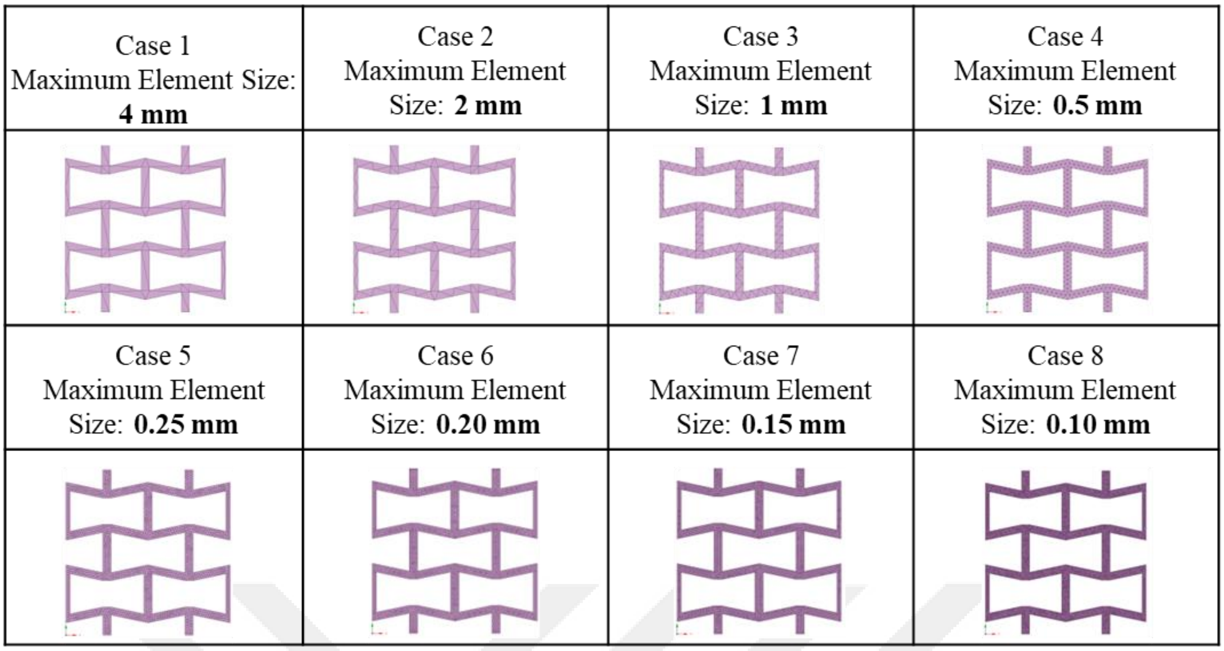

Figure 2.89: Re-entrant FE model – Mesh Convergence Study.

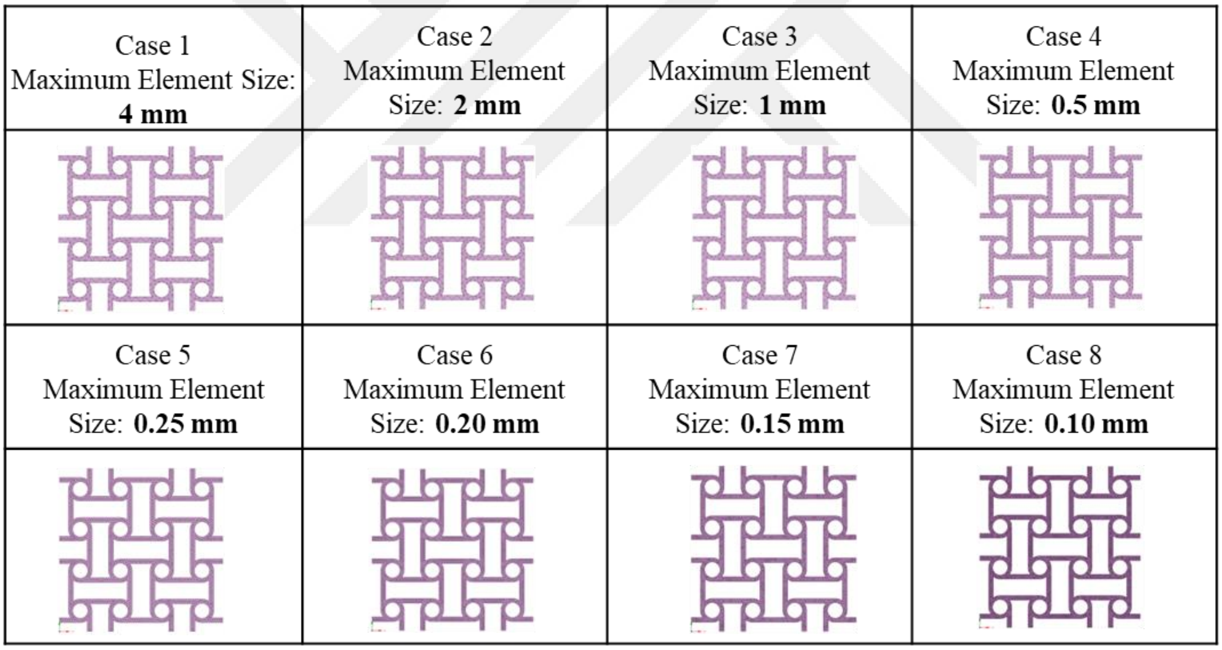

Figure 2.90: Anti-tetrachiral FE model – Mesh Convergence Study.

This configuration resulted in 702 nodes for Case 1, 2,282 nodes for Case 2, 7,965 nodes for Case 3, 42,277 nodes for Case 4, 303,751 nodes for Case 5, 576,411 nodes for Case 6, 1,318,237 nodes for Case 7, and 4,296,451 nodes for Case 8 in the re-entrant models. For the anti-tetrachiral models, the corresponding node counts were 36,219 for Case 1, 36,291 for Case 2, 37,794 for Case 3, 63,302 for Case 4, 351,723 for Case 5, 662,706 for Case 6, 1,482,904 for Case 7, and 4,767,335 for Case 8.

The resulting homogenized material properties, including the stiffness matrix and density, are presented in Figure 2.91 for the re-entrant structure and Figure 2.94 for the anti-tetrachiral structure. Sensitivity plots illustrating the variation of Ex and NUxy with respect to the total number of nodes are shown in Figure 2.92 for the re-entrant structure and Figure 2.95 for the anti-tetrachiral structure, while their variation with respect to maximum element size is presented in Figure 2.93 and Figure 2.96, respectively.

In terms of computational performance, Case 8 required approximately 27 times longer solve time than Case 1, while Case 7 required 10 times longer, Case 6 required 4 times longer, Case 5 required 2.5 times longer, Case 4 required 1.5 times longer, Case 3 required 1.2 times longer, and Case 2 required 1.1 times longer than Case 1.

As the element size decreased and the number of nodes increased, the homogenized material properties gradually converged toward stable and optimal values. This convergence behavior was observed to stabilize around a maximum element size of 0.25 mm. Therefore, a maximum element size of 0.25 mm, or a finer mesh, was selected for all subsequent analyses, as it offers a practical balance between computational efficiency and accuracy in the homogenized material properties.

Engineering Constants for Case 1		
E1 (Ex)	3.88E+08	Pa
E2 (Ey)	4.91E+07	Pa
E3 (Ez)	6.42E+08	Pa
G12 (Gxy)	1.30E+07	Pa
G23 (Gyz)	5.64E+07	Pa
G31 (Gzx)	1.58E+08	Pa
Nu12 (Nuxy)	-0.964	
Nu13 (Nuxz)	0.253	
Nu23 (Nuyz)	0.032	
Density	0.349	g/cm^3

Engineering Constants for Case 2		
E1 (Ex)	2.95E+08	Pa
E2 (Ey)	2.85E+07	Pa
E3 (Ez)	6.42E+08	Pa
G12 (Gxy)	6.93E+06	Pa
G23 (Gyz)	5.43E+07	Pa
G31 (Gzx)	1.54E+08	Pa
Nu12 (Nuxy)	-1.734	
Nu13 (Nuxz)	0.193	
Nu23 (Nuyz)	0.018	
Density	0.349	g/cm^3

Engineering Constants for Case 3		
E1 (Ex)	2.78E+08	Pa
E2 (Ey)	2.61E+07	Pa
E3 (Ez)	6.42E+08	Pa
G12 (Gxy)	5.85E+06	Pa
G23 (Gyz)	5.37E+07	Pa
G31 (Gzx)	1.53E+08	Pa
Nu12 (Nuxy)	-1.854	
Nu13 (Nuxz)	0.181	
Nu23 (Nuyz)	0.017	
Density	0.349	g/cm^3

Engineering Constants for Case 4		
E1 (Ex)	2.65E+08	Pa
E2 (Ey)	2.45E+07	Pa
E3 (Ez)	6.42E+08	Pa
G12 (Gxy)	5.37E+06	Pa
G23 (Gyz)	5.32E+07	Pa
G31 (Gzx)	1.52E+08	Pa
Nu12 (Nuxy)	-1.935	
Nu13 (Nuxz)	0.173	
Nu23 (Nuyz)	0.016	
Density	0.349	g/cm^3

Engineering Constants for Case 5		
E1 (Ex)	2.59E+08	Pa
E2 (Ey)	2.38E+07	Pa
E3 (Ez)	6.42E+08	Pa
G12 (Gxy)	5.18E+06	Pa
G23 (Gyz)	5.30E+07	Pa
G31 (Gzx)	1.51E+08	Pa
Nu12 (Nuxy)	-1.971	
Nu13 (Nuxz)	0.169	
Nu23 (Nuyz)	0.015	
Density	0.349	g/cm^3

Engineering Constants for Case 6		
E1 (Ex)	2.58E+08	Pa
E2 (Ey)	2.37E+07	Pa
E3 (Ez)	6.42E+08	Pa
G12 (Gxy)	5.15E+06	Pa
G23 (Gyz)	5.29E+07	Pa
G31 (Gzx)	1.51E+08	Pa
Nu12 (Nuxy)	-1.977	
Nu13 (Nuxz)	0.169	
Nu23 (Nuyz)	0.015	
Density	0.349	g/cm^3

Engineering Constants for Case 7		
E1 (Ex)	2.58E+08	Pa
E2 (Ey)	2.36E+07	Pa
E3 (Ez)	6.42E+08	Pa
G12 (Gxy)	5.12E+06	Pa
G23 (Gyz)	5.29E+07	Pa
G31 (Gzx)	1.51E+08	Pa
Nu12 (Nuxy)	-1.983	
Nu13 (Nuxz)	0.168	
Nu23 (Nuyz)	0.015	
Density	0.349	g/cm^3

Engineering Constants for Case 8		
E1 (Ex)	2.57E+08	Pa
E2 (Ey)	2.35E+07	Pa
E3 (Ez)	6.42E+08	Pa
G12 (Gxy)	5.09E+06	Pa
G23 (Gyz)	5.28E+07	Pa
G31 (Gzx)	1.51E+08	Pa
Nu12 (Nuxy)	-1.988	
Nu13 (Nuxz)	0.167	
Nu23 (Nuyz)	0.015	
Density	0.349	g/cm^3

Figure 2.91: Homogenization results for Re-entrant FE models – Mesh Convergence Study.

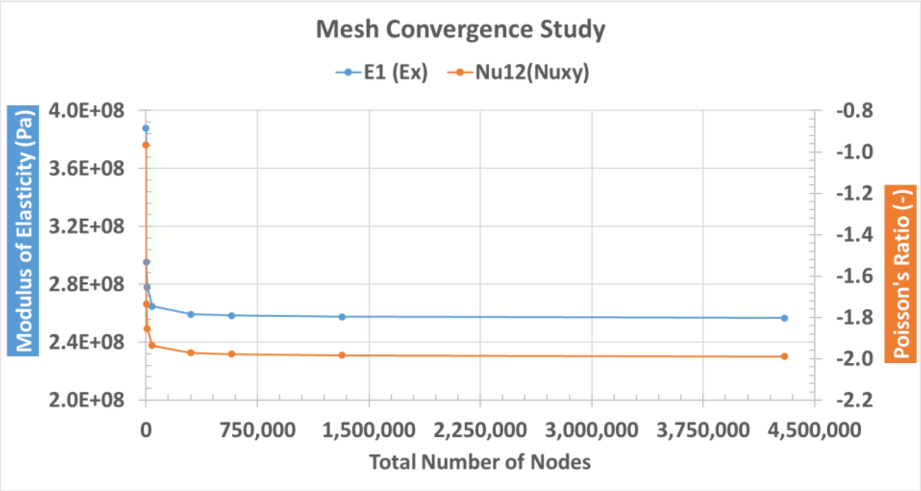

Figure 2.92: Sensitivty result against number of nodes for Re-entrant FE model – Mesh Convergence Study.

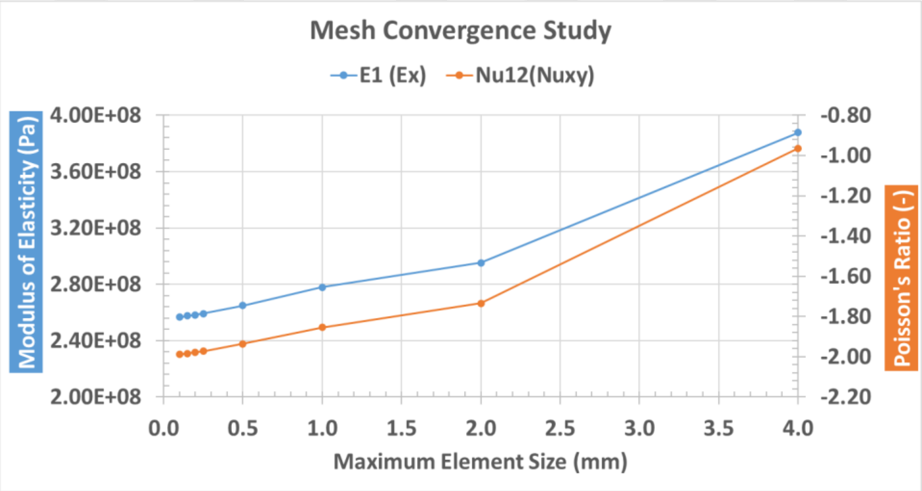

Figure 2.93: Sensitivty result against maximum element size for Re-entrant FE model – Mesh Convergence Study.

It was observed that for the anti-tetrachiral models, the coarsest mesh sizes (4 mm and 2 mm in Case 1 and Case 2) could not be generated successfully, as the coarse mesh could not adequately capture the detailed geometry around the holes. In these cases, the Material Designer automatically adjusted the mesh settings to a finer resolution to ensure a valid mesh.

Engineering Constants for Case 1		
E1 (Ex)	2.00E+07	Pa
E2 (Ey)	2.00E+07	Pa
E3 (Ez)	6.88E+08	Pa
G12 (Gxy)	4.37E+06	Pa
G23 (Gyz)	9.30E+07	Pa
G31 (Gzx)	9.30E+07	Pa
Nu12 (Nuxy)	-0.853	
Nu13 (Nuxz)	0.012	
Nu23 (Nuyz)	0.012	
Density	0.374	g/cm³

Engineering Constants for Case 2		
E1 (Ex)	2.00E+07	Pa
E2 (Ey)	2.00E+07	Pa
E3 (Ez)	6.88E+08	Pa
G12 (Gxy)	4.38E+06	Pa
G23 (Gyz)	9.30E+07	Pa
G31 (Gzx)	9.30E+07	Pa
Nu12 (Nuxy)	-0.853	
Nu13 (Nuxz)	0.012	
Nu23 (Nuyz)	0.012	
Density	0.374	g/cm³

Engineering Constants for Case 3		
E1 (Ex)	2.00E+07	Pa
E2 (Ey)	2.00E+07	Pa
E3 (Ez)	6.88E+08	Pa
G12 (Gxy)	4.35E+06	Pa
G23 (Gyz)	9.29E+07	Pa
G31 (Gzx)	9.29E+07	Pa
Nu12 (Nuxy)	-0.853	
Nu13 (Nuxz)	0.012	
Nu23 (Nuyz)	0.012	
Density	0.374	g/cm³

Engineering Constants for Case 4		
E1 (Ex)	1.98E+07	Pa
E2 (Ey)	1.98E+07	Pa
E3 (Ez)	6.88E+08	Pa
G12 (Gxy)	4.23E+06	Pa
G23 (Gyz)	9.27E+07	Pa
G31 (Gzx)	9.27E+07	Pa
Nu12 (Nuxy)	-0.853	
Nu13 (Nuxz)	0.012	
Nu23 (Nuyz)	0.012	
Density	0.374	g/cm³

Engineering Constants for Case 5		
E1 (Ex)	1.93E+07	Pa
E2 (Ey)	1.93E+07	Pa
E3 (Ez)	6.88E+08	Pa
G12 (Gxy)	3.97E+06	Pa
G23 (Gyz)	9.19E+07	Pa
G31 (Gzx)	9.19E+07	Pa
Nu12 (Nuxy)	-0.853	
Nu13 (Nuxz)	0.011	
Nu23 (Nuyz)	0.011	
Density	0.374	g/cm³

Engineering Constants for Case 6		
E1 (Ex)	1.92E+07	Pa
E2 (Ey)	1.92E+07	Pa
E3 (Ez)	6.88E+08	Pa
G12 (Gxy)	3.92E+06	Pa
G23 (Gyz)	9.18E+07	Pa
G31 (Gzx)	9.18E+07	Pa
Nu12 (Nuxy)	-0.853	
Nu13 (Nuxz)	0.011	
Nu23 (Nuyz)	0.011	
Density	0.374	g/cm³

Engineering Constants for Case 7		
E1 (Ex)	1.91E+07	Pa
E2 (Ey)	1.91E+07	Pa
E3 (Ez)	6.88E+08	Pa
G12 (Gxy)	3.89E+06	Pa
G23 (Gyz)	9.17E+07	Pa
G31 (Gzx)	9.17E+07	Pa
Nu12 (Nuxy)	-0.853	
Nu13 (Nuxz)	0.011	
Nu23 (Nuyz)	0.011	
Density	0.374	g/cm³

Engineering Constants for Case 8		
E1 (Ex)	1.91E+07	Pa
E2 (Ey)	1.91E+07	Pa
E3 (Ez)	6.88E+08	Pa
G12 (Gxy)	3.86E+06	Pa
G23 (Gyz)	9.16E+07	Pa
G31 (Gzx)	9.16E+07	Pa
Nu12 (Nuxy)	-0.853	
Nu13 (Nuxz)	0.011	
Nu23 (Nuyz)	0.011	
Density	0.374	g/cm³

Figure 2.94: Homogenization results for Anti-tetrachiral FE models – Mesh Convergence Study.

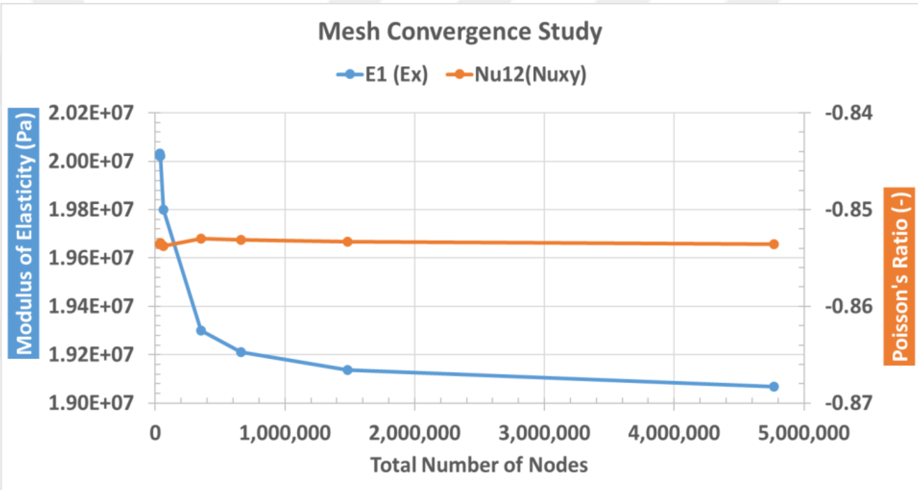

Figure 2.95: Sensitivty result against number of nodes for Anti-tetrachiral FE model – Mesh Convergence Study.

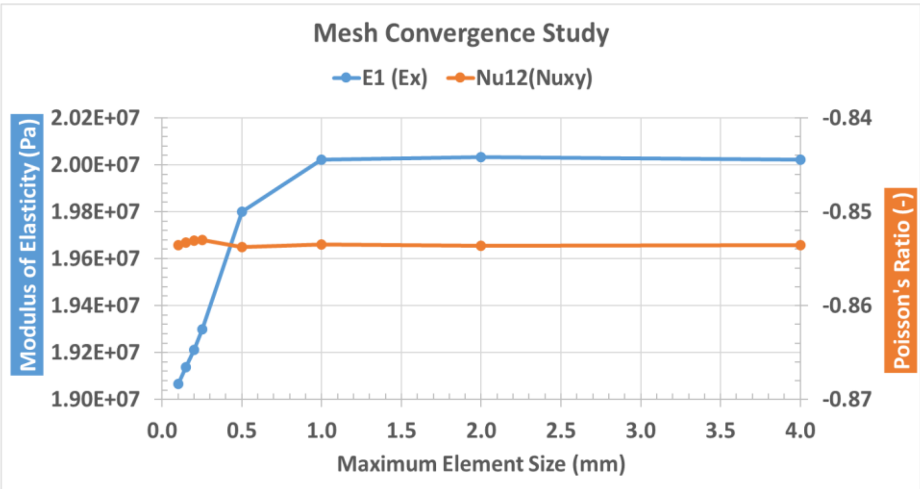

Figure 2.96: Sensitivty result against maximum element size for Anti-tetrachiral FE model – Mesh Convergence Study.

2.3.4.Homogenized material properties

After the unit cell selections were finalized for both the re-entrant and anti-tetrachiral structures, and upon completion of the homogenization sensitivity studies, the final homogenized material properties were obtained. These results are presented in Table 2.6 for the re-entrant structure and in Table 2.7 for the anti-tetrachiral structure. The obtained homogenized material properties were used in all subsequent finite element models and analyses.

Table 2.6: Homogenized Material Result for Re-entrant Structure.

Engineering Constants	Results	Units
E1 (Ex)	2.57E+08	Pa
E2 (Ey)	2.35E+07	Pa
E3 (Ez)	6.42E+08	Pa
G12 (Gxy)	5.09E+06	Pa
G23 (Gyz)	5.28E+07	Pa
G31 (Gzx)	1.51E+08	Pa
Nu12 (Nuxy)	-1.988	
Nu13 (Nuxz)	0.167	
Nu23 (Nuyz)	0.015	
Density	0.349	g/cm^3

For the re-entrant structure (Table 2.6), the highest elastic modulus was observed in the Z-direction (Ez) at 6.42×10^8 Pa, indicating greater stiffness along the out-of-plane axis. The modulus in the in-plane directions were significantly lower, with Ex at 2.57×10^8 Pa and Ey at 2.35×10^7 Pa, reflecting the anisotropic behavior characteristic of auxetic lattices. The shear modulus ranged from 5.09×10^6 Pa to 1.51×10^8 Pa, capturing the varying resistance to shear deformation across different planes. Notably, the Poisson's ratio in the X–Y plane (NUxy) was calculated as -1.988, demonstrating a highly auxetic response. The effective density of the homogenized re-entrant structure was found to be 0.349 g/cm^3, considerably lower than the solid material density due to the porous lattice architecture.

Table 2.7: Homogenized Material Result for Anti-tetrachiral Structure.

Engineering Constants	Results	Units
E1 (Ex)	1.91E+07	Pa
E2 (Ey)	1.91E+07	Pa
E3 (Ez)	6.88E+08	Pa
G12 (Gxy)	3.86E+06	Pa
G23 (Gyz)	9.16E+07	Pa
G31 (Gzx)	9.16E+07	Pa
Nu12 (Nuxy)	-0.853	
Nu13 (Nuxz)	0.011	
Nu23 (Nuyz)	0.011	
Density	0.374	g/cm^3

For the anti-tetrachiral structure (Table 2.7), the elastic modulus values for Ex and Ey were identical at 1.91×10^7 Pa, while Ez reached a higher value of 6.88×10^8 Pa, consistent with the structural orientation of the lattice. The shear modulus were determined as 9.16×10^7 Pa for Gyz and Gzx, and 3.86×10^6 Pa for Gxy, indicating directional differences in shear resistance. The Poisson's ratio in the X–Y plane was calculated as -0.853, confirming the auxetic behavior of the anti-tetrachiral configuration. The homogenized density was calculated as 0.374 g/cm^3, slightly higher than that of the re-entrant structure due to differences in geometric density.

The observations from the homogenized material results are as follows:

- The re-entrant structure exhibits an E1 (Ex) modulus of 2.57×10^8 Pa, which is approximately ten times higher than that of the anti-tetrachiral structure (1.91×10^7 Pa). This indicates a significantly stiffer response of the re-entrant topology along the X-direction.
- The Poisson's ratio Nu12 (Nuxy) of the re-entrant structure is approximately –1.99, which is more than twice the absolute value observed for the anti-tetrachiral topology (–0.85). This suggests that the re-entrant geometry demonstrates a much stronger auxetic effect under in-plane loading.
- In terms of shear modulus, the re-entrant structure has higher values of G12 and G31, while the anti-tetrachiral structure shows a relatively higher G23. This reflects the anisotropic nature of both lattices, where stiffness varies depending on the loading direction.

- The densities of the two structures are similar, with the re-entrant structure at 0.349 g/cm³ and the anti-tetrachiral structure at 0.374 g/cm³, indicating comparable mass characteristics despite their different topologies.

These homogenized material properties form the foundation for all subsequent finite element analyses, enabling efficient simulation of the complex auxetic sandwich structures while maintaining the essential mechanical characteristics of their full-scale geometries.

2.4.Experimental Testings

This section presents the experimental tests conducted to investigate the mechanical and dynamic behavior of the fabricated auxetic structures. The primary objective of these tests was to generate reliable reference data for comparison with the results obtained from finite element analyses.

The test samples were fabricated using additive manufacturing technology, incorporating the selected re-entrant and anti-tetrachiral auxetic lattice geometries. VeroBlue RGD840 was used as the base material, in line with the specifications detailed in the previous sections.

Three distinct types of experimental tests were performed to assess the mechanical and dynamic behavior of the auxetic structures under various loading conditions.

First, modal testing was conducted to determine the natural frequencies and corresponding mode shapes of the auxetic structures. The primary aim of this dynamic analysis was to evaluate the vibrational characteristics of the samples, which are directly influenced by geometry, material properties, and boundary conditions.

Following the modal testing, three-point (3P) bending tests were conducted on the same fabricated parts to investigate their flexural behavior. These tests were designed to assess the load–deflection response of the auxetic structures under transverse loading, which is critical for evaluating their performance in real-world applications such as panels, beams, and sandwich cores.

Lastly, compression tests were performed on cube-shaped specimens produced using the same lattice geometries and base material. These tests aimed to evaluate the load-bearing capacity and deformation behavior of the structures under compressive loading. Compression tests are particularly important for auxetic structures, as their unique deformation mechanisms, such as lateral expansion under axial compression, can lead to enhanced energy absorption and mechanical resilience. The data obtained from the compression tests provided a key reference point for comparing the corresponding static structural analyses in the finite element models.

Overall, the experimental tests provided a critical foundation for comparing the homogenized and full-scale finite element models developed in this study. By systematically evaluating the experimental outcomes against numerical predictions across different loading scenarios, the study offered a comprehensive assessment of the accuracy, applicability, and limitations of homogenization techniques for modeling complex auxetic lattice structures.

2.4.1.Modal testing

In this study, the roving hammer method was employed to conduct experimental modal testing and assess the dynamic characteristics of the fabricated auxetic structures. A schematic representation of the experimental setup for the roving hammer method, as referenced in the literature, is shown in Figure 2.97 [29]. This method is widely recognized in experimental modal analysis of mechanical systems, particularly when a fixed accelerometer is combined with sequential impacts at multiple excitation points.

The test setup involved exciting the structures at six designated points, labeled 1 to 6, as illustrated in Figure 2.98. The excitation was applied using an impact hammer (DJB IH-2) with a force range of 2000 N and a sensitivity of 2.36 mV/N. A stationary three-axis accelerometer was mounted to record acceleration responses corresponding to each impact. To ensure reliability and repeatability of the results, each impact was repeated three times at every excitation point.

Data acquisition was performed using Dewesoft SIRIUS, and the frequency response functions (FRFs) were computed through post-processing using DewesoftX 2024 software. The FRF results provided critical information for identifying the natural frequencies and mode shapes of the structures.

A limitation of the modal experimental setup is that all frequency modes not captured during the testing correspond to torsional modes. Since the setup employed in this study was restricted to a single-row accelerometer configuration, the vibrational responses associated with torsional motions could not be measured.

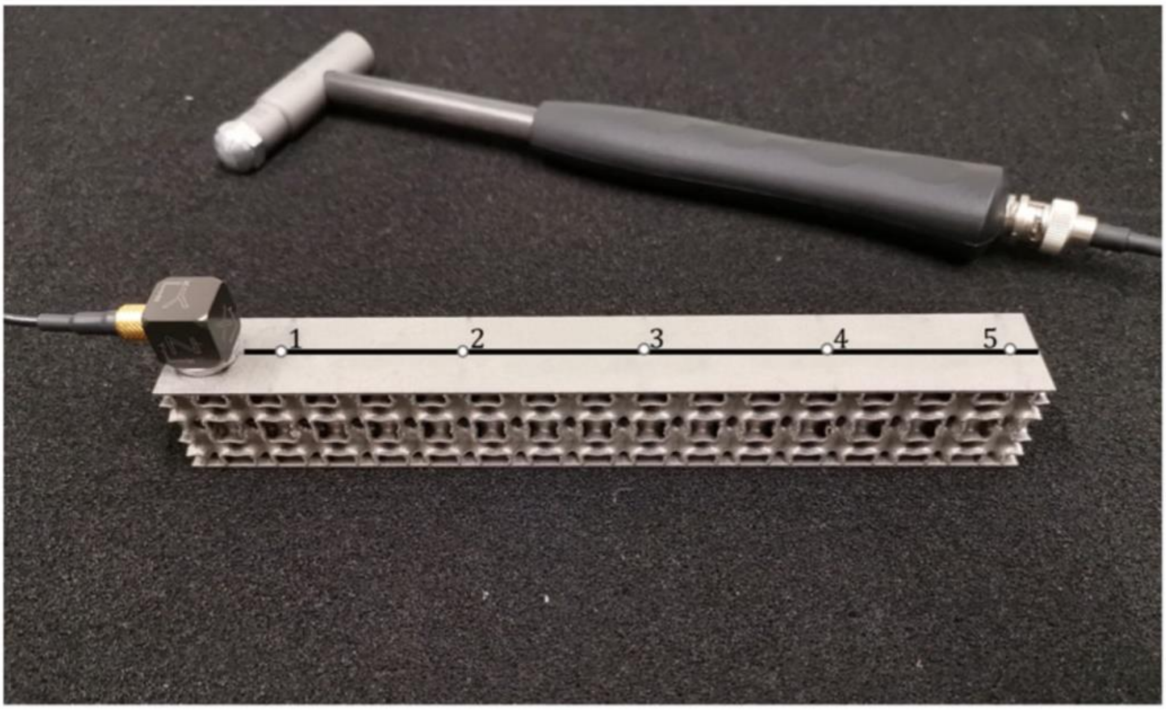

Figure 2.97: Schematic Example of Modal Testing Setup Using the Roving Hammer Method [29].

Reproduced from [29] with permission of Spring Nature.

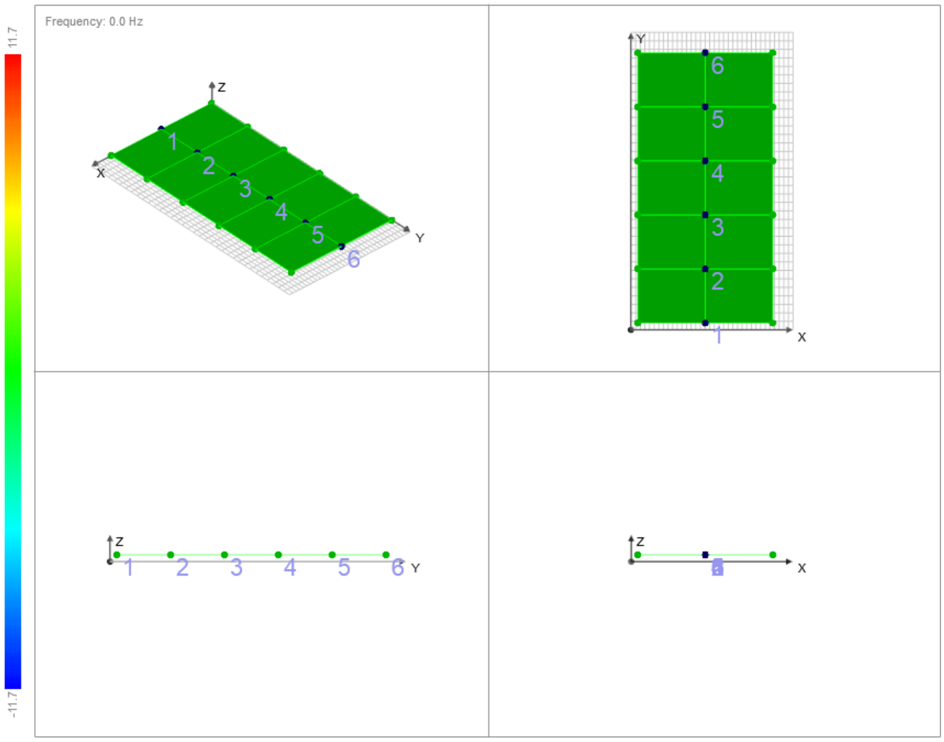

Figure 2.98: Modal Testing Six Designated Points.

The processed FRF plots for the re-entrant structure and the anti-tetrachiral structure are presented in Figure 2.99 and Figure 2.100, respectively.

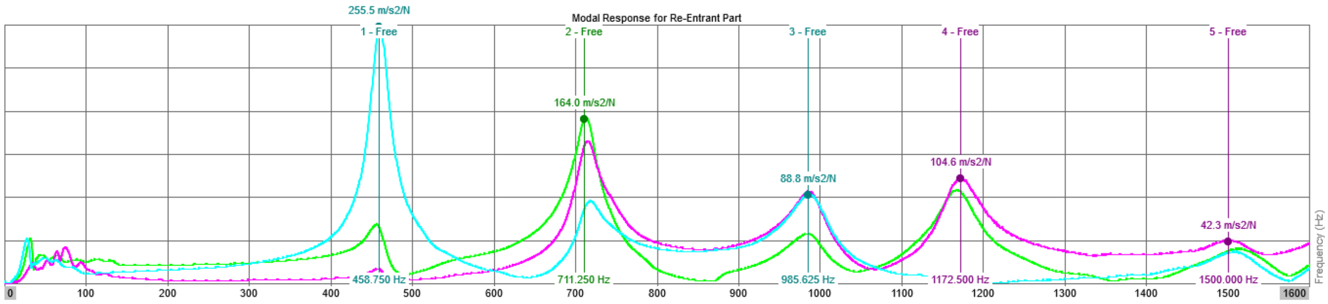

Figure 2.99: Modal Testing Frequency Results for Re-entrant Structure.

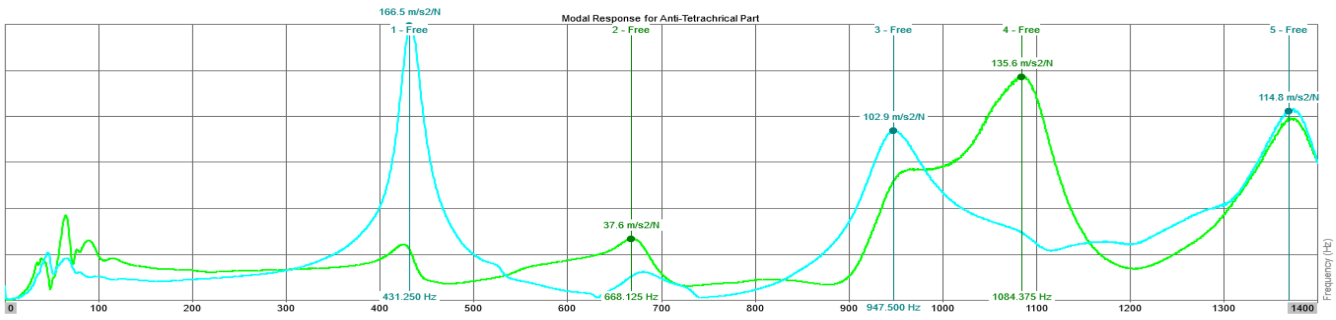

Figure 2.100: Modal Testing Frequency Results for Anti-tetrachiral Structure.

For the re-entrant structure, the identified mode shapes and corresponding deformation patterns were observed at natural frequencies of 458.8 Hz (Figure 2.101), 711.3 Hz (Figure 2.102), 985.6 Hz (Figure 2.103), 1173.0 Hz (Figure 2.104), and 1500.0 Hz (Figure 2.105).

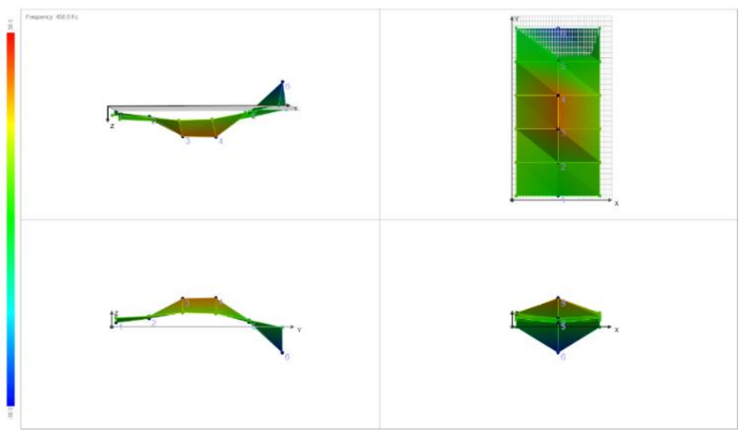

Figure 2.101: Modal Testing Results at 458.8 Hz for Re-entrant Structure.

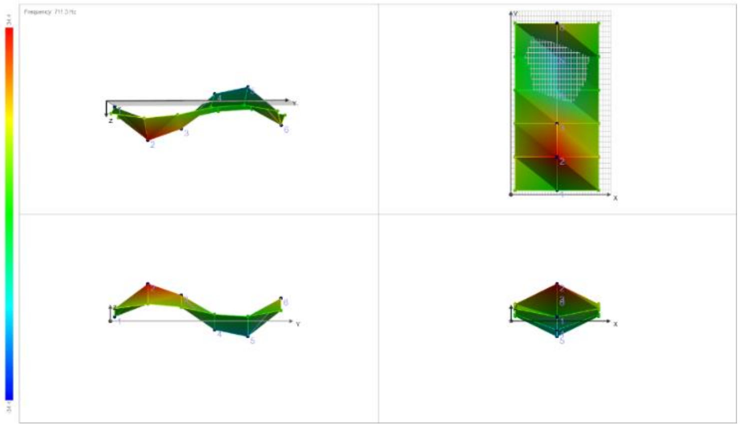

Figure 2.102: Modal Testing Results at 711.3 Hz for Re-entrant Structure.

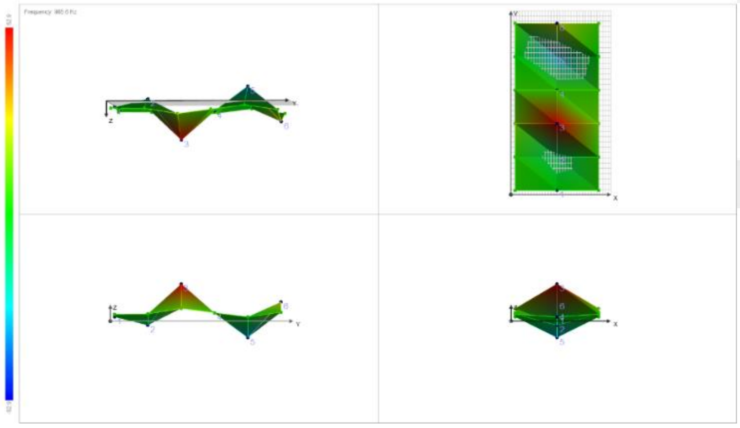

Figure 2.103: Modal Testing Results at 985.6 Hz for Re-entrant Structure.

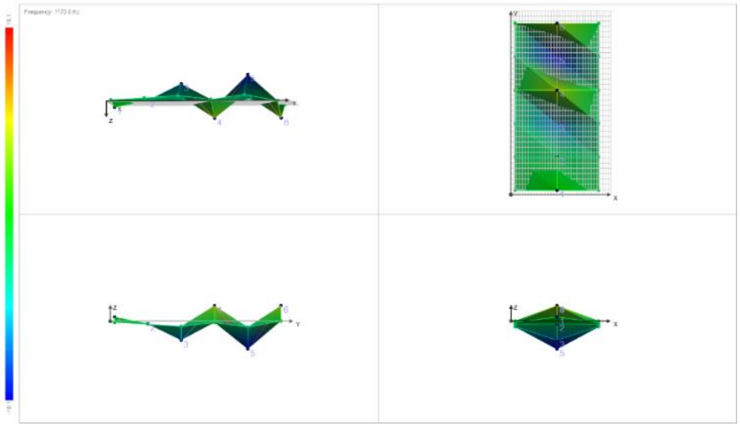

Figure 2.104: Modal Testing Results at 1173.0 Hz for Re-entrant Structure.

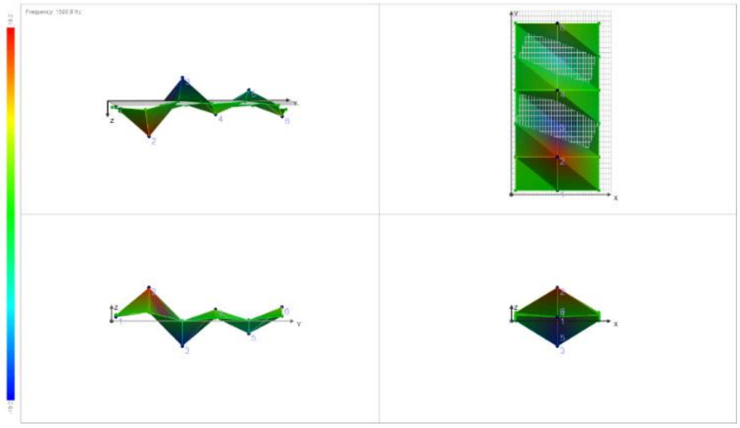

Figure 2.105: Modal Testing Results at 1500.0 Hz for Re-entrant Structure.

For the anti-tetrachiral structure, the identified mode shapes and corresponding deformation patterns were observed at natural frequencies 431.3 Hz (Figure 2.106), 668.1 Hz (Figure 2.107), 947.5 Hz (Figure 2.108), 1084.0 Hz (Figure 2.109), and 1370.0 Hz (Figure 2.110).

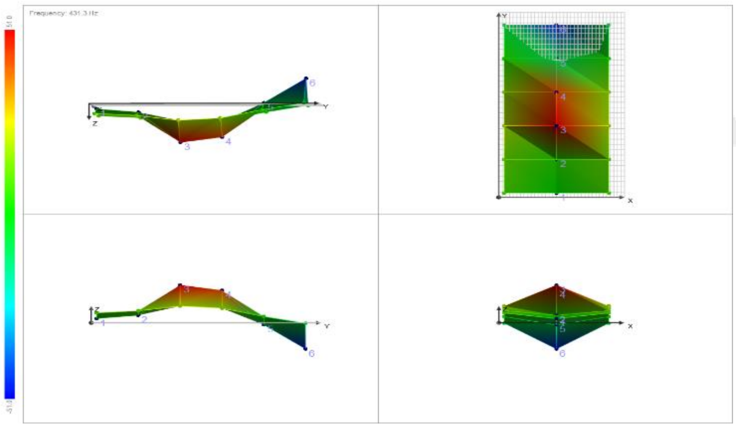

Figure 2.106: Modal Testing Results at 431.3 Hz for Anti-tetrachiral Structure.

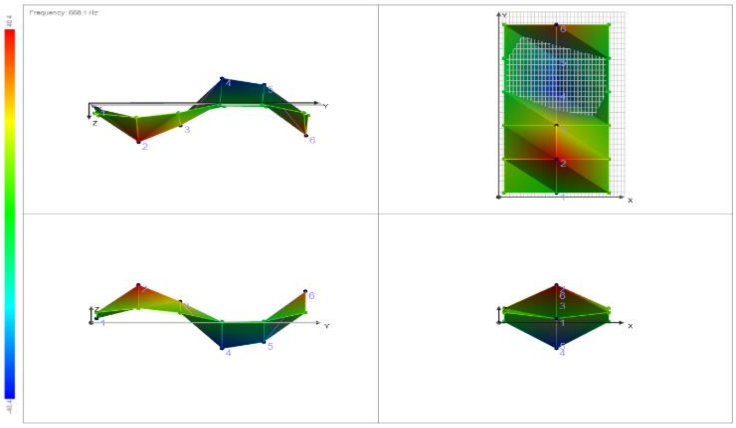

Figure 2.107: Modal Testing Results at 668.1 Hz for Anti-tetrachiral Structure.

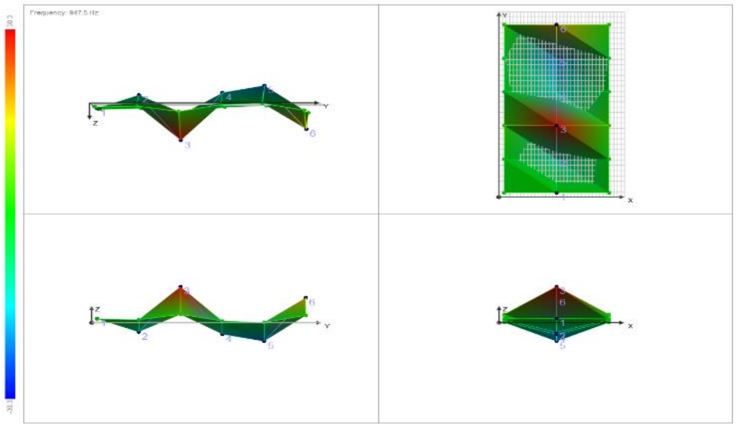

Figure 2.108: Modal Testing Results at 947.5 Hz for Anti-tetrachiral Structure.

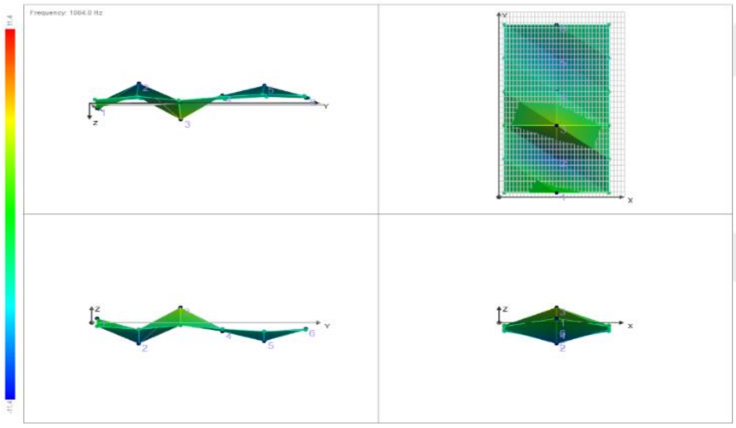

Figure 2.109: Modal Testing Results at 1084.0 Hz for Anti-tetrachiral Structure.

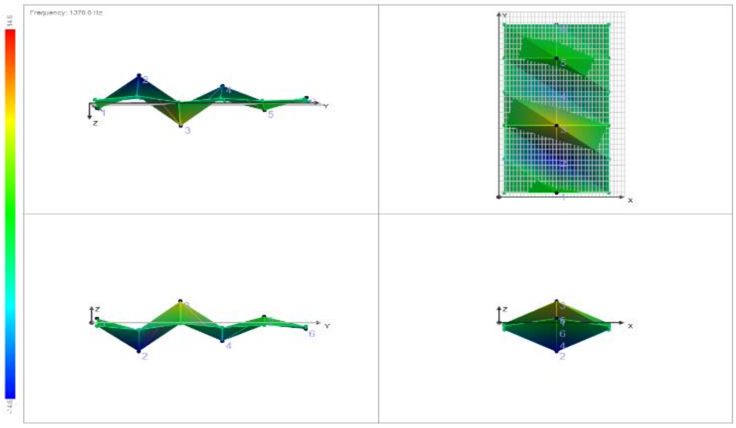

Figure 2.110: Modal Testing Results at 1370.0 Hz for Anti-tetrachiral Structure.

2.4.2.Three-point bending testing

The three-point (3P) bending tests were conducted to investigate the flexural behavior of the fabricated auxetic structures under transverse loading. In the 3P bending setup, the specimens were simply supported at two ends, while a concentrated load was applied at the midspan using an MTS 647 Hydraulic Wedge Grips universal testing machine. A constant crosshead velocity of 2 mm/min was applied throughout the test to ensure consistent loading conditions. Displacement and load data were recorded in real time using the MTS 793 Series Controller Software.

The test rig, including detailed views of the experimental setup, specimen positioning, support fixtures, gripping mechanisms, and loading head, is shown in Figure 2.111 for the re-entrant structure and in Figure 2.112 for the anti-tetrachiral structure.

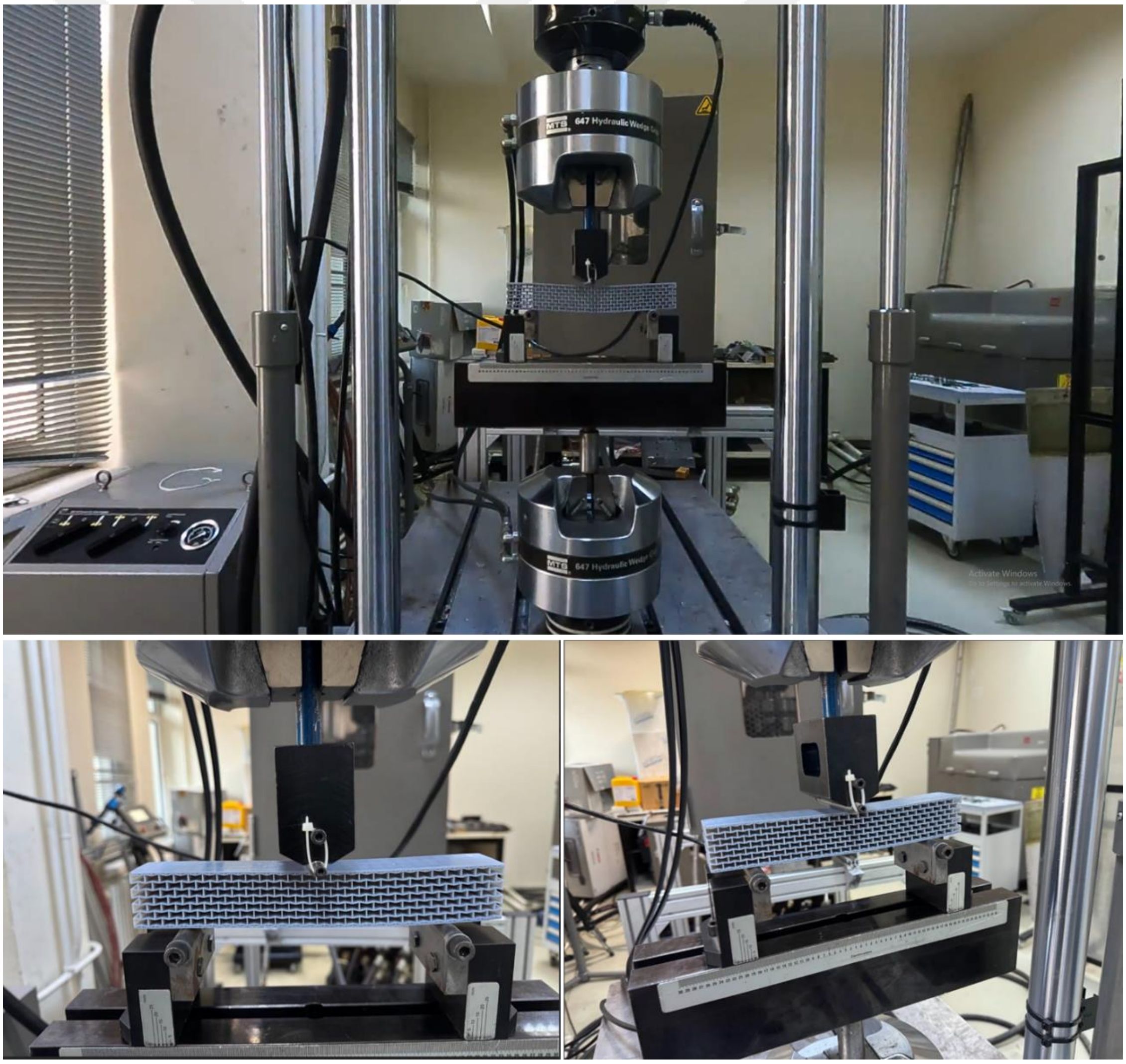

Figure 2.111: 3-Point Bending Test Setup for Re-entrant Structure.

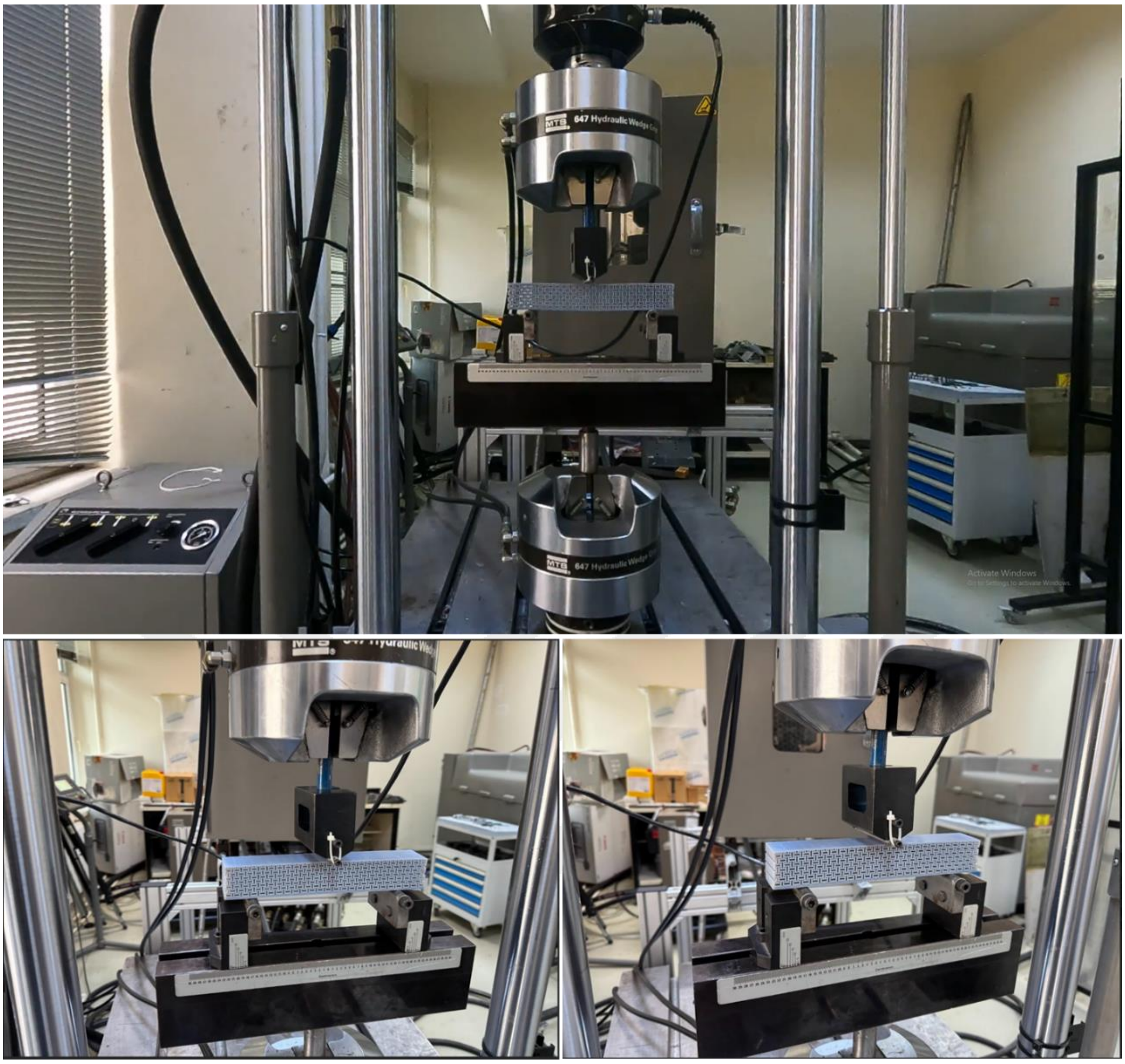

Figure 2.112: 3-Point Bending Test Setup for Anti-tetrachiral Structure.

Upon completion of the three-point (3P) bending tests, applied load versus measured displacement data were extracted from the test specimens. The load–displacement curves obtained from the experiments provide valuable insights into the flexural behavior, structural response and stiffness characteristics of the fabricated auxetic designs.

The complete load–displacement versus time responses are presented in Figure 2.113 for the re-entrant structure and in Figure 2.116 for the anti-tetrachiral structure under three-point bending. Corresponding load–displacement curves are shown in Figures 2.114 and 2.117 for the re-entrant and anti-tetrachiral lattices, respectively.

For the re-entrant structure, the load–displacement response within the range of 0–4 mm (Figure 2.115) shows an almost perfectly linear trend, indicating elastic behavior under the applied bending load.

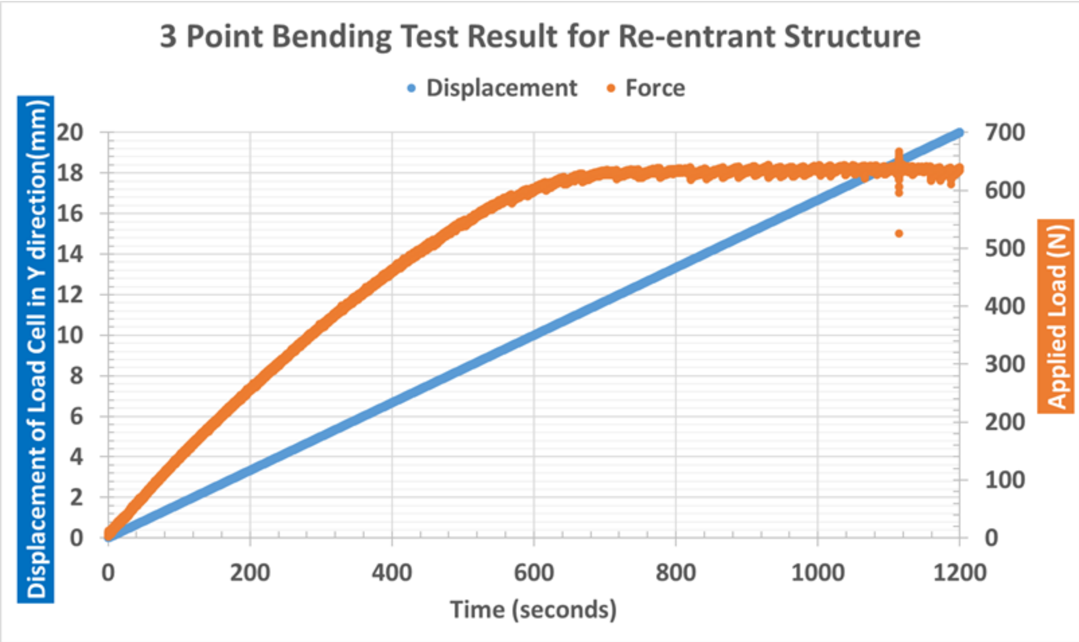

Figure 2.113: Experimental load–displacement versus time curve of the re-entrant structure under three-point bending.

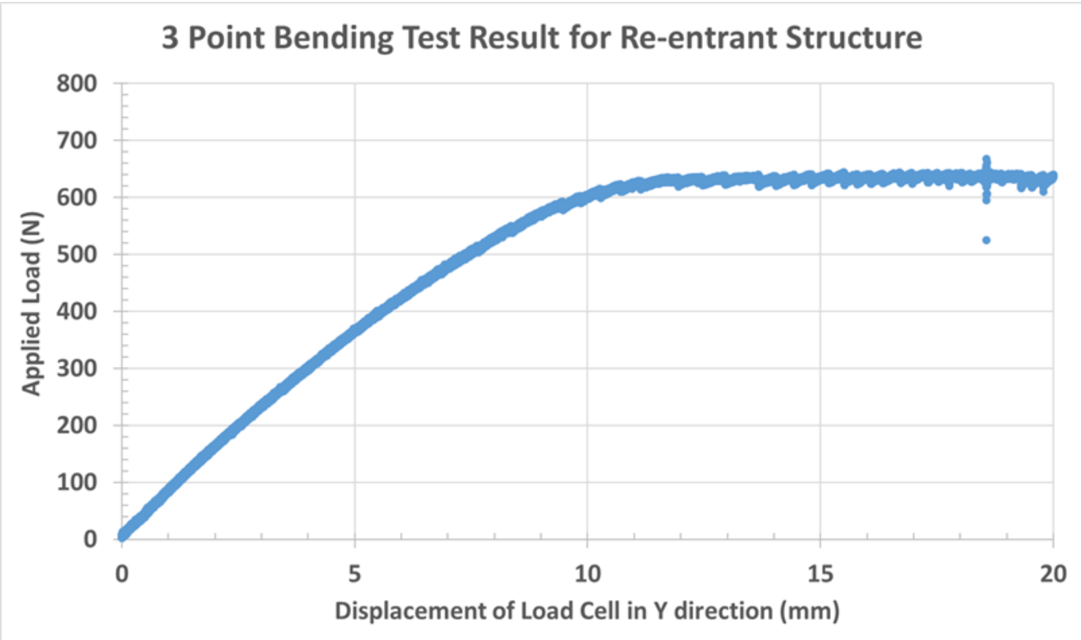

Figure 2.114: Load versus displacement curve obtained from 3P bending test of the re-entrant auxetic structure.

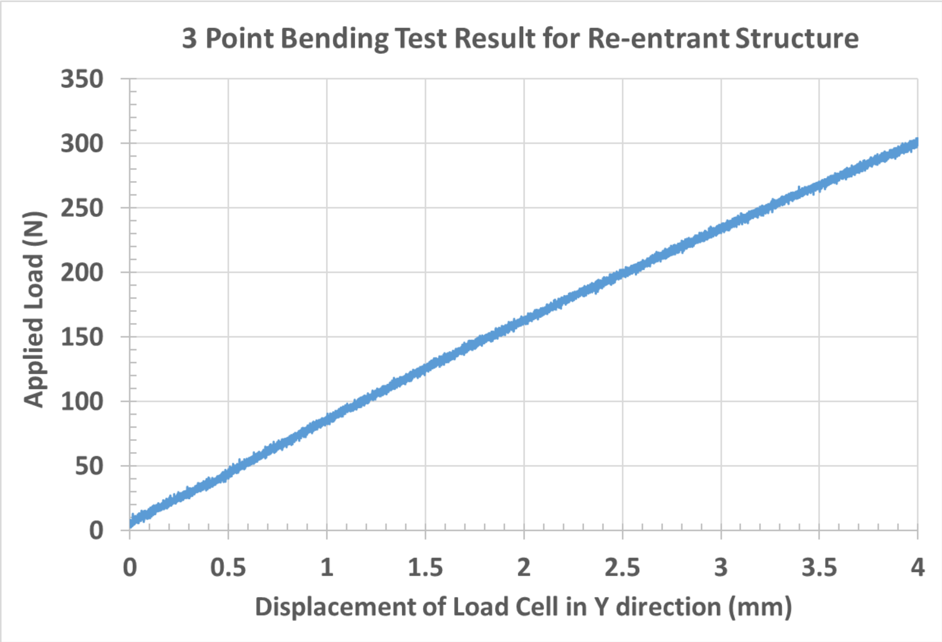

Figure 2.115: Load–displacement response of the re-entrant auxetic structure in the elastic region obtained from the three-point bending test.

A similar response is observed for the anti-tetrachiral structure (Figure 2.118), which also displays linearity in the same displacement range, confirming its elastic performance.

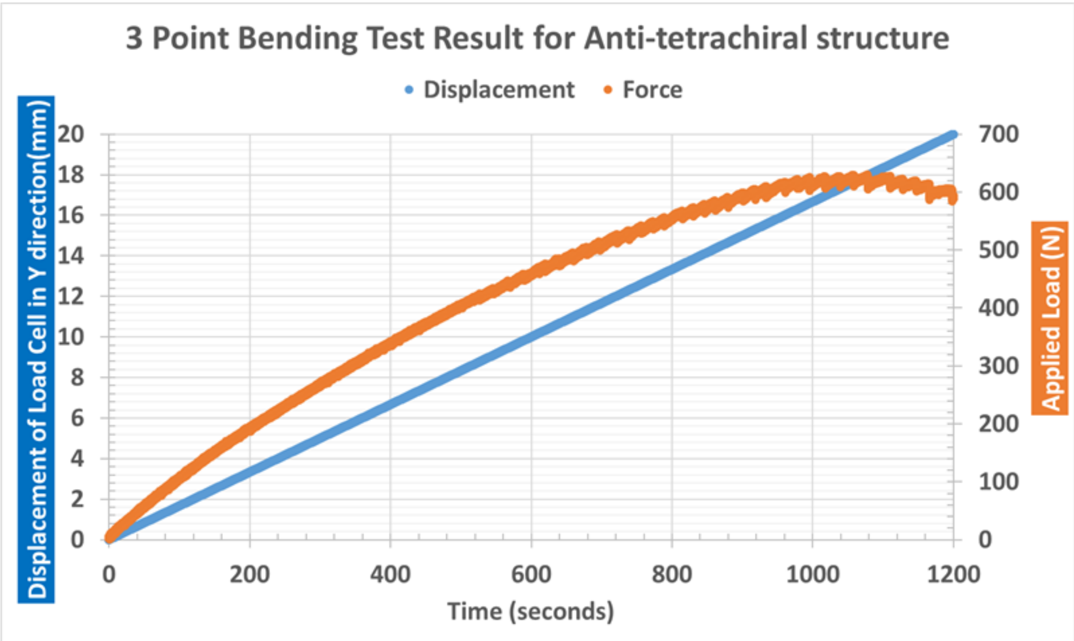

Figure 2.116: Experimental load–displacement versus time curve of the anti-tetrachiral structure under three-point bending.

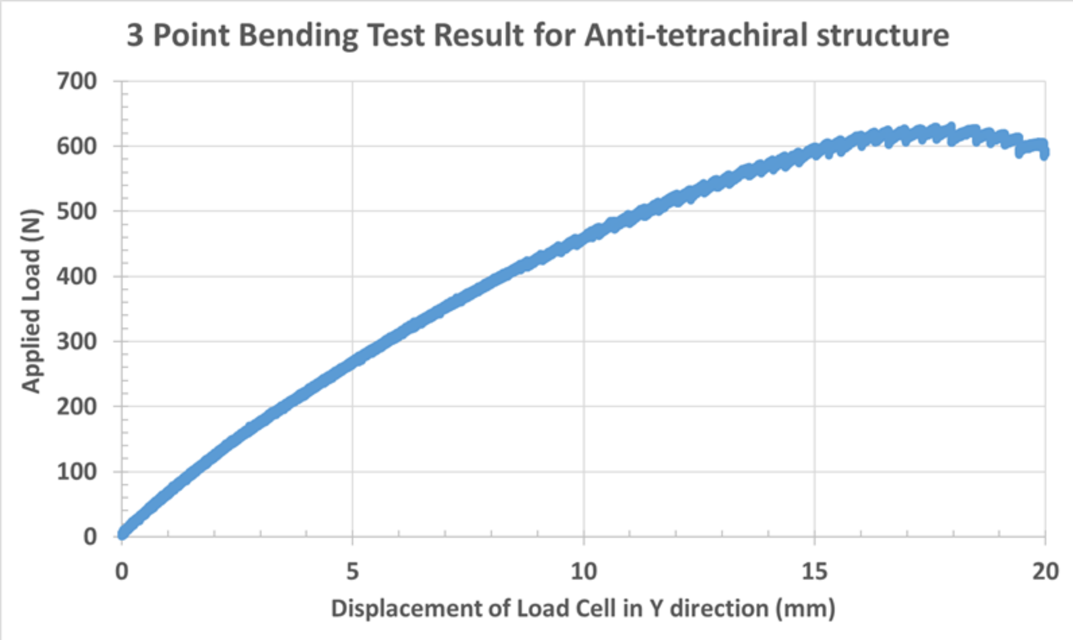

Figure 2.117: Load versus displacement curve obtained from 3P bending test of the anti-tetrachiral auxetic structure.

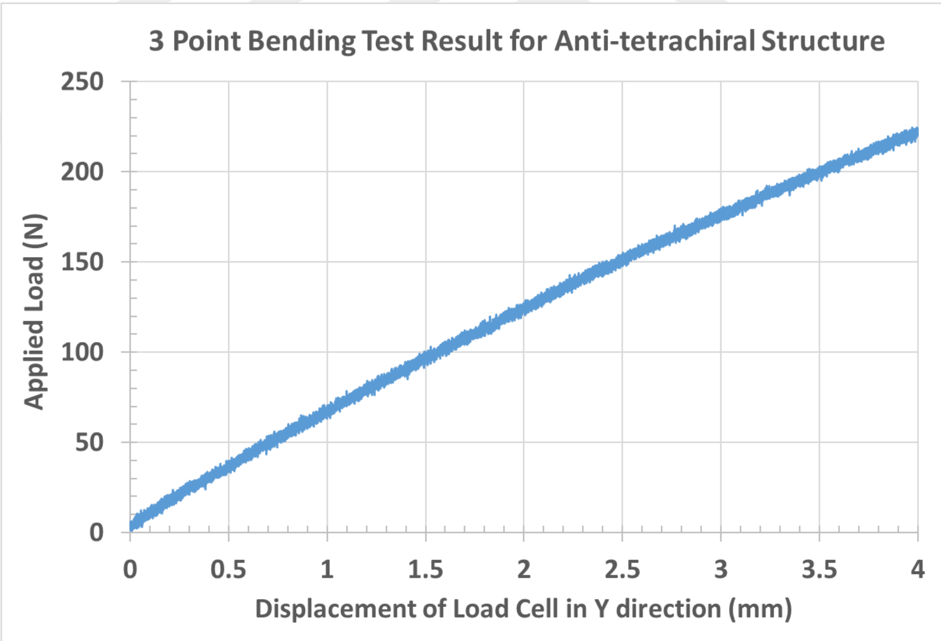

Figure 2.118: Load–displacement response of the anti-tetrachiral auxetic structure in the elastic region obtained from the three-point bending test.

2.4.3.Compression testing

To investigate the static structural behavior of the auxetic structures under compressive loading, compression tests were conducted as part of a related and ongoing study in which my co-advisor is actively involved. These experimental tests were performed by Dr. Kadir Günaydın and Prof. Dr. Halit Süleyman Türkmen, and the results have not been published previously. Courtesy of Prof. Dr. Halit Süleyman Türkmen and Dr. Kadir Günaydın, these test results, limited to the linear elastic region, are utilized in this thesis to enable direct comparisons with the numerical finite element analysis results for both re-entrant and anti-tetrachiral structures.

To determine the isotropic material properties of the base material, tensile tests were conducted using an MTS universal testing machine equipped with MTS 647 Hydraulic Wedge Grips. Data acquisition was performed through the MTS 793 Series Controller Software, and a constant crosshead velocity of 2 mm/min was applied throughout the testing process. The specimens were fabricated from VeroBlue RGD840 polymer, identical to the material used in the numerical analyses presented in this thesis. The experimental procedure followed standard testing protocols, with force–displacement data collected and subsequently converted into stress–strain curves for further analysis.

The compression specimens were designed as cubic structures incorporating the selected lattice geometries. The re-entrant specimen had dimensions of 45.4 mm in width (X-direction), 45.9 mm in height (Y-direction), as shown in Figure 2.119, and 45.0 mm in depth (Z-direction), as shown in Figure 2.120. The anti-tetrachiral specimen had dimensions of 43.75 mm in width (X-direction), 45.75 mm in height (Y-direction), as shown in Figure 2.121, and 45.0 mm in depth (Z-direction), as shown in Figure 2.122.

The internal geometries of the specimens precisely matched those used in the finite element models presented in this thesis, with detailed geometries provided in Figure 2.8 and Figure 2.9 for the re-entrant structure and in Figure 2.12 and Figure 2.13 for the anti-tetrachiral structure.

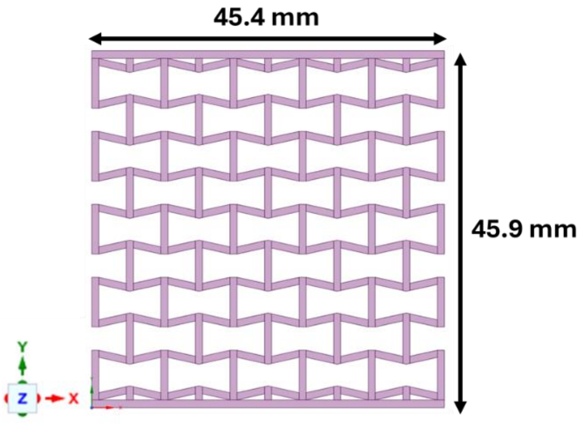

Figure 2.119: Width and Height of Re-entrant structure Used In Compression Test.

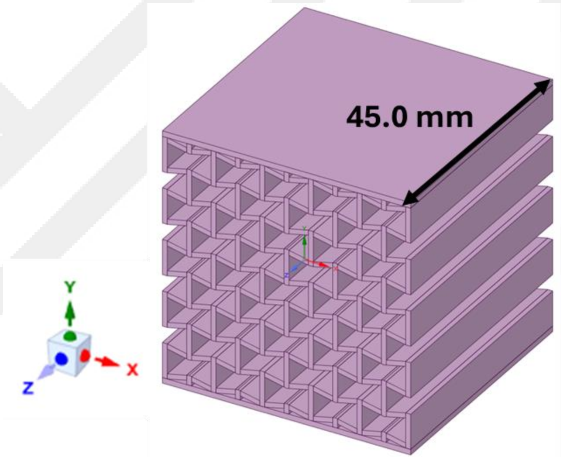

Figure 2.120: Depth of Re-entrant structure Used In Compression Test.

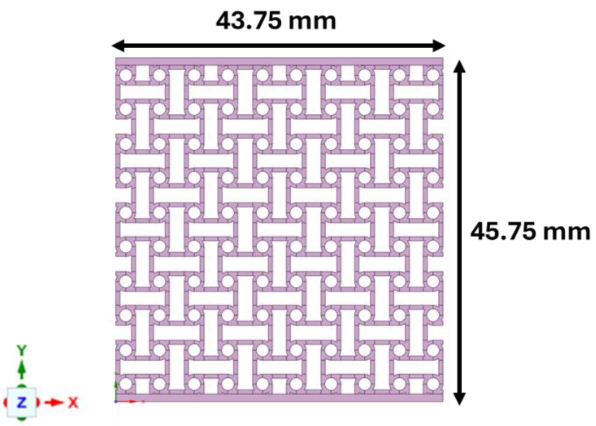

Figure 2.121: Width and Height of Anti-tetrachiral Structure Used In Compression.

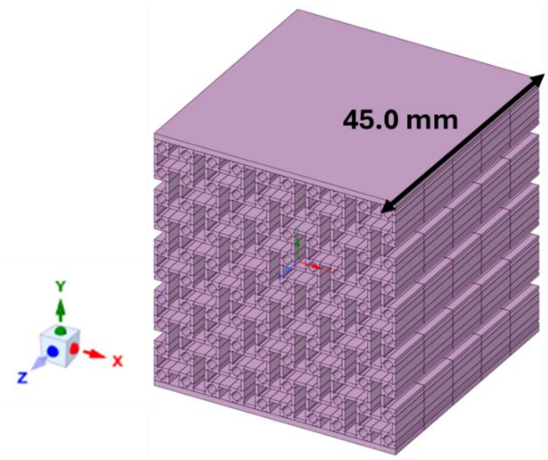

Figure 2.122: Depth of Anti-tetrachiral Structure Used In Compression Test.

Upon completion of the compression tests, the applied load versus displacement data were extracted. These load–displacement curves offer valuable insights into the mechanical response of the auxetic structures under compressive loading, providing a clear understanding of their load-bearing capacity and deformation behavior.

The experimental compression results of the re-entrant and anti-tetrachiral structures are presented in Figures 2.123–2.126. For the re-entrant structure, Figures 2.123 and 2.124 illustrate the load–displacement response, which exhibits a predominantly linear trend during the initial loading stage. At higher displacements, slight deviations from linearity become evident, suggesting the onset of localized deformation, stiffness reduction, or potential micro-buckling within the lattice. In contrast, the anti-tetrachiral structure, shown in Figures 2.125 and 2.126, displays an initial linear elastic region but gradually loses stiffness as the applied load increases. This softening trend is likely associated with deformation mechanisms characteristic of the anti-tetrachiral geometry, including rotational node motions and localized ligament bending.

Overall, the experimental results will be used as key reference points for verifying the numerical analyses and for examining how well the homogenization method can capture the compressive response of auxetic lattices.

Figure 2.123: Experimental load–displacement versus time curve of the re-entrant structure under compression.

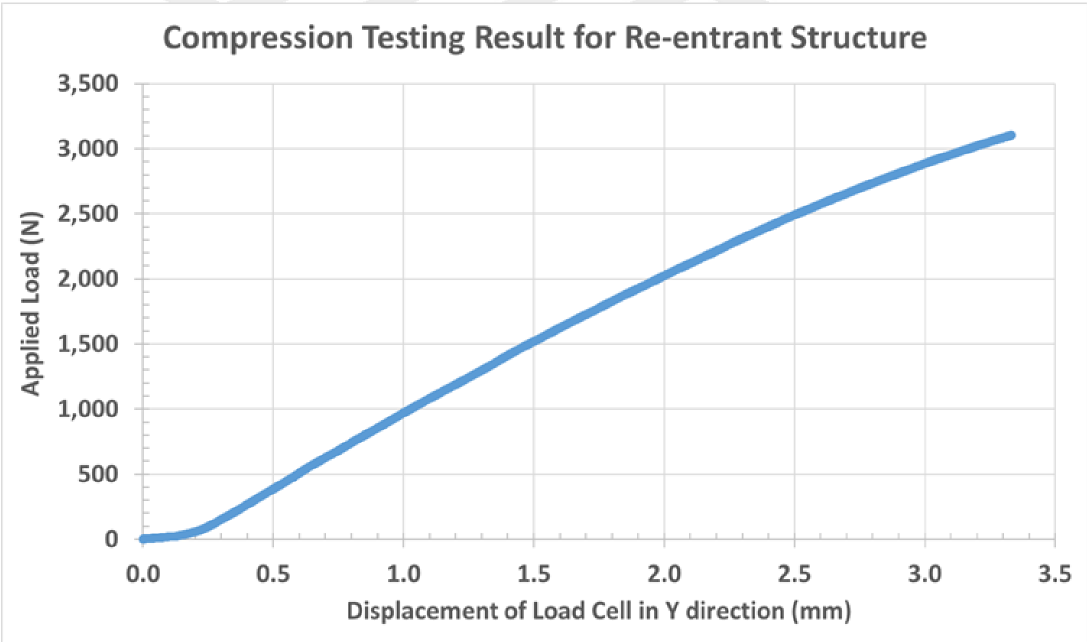

Figure 2.124: Experimental Load–Displacement Curve for Re-entrant Structure from Compression Test.

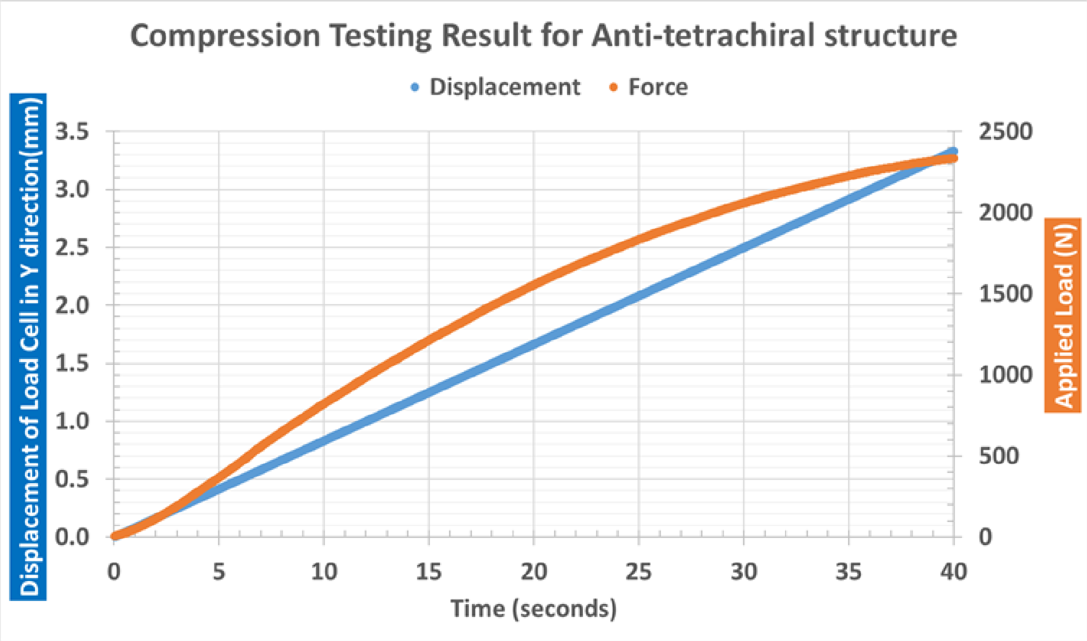

Figure 2.125: Experimental load–displacement versus time curve of the anti-tetrachiral structure under compression.

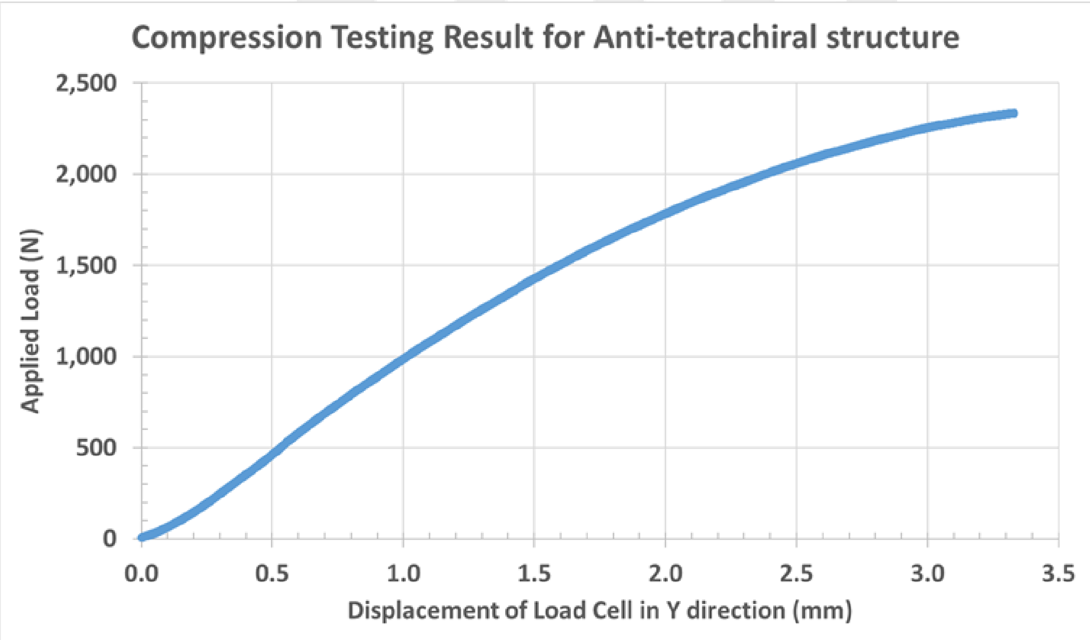

Figure 2.126: Experimental Load–Displacement Curve for Anti-tetrachiral Structure from Compression Test.

3.FINITE ELEMENT MODELS

This section presents the development of the finite element (FE) models created for both the full-scale (real-case) and homogenized (simplified-case) representations of the auxetic lattice structures. The objective of these models is to simulate and analyze the mechanical behavior of the re-entrant and anti-tetrachiral structures under various loading scenarios, including modal analysis, compressive loading, tensile loading, and three-point bending. All finite element models were developed using ANSYS Workbench 2020 R2 software.

A high-level overview of the finite element modeling framework is provided, covering the setup of modal analysis models for dynamic characterization, static structural models for compressive and tensile loading conditions, and static structural models for bending scenarios. The subsequent sections will provide details about the modeling approach, including geomery definitions, material property assignments, meshing details and boundary condition applications for both full-scale and simplified-scale cases.

3.1.Modal Response FEM

Modal response finite element models were developed using ANSYS Workbench 2020 R2, employing the Modal Analysis module from the Analysis Systems toolbox. The primary objective of these simulations was to identify the natural frequencies and corresponding mode shapes of both the re-entrant and anti-tetrachiral structures, facilitating a comparative evaluation between the full-scale and homogenized finite element models. Additionally, these simulations provided a reference point for comparison with the experimental modal test results presented earlier in Section 2.4.1 (Modal Testing).

For the re-entrant structure, two distinct finite element models were constructed, based on the geometric specifications described in Section 2.1.1 (Re-entrant Structure). The first model represented the full-scale configuration, capturing the complete three-dimensional geometry of the core and face plates as manufactured. This detailed geometry is illustrated in Figure 3.1, with the visual styling and color scheme matching the physical materials used in the fabricated specimens. All components in the full-scale model were assigned isotropic material properties, as summarized in Table 2.1.

The second model represented the homogenized configuration, where the internal auxetic core was replaced by a simplified solid volume. This model geometry is shown in Figure 3.2. In this homogenized model, the core region (highlighted in green) was assigned an orthotropic material definition based on the homogenization results, with the specific properties listed in Table 2.6. The top and bottom plates (colored brown) retained the isotropic material definition as per Table 2.1.

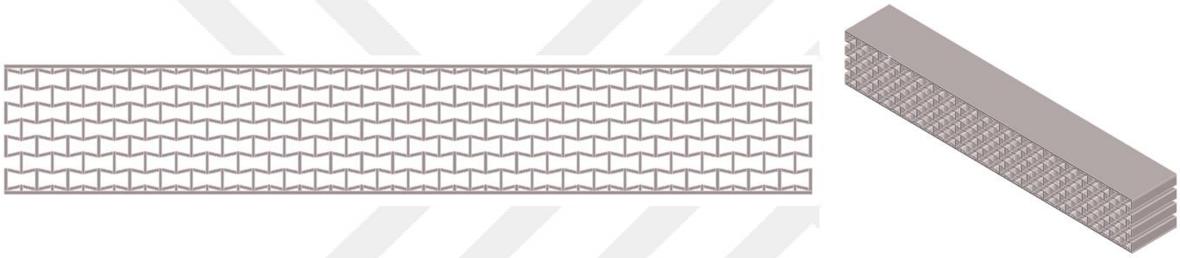

Figure 3.1: Full-scale geometry of re-entrant used in the modal response FEM.

Figure 3.2: Simplified-scale geometry of re-entrant used in the modal response FEM.

A similar modeling strategy was used for the anti-tetrachiral structure, as described in Section 2.1.2 (Anti-tetrachiral Structure). Two finite element (FE) models were developed: the full-scale model, which captures the detailed lattice geometry of the anti-tetrachiral core and face plates, is shown in Figure 3.3. In this model, all components were assigned the isotropic material properties listed in Table 2.1. The homogenized model, illustrated in Figure 3.4, simplifies the intricate lattice geometry by replacing the core with a solid volume. The core region (green) was assigned the orthotropic homogenized material properties summarized in Table 2.7, while the face plates (brown) retained the isotropic material properties from Table 2.1. This approach mirrors the modeling strategy used for the re-entrant structure, enabling a direct and consistent comparison between full-scale and homogenized finite element models across both auxetic geometries.

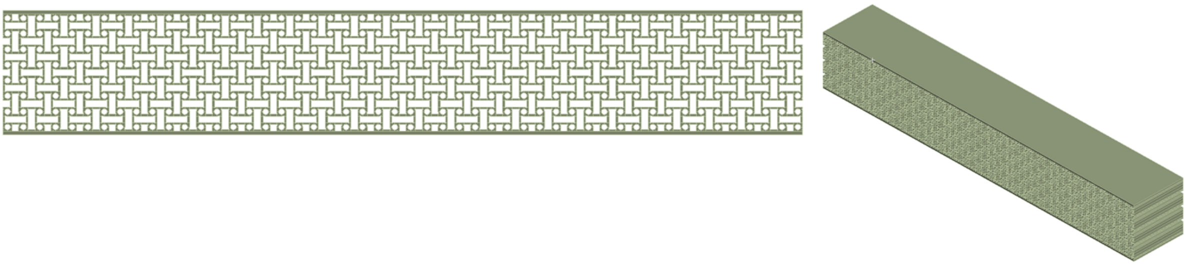

Figure 3.3: Full-scale geometry of anti-tetrachiral used in the modal response FEM.

Figure 3.4: Simplified-scale geometry of anti-tetrachiral used in the modal response FEM.

All finite element models, both full-scale and homogenized, of the re-entrant and anti-tetrachiral structures were developed using SOLID185 elements in ANSYS Workbench 2020 R2.

SOLID185 is a three-dimensional, eight-node brick element with three translational degrees of freedom per node (UX, UY, UZ), enabling accurate simulation of displacement in the X, Y, and Z directions. This element type is well-suited for modeling solid structures under static loading, modal response, and large deformation scenarios, and was selected to ensure consistency across all models while capturing the mechanical behavior of both complex lattice and simplified geometries.

For the full-scale models, fine tetrahedral meshes were generated to capture the intricate features of the lattice geometries, while the homogenized models employed coarser hexahedral meshes, reflecting their simplified geometry. Mesh details and visualizations for the full-scale re-entrant structure are shown in Figure 3.5, containing 897,600 elements and 1,185,500 nodes, while the simplified-scale version is shown in Figure 3.6, with 311,808 elements and 337,125 nodes.

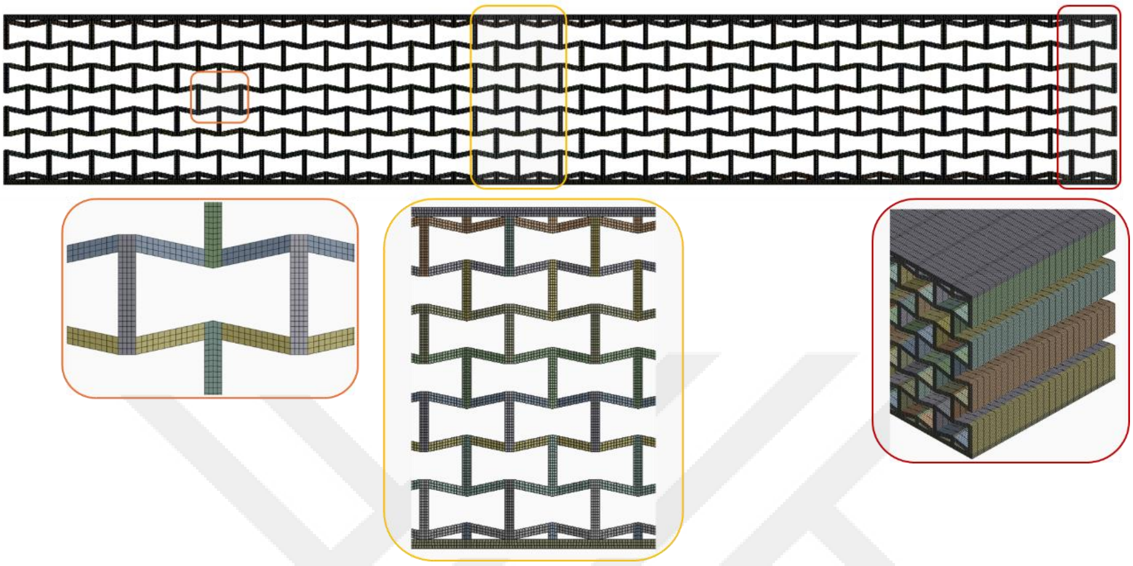

Figure 3.5: Finite element mesh of the full-scale re-entrant used in the modal response analysis.

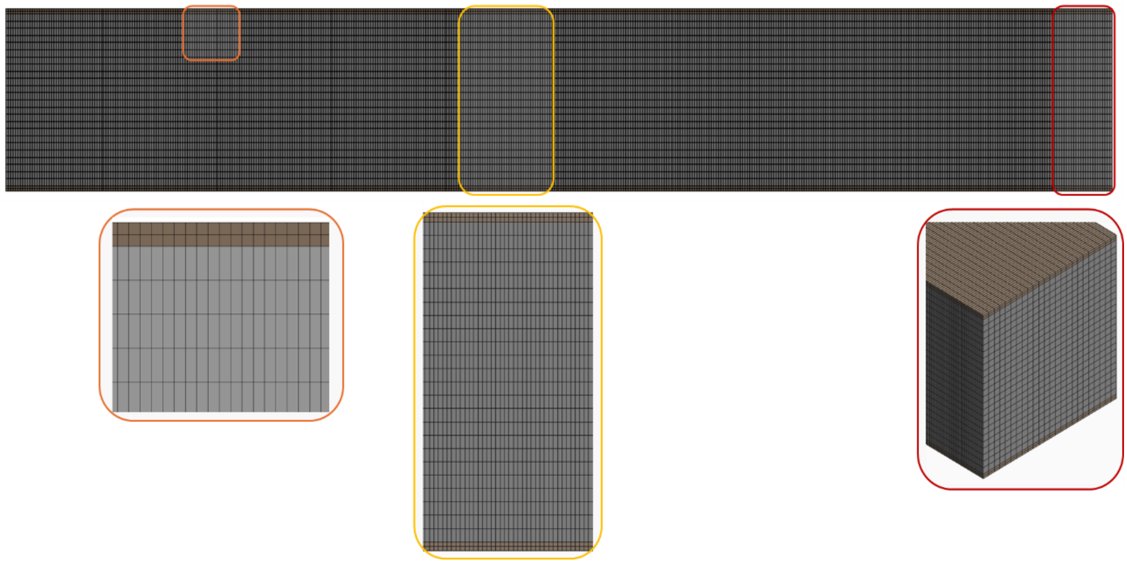

Figure 3.6: Finite element mesh of the simplified-scale re-entrant used in the modal response analysis.

Similarly, mesh details for the full-scale anti-tetrachiral structure are presented in Figure 3.7, comprising 2,928,720 elements and 3,722,325 nodes. The simplified-scale anti-tetrachiral model, shown in Figure 3.8, consists of 283,296 elements and 307,125 nodes.

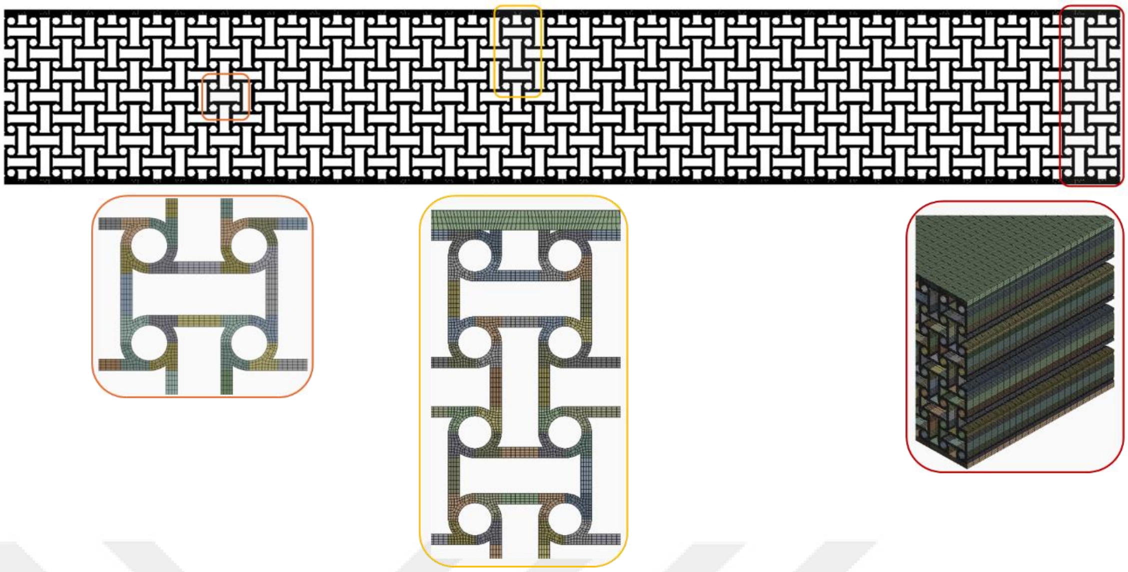

Figure 3.7: Finite element mesh of the full-scale anti-tetrachiral used in the modal response analysis.

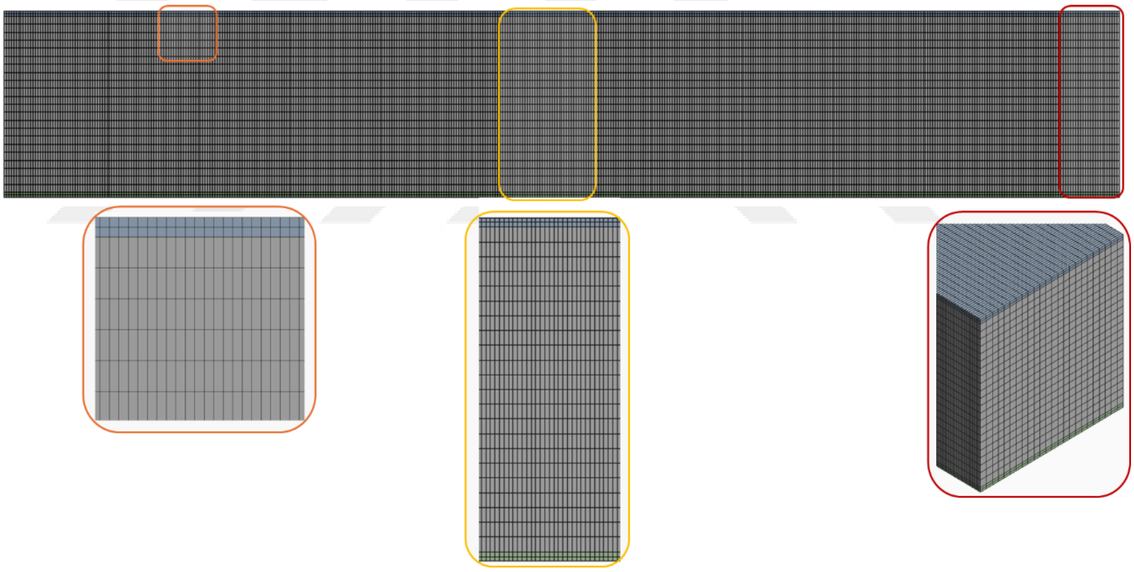

Figure 3.8: Finite element mesh of the simplified-scale anti-tetrachiral used in the modal response analysis.

In all four finite element models, both full-scale and simplified-scale versions of the re-entrant and anti-tetrachiral structures, no contact definitions were applied between the sub-components. Instead, the auxetic cores and face plates were integrated into a single continuous part by sharing nodes at their intersections. This modeling approach eliminates the need for contact elements and ensuring full geometric and mechanical compatibility at the interfaces between different regions of the structure.

Additionally, a free–free boundary condition was applied to all models. This means that no constraints, external forces, or imposed displacements were introduced, allowing the structure to deform and vibrate freely. This setup is standard for modal analysis, as it enables the accurate extraction of natural frequencies and mode shapes without the influence of boundary constraints.

A detailed comparison of computational solve times highlights the substantial efficiency gains achieved through homogenization. Specifically, the total computational time for the full-scale re-entrant model in the modal analysis was approximately 44 times longer than that of its simplified counterpart, while the full-scale anti-tetrachiral model required approximately 70 times more computation time than the corresponding homogenized model. These significant differences underscore the effectiveness of the homogenization approach in reducing computational demands for the analysis of complex auxetic structures.

The resulting natural frequencies and mode shapes obtained from the finite element simulations are presented and discussed in the following sections, enabling a comprehensive comparison between the full-scale and homogenized models, as well as with the experimental results from Section 2.4.1.

3.2.Three Point Bending Load Static Structural FEM

Three-point bending static structural finite element models were developed using ANSYS Workbench 2020 R2, utilizing the Static Structural module from the Analysis Systems toolbox. The primary objective of these simulations was to evaluate the flexural behavior of both the re-entrant and anti-tetrachiral structures under bending loads and to enable a direct comparison between the full-scale and simplified-scale FE models. Additionally, the simulation results provided a reference for comparison with the experimental three-point bending test results presented earlier in Section 2.4.2 (Three-Point Bending Testing).

Two finite element models were constructed for the re-entrant structure, based on the geometry described in Section 2.1.1 (Re-entrant Structure). The first model represents the full-scale configuration, incorporating the detailed 3D geometry of the auxetic core, top and bottom face plates, as well as the load cell and support roller components, to accurately simulate the real three-point bending test setup. The geometry of this model is shown in Figure 3.9, where component colors indicate their respective material assignments. The auxetic core and face plates (gray) were modeled using isotropic material properties with a flexural modulus derived from literature values, as provided in Table 2.1, while the load cell and support rollers (dark blue) were assigned structural steel properties.

The second model represents the simplified (homogenized) case, where the internal auxetic core was replaced with a solid volume representing the equivalent homogenized material. The geometry of this model is presented in Figure 3.10. In this configuration, the core region (green) was assigned orthotropic homogenized material properties, as detailed in Table 2.6, while the face plates (brown) retained the isotropic material properties from Table 2.1. The load cell and support rollers (dark blue) were similarly assigned structural steel properties.

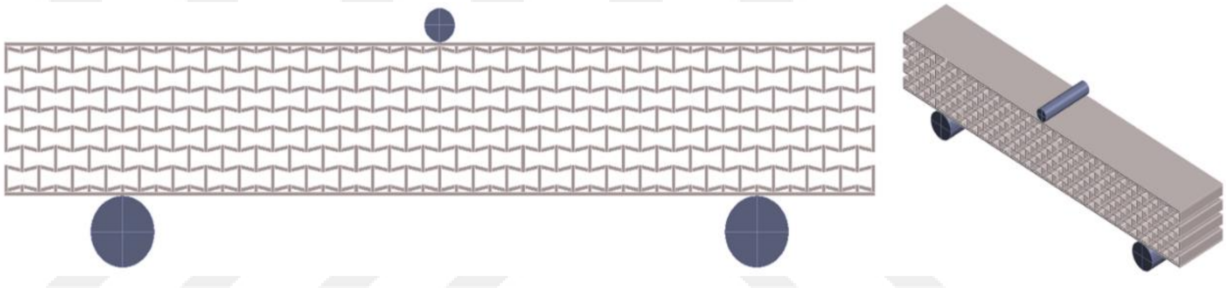

Figure 3.9: Full-scale geometry of re-entrant 3-point bending load FEM.

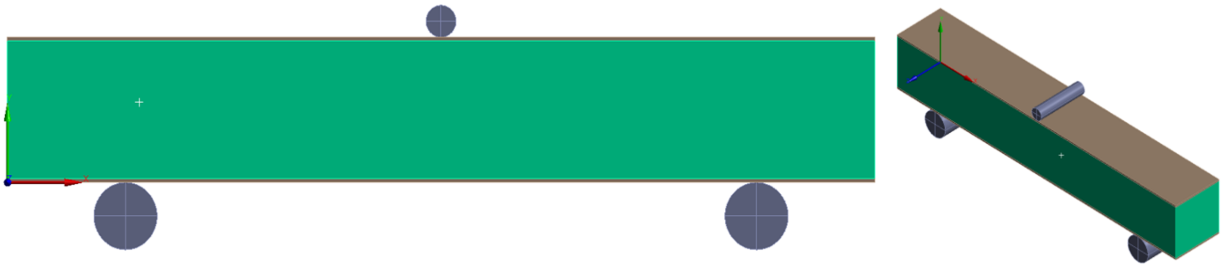

Figure 3.10: Simplified-scale geometry of re-entrant 3-point bending load FEM.

A comparable modeling strategy was applied for the anti-tetrachiral structure, based on the geometry described in Section 2.1.2 (Anti-tetrachiral Structure). The full-scale model, illustrated in Figure 3.11, includes the complete 3D lattice geometry of the auxetic core, the top and bottom face plates, and the load cell and support rollers, with color-coding reflecting material assignments. The auxetic core and plates (dark green) were modeled with isotropic material properties, as summarized in Table 2.1, while the load cell and rollers (dark blue) were assigned structural steel properties.

The homogenized model of the anti-tetrachiral structure is shown in Figure 3.12. Here, the intricate auxetic core was replaced with an equivalent solid volume, assigned orthotropic homogenized material properties from Table 2.7, while the face plates (gray) used isotropic material properties in accordance with Table 2.1. The load cell and support rollers (dark blue) remained modeled as structural steel components.

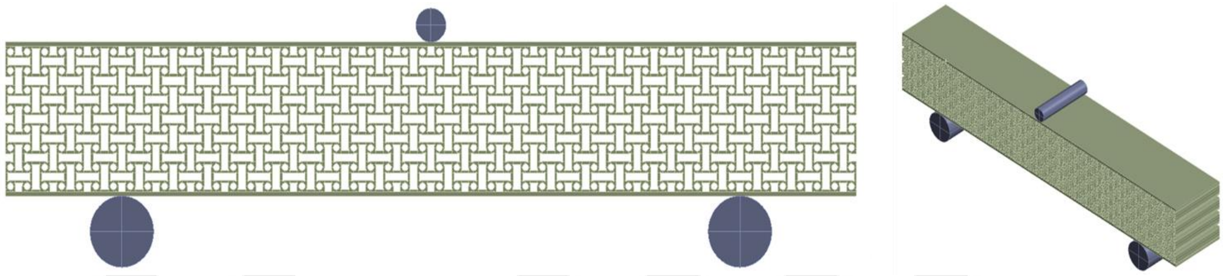

Figure 3.11: Full-scale geometry of anti-tetrachiral 3-point bending load FEM.

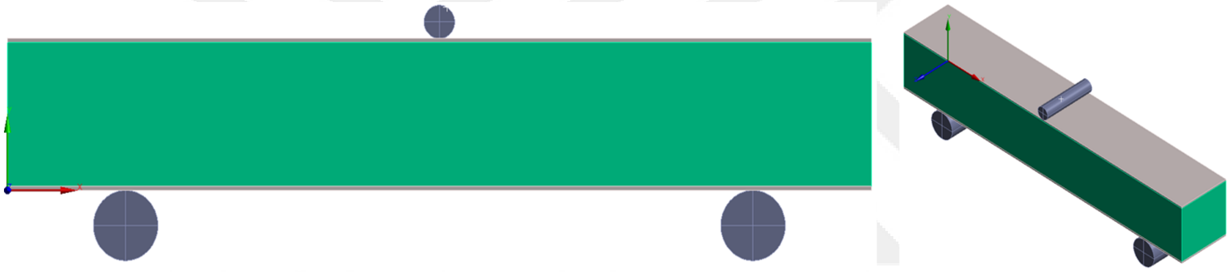

Figure 3.12: Simplified -scale geometry of anti-tetrachiral 3-point bending load FEM.

All finite element models, including both the full-scale and simplified (homogenized) versions of the re-entrant and anti-tetrachiral structures, were meshed using SOLID185 elements.

For the re-entrant structure, the mesh details and visualizations of the full-scale model are presented in Figure 3.13. This model contains 999,984 elements and 1,296,125 nodes. The mesh details and visualization of the simplified-scale model are shown in Figure 3.14, with a total of 414,192 elements and 447,750 nodes.

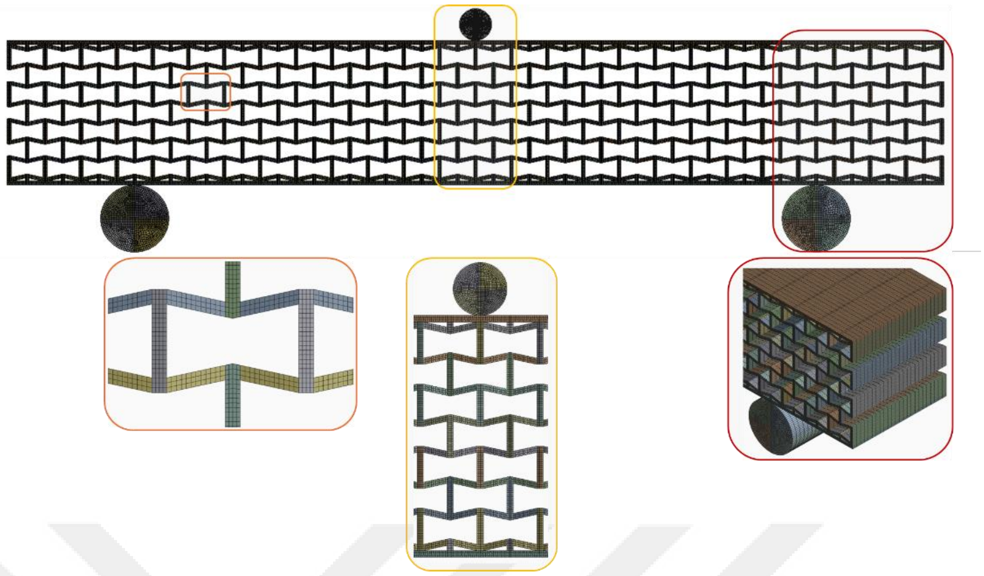

Figure 3.13: FE mesh of the full-scale re-entrant for 3-point bending load FEM.

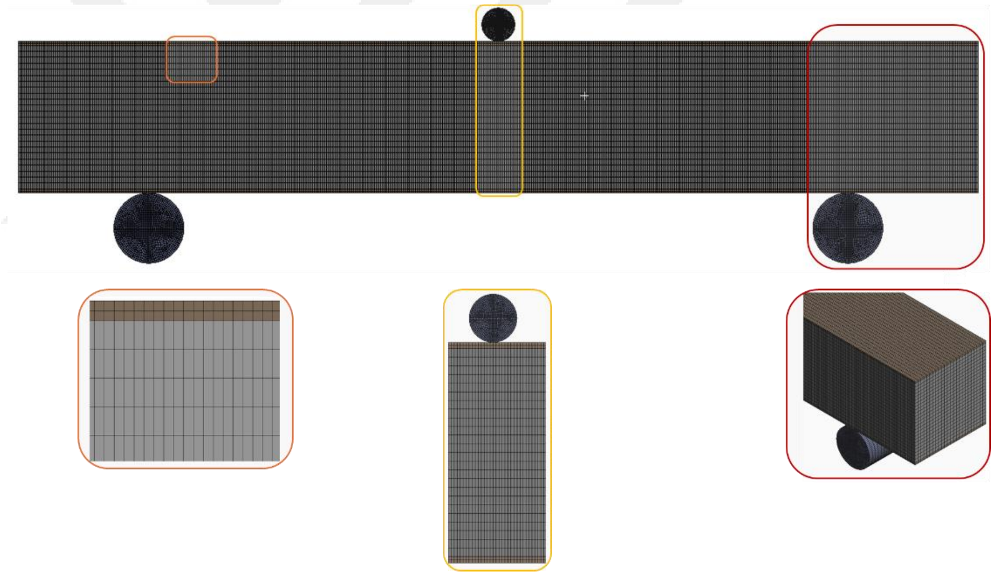

Figure 3.14: FE mesh of the simplified-scale re-entrant for 3-point bending load FEM.

For the anti-tetrachiral structure, the full-scale model mesh is shown in Figure 3.15, consisting of 3,034,752 elements and 3,836,725 nodes, while the simplified-scale model, shown in Figure 3.16, contains 389,328 elements and 421,525 nodes.

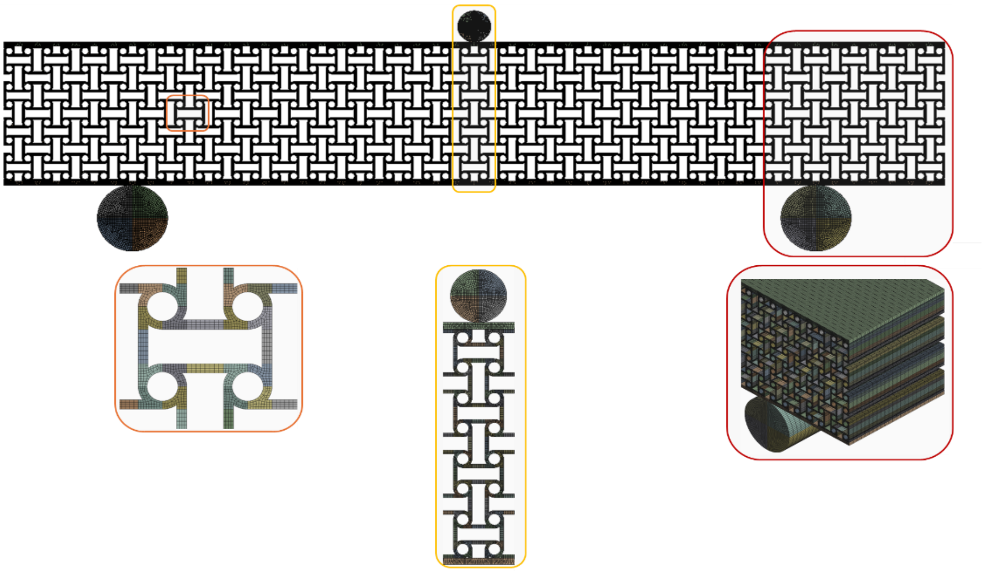

Figure 3.15: FE mesh of the full-scale anti-tetrachiral for 3-point bending load FEM.

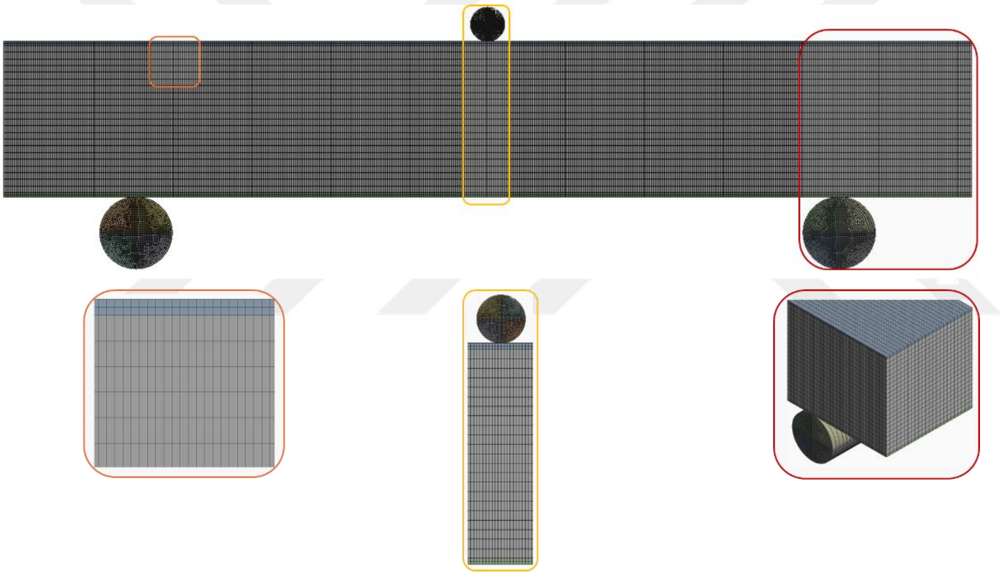

Figure 3.16: FE mesh of the simplified-scale anti-tetrachiral for 3-point bending load FEM.

In all four finite element models, including the full-scale and simplified-scale versions of both the re-entrant and anti-tetrachiral structures, frictional contact definition with a friction coefficient of 0.3, was applied at the interfaces between the top and bottom surfaces of the auxetic structures and the corresponding surfaces of the load cell and support rollers. This contact type was chosen to isolate structural deflection in the Y-direction, where the compressive or bending load is applied, without introducing shear effects. The same contact strategy was consistently applied to all models for comparability.

For the re-entrant structure, a frictional contact definition was defined between the top and bottom surfaces of the auxetic core (contact surfaces) and the inner surfaces of the top load cell and bottom support rollers (target surfaces). A friction coefficient of 0.3 was used to represent static friction behavior between polymeric materials and steel surfaces, ensuring realistic constraint conditions and accounting for potential sliding resistance during compressive deformation. This value was applied consistently across all models to ensure comparability. These contact regions are illustrated in Figure 3.17 for the full-scale model and Figure 3.18 for the simplified-scale model. In the figures, continuous red lines represent target surfaces, while dashed black lines represent the contact surfaces. The same contact configuration was applied identically to both versions of the model.

Similarly, the anti-tetrachiral structure followed the same contact configuration. Frictional contact definition, with a friction coefficient of 0.3, was defined between the top and bottom surfaces of the auxetic structure (contact surfaces) and the inner surfaces of the top load cell and bottom support rollers (target surfaces). These regions are shown in Figure 3.19 for the full-scale model and Figure 3.20 for the simplified-scale model. As in the re-entrant case, continuous red lines indicate the target surfaces and dashed black lines represent the contact surfaces. The same contact setup was consistently applied across both configurations to ensure modeling uniformity.

Boundary conditions were defined to replicate the physical test setup. The upper half of the load cell, highlighted with a solid blue line, was constrained in the horizontal directions (Ux = Uz = 0) and subjected to a vertical downward displacement of Uy = –4.0 mm, simulating the applied bending load at the midpoint of the specimen. The bottom halves of the support rollers, also highlighted with a solid blue line, were fully fixed in all directions (Ux = Uy = Uz = 0), representing rigid supports. Additionally, the bottom surfaces of the auxetic structures, marked with a dashed black line, were constrained in the horizontal directions (Ux = Uz = 0) while remaining free in the vertical direction (Uy = free) to allow realistic flexural deformation during loading.

These boundary conditions were consistently applied across all four finite element models, ensuring consistency and comparability between the full-scale and simplified-scale representations. Boundary locations are shown in Figure 3.17 for the re-entrant full-scale model, Figure 3.18 for the re-entrant simplified-scale model, Figure 3.19 for the anti-tetrachiral full-scale model, and Figure 3.20 for the anti-tetrachiral simplified-scale model.

Regarding computational performance, the total solve time for the full-scale re-entrant structure in the three-point bending analysis was approximately 3 times longer than that of its simplified-scale model. For the anti-tetrachiral structure, the full-scale model required approximately 6 times longer to compute compared to its homogenized counterpart. These results highlight the significant reduction in computational effort achieved through homogenization.

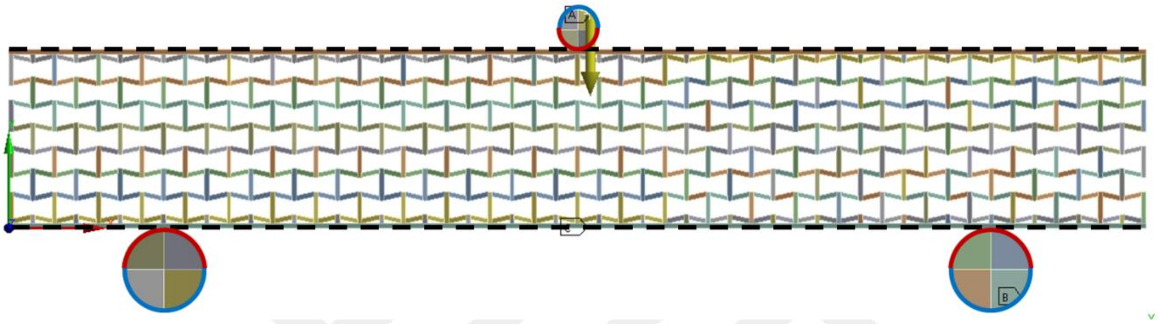

Figure 3.17: Boundary Conditions of the full-scale re-entrant for 3-point bending load FEM.

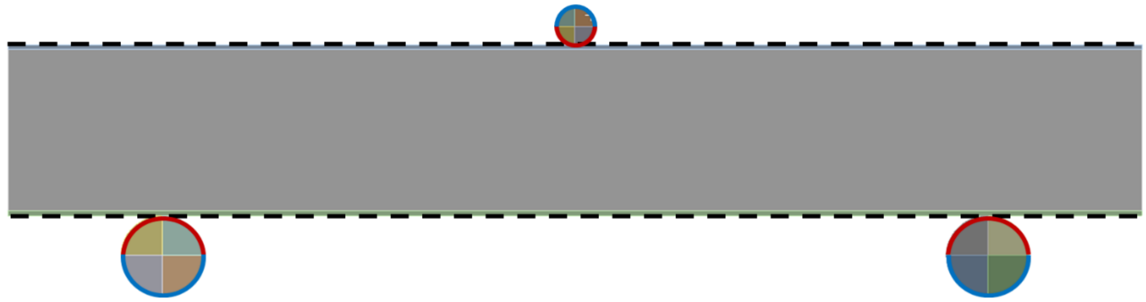

Figure 3.18: Boundary Conditions of the simplified-scale re-entrant for 3-point bending load FEM.

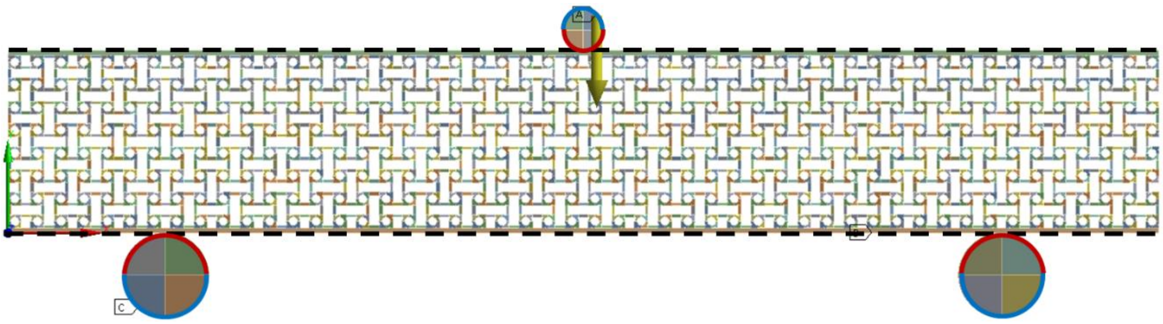

Figure 3.19: Boundary Conditions of the full-scale anti-tetrachiral for 3-point bending load FEM.

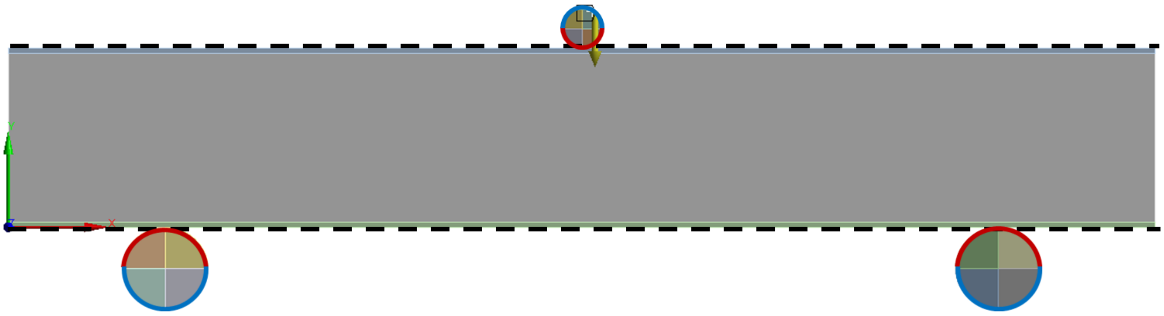

Figure 3.20: Boundary Conditions of the simplified-scale anti-tetrachiral for 3-point bending load FEM.

3.2.1.Three-point bending static structural FEM with the average young's modulus obtained from tensile and compression tests

In a three-point bending test, the specimen is simultaneously subjected to both compressive and tensile stresses. This makes it difficult to accurately represent the material behavior in FEA when the elastic modulus is derived solely from tensile testing. To address this limitation, a sensitivity model was developed in which the Young's modulus was updated to the arithmetic average of the values obtained from both tensile and compression tests.

In this setup, the FEM model was constructed identically to the main configuration introduced in Section 3.2, with the only difference being the definition of material properties. All geometry, meshing details, contact definitions, boundary conditions, and analysis settings remained unchanged.

For the re-entrant structure, the auxetic core and face plates (light green) were modeled as isotropic materials using the averaged Young's modulus from tensile and compression results, as listed in Table 2.4. The load cell and support rollers (dark blue) were defined with structural steel properties. The corresponding model is shown in Figure 3.21. For the anti-tetrachiral structure, the auxetic core and face plates (dark green) were similarly modeled with isotropic properties based on the averaged modulus, as listed in Table 2.5, while the load cell and rollers were again represented as structural steel. The final model is illustrated in Figure 3.22.

In this sensitivity study, the homogenized representation of the FEM model was not considered, as the primary objective was to examine how the model response changes with updated material properties. The comparison between full-scale geometry and its simplified (homogenized) representation will instead be presented in Section 4.2 for the main models introduced in Section 3.2.

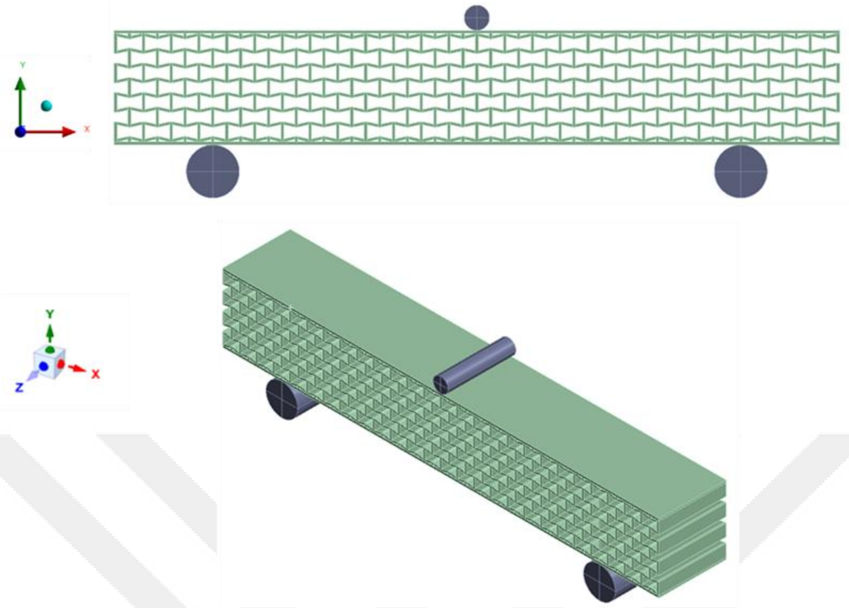

Figure 3.21: Materials of re-entrant 3-point bending load FEM with Average Young's Modulus.

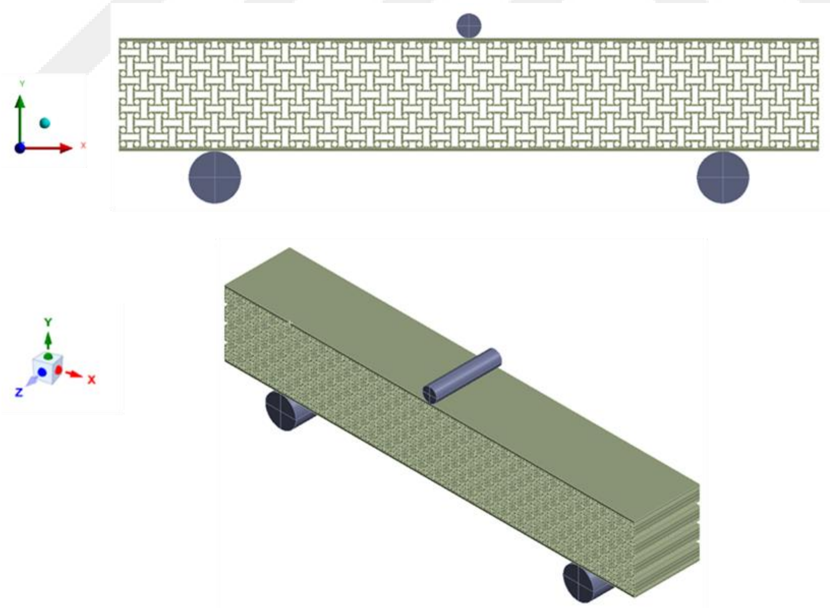

Figure 3.22: Materials of anti-tetrachiral 3-point bending load FEM with Average Young's Modulus.

3.2.2. Three-point bending static structural FEM using separate young's modulus for tension and compression with neutral axis consideration

As in the case of three-point bending, the specimen is simultaneously subjected to compressive and tensile stresses, making it difficult to capture the actual material response in FEA when the elastic modulus is defined solely from tensile testing. To overcome this limitation, a second sensitivity model was developed in which an imaginary neutral axis was introduced at Uy = 18.3 mm, corresponding to the mid-plane of the specimen in the Y-direction.

The FEM configuration was kept identical to the reference model described in Section 3.2, with the only modification being the material definitions. All geometry, meshing details, contact definitions, boundary conditions, and analysis settings remained unchanged.

For the re-entrant structure, the model visualization is shown in Figure 3.23, where the neutral axis is defined at Uy = 18.3 mm and illustrated by an imaginary red line.

In this configuration, the upper regions of the auxetic core (blue) and the upper face plate (blue) were modeled as isotropic materials using the Young's modulus obtained from compression testing (Table 2.2). Conversely, the lower regions of the auxetic core (yellow) and the bottom face plate (yellow) were modeled with the modulus obtained from tensile testing (Table 2.1). The load cell and support rollers were again modeled as structural steel.

For the anti-tetrachiral structure, the model visualization is shown in Figure 3.24, where the neutral axis is defined at Uy = 18.3 mm and illustrated by an imaginary red line. Similarly, the upper regions of the auxetic core (blue) and upper face plate (blue) were assigned isotropic properties based on the compression test results (Table 2.3), while the lower regions of the auxetic core (yellow) and bottom face plate (yellow) were assigned properties derived from tensile testing (Table 2.1). The load cell and rollers were once more represented as structural steel.

As in the previous sensitivity study, the homogenized representation of the FEM model was not considered here, since the primary aim was to investigate how the model response changes with updated material properties. The comparison between the full-scale geometry and its simplified (homogenized) counterpart will instead be presented in Section 4.2 for the main models introduced in Section 3.2.

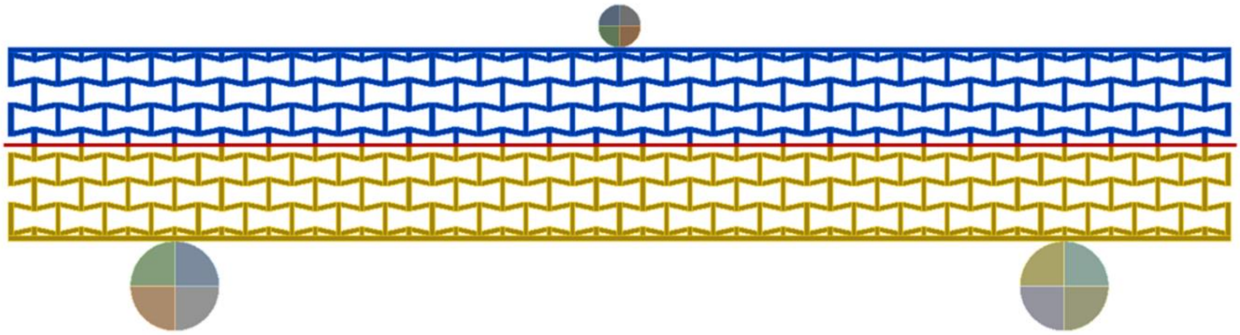

Figure 3.23: Materials of re-entrant 3-point bending load FEM with neutral axis.

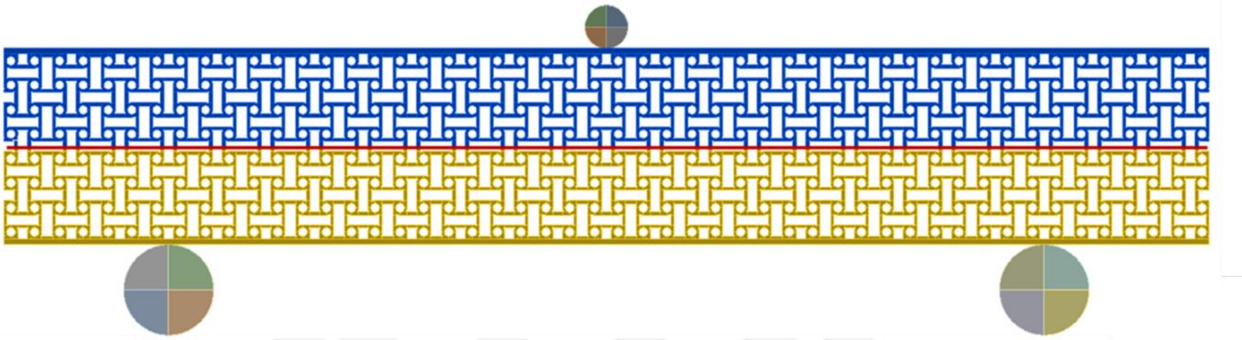

Figure 3.24: Materials of anti-tetrachiral 3-point bending load FEM with neutral axis.

3.3.Compressive Load Static Structural FEM

Compressive loading static structural finite element models were developed using ANSYS Workbench 2020 R2, utilizing the Static Structural analysis module from the Analysis Systems toolbox. The primary objective of these simulations was to evaluate the structural behavior of both the re-entrant and anti-tetrachiral structures under compressive loading and to enable a direct comparison between the full-scale and simplified-scale FE models. Additionally, the numerical results provide a good reference for comparison with the experimental compression test data presented earlier in Section 2.4.3 (Compression Testing).

Two finite element (FE) models were constructed for the re-entrant structure, based on the geometry detailed in Section 2.4.3. The first model represents the full-scale configuration, incorporating the complete 3D geometry of the auxetic core, the top and bottom face plates, and the support components used in the experimental setup. These include the load cell plate and support plates, modeled to replicate the boundary conditions and constraints of the physical testing environment. The geometry of this model is shown in Figure 3.25, with component colors reflecting their respective material types. The structural components of the re-entrant specimen (gray) were assigned isotropic material properties as defined in Table 2.1, while the load cell and support plates (dark blue) were modeled using structural steel material properties.

The second model represents the simplified (homogenized) case, in which the complex lattice geometry of the auxetic core was replaced by a solid volume with equivalent homogenized material properties. This geometry is illustrated in Figure 3.26. The core region (green) was assigned orthotropic homogenized material properties from Table 2.6, while the top and bottom face plates (light blue) were modeled using isotropic material properties from Table 2.1. The load cell and support plates (dark blue) were again assigned structural steel properties to ensure consistency with the experimental configuration.

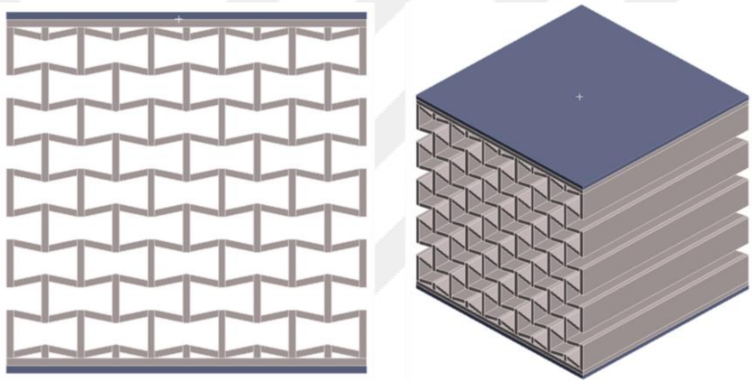

Figure 3.25: Full-scale geometry of re-entrant compression load FEM.

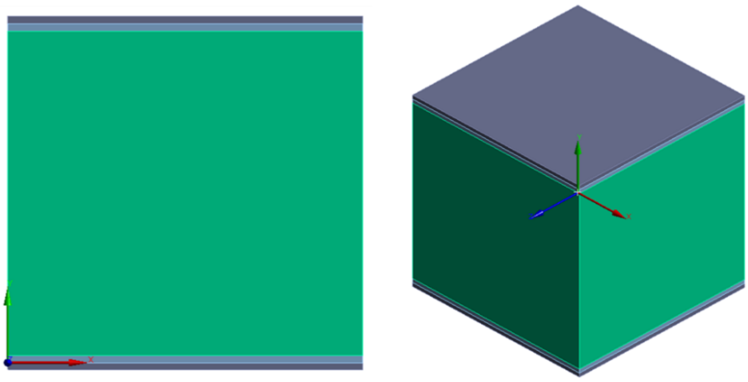

Figure 3.26: Simplified-scale geometry of re-entrant compression load FEM.

Similarly, two finite element models were developed for the anti-tetrachiral structure, based on the geometry described in Section 2.4.3. The first model represents the full-scale configuration, incorporating the complete 3D geometry of the anti-tetrachiral core, the top and bottom face plates, and the load cell and support plates used in the experimental setup. The geometry of this model is shown in Figure 3.27, with component colors corresponding to their material definitions. The auxetic core (dark green) was modeled using isotropic material properties as defined in Table 2.1, while the load cell and support plates (dark blue) were assigned structural steel properties.

The second model corresponds to the simplified (homogenized) version of the anti-tetrachiral structure, in which the complex lattice geometry of the auxetic core was replaced by an equivalent solid volume. This geometry is presented in Figure 3.28. The core region (green) was assigned orthotropic homogenized material properties from Table 2.7, while the face plates (brown) were modeled with isotropic material properties consistent with Table 2.1. The load cell and support plates (dark blue) were again assigned structural steel properties, matching the experimental boundary conditions and ensuring consistency across all models.

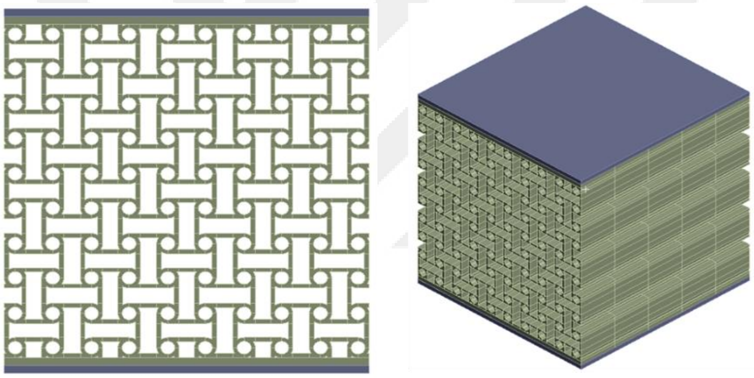

Figure 3.27: Full-scale geometry of anti-tetrachiral compression load FEM.

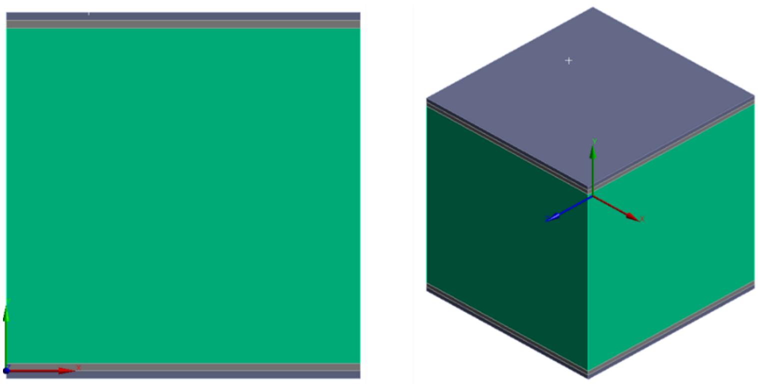

Figure 3.28: Simplified-scale geometry of anti-tetrachiral compression load FEM.

All finite element models, both full-scale and homogenized versions of the re-entrant and anti-tetrachiral structures, were meshed using SOLID185 elements.

Mesh details and visualizations for the full-scale re-entrant structure are shown in Figure 3.29, consisting of 306,240 elements and 403,930 nodes. The simplified-scale re-entrant structure is presented in Figure 3.30, containing 37,800 elements and 43,245 nodes.

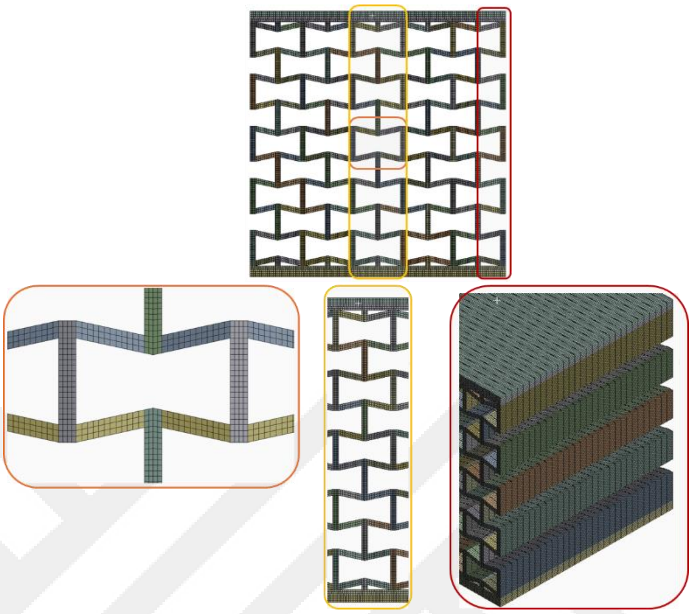

Figure 3.29: Finite element mesh of the full-scale re-entrant compression load FEM.

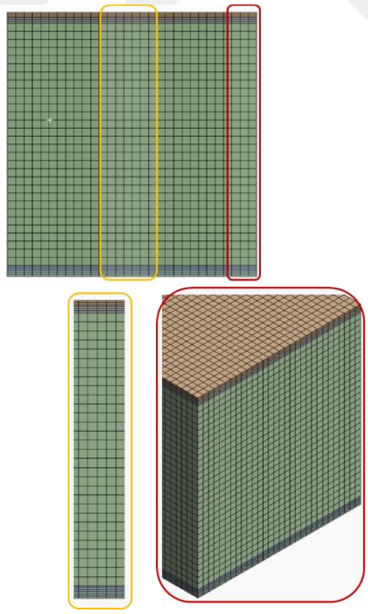

Figure 3.30: FE mesh of the simplified-scale re-entrant compression load FEM.

Similarly, the full-scale anti-tetrachiral model, illustrated in Figure 3.31, includes 923,940 elements and 1,171,211 nodes, while the simplified anti-tetrachiral model, shown in Figure 3.32, consists of 43,245 elements and 37,800 nodes.

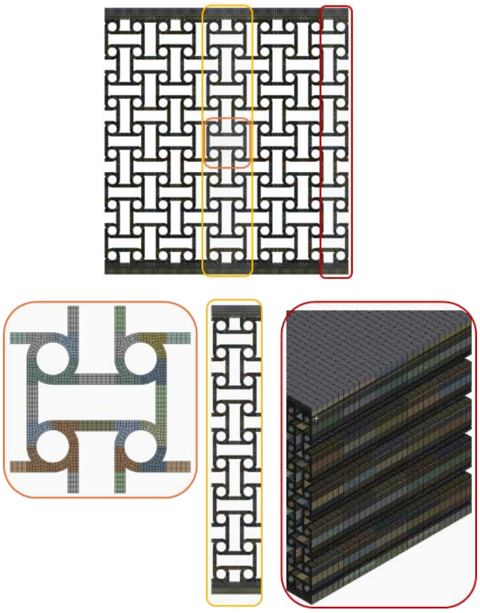

Figure 3.31: FE mesh of the full-scale anti-tetrachiral compression load FEM.

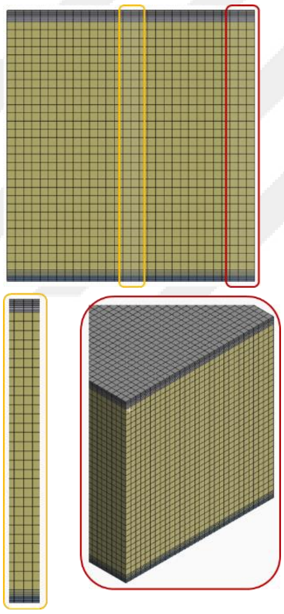

Figure 3.32: FE mesh of the simplified-scale anti-tetrachiral compression load FEM.

In all four finite element models, including the full-scale and simplified-scale versions of both the re-entrant and anti-tetrachiral structures, a frictional contact definition was applied at the interfaces between the top and bottom surfaces of the auxetic structures and the adjacent load cell and support plates. A friction coefficient of 0.3 was applied to represent static friction behavior between polymeric materials and steel surfaces, ensuring realistic constraint conditions and accounting for potential sliding resistance during compressive deformation. This value was applied consistently across all models to ensure comparability.

For the re-entrant structure, frictional contact was defined between the top and bottom surfaces of the auxetic core (as the contact surfaces) and the inner faces of the load cell and support plates (as the target surfaces). These contact locations are illustrated in Figure 3.33 for the full-scale model and in Figure 3.34 for the simplified-scale model. The same contact setup was consistently applied to both configurations.

Similarly, for the anti-tetrachiral structure, frictional contact was defined between the top and bottom surfaces of the auxetic core (as the contact surfaces) and the inner faces of the load cell and support plates as the target surfaces). These contact regions are shown in Figure 3.35 for the full-scale model and Figure 3.36 for the simplified model. As with the re-entrant case, the same frictional setup was implemented in both FE models for consistency.

In the static structural compression models, displacement constraints were defined to replicate the experimental setup accurately. The bottom surface of the top load plate, indicated by a dashed black line at top in the figures, was constrained in the horizontal directions (Ux = Uz = 0) and subjected to a vertical downward displacement of Uy = –2.0 mm to simulate the applied compressive load. The bottom surface of the auxetic structures, also shown as a dashed black line at bottom, was fixed in the vertical direction (Uy = 0) but left free in the horizontal directions (Ux, Uz = free) to allow for realistic compressive deformation during loading. Additionally, the top surface of the bottom support plate, again marked with a dashed black line at bottom, was fully fixed in all directions (Ux = Uy = Uz = 0) to represent a rigid base, consistent with the experimental boundary conditions.

These boundary conditions were applied consistently across all four finite element models, including both the full-scale and simplified-scale versions of the re-entrant and anti-tetrachiral structures. Boundary locations are shown in Figure 3.33 for the re-entrant full-scale model, Figure 3.34 for the re-entrant simplified model, Figure 3.35 for the anti-tetrachiral full-scale model, and Figure 3.36 for the anti-tetrachiral simplified model. The same boundary definitions were applied in both modeling approaches to ensure uniformity and comparability with the experimental compression tests discussed in Section 2.4.3.

The total computational solve time for the full-scale re-entrant structure in the static structural compression analysis was approximately 10 times longer than that of its simplified-scale counterpart. For the anti-tetrachiral structure, the full-scale model required approximately 50 times more computation time than the corresponding simplified model. These findings highlight the significant efficiency gains achieved through homogenization.

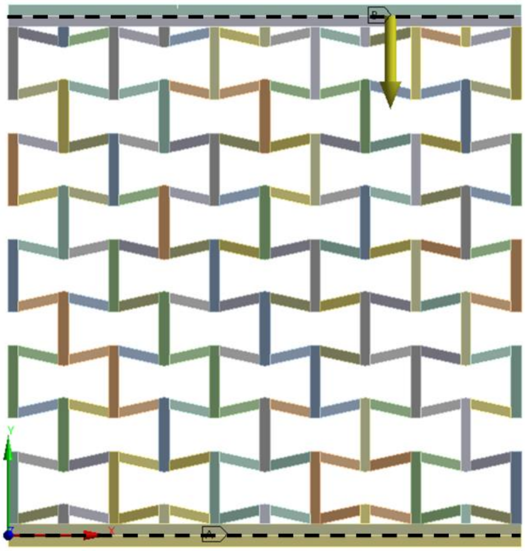

Figure 3.33: Boundary Conditions of the full-scale re-entrant compression load FEM.

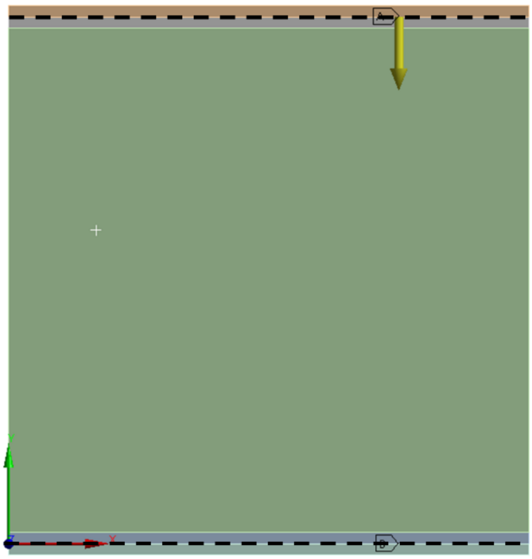

Figure 3.34: Boundary Conditions of the simplified-scale re-entrant used compression load FEM.

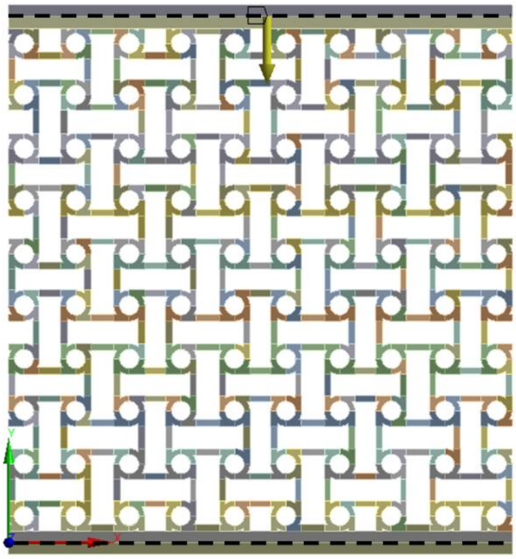

Figure 3.35: Boundary Conditions of the full-scale anti-tetrachiral compression load FEM.

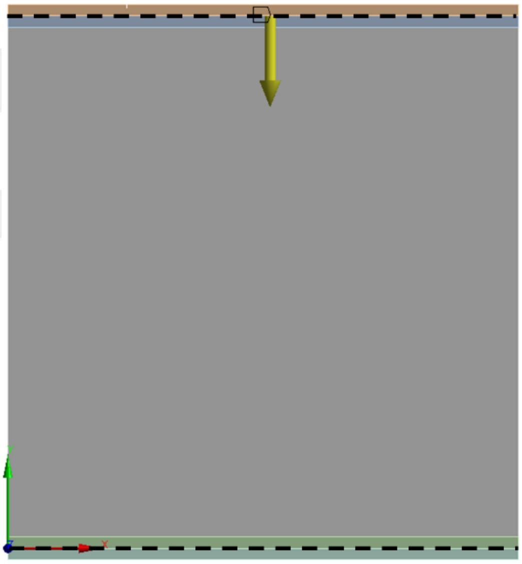

Figure 3.36: Boundary Conditions of the simplified-scale anti-tetrachiral compression load FEM.

3.4.Tensile Load Static Structural FEM

Tensile loading static structural finite element models were developed using ANSYS Workbench 2020 R2, utilizing the Static Structural analysis module under the Analysis Systems toolbox. The primary objective of these simulations was to evaluate the mechanical behavior of both the re-entrant and anti-tetrachiral structures under uniaxial tensile loading.

Since no experimental tensile tests were conducted in this study, the evaluation of tensile behavior relies solely on numerical results obtained from the full-scale and homogenized finite element models. By analyzing the structural response under tensile loading in both the X and Y directions, the study offers valuable insights into the accuracy and applicability of the homogenization methodology for complex lattice geometries.

The tensile loading models were constructed based on the geometrical definitions provided in Section 2.1.1 for the re-entrant structure and Section 2.1.2 for the anti-tetrachiral structure. The finite element models used for the tensile analyses are identical to those developed for the modal response analysis presented in Section 3.1.1 (Modal Response FEM). Therefore, Section 3.4 builds upon the existing FE models from the modal analysis, maintaining consistent geometry, material definitions, and meshing strategies.

The full-scale models retained the detailed lattice geometries and utilized isotropic material properties, as summarized in Table 2.1. The simplified models replaced the intricate auxetic cores with equivalent orthotropic solids, using homogenized material properties provided in Table 2.6 for the re-entrant structure and Table 2.7 for the anti-tetrachiral structure.

This section provides the details of the tensile finite element models and their configurations.

3.4.1.Tensile load in y direction only

Tensile loading finite element models in the Y-direction were developed to investigate tensile response of the auxetic structures under uniaxial loading along the Y-axis. The modeling approach, material assignments, and mesh configurations were consistent with those described in the preceding sections.

The tensile load in the Y-direction was applied by imposing a uniform displacement constraint of 2.0 mm along the Y-axis ($U_y = 2.0$ mm) on the top face of the structures, indicated by the dashed black line at the top. The bottom face was fully fixed in all degrees of freedom ($U_x = U_y = U_z = 0$), as indicated by the dashed black line at the bottom. These boundary conditions were consistently applied to both the full-scale and homogenized models to ensure a direct comparison of the results.

The boundary conditions and displacement constraints are illustrated in Figure 3.37 for the re-entrant full-scale model, Figure 3.38 for the re-entrant simplified model,

Figure 3.39 for the anti-tetrachiral full-scale model, and Figure 3.40 for the anti-tetrachiral simplified model.

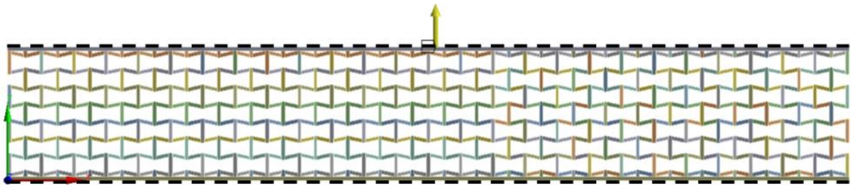

Figure 3.37: Boundary Conditions of the full-scale re-entrant for Tensile Load in Y direction FEM.

Figure 3.38: Boundary Conditions of the simplified-scale re-entrant for Tensile Load in Y direction FEM.

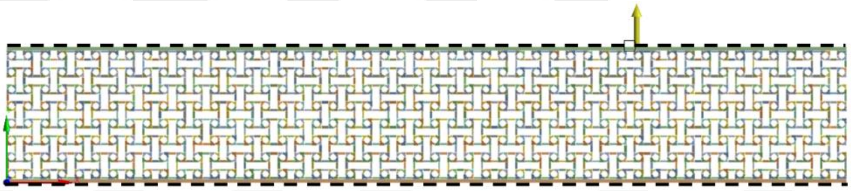

Figure 3.39: Boundary Conditions of the full-scale anti-tetrachiral for Tensile Load in Y direction FEM.

Figure 3.40: Boundary Conditions of the simplified-scale anti-tetrachiral for Tensile Load in Y direction FEM.

3.4.2.Tensile load in x direction only

Similarly, tensile loading finite element models in the X-direction were developed to investigate the tensile response of the auxetic structures under uniaxial loading along the X-axis. The modeling approach, material properties, and mesh configurations remained consistent with those described in the preceding sections.

The tensile load in the X-direction was applied by imposing a uniform displacement constraint of 2.0 mm along the X-axis (Ux = 2.0 mm) on the left faces of the structures, as indicated by the dashed black line on the left side of the models. The right faces were fully fixed in all degrees of freedom (Ux = Uy = Uz = 0), as shown by the dashed black line on the right. These boundary conditions were consistently applied to both the full-scale and homogenized models to ensure a direct comparison of the results.

The boundary locations and displacement constraints are illustrated in Figure 3.41 for the re-entrant full-scale model, Figure 3.42 for the re-entrant simplified model, Figure 3.43 for the anti-tetrachiral full-scale model, and Figure 3.44 for the anti-tetrachiral simplified model.

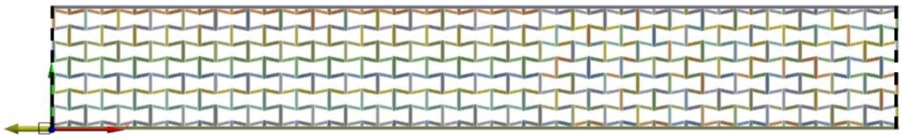

Figure 3.41: Boundary Conditions of the full-scale re-entrant for Tensile Load in X direction FEM.

Figure 3.42: Boundary Conditions of the simplified-scale re-entrant for Tensile Load in X direction FEM.

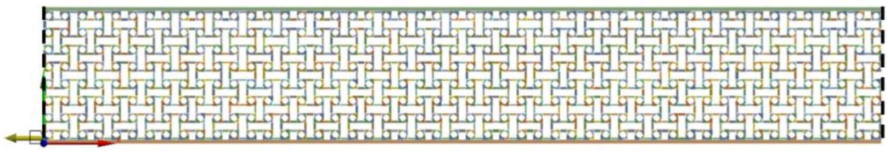

Figure 3.43: Boundary Conditions of the full-scale anti-tetrachiral for Tensile Load in X direction FEM.

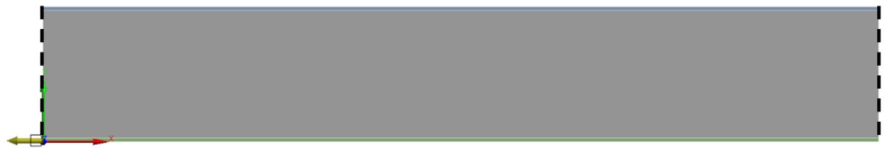

Figure 3.44: Boundary Conditions of the simplified-scale anti-tetrachiral for Tensile Load in X direction FEM.

4.FINITE ELEMENT ANALYSIS RESULTS, AND COMPARISON AGAINST EXPERIMENTAL RESULTS

This chapter presents the results obtained from the finite element analyses (FEA) of both the re-entrant and anti-tetrachiral auxetic structures, alongside a comparative evaluation against the available experimental data. The analyses were conducted using the numerical models developed in Chapter 3, which include both full-scale (real-case) models that explicitly represent the lattice geometries and homogenized (simplified-case) models that approximate the lattice cores as orthotropic continuum materials.

The primary objective of this chapter is to present and assess the structural and dynamic behavior of the auxetic designs under various loading conditions. The FEA results are systematically compared with the experimental outcomes, thereby offering insights into the accuracy, strengths, and limitations of the homogenization approach in capturing the mechanical response of complex lattice geometries.

This chapter is organized into four main sections, each dedicated to a specific loading scenario. Section 4.1 presents the modal response analysis results, comparing the natural frequencies and mode shapes predicted by the finite element models with the experimental modal test data. Section 4.2 discusses the results of static structural simulations under three-point bending loading conditions, comparing the numerical predictions with experimental bending test results. Section 4.3 examines the structural response of the auxetic structures under compressive loading, comparing the finite element results with the experimental compression test data. Lastly, Section 4.4 presents the results of tensile loading analyses, which were conducted exclusively through numerical simulations, as no experimental tensile tests were performed in this study.

Overall, this chapter aims to assess the capabilities and limitations of the homogenization approach in simulating the structural and dynamic behavior of complex auxetic structures. While homogenization provides significant computational efficiency gains, the level of agreement between the homogenized and full-scale models varies depending on the loading condition. In particular, the discrepancies observed in three-point bending simulations highlight the limitations of the homogenization approach in capturing certain flexural behaviors. The insights gained from this comparative analysis are expected to inform the development of improved modeling strategies for complex lattice structures, balancing computational efficiency with model fidelity in future research.

4.1.Modal Response FE Analysis Results and Comparison Against Experimental Results

The modal responses of the re-entrant and anti-tetrachiral auxetic structures were analyzed using both full-scale and simplified (homogenized) finite element (FE) models. The objective was to evaluate the accuracy of these models by comparing the simulated natural frequencies and mode shapes against experimental modal test data presented earlier in Section 2.4.1. This comparison provides a critical assessment of the accuracy of the numerical models in predicting modal response behavior. All results in this section are derived from the FE models described previously in Section 3.1 (Modal Response FEM).

A key limitation of the experimental setup was its inability to capture torsional modes. Because a single-row accelerometer configuration was employed, vibrational responses associated with torsional behavior could not be recorded. Consequently, the comparison between experimental and numerical results in this study is restricted to translational modes, which were measured with sufficient accuracy.

According to the ANSYS Workbench modal response analysis, mode shapes 1, 3, 5, 8, and 9 for the re-entrant structure correspond to torsional modes. Since no experimental measurements are available for these cases, the comparison was performed only between the full-scale and simplified FE models.

Likewise, for the anti-tetrachiral structure, mode shapes 1, 3, 5, 7, and 9 correspond to torsional modes, for which no experimental data could be obtained.

For this section and the subsequent sections, the percentage differences among results were calculated using the following three formulas:

- Simplified FEA vs. Full-Scale FEA (%) =

((Simplified FEA result – Full-scale FEA result) / Full-scale FEA result) × 100

- Full-Scale FEA vs. Test Results (%) =

((Full-scale FEA result – Test result) / Test result) × 100

- Simplified FEA vs. Test Results (%) =

((Simplified FEA result – Test result) / Test result) × 100

For the re-entrant structure, the natural frequencies obtained from the full-scale FE model, simplified FE model, and experimental modal tests are presented in Table 4.1, while the corresponding percentage differences are detailed in Table 4.2.

The full-scale FE model predicted natural frequencies with a maximum difference of 7.3% from the experimental results, observed at the 2nd mode shape, while all other modes exhibited differences below 7%. Moreover, the difference gradually decreased as the frequency increased.

The simplified model predicted frequencies with a maximum difference of 9.7% from the experimental results, also at the 2nd mode shape, with the remaining modes showing differences under 9%. Furthermore, the differences decreased progressively with increasing frequency.

When comparing the simplified FE model to the full-scale model, the maximum difference was 4.3% at the 10th mode shape, with the other nine modes displaying differences below 4%.

These differences are all within the acceptable levels, indicating that both FE models provide reliable predictions of the modal behavior of the re-entrant structure. Furthermore, the simplified model also offers a substantial computational advantage, achieving a 44 times reduction in solve time and requiring 72% fewer nodes than the full-scale model.

Figure 4.1 shows the total deformation results for the re-entrant structure across different mode shapes. The visual comparison confirms that the simplified model captures the global deformation patterns observed in the full-scale model. The mode shapes in the simplified model closely resemble those of the full-scale model.

From a computational perspective, the full-scale model of the re-entrant structure consists of 897,600 elements and 1,185,500 nodes, whereas the simplified model contains 311,808 elements and 337,125 nodes. The total computational solve time for the full-scale model was approximately 44 times longer than that of its simplified counterpart, emphasizing the substantial computational savings of the simplified approach.

Table 4.1: Natural Frequencies (Hz) for Re-entrant Structure.

Mode Shape Number from Modal Analysis	Full-Scale FE Model Natural Frequencies (Hz)	Simplified-Scale FE Model Natural Frequencies (Hz)	Experimental Test Results Natural Frequencies (Hz)
1	342.6	335.4	-
2	425.1	414.3	458.8
3	624.8	606.4	-
4	666.4	651.3	711.3
5	855.1	831.1	-
6	965.8	934.0	985.6
7	1191.0	1149.8	1172.5
8	1472.3	1441.5	-
9	1498.5	1456.3	-
10	1528.1	1462.1	1500

Table 4.2: Difference (%) of Natural Frequencies for Re-entrant Structure.

Mode Shape Number from Modal Analysis	Simplified FEA vs. Full-Scale FEA (%)	Full-Scale FEA vs. Test Results (%)	Simplified FEA vs. Test Results (%)
1	-2.1%	-	-
2	-2.5%	-7.3%	-9.7%
3	-2.9%	-	-
4	-2.3%	-6.3%	-8.4%
5	-2.8%	-	-
6	-3.3%	-2.0%	-5.2%
7	-3.5%	1.6%	-1.9%
8	-2.1%	-	-
9	-2.8%	-	-
10	-4.3%	1.9%	-2.5%

Mode Shape Number	Full-Scale FE Model Natural Frequencies (Hz)	Simplified-Scale FE Model Natural Frequencies (Hz)	Simplified vs. Full-Scale Difference (%)
1	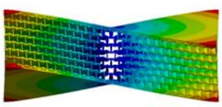 Frequency = 342.6 Hz	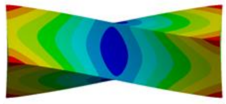 Frequency = 335.4 Hz	-2.1 %
2	 Frequency = 425.1 Hz	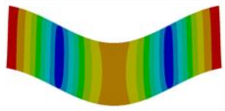 Frequency = 414.3 Hz	-2.5 %
3	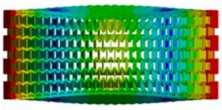 Frequency = 624.8 Hz	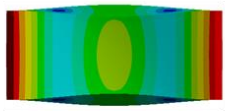 Frequency = 606.4 Hz	-2.9 %
4	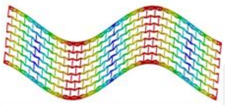 Frequency = 666.4 Hz	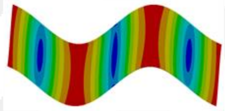 Frequency = 651.3 Hz	-2.3 %
5	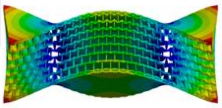 Frequency = 855.1 Hz	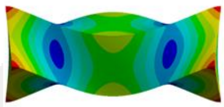 Frequency = 831.1 Hz	-2.8 %
6	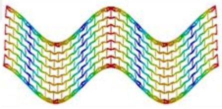 Frequency = 965.8 Hz	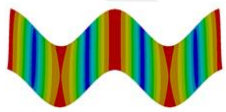 Frequency = 934.0 Hz	-3.3 %
7	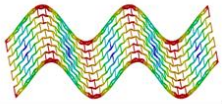 Frequency = 1191.0 Hz	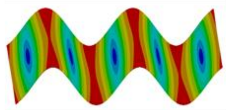 Frequency = 1149.8 Hz	-3.5 %
8	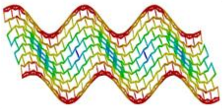 Frequency = 1472.3 Hz	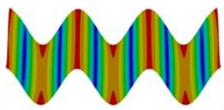 Frequency = 1441.5 Hz	-2.1 %
9	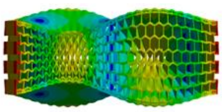 Frequency = 1498.5 Hz	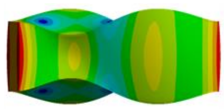 Frequency = 1456.3 Hz	-2.8 %
10	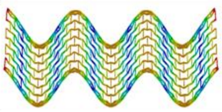 Frequency = 1528.1 Hz	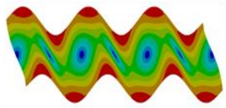 Frequency = 1462.1 Hz	-4.3 %

Figure 4.1: Modal Response Results, Natural Frequencises (Hz) for Re-entrant structure.

For the anti-tetrachiral structure, the natural frequencies from the full-scale FE model, simplified FE model, and experimental tests are shown in Table 4.3, with the corresponding percentage differences summarized in Table 4.4.

The full-scale model exhibited a maximum difference of 8.0% compared to the experimental results, occurring at the 2nd mode shape, while the remaining modes showed differences below 8%. Moreover, the difference gradually decreased as the frequency increased.

The simplified model showed a maximum difference of 15.5% from the experimental results at the 2nd mode shape, with the other modes exhibiting differences under 15%. Furthermore, the differences decreased progressively with increasing frequency.

The comparison between the simplified and full-scale FE models revealed a maximum difference of 12.7% at the 1st mode shape, with the remaining modes showing differences below 12.5%.

These differences are all within the acceptable levels, confirming that both FE models provide reliable predictions of the modal behavior of the anti-tetrachiral structure. The simplified model also offers a substantial computational advantage, achieving a 70 times reduction in solve time and using 92% fewer nodes than the full-scale model.

Figure 4.2 shows the total deformation results for the anti-tetrachiral structure, illustrating strong agreement between the simplified and full-scale models in terms of global deformation patterns. The simplified model accurately captures the essential modal characteristics of the structure.

In terms of computational efficiency, the full-scale anti-tetrachiral model contains 2,928,720 elements and 3,722,325 nodes, while the simplified model includes 283,296 elements and 307,125 nodes. The full-scale model required approximately 70 times longer solve time than the homogenized model, emphasizing the substantial computational savings of the simplified approach.

Table 4.3: Natural Frequencies (Hz) for Anti-tetrachiral Structure.

Mode Shape Number from Modal Analysis	Full-Scale FE Model Natural Frequencies (Hz)	Simplified-Scale FE Model Natural Frequencies (Hz)	Experimental Test Results Natural Frequencies (Hz)
1	335.8	293.2	-
2	396.9	364.5	431.3
3	426.3	380.2	-
4	619.5	569.5	668.1
5	791.0	708.9	-
6	896.8	815.3	947.5
7	1015.2	888.1	-
8	1096.6	1000.6	1084.4
9	1211.3	1067.4	-
10	1314.8	1251.2	1370

Table 4.4: Difference (%) of Natural Frequencies for Anti-tetrachiral Structure.

Mode Shape Number from Modal Analysis	Simplified FEA vs. Full-Scale FEA (%)	Full-Scale FEA vs. Test Results (%)	Simplified FEA vs. Test Results (%)
1	-12.7%	-	-
2	-8.2%	-8.0%	-15.5%
3	-10.8%	-	-
4	-8.1%	-7.3%	-14.8%
5	-10.4%	-	-
6	-9.1%	-5.3%	-14.0%
7	-12.5%	-	-
8	-8.8%	1.1%	-7.7%
9	-11.9%	-	-
10	-4.8%	-4.0%	-8.7%

Mode Shape Number	Full-Scale FE Model Natural Frequencies (Hz)	Simplified-Scale FE Model Natural Frequencies (Hz)	Simplified vs. Full-Scale Difference (%)
1	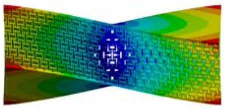 Frequency = 335.8 Hz	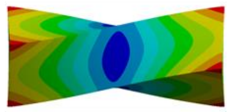 Frequency = 293.2 Hz	-12.7 %
2	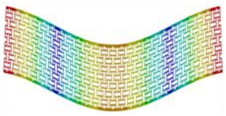 Frequency = 396.9 Hz	 Frequency = 364.5 Hz	-8.2 %
3	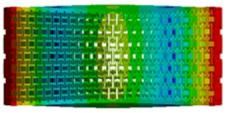 Frequency = 426.3 Hz	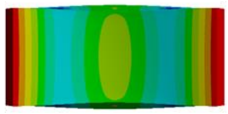 Frequency = 380.2 Hz	-10.8 %
4	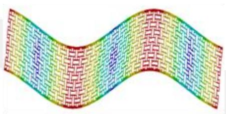 Frequency = 619.5 Hz	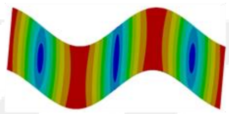 Frequency = 596.5 Hz	-8.1 %
5	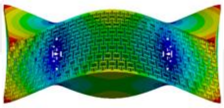 Frequency = 791.0 Hz	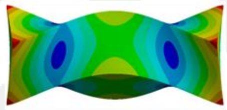 Frequency = 708.9 Hz	-10.4 %
6	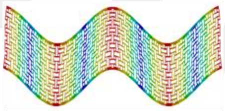 Frequency = 896.8 Hz	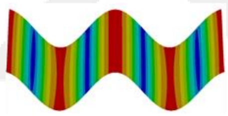 Frequency = 815.3 Hz	-9.1 %
7	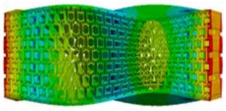 Frequency = 1015.2 Hz	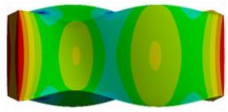 Frequency = 888.1 Hz	-12.5 %
8	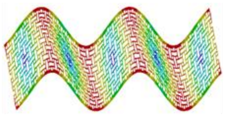 Frequency = 1096.6 Hz	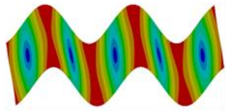 Frequency = 1000.6 Hz	-8.8 %
9	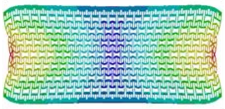 Frequency = 1211.3 Hz	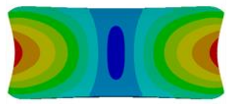 Frequency = 1067.4 Hz	-11.9 %
10	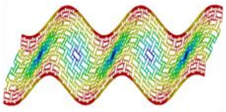 Frequency = 1314.8 Hz	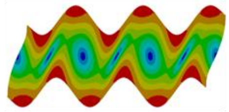 Frequency = 1251.2 Hz	-4.8 %

Figure 4.2: Modal Response Results, Natural Frequencises (Hz) for Anti-tetrachiral structure.

The modal response analyses demonstrate that both full-scale and simplified (homogenized) finite element models effectively predict the dynamic behavior of re-entrant and anti-tetrachiral auxetic structures. The full-scale models exhibit good agreement with experimental results, with difference in natural frequencies typically within 8% for both the re-entrant structure and the anti-tetrachiral structure. The simplified homogenized models also perform well, capturing the global mode shapes and natural frequencies with differences generally between 8% and 15% compared to experimental measurements, and with differences tend to decrease at higher frequencies. These findings indicate that both modeling approaches can provide meaningful insights into the dynamic characteristics of auxetic lattices, with the full-scale models offering the highest fidelity in capturing detailed modal behavior.

A key distinction between the two approaches lies in computational efficiency. The full-scale models require substantially greater resources, up to 44 times longer solve times for the re-entrant structure and 70 times longer for the anti-tetrachiral structure, due to the need for fine tetrahedral meshing to resolve intricate lattice geometries. In contrast, the homogenized models, which simplify the lattice cores into equivalent orthotropic solids, achieve significant reductions in computational time and node counts, using up to 72% fewer nodes for the re-entrant structure and 92% fewer nodes for the anti-tetrachiral structure.

Overall, the analysis highlights that while full-scale models remain the most accurate choice for final validation and high-fidelity dynamic studies, homogenized models provide a computationally efficient alternative with acceptable accuracy for early-stage design, parametric exploration, and iterative optimization tasks. The results demonstrate that selecting an appropriate modeling strategy depends on the balance between required precision and available computational resources, and confirm the viability of the homogenization approach in representing the dynamic behavior of complex auxetic structures.

4.2. Three Point Bending Load Static Structural FE Analysis Results and Comparison Against Experimental Results

This section presents the static structural finite element analysis (FEA) results for the re-entrant and anti-tetrachiral auxetic structures under three-point bending load, alongside comparisons with experimental data. The aim is to evaluate the predictive accuracy of the full-scale and simplified (homogenized) FE models and to assess the effectiveness of the homogenization approach in representing the bending behavior of complex auxetic geometries. All results in this section are based on the FE models described previously in Section 3.2 (Three Point Bending Load Static Structural FEM).

For the re-entrant structure, the force-deflection results obtained from the full-scale FEA, simplified FEA, and experimental tests are summarized in Table 4.5 and visually presented in Figure 4.3. The corresponding percentage differences among these results are detailed in Table 4.6.

At a load cell displacement of 1.0 mm, the full-scale FEA predicted a reaction force of 115 N, while the simplified model predicted 97 N and the experimental test measured 86 N. At 2.0 mm displacement, the predictions were 229 N for the full-scale FEA, 193 N for the simplified model, and 165 N from the experiment. At 3.0 mm, the reaction forces were 343 N, 289 N, and 244 N for the full-scale FEA, simplified FEA, and experiment, respectively. Finally, at 4.0 mm displacement, the full-scale FEA predicted 457 N, the simplified model 385 N, and the experimental test 323 N.

The percentage differences indicate that the simplified FEA model consistently underestimates the reaction force compared to the full-scale model by approximately 15.7% across the entire displacement range. In contrast, the full-scale FEA systematically overestimates the reaction force relative to the experimental measurements, with deviations increasing from 34.4% at 1.0 mm to 41.8% at 4.0 mm. Meanwhile, the simplified FEA model demonstrates closer agreement with the experimental results, overestimating the reaction force by 13.3% at 1.0 mm and by 19.5% at 4.0 mm. This suggests that although the simplified model is less accurate than the full-scale model, it offers faster computation and matches the experimental results more closely.

The differences between the simulation and experimental results tend to increase gradually as the load cell displacement increases, indicating a slight divergence in the linear response of the models compared to the physical tests at higher deflections.

The visual comparison of the deformation patterns, presented in Figure 4.4 for the re-entrant structure, reinforces these findings. The simplified models effectively capture the global bending behavior, demonstrating similar overall deformation trends to the full-scale models. The full-scale models, while providing a more precise geometric representation of the lattice, predict higher stiffness and consequently higher reaction forces than those observed in the experimental tests.

From a computational perspective, the full-scale model of the re-entrant structure consists of 999,984 elements and 1,296,125 nodes, whereas the simplified model contains 414,192 elements and 447,750 nodes. The total computational solve time for the full-scale model was approximately 3 times longer than that of its simplified counterpart, underscoring the efficiency gains achieved through homogenization.

Table 4.5: 3-Point Bending Load FEA Results for Re-entrant Structure.

Deflection of Load Cell (mm)	Full-Scale FEM Force Reaction (N)	Simplified-Scale FEM Force Reaction (N)	Experimental Test Results Force (N)
1.0	115	97	86
2.0	229	193	165
3.0	343	289	244
4.0	457	385	323

Table 4.6: Difference(%) of Bending Load Results for Re-entrant Structure.

Deflection of Load Cell (mm)	Simplified FEA vs. Full-Scale FEA (%)	Full-Scale FEA vs. Test Results (%)	Simplified FEA vs. Test Results (%)
1.0	-15.7%	34.4%	13.3%
2.0	-15.7%	39.2%	17.4%
3.0	-15.7%	40.9%	18.8%
4.0	-15.7%	41.8%	19.5%

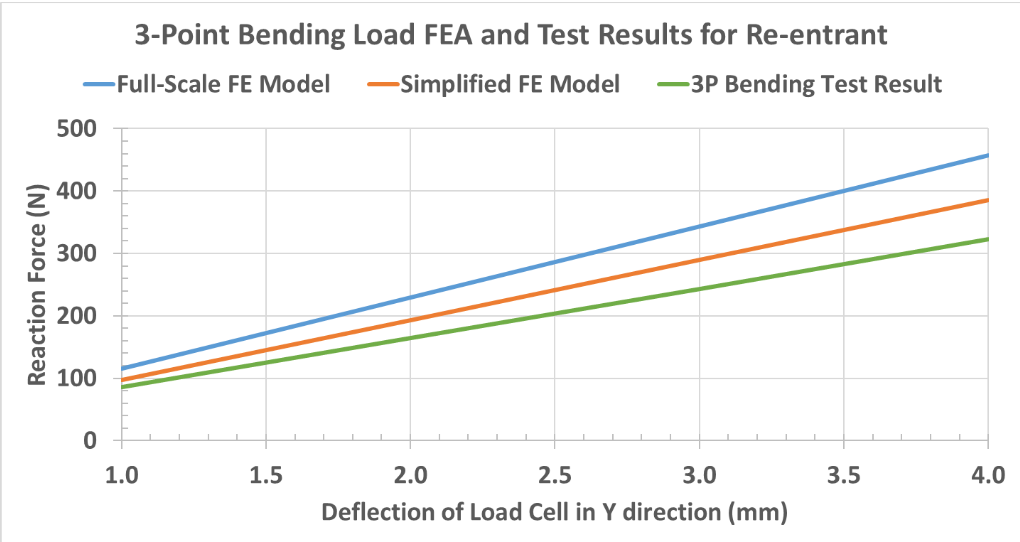

Figure 4.3: 3-Point Bending Load FEA and Test Results for Re-entrant Structure.

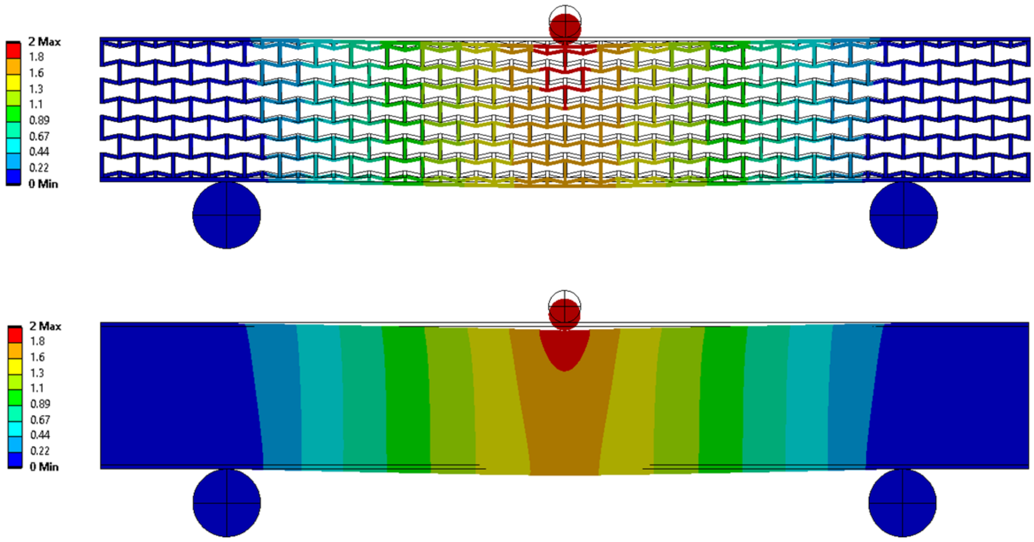

Figure 4.4: Total Deformation Distribution for the Re-entrant Structure under 3P Bending Load: Full-Scale and Simplified FE Models.

For the anti-tetrachiral structure, the results follow a similar trend to those observed for the re-entrant structure. As summarized in Table 4.7 and illustrated in Figure 4.5, at a displacement of 1.0 mm, the full-scale FEA predicted a reaction force of 108 N, the simplified model predicted 81 N, and the experimental test measured 70 N. At 2.0 mm displacement, these values increased to 214 N, 162 N, and 132 N, respectively. At 3.0 mm, the full-scale, simplified, and experimental results were 321 N, 242 N, and 194 N, respectively. Finally, at 4.0 mm displacement, the corresponding forces were 428 N, 322 N, and 256 N.

The percentage differences, detailed in Table 4.8, show that the simplified model consistently underestimates the reaction force compared to the full-scale model by approximately 24.6% across the displacement range. Meanwhile, the full-scale FEA substantially overestimates the experimental results, with deviations starting at 54.7% for 1.0 mm and increasing to 67.4% at 4.0 mm. In contrast, the simplified model provides a closer agreement with the experiments, with differences ranging from 16.9% at 1.0 mm to 26.1% at 4.0 mm. This indicates that although the simplified model reduces accuracy compared to the full-scale representation, it captures the experimental trend more consistently and with lower differences.

The visual comparison of the deformation patterns, presented in Figure 4.6 for the anti-tetrachiral structure, reinforces these findings. The simplified models effectively capture the global bending behavior. The full-scale models, while more geometrically precise, predict higher stiffness and consequently higher reaction forces than observed in the experiments.

In terms of computational efficiency, the full-scale anti-tetrachiral model contains 3,034,752 elements and 3,836,725 nodes, while the simplified model includes 389,328 elements and 421,525 nodes. The full-scale model required approximately 6 times longer solve time than the homogenized model, emphasizing the substantial computational savings of the simplified approach.

Table 4.7: 3-Point Bending Load FEA Results for Anti-tetrachiral Structure.

Deflection of Load Cell (mm)	Full-Scale FEM Force Reaction (N)	Simplified-Scale FEM Force Reaction (N)	Experimental Test Results Force (N)
1.0	108	81	70
2.0	214	162	132
3.0	321	242	194
4.0	428	322	256

Table 4.8: Difference(%) of Bending Load Results for Anti-tetrachiral.

Deflection of Load Cell (mm)	Simplified FEA vs. Full-Scale FEA (%)	Full-Scale FEA vs. Test Results (%)	Simplified FEA vs. Test Results (%)
1.0	-24.6%	54.7%	16.9%
2.0	-24.6%	63.0%	22.9%
3.0	-24.6%	65.9%	25.0%
4.0	-24.6%	67.4%	26.1%

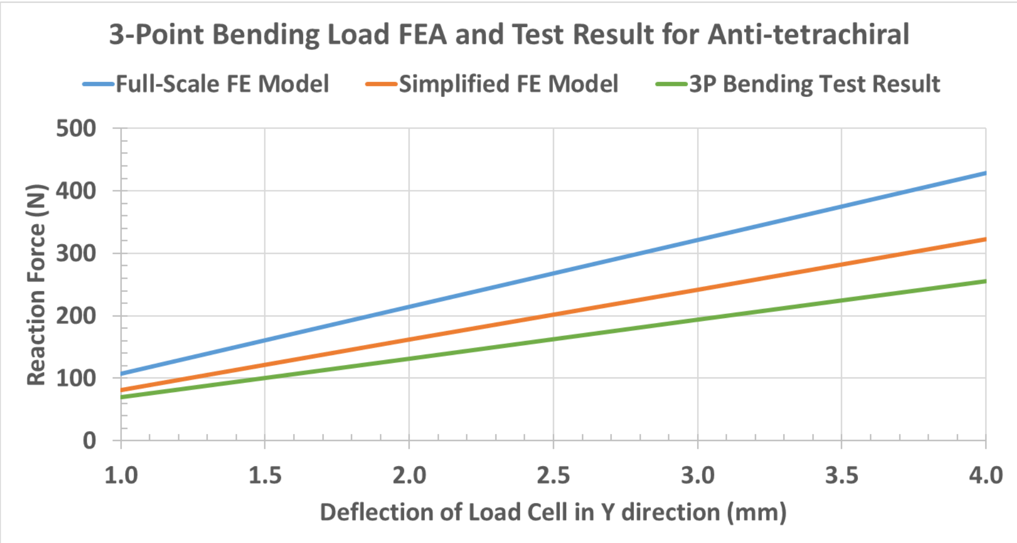

Figure 4.5: 3-Point Bending Load FEA and Test Results for Anti-tetrachiral Structure.

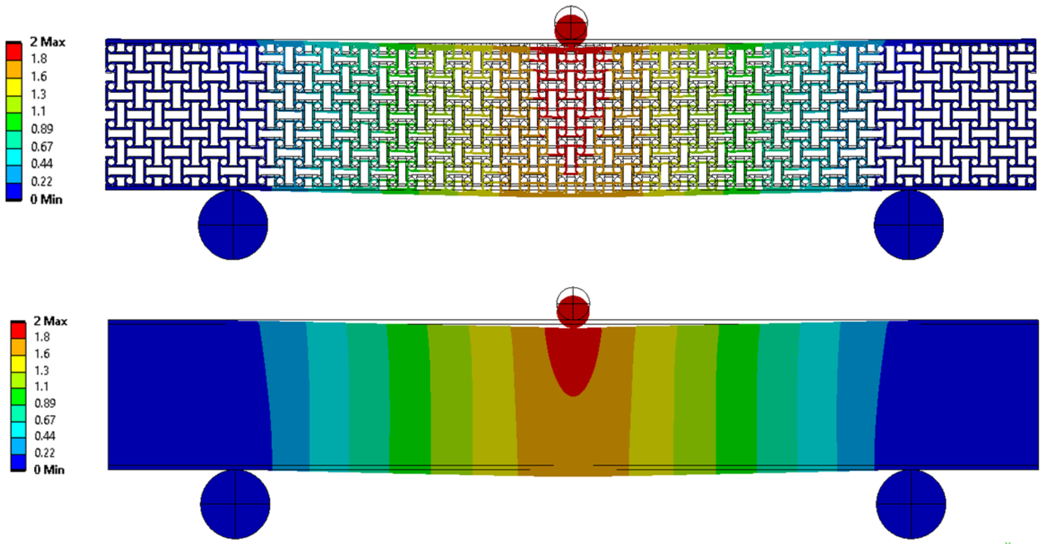

Figure 4.6: Total Deformation Distribution for the Anti-tetrachiral Structure under 3P Bending Load: Full-Scale and Simplified FE Models.

These findings highlight a fundamental trade-off in modeling strategies for auxetic structures: while full-scale finite element models provide detailed geometric representation and capture structural features more precisely, they tend to overestimate the bending stiffness compared to experimental results, with differences reaching up to 42% for the re-entrant and 67% for the anti-tetrachiral structures. In contrast, simplified homogenized models, though less geometrically detailed, achieve a closer match to the experimental outcomes, with differences generally below 20% for the re-entrant and 26% for the anti-tetrachiral structures.

This improved agreement might be valuable in the context of additive manufacturing processes such as Material Jetting, where achieving precise net-shaping is often not possible due to inherent process limitations. Parts fabricated through Material Jetting commonly exhibit dimensional deviations, and their final dimensions may differ from the original CAD geometry, leading to alterations in the structural behavior of the printed components. Additionally, the layer-by-layer fabrication process introduces material property inconsistencies, preventing the realization of perfect isotropy and homogeneity within the printed structures. These factors contribute to deviations in mechanical performance when compared to idealized numerical models.

Another major factor behind the discrepancy between FEA predictions and experimental outcomes in three-point bending tests may be the complex loading state, where specimens are simultaneously subjected to both tension and compression. In the numerical models developed here, the material definition was initially based only on the Young's modulus obtained from tensile testing. This approach inherently makes the model artificially stiff, leading to reaction forces that are significantly higher than those recorded in the experiments. It raises the question of whether incorporating separate material definitions for tension and compression could improve the predictive accuracy of the simulations. To explore this idea, sensitivity studies have been carried out, and the corresponding results are presented in the following two chapters.

Overall, the results indicate that for three-point bending simulations, simplified homogenized models provide a reasonable approximation of experimental behavior, offering a practical balance between accuracy and computational efficiency.

The simplified models tend to slightly underestimate structural stiffness compared to the full-scale models, while the full-scale models consistently overestimate stiffness relative to experimental measurements. This discrepancy suggests that although full-scale models provide detailed geometric fidelity, they may not necessarily yield more accurate predictions due to factors such as manufacturing deviations and material inconsistencies.

Nonetheless, full-scale modeling remains essential for high-fidelity bending analyses where accurate force–deflection relationships are critical, despite its significantly higher computational cost and complexity.

For broader design explorations, parametric studies, and iterative optimizations, simplified homogenized models represent a computationally efficient and sufficiently accurate alternative, especially in the presence of the uncertainties inherent to additive manufacturing processes.

For a supplementary comparison between the full-scale and simplified (homogenized) finite element models, Figures 4.7(a–h) present the detailed results for the re-entrant structure. Specifically, Figure 4.7(a) illustrates the total deformation, (b) the equivalent von Mises stress, (c) the maximum principal stress (σ_1), (d) the minimum principal stress (σ_3), (e) the strain energy, (f) the equivalent elastic strain, (g) the maximum principal strain (ε_1), and (h) the minimum principal strain (ε_3), with both modeling approaches shown side by side. A close look of the results reveals that the homogenized model is capable of capturing both global and local responses with good accuracy. In Figure 4.7(a), the total deformation contours indicate a nearly identical bending profile for both models, with the maximum deflection located at the mid-span. Similarly, the von Mises stress distribution shown in Figure 4.7(b) exhibits consistent concentration zones around the loading point and supports, suggesting that the homogenized material can replicate the critical stress regions of the lattice geometry. Figures 4.7(c) and 4.7(d), which represent maximum and minimum principal stresses, further support this observation by demonstrating similar tensile and compressive stress paths across the specimen thickness. Although minor deviations are observed in peak values, the overall patterns remain highly comparable. Energy-based parameters such as strain energy (Figure 4.7(e)) and equivalent elastic strain (Figure 4.7(f)) also show good alignment between the two models, confirming that the homogenized representation accurately reflects the global stiffness of the lattice system. The principal strain contours in Figures 4.7(g) and 4.7(h) reinforce this agreement, with both models capturing the expected tensile–compressive symmetry about the neutral axis.

For the anti-tetrachiral structure, the comparison between the full-scale and homogenized FE models is presented in Figure 4.8, where subfigures (a) through (h) illustrate total deformation, equivalent von-Mises stress, maximum principal stress (σ_1), minimum principal stress (σ_3), strain energy, equivalent elastic strain, maximum principal strain (ε_1), and minimum principal strain (ε_3), respectively. Both models capture a similar deformation pattern, with the maximum displacement localized at the central loading region as shown in Figure 4.8a. The stress distributions presented in Figures 4.8b–d also demonstrate consistent trends, with stress concentrations occurring around the loading point and supports, which is characteristic of bending-dominated behavior. Strain energy results in Figure 4.8e reveal that the homogenized model slightly underestimates the stored energy compared to the full-scale model; nevertheless, the deviation is minor and the general trend is preserved. Likewise, Figures 4.8f–h confirm that both models predict tensile strains concentrated in the lower regions and compressive strains in the upper regions, validating the correct positioning of the neutral axis. These observations confirm that the homogenized model successfully replicates the essential mechanical behavior of the anti-tetrachiral lattice while reducing computational effort, demonstrating the robustness and practicality of the homogenization strategy for bending load applications.

For both the re-entrant and anti-tetrachiral structures, in both the full-scale and simplified (homogenized) models, a local stress singularity appears at the loading contact point due to the concentrated load application; however, this effect is non-physical and confined to the immediate contact region. The effective von Mises stress distributions remain within the ranges of 6–12 MPa (Figure 4.7(b)) and 4–12 MPa (Figure 4.8(b)), respectively, indicating uniform load transfer and no localized failure risk. The tensile strength of VeroBlue RGD840 was assumed to be approximately 55 MPa, based on the specification sheet provided by Stratasys Inc. (Figure 2.17). Since all effective stresses are well below this limit, both structures remain fully within the elastic region, confirming purely elastic behavior with no localized yielding under the applied bending load.

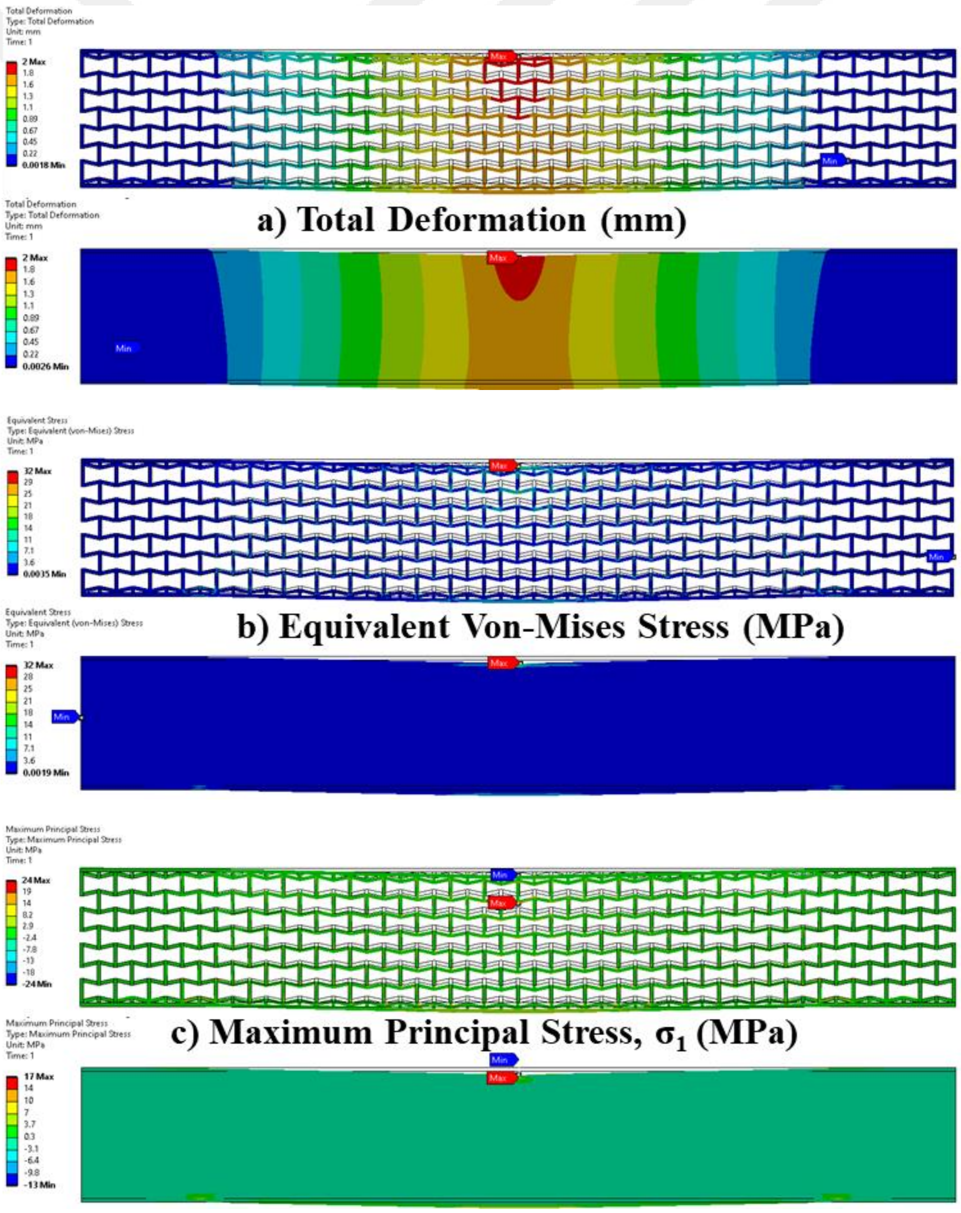

(a)

(b)

(c)

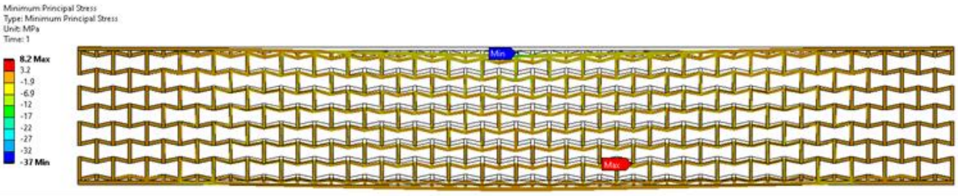

d) Minimum Principal Stress, σ_3 (MPa)

(d)

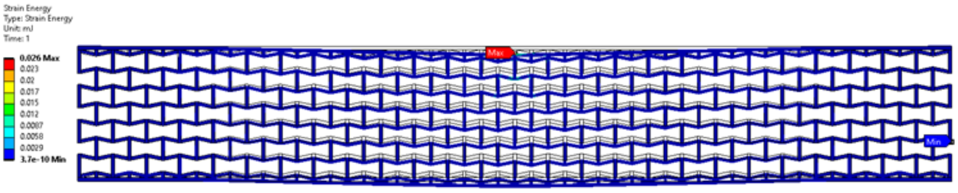

e) Strain Energy (mJ)

(e)

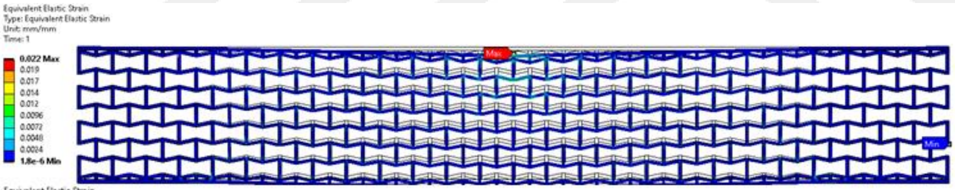

f) Equivalent Elastic Strain (mm/mm)

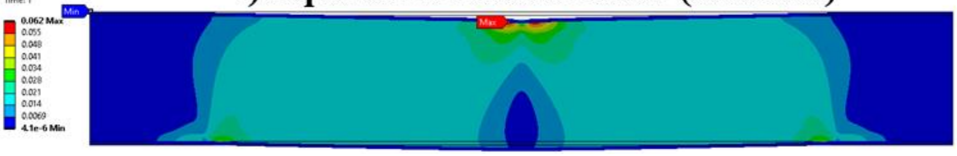

(f)

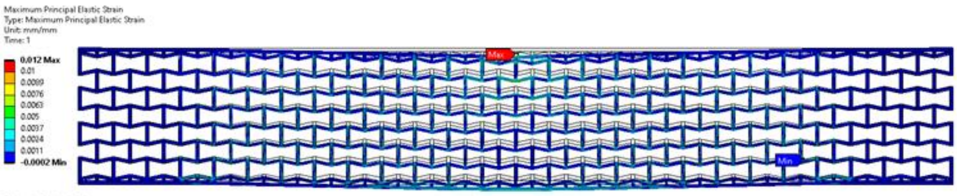

g) Maximum Principal Strain, ε_1 (mm/mm)

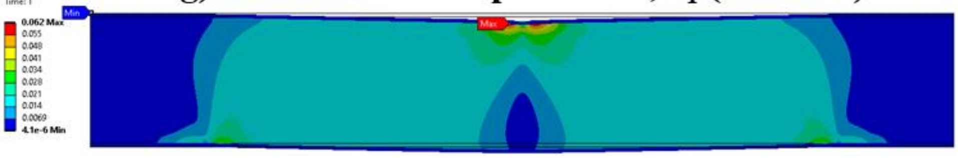

(g)

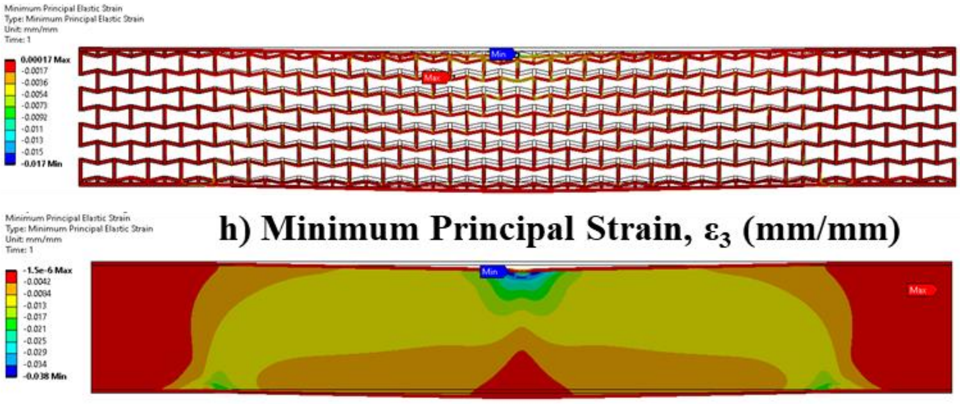

(h)

Figure 4.7: Three-point bending results for the re-entrant structure (full-scale vs. homogenized FE models): (a) total deformation, (b) von Mises stress, (c) σ_1, (d) σ_3, (e) strain energy, (f) elastic strain, (g) ε_1, (h) ε_3.

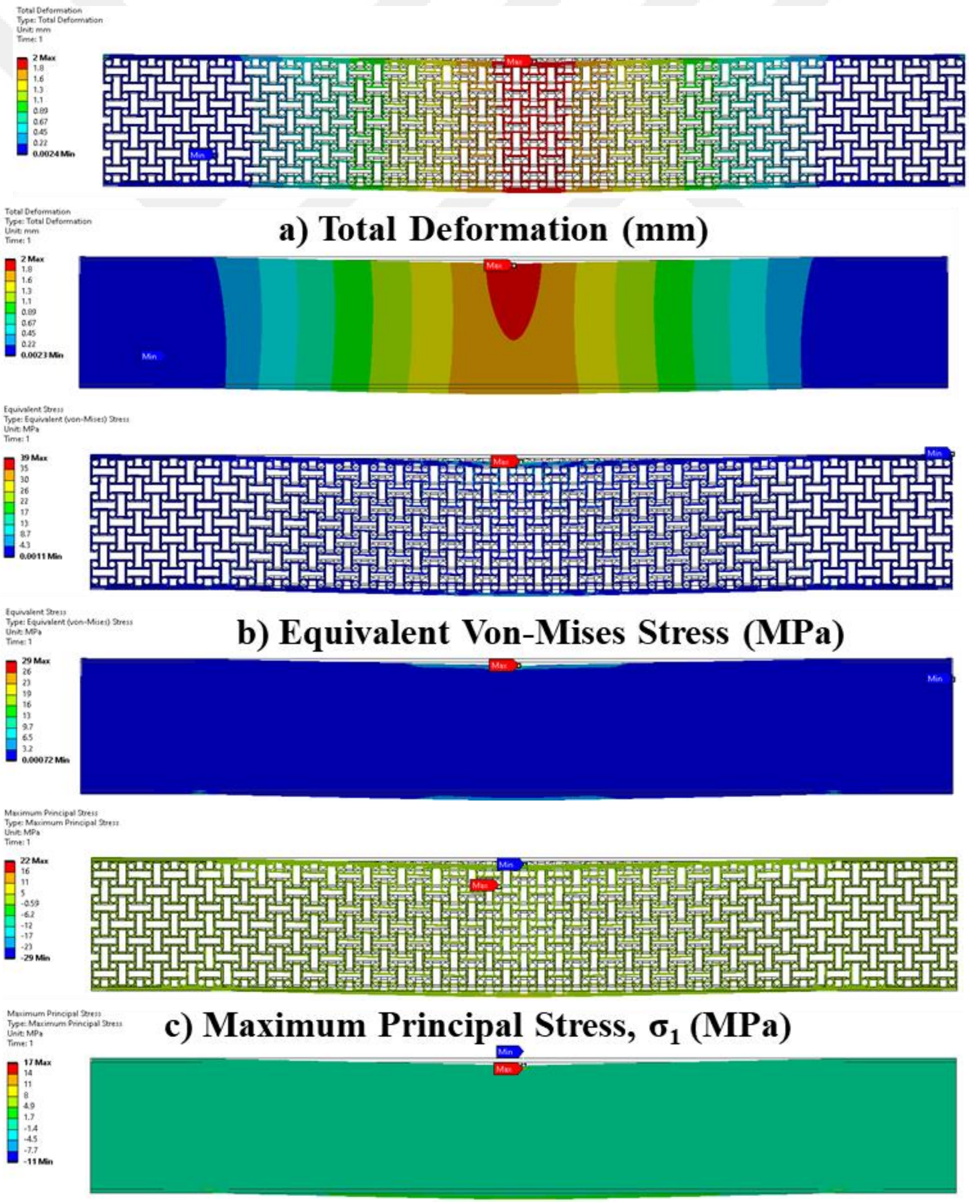

(a)

(b)

(c)

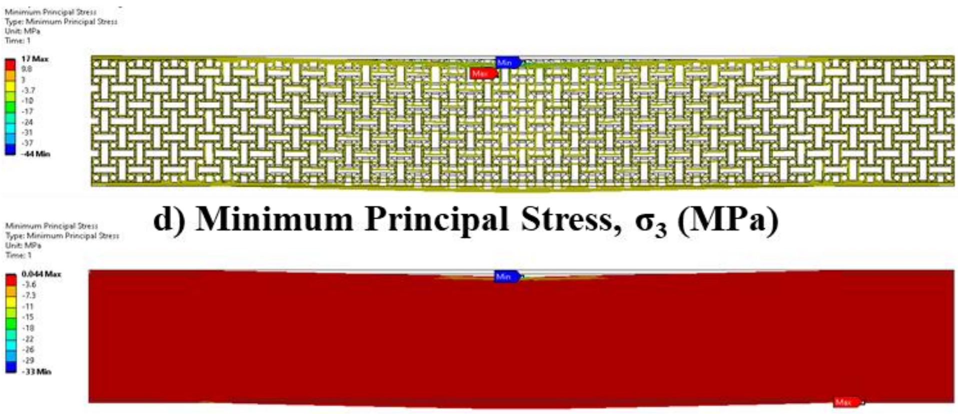
d) Minimum Principal Stress, σ3 (MPa)

(d)

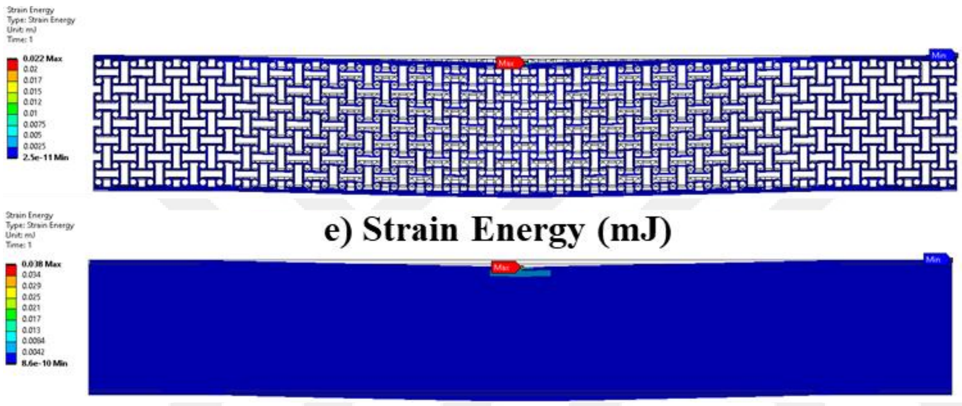
e) Strain Energy (mJ)

(e)

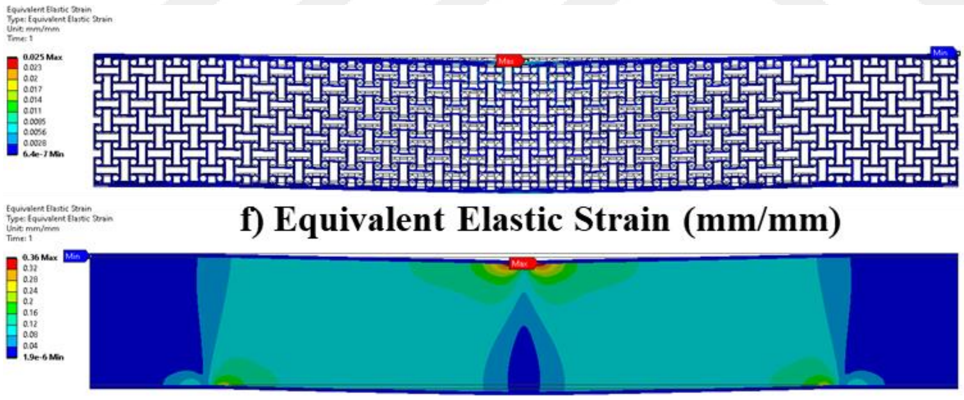
f) Equivalent Elastic Strain (mm/mm)

(f)

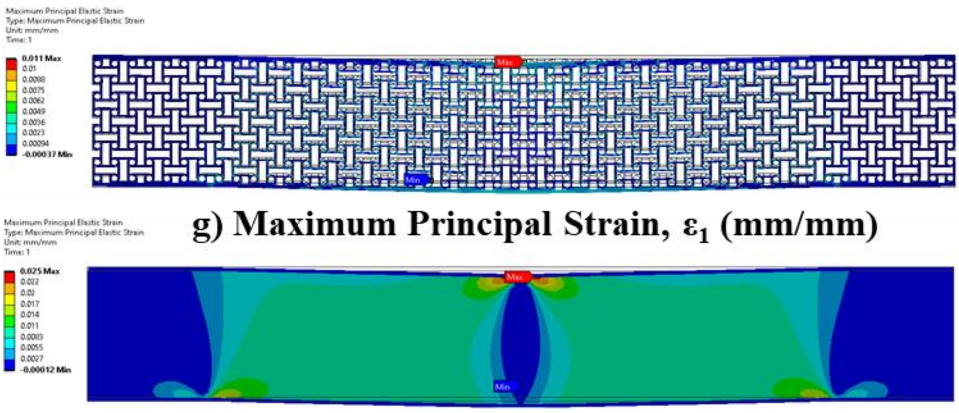
g) Maximum Principal Strain, ε1 (mm/mm)

(g)

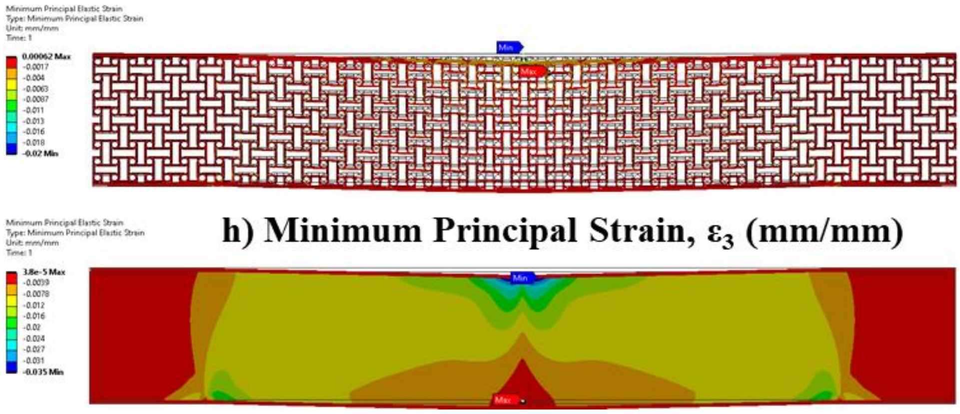

(h)

Figure 4.8: Three-point bending results for the anti-tetrachiral structure (full-scale vs. homogenized FE models): (a) total deformation, (b) von Mises stress, (c) σ_1, (d) σ_3, (e) strain energy, (f) elastic strain, (g) ε_1, (h) ε_3.

Overall, these findings indicate that while the full-scale model provides detailed geometric fidelity, the homogenized model successfully reproduces the deformation, stress, and strain fields in both magnitude and distribution. This validates homogenization as a reliable and computationally efficient alternative for analyzing auxetic lattice structures, enabling substantial reductions in model complexity without compromising accuracy.

4.2.1.Results of three-point bending static structural FE analysis with average young's modulus derived from tensile and compression tests, and comparison with experiments

This section presents the static structural finite element analysis (FEA) results together with comparisons to experimental data for re-entrant and anti-tetrachiral auxetic structures under three-point bending. In this approach, the material definition was based on the arithmetic average of the Young's modulus obtained from both tensile and compression tests.

The aim for this approach comes from the fact that three-point bending simultaneously subjects the specimen to both tensile and compressive stresses, making it difficult to accurately capture the structural response using material data derived solely from tensile testing. By employing an averaged modulus, the analysis seeks to provide a more balanced representation of the global stiffness and to improve the consistency between numerical predictions and experimental measurements.

The finite element models were constructed identically to the reference configurations described in Section 3.2, with the only modification being the material definition as outlined in Section 3.2.1. The comparison between full-scale FE model predictions and experimental results provides an evaluation of the effectiveness of this averaging approach in simulating the bending response of complex auxetic structures.

For the re-entrant structure, the force–deflection results obtained from the full-scale FEA and the experimental tests are summarized in Table 4.9 and visually presented in Figure 4.9. The corresponding percentage differences are also included in Table 4.9.

At a load cell displacement of 1.0 mm, the full-scale FEA predicted a reaction force of 92 N, while the experimental test measured 86 N, corresponding to a difference of 7.0%. At 2.0 mm, the full-scale model predicted 166 N compared to the experimental value of 165 N, resulting in a very close agreement with only 1.1% deviation.

At 3.0 mm, the FEA prediction was 241 N, whereas the experimental result was 244 N, giving a difference of –1.1%. Finally, at 4.0 mm, the full-scale FEA estimated 316 N compared to 323 N in the experimental test, with a deviation of –2.1%.

Overall, the results show excellent agreement between the full-scale numerical model and the physical experiments across the entire deflection range. Unlike earlier cases where significant overestimation was observed, the use of the averaged Young's modulus enables the full-scale FEA to accurately capture the bending response of the re-entrant structure, with deviations consistently within ±7%. This shows the effectiveness of the averaging approach in representing the mixed tensile–compressive loading state of three-point bending tests.

Table 4.9: 3-Point Bending Results for Re-entrant Structure Using Average Young's Modulus – FEA vs Experiment.

Deflection of Load Cell (mm)	Full-Scale FEM Force Reaction (N)	Experimental Test Results Force (N)	Full-Scale FEA vs. Test Results (%)
1.0	92	86	7.0%
2.0	166	165	1.1%
3.0	241	244	-1.1%
4.0	316	323	-2.1%

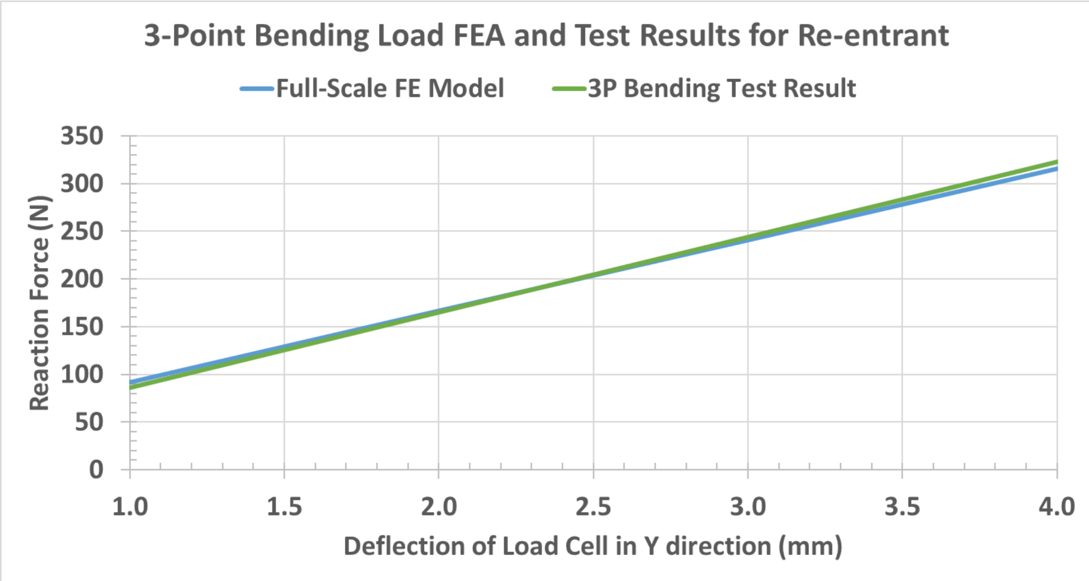

Figure 4.9: 3-Point Bending Force–Deflection Comparison for Re-entrant Structure Using Average Young's Modulus (FEA vs Experiment).

For the anti-tetrachiral structure, the force–deflection results obtained from the full-scale FEA and the experimental tests are summarized in Table 4.10 and illustrated in Figure 4.10. The corresponding percentage differences are also presented in Table 4.10.

At a load cell displacement of 1.0 mm, the full-scale FEA predicted a reaction force of 77 N, while the experimental test measured 70 N, corresponding to a difference of 11.0%. At 2.0 mm, the full-scale model predicted 150 N compared to 132 N from the experiment, resulting in a deviation of 13.8%. At 3.0 mm, the FEA result was 222 N, while the experimental value was 194 N, giving a difference of 14.8%. Finally, at 4.0 mm, the model predicted 295 N compared to 256 N measured experimentally, corresponding to a 15.3% difference.

Overall, the results indicate that while the full-scale model systematically overestimates the reaction force compared to the experimental findings, the level of deviation remains consistent, within approximately 11–15% across the displacement range. This shows that the averaged Young's modulus approach provides a reasonable approximation of the global bending response of the anti-tetrachiral structure, though it tends to predict a slightly stiffer behavior than observed in physical testing.

Table 4.10: 3-Point Bending Results for Anti-tetrachiral Structure Using Average Young's Modulus – FEA vs Experiment.

Deflection of Load Cell (mm)	Full-Scale FEM Force Reaction (N)	Experimental Test Results Force (N)	Full-Scale FEA vs. Test Results (%)
1.0	77	70	11.0%
2.0	150	132	13.8%
3.0	222	194	14.8%
4.0	295	256	15.3%

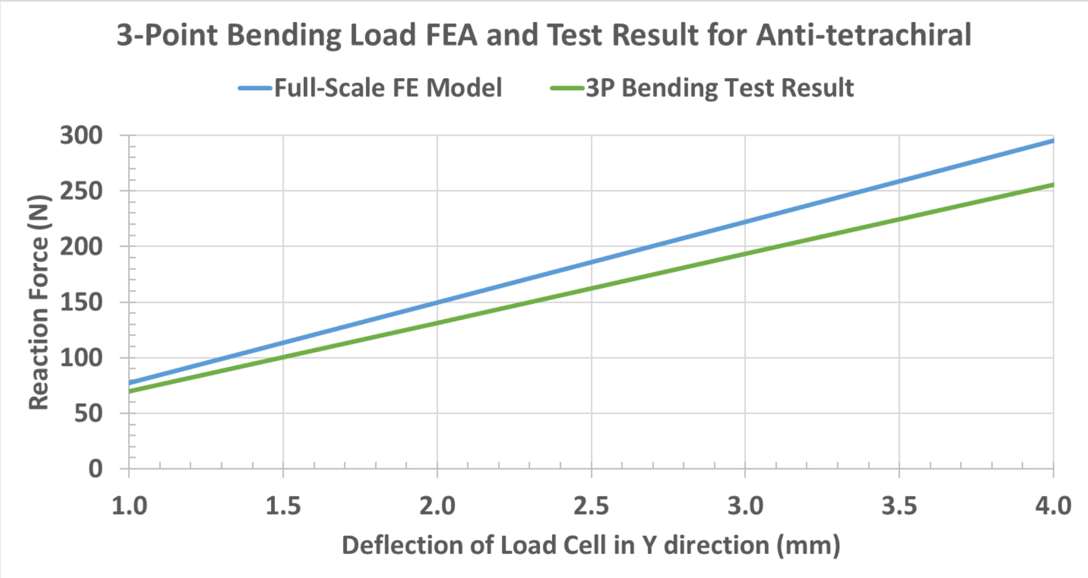

Figure 4.10: 3-Point Bending Force–Deflection Comparison for Anti-tetrachiral Structure Using Average Young's Modulus (FEA vs Experiment).

The results demonstrate that applying the averaged Young's modulus substantially improves the correlation between numerical predictions and experimental bending responses. For the re-entrant structure, the deviations between full-scale FE simulations and experiments were consistently small, remaining within ±7% across the entire displacement range. This indicates that the averaged modulus effectively mitigates the excessive stiffness overestimation observed in tensile-only models, allowing the numerical simulations to accurately reproduce the experimental bending behavior.

For the anti-tetrachiral structure, the full-scale model still tended to overpredict the reaction forces; however, the deviations were limited to approximately 11–15% throughout the displacement range. Despite this moderate overestimation, the overall experimental trend was captured with reasonable accuracy, confirming the validity of the averaging approach as a first-level approximation.

Overall, the use of an averaged modulus provides a practical compromise for representing the complex mixed stress state of three-point bending within a single isotropic material definition. These findings further motivate the investigation of a more refined modeling approach that incorporates separate tensile and compressive moduli, as presented in the sensitivity study in Section 4.2.2.

For supplementary results of the full-scale finite element model, the total deformation of the re-entrant FE model is presented in Figure 4.11. The detailed outcomes for the re-entrant structure are further illustrated in Figures 4.12(a–h). Specifically, Figure 4.12(a) shows the total deformation, (b) the equivalent von Mises stress, (c) the maximum principal stress (σ_1), (d) the minimum principal stress (σ_3), (e) the strain energy, (f) the equivalent elastic strain, (g) the maximum principal strain (ε_1), and (h) the minimum principal strain (ε_3), with results reported for the full-scale modeling approach only.

For the anti-tetrachiral structure, the total deformation of the FE model is presented in Figure 4.13. Additionally, the detailed full-scale FE model results are provided in Figures 4.14(a–h), where the subfigures correspond to: (a) total deformation, (b) equivalent von Mises stress, (c) maximum principal stress (σ_1), (d) minimum principal stress (σ_3), (e) strain energy, (f) equivalent elastic strain, (g) the maximum principal strain (ε_1), and (h) the minimum principal strain (ε_3).

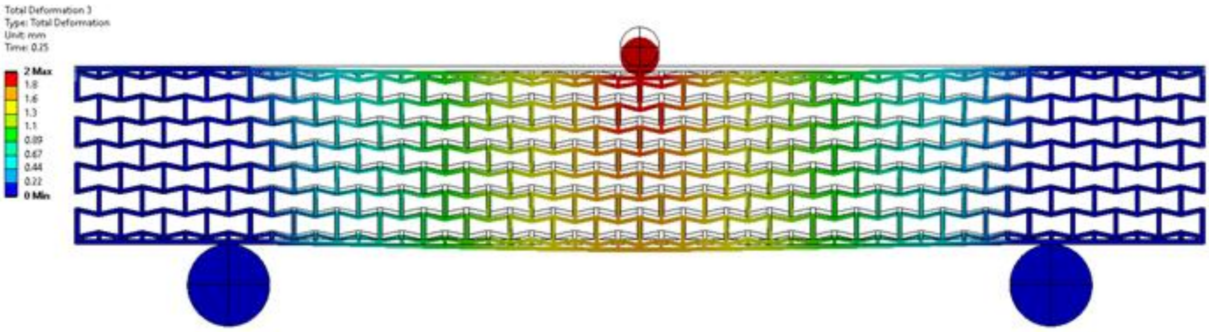

Figure 4.11: Total Deformation Distribution for the Re-entrant Structure under 3P Bending Load Using the Averaged Young's Modulus (Full-Scale FE Model).

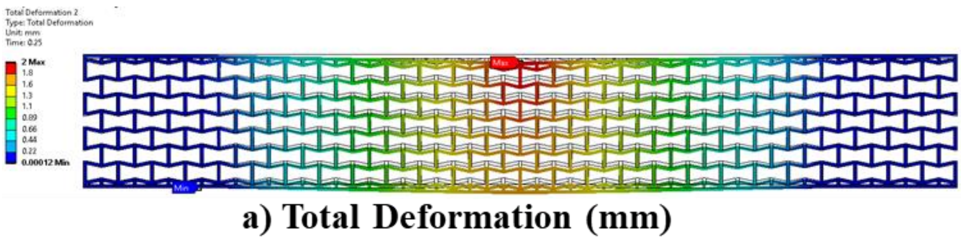
a) Total Deformation (mm)

(a)

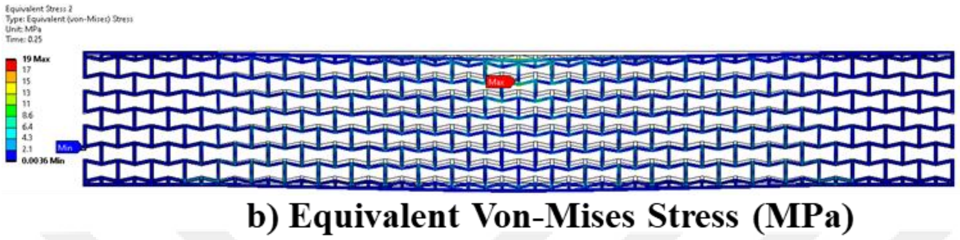
b) Equivalent Von-Mises Stress (MPa)

(b)

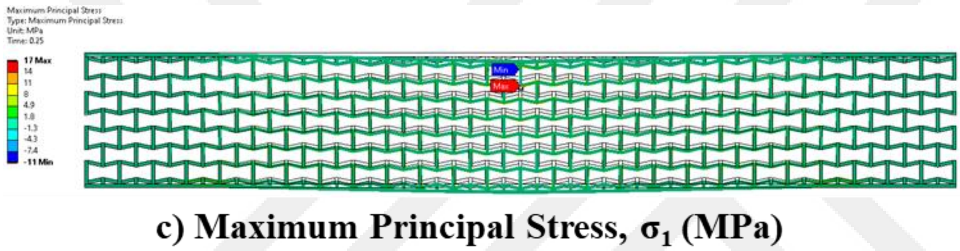
c) Maximum Principal Stress, σ1 (MPa)

(c)

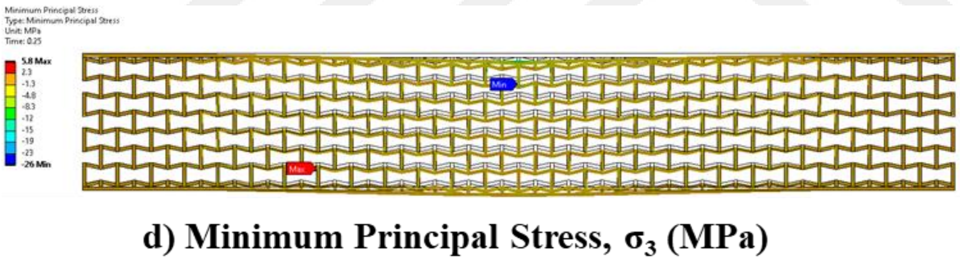
d) Minimum Principal Stress, σ3 (MPa)

(d)

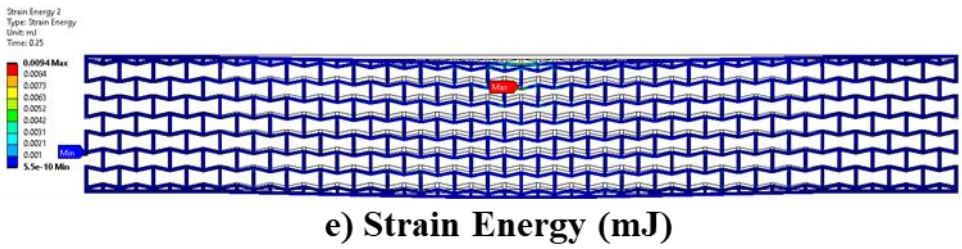
e) Strain Energy (mJ)

(e)

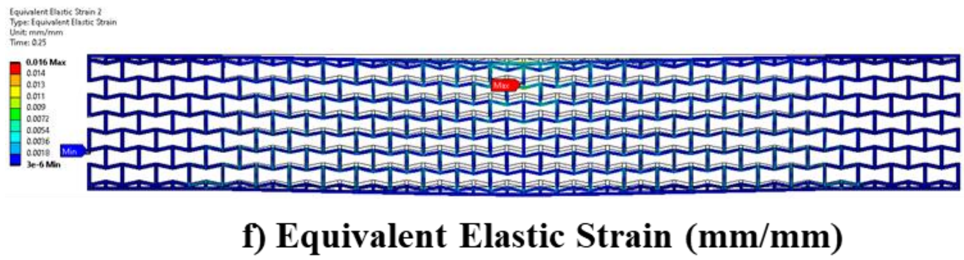
f) Equivalent Elastic Strain (mm/mm)

(f)

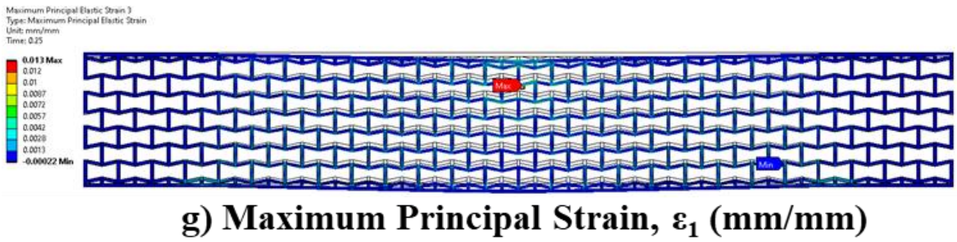

(g)

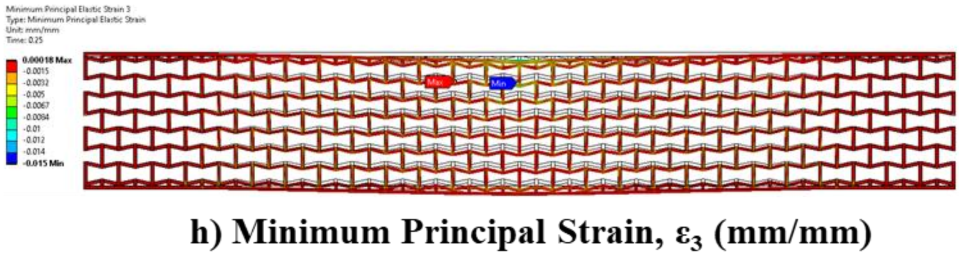

(h)

Figure 4.12: Three-point bending results for the re-entrant structure with averaged Young's modulus (full-scale FE): (a) deformation, (b) von Mises stress, (c) σ_1, (d) σ_3, (e) strain energy, (f) elastic strain, (g) ε_1, (h) ε_3.

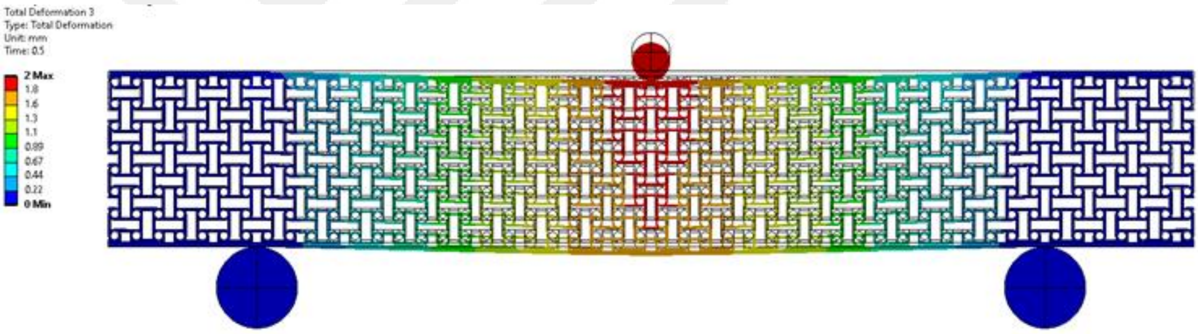

Figure 4.13: Total Deformation Distribution for the Anti-tetrachiral Structure under 3P Bending Load Using the Averaged Young's Modulus (Full-Scale FE Model).

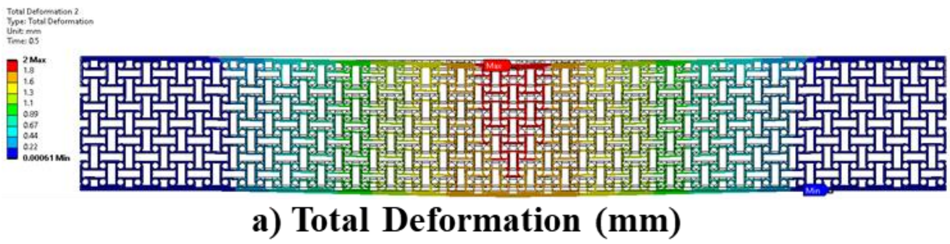

(a)

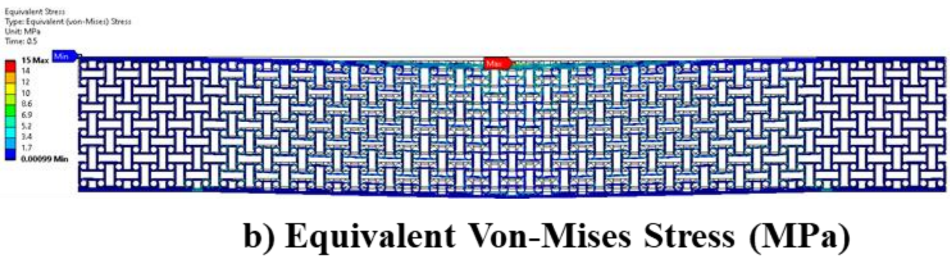

(b)

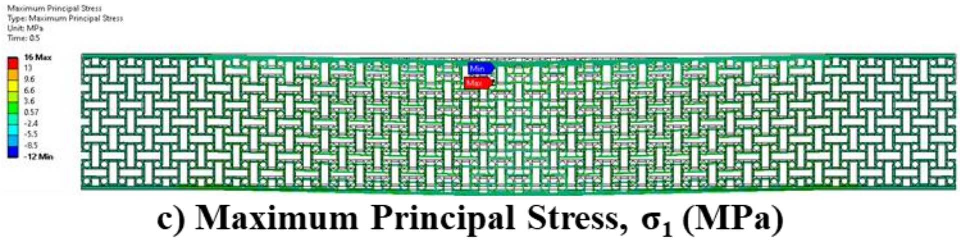

(c)

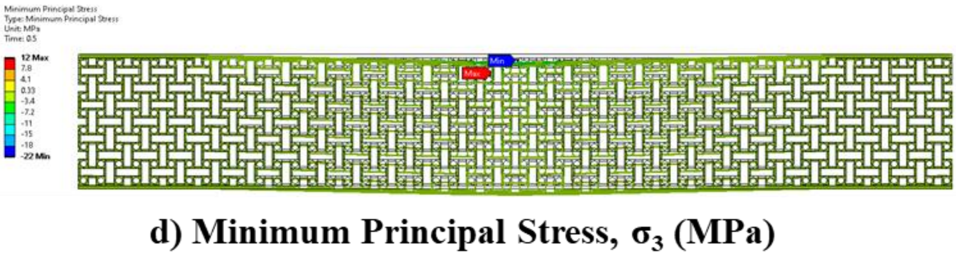

(d)

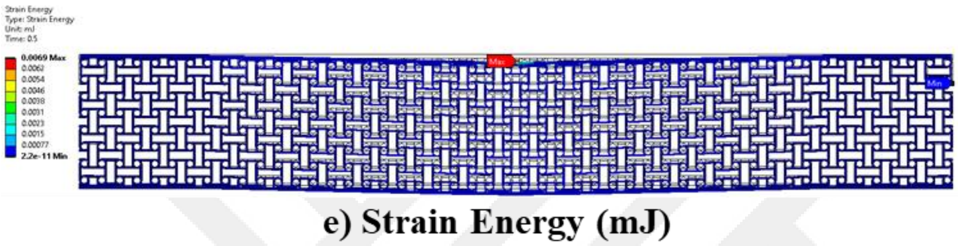

(e)

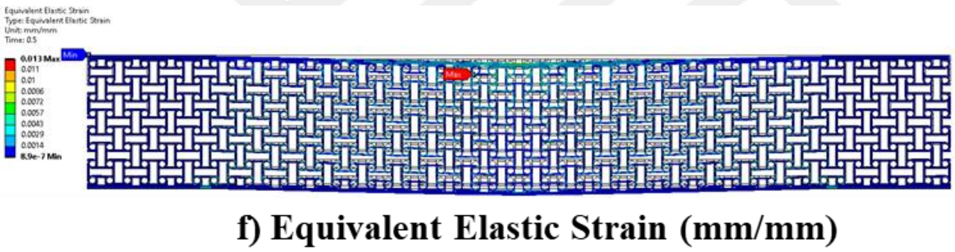

(f)

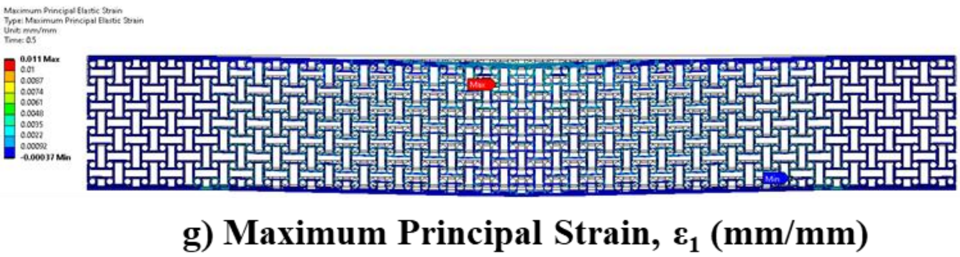

(g)

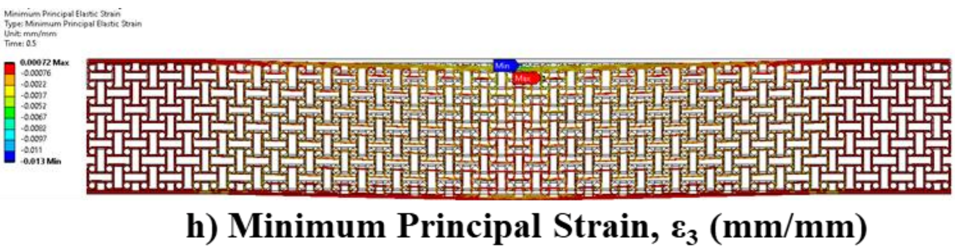

(h)

Figure 4.14: Three-point bending results for the anti-tetrachiral structure with averaged Young's modulus (full-scale FE): (a) deformation, (b) von Mises stress, (c) σ_1, (d) σ_3, (e) strain energy, (f) elastic strain, (g) ε_1, (h) ε_3.

4.2.2. Results of three-point bending static structural FE analysis using separate young’s modulus for tension and compression with neutral axis consideration and experimental comparison

This section presents the static structural finite element analysis (FEA) results together with comparisons to experimental data for re-entrant and anti-tetrachiral auxetic structures under three-point bending. In this approach, the material model was defined by assigning separate Young’s modulus for tension and compression, combined with a neutral axis consideration to differentiate the stress state across the specimen.

The aim for this approach comes from the fact that three-point bending subjects the structure simultaneously to tensile stresses on one side of the neutral axis and compressive stresses on the other. Using a single modulus obtained from tensile testing alone leads to artificial stiffness and reduced predictive accuracy. By distinguishing between tensile and compressive elastic modulus and incorporating the neutral axis location, the analysis seeks to more realistically represent the mixed stress state and better capture the true bending behavior observed in experiments.

The finite element models were constructed identically to the reference configurations described in Section 3.2, with the only modification being the material definition strategy as detailed in Section 3.2.2. Comparisons between full-scale FE predictions and experimental results were conducted to assess the effectiveness of this refined material modeling approach.

For the re-entrant structure, the force–deflection results obtained from the full-scale FEA and the experimental tests are summarized in Table 4.11 and visually presented in Figure 4.15. The corresponding percentage differences are also listed in Table 4.11.

At a load cell displacement of 1.0 mm, the full-scale FEA predicted a reaction force of 89 N, while the experimental test measured 86 N, corresponding to a difference of 4.1%. At 2.0 mm, the full-scale model predicted 169 N compared to the experimental value of 165 N, with a deviation of 2.9%. At 3.0 mm, the FEA result was 250 N, whereas the experiment measured 244 N, giving a difference of 2.5%. Finally, at 4.0 mm, the FEA predicted 330 N compared to 323 N from the experiment, corresponding to a difference of 2.3%.

Overall, the force–deflection curves demonstrate excellent consistency between the numerical and experimental results for the re-entrant structure, with differences remaining within 5% across the entire deflection range. This shows that applying separate tensile and compressive Young's modulus with neutral axis consideration successfully eliminates the excessive stiffness previously observed in tensile-only or averaged modulus models.

Table 4.11: 3-Point Bending Results for the Re-entrant Structure Using Separate Tensile and Compressive Young's Modulus with Neutral Axis Consideration – Comparison of FEA and Experiments.

Deflection of Load Cell (mm)	Full-Scale FEM Force Reaction (N)	Experimental Test Results Force (N)	Full-Scale FEA vs. Test Results (%)
1.0	89	86	4.1%
2.0	169	165	2.9%
3.0	250	244	2.5%
4.0	330	323	2.3%

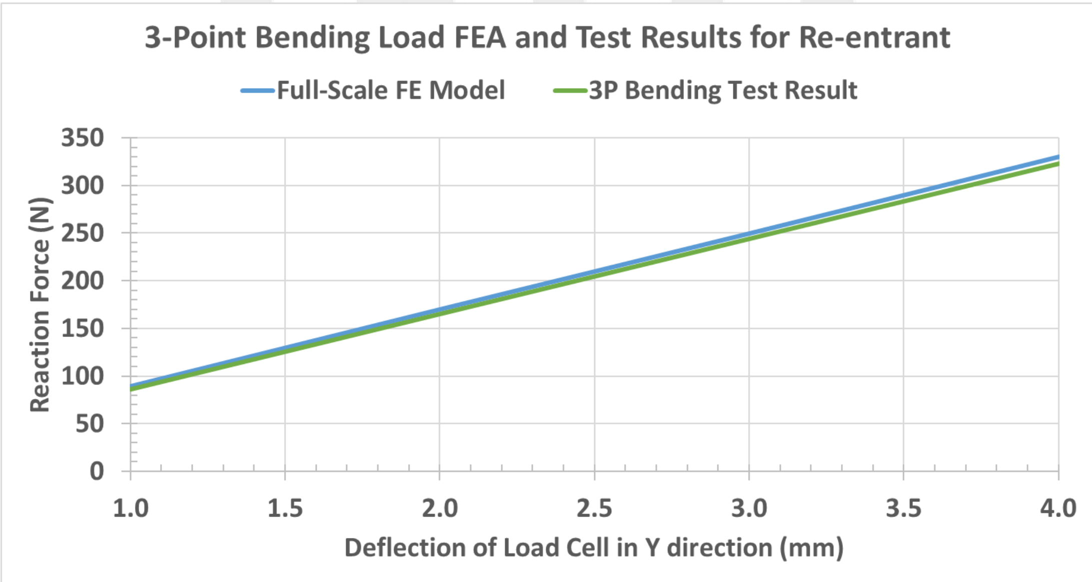

Figure 4.15: 3-Point Bending Force–Deflection Comparison for Re-entrant Structure with Separate Tension/Compression Modulus (FEA vs Experiment).

For the anti-tetrachiral structure, the force–deflection results obtained from the full-scale FEA and the experimental tests are summarized in Table 4.12 and visually presented in Figure 4.16. The corresponding percentage differences are also listed in Table 4.12.

At a load cell displacement of 1.0 mm, the full-scale FEA predicted a reaction force of 73 N, while the experimental test measured 70 N, corresponding to a difference of 4.9%. At 2.0 mm, the FEA result was 142 N compared to 132 N from the experiment, with a deviation of 7.7%. At 3.0 mm, the full-scale model estimated 210 N versus 194 N in the experimental test, giving a difference of 8.6%. Finally, at 4.0 mm displacement, the FEA predicted 279 N, while the experiment measured 256 N, corresponding to a deviation of 9.1%.

Overall, the results show that while the full-scale FEA tends to slightly overpredict the reaction forces for the anti-tetrachiral structure, the deviations remain within 5–9% across the entire displacement range. This indicates that employing separate tensile and compressive Young's modulus with neutral axis consideration substantially improves the predictive capability of the simulations compared to previous approaches, capturing the experimental bending response with good accuracy.

Table 4.12: 3-Point Bending Results for the Anti-tetrachiral Structure Using Separate Tensile and Compressive Young's Modulus with Neutral Axis Consideration – Comparison of FEA and Experiments.

Deflection of Load Cell (mm)	Full-Scale FEM Force Reaction (N)	Experimental Test Results Force (N)	Full-Scale FEA vs. Test Results (%)
1.0	73	70	4.9%
2.0	142	132	7.7%
3.0	210	194	8.6%
4.0	279	256	9.1%

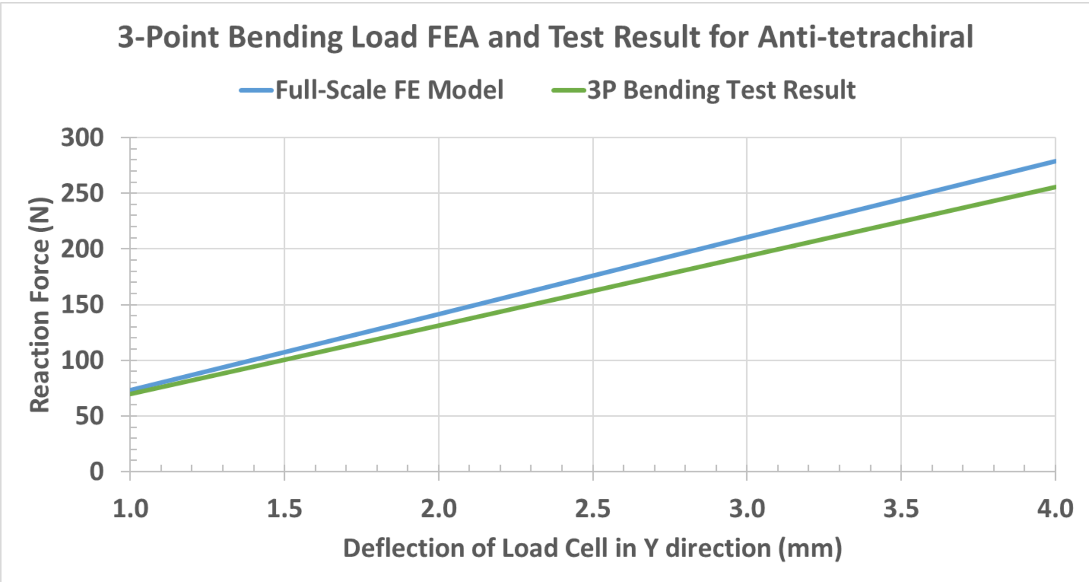

Figure 4.16: 3-Point Bending Force–Deflection Comparison for Anti-tetrachiral Structure with Separate Tension/Compression Modulus (FEA vs Experiment).

The results of this sensitivity study show that incorporating separate tensile and compressive Young's modulus with neutral axis consideration provides a much more accurate representation of the bending response of auxetic sandwich structures than both tensile-only and averaged modulus approaches. For the re-entrant structure, the deviations between simulation and experiment were reduced to within 2–4% across the full displacement range, representing excellent correlation. For the anti-tetrachiral structure, while the full-scale model still slightly overpredicted the reaction forces, the discrepancies were limited to approximately 5–9%, which marks a substantial improvement over the larger errors obtained in previous modeling strategies.

These findings underline the importance of accounting for asymmetric elastic behavior under complex loading conditions such as three-point bending, where the specimen is subjected simultaneously to tensile and compressive stresses. By applying this refined material definition, the finite element models were able to capture both global stiffness and experimental force–deflection behavior with high fidelity. This demonstrates that a single isotropic modulus is insufficient to describe the true mechanical response of auxetic lattices under bending, and separating tensile and compressive properties significantly improves predictive capability.

Overall, the outcomes of Section 4.2.2 confirm that the use of separate modulus for tension and compression combined with neutral axis consideration provides a more realistic description of the mixed stress state in bending. This strategy not only reduces the overestimation tendency of earlier models but also enhances the reliability of finite element predictions for the design and optimization of auxetic sandwich structures. By adopting this approach, future modeling efforts can achieve both improved accuracy and practical value, offering stronger support for engineering applications of auxetic lattices.

For supplementary results of the full-scale finite element model, the total deformation of the re-entrant FE model is presented in Figure 4.17. The detailed outcomes for the re-entrant structure are further illustrated in Figures 4.18(a–h). Specifically, Figure 4.18(a) shows the total deformation, (b) the equivalent von Mises stress, (c) the maximum principal stress (σ_1), (d) the minimum principal stress (σ_3), (e) the strain energy, (f) the equivalent elastic strain, (g) the maximum principal strain (ε_1), and (h) the minimum principal strain (ε_3), with results reported for the full-scale modeling approach only.

For the anti-tetrachiral structure, the total deformation of the FE model is presented in Figure 4.19. Additionally, the detailed full-scale FE model results are provided in Figures 4.20(a–h), where the subfigures correspond to: (a) total deformation, (b) equivalent von Mises stress, (c) maximum principal stress (σ_1), (d) minimum principal stress (σ_3), (e) strain energy, (f) equivalent elastic strain, (g) the maximum principal strain (ε_1), and (h) the minimum principal strain (ε_3).

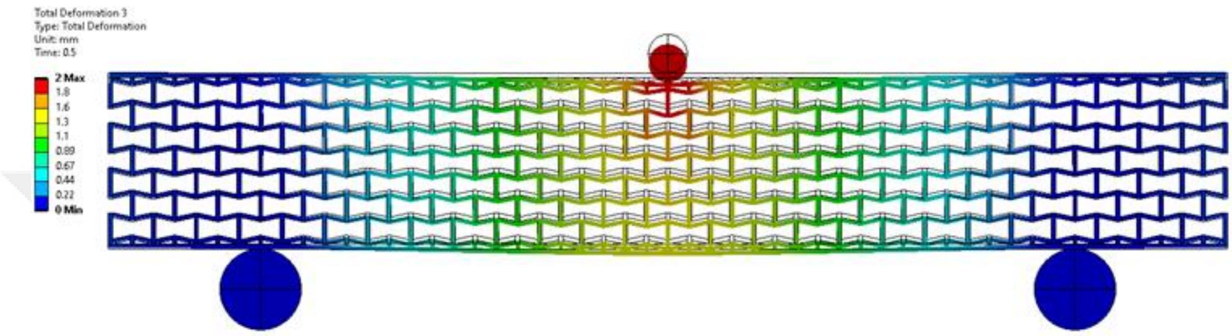

Figure 4.17: Total Deformation Distribution for the Re-entrant Structure under Three-Point Bending with Separate Tensile and Compressive Young's Modulus (Full-Scale FE Model).

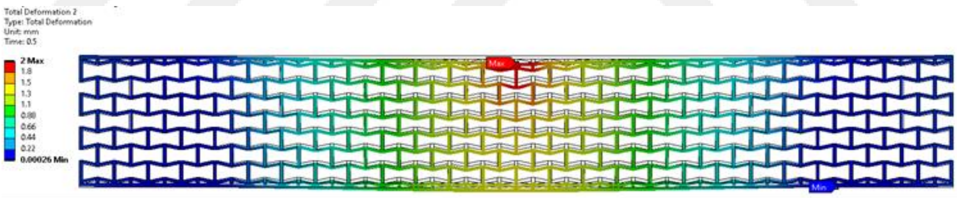

a) Total Deformation (mm)

(a)

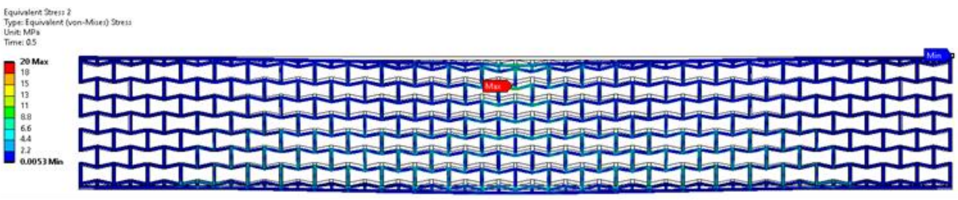

b) Equivalent Von-Mises Stress (MPa)

(b)

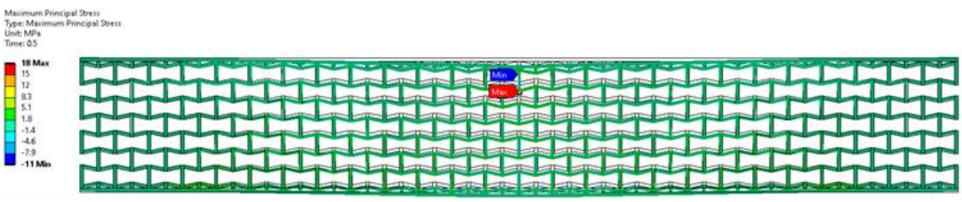

c) Maximum Principal Stress, σ_1 (MPa)

(c)

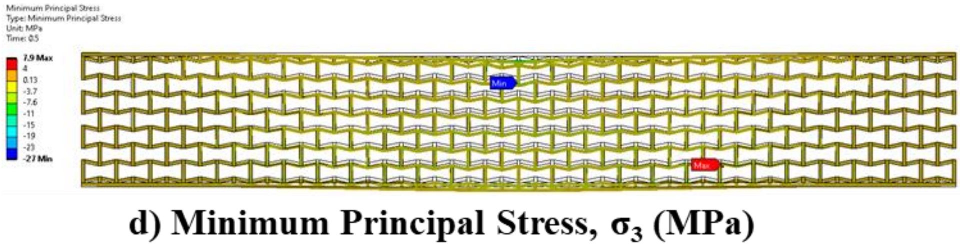

(d)

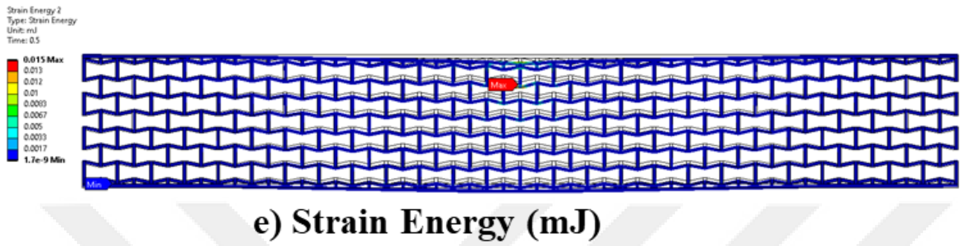

(e)

(f)

(g)

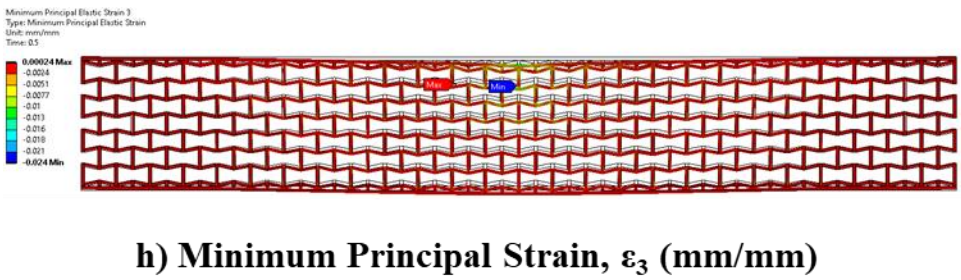

(h)

Figure 4.18: 3P Bending Results for the Re-entrant Structure with Separate Tension/Compression Modulus (Full-Scale FE): (a) deformation, (b) von Mises stress, (c) σ_1, (d) σ_3, (e) strain energy, (f) elastic strain, (g) ε_1, (h) ε_3.

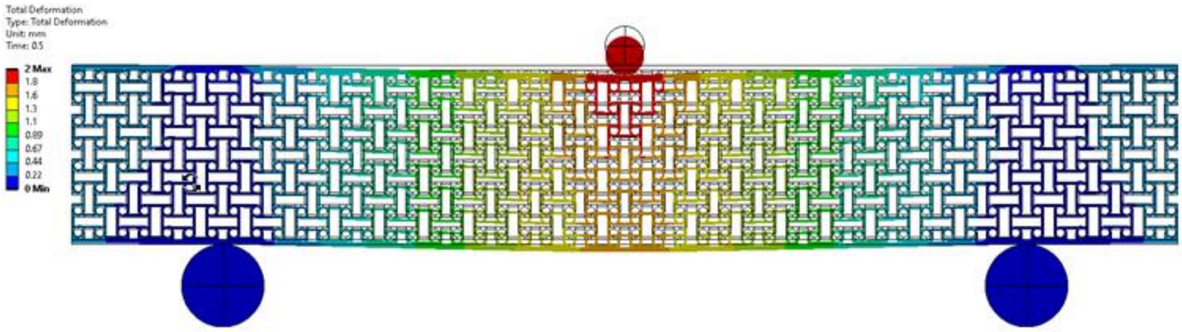

Figure 4.19: Total Deformation Distribution for the Anti-tetrachiral Structure under Three-Point Bending with Separate Tensile and Compressive Young's Modulus (Full-Scale FE Model).

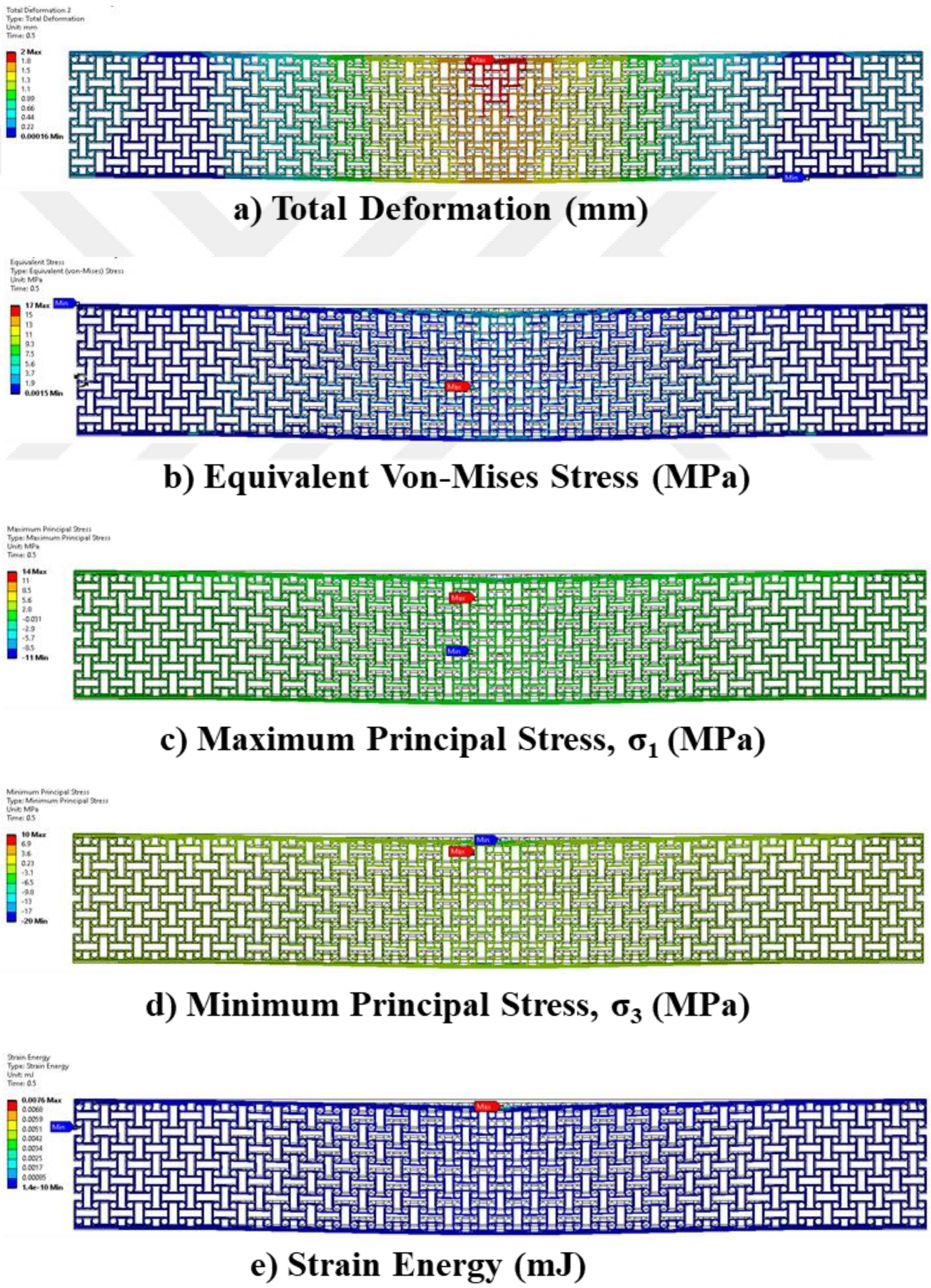

(a)

(b)

(c)

(d)

(e)

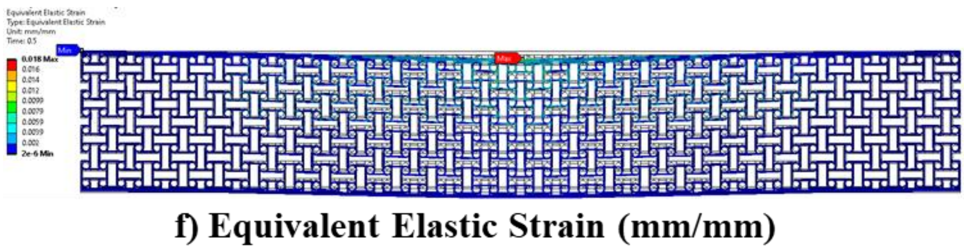

(f)

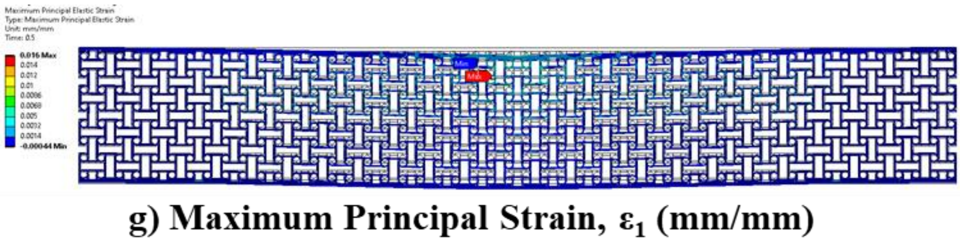

(g)

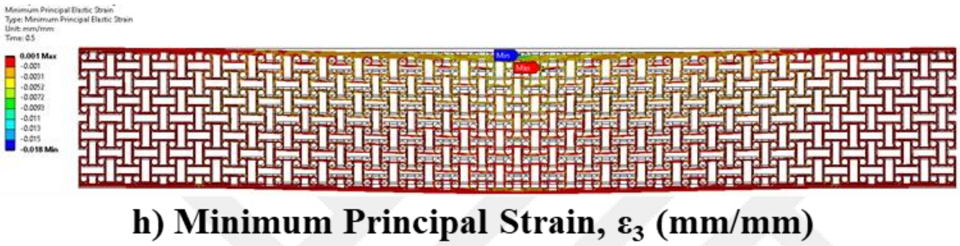

(h)

Figure 4.20: 3P Bending Results for the Anti-tetrachiral Structure with Separate Tension/Compression Modulus (Full-Scale FE): (a) deformation, (b) von Mises stress, (c) σ_1, (d) σ_3, (e) strain energy, (f) elastic strain, (g) ε_1, (h) ε_3.

4.3. Compression Load Static Structural FE Analysis Results and Comparison Against Experimental Results

This section presents the static structural finite element analysis (FEA) results for the re-entrant and anti-tetrachiral auxetic structures under compressive loading, alongside comparisons with experimental data. The objective is to evaluate the predictive accuracy of the full-scale and simplified (homogenized) FE models and to assess the effectiveness of the homogenization approach in representing the compressive behavior of complex auxetic geometries. All results in this section are based on the FE models described previously in Section 3.3 (Compressive Load Static Structural FEM).

For the re-entrant structure, the force-deflection results obtained from the full-scale FEA, simplified FEA, and experimental tests are summarized in Table 4.13 and visually presented in Figure 4.21. The corresponding percentage differences among these results are detailed in Table 4.14.

At a load cell displacement of 1.0 mm, the full-scale FEA predicted a reaction force of 1101 N, the simplified model predicted 1100 N, while the experimental test measured 981 N. As the displacement increased to 2.0 mm, the full-scale FEA predicted 2210 N, the simplified model 2214 N, and the experimental test 2014 N.

The percentage differences indicate that the simplified FEA model closely matches the reaction forces of the full-scale model, with an average difference of approximately 0.2% across the displacement range. The full-scale FEA overestimates the reaction forces relative to the experimental test results by 12.3% at 1.0 mm, decreasing slightly to 9.7% at 2.0 mm. The simplified FEA model similarly overestimates the experimental results, with differences of 12.1% at 1.0 mm and 9.9% at 2.0 mm. Notably, the discrepancies between the simulation and experimental results tend to decrease progressively as the load cell displacement increases.

The visual comparison of the deformation patterns, presented in Figure 4.22 for the re-entrant structure, reinforces these findings. The simplified model effectively captures the global compression behavior, demonstrating similar overall deformation trends to the full-scale model. While the full-scale model provides a more detailed representation of the local geometric features, both models predict comparable global responses under compressive loading.

From a computational perspective, the full-scale model of the re-entrant structure consists of 306,240 elements and 403,930 nodes, whereas the simplified model contains 37,800 elements and 43,245 nodes. The total computational solve time for the full-scale model was approximately 10 times longer than that of the simplified counterpart, underscoring the substantial efficiency gains achieved through the homogenization approach.

Table 4.13: Compressive Load FEA Results for Re-entrant Structure.

Deflection of Load Cell (mm)	Full-Scale FEM Force Reaction (N)	Simplified-Scale FEM Force Reaction (N)	Experimental Test Results Force (N)
1.0	1101	1100	981
1.5	1656	1657	1498
2.0	2210	2214	2014

Table 4.14: Difference(%) of Compressive Load Results for Re-entrant Structure.

Deflection of Load Cell (mm)	Simplified FEA vs. Full-Scale FEA (%)	Full-Scale FEA vs. Test Results (%)	Simplified FEA vs. Test Results (%)
1.0	-0.2%	12.3%	12.1%
1.5	0.1%	10.5%	10.7%
2.0	0.2%	9.7%	9.9%

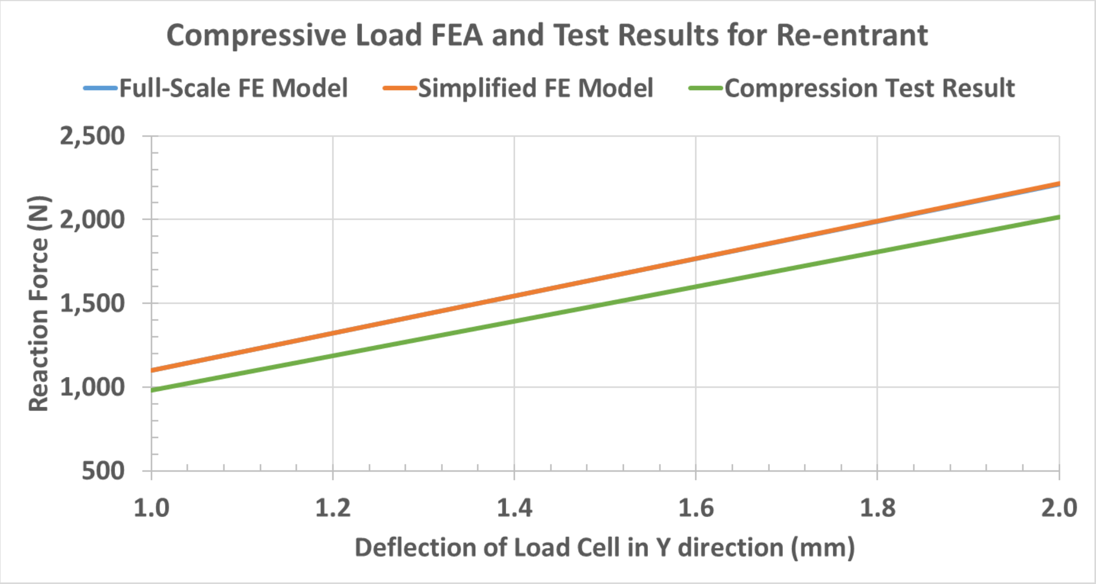

Figure 4.21: Compression Load FEA and Test Results for Re-entrant Structure.

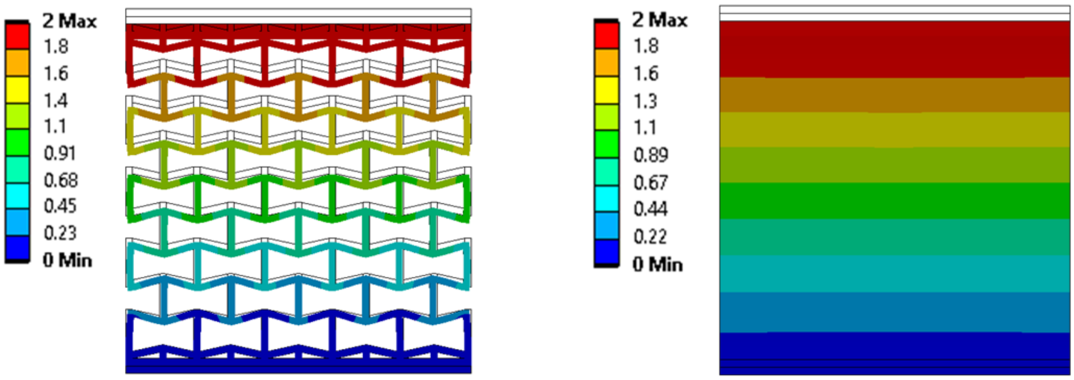

Figure 4.22: Total Deformation Distribution for the Re-entrant Structure under Compression Load: Full-Scale and Simplified FE Models.

For the anti-tetrachiral structure, the results follow a similar trend to those observed for the re-entrant structure. As shown in Table 4.15 and visually illustrated in Figure 4.23, at a displacement of 1.0 mm, the full-scale FEA predicts a reaction force of 1120 N, the simplified model predicts 984 N, and the experimental test measures 977 N. At 2.0 mm displacement, these values increase to 2081 N, 1933 N, and 1859 N, respectively.

Table 4.16 shows that the simplified model consistently underestimates the reaction force compared to the full-scale model, with differences of approximately 12.1% at 1.0 mm and 7.1% at 2.0 mm.

More notably, the full-scale FEA overestimates the experimental test results, with percentage differences of 14.6% at 1.0 mm, decreasing slightly to 12.0% at 2.0 mm. In contrast, the simplified model provides a closer estimate of the experimental results, with differences ranging from 0.8% at 1.0 mm to 4.0% at 2.0 mm. The differences show a slight increase as the displacement grows.

The visual comparison of the deformation patterns, presented in Figure 4.24 for the anti-tetrachiral structure, reinforces these findings. The simplified models effectively capture the global compression behavior, while the full-scale models, although more detailed, tend to over-predict the stiffness and reaction forces compared to experimental data.

From a computational perspective, the full-scale anti-tetrachiral model consists of 923,940 elements and 1,171,211 nodes, while the simplified model contains 43,245 elements and 37,800 nodes. The full-scale model required approximately 50 times longer solve time than the simplified model, underscoring the significant computational advantages offered by the homogenization approach.

Table 4.15: Compressive Load FEA Results for Anti-tetrachiral Structure.

Deflection of Load Cell (mm)	Full-Scale FEM Force Reaction (N)	Simplified-Scale FEM Force Reaction (N)	Experimental Test Results Force (N)
1.0	1120	984	977
1.5	1600	1459	1418
2.0	2081	1933	1859

Table 4.16: Difference (%) of Compressive Load Results for Anti-tetrachiral.

Deflection of Load Cell (mm)	Simplified FEA vs. Full-Scale FEA (%)	Full-Scale FEA vs. Test Results (%)	Simplified FEA vs. Test Results (%)
1.0	-12.1%	14.6%	0.8%
1.5	-8.9%	12.9%	2.9%
2.0	-7.1%	12.0%	4.0%

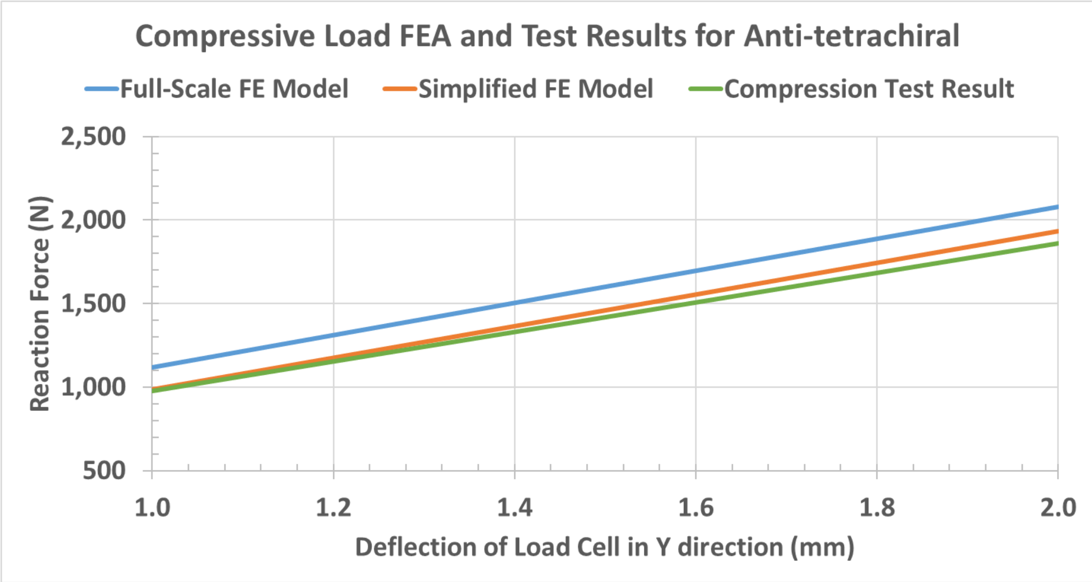

Figure 4.23: Compression Load FEA and Test Results for Anti-tetrachiral Structure.

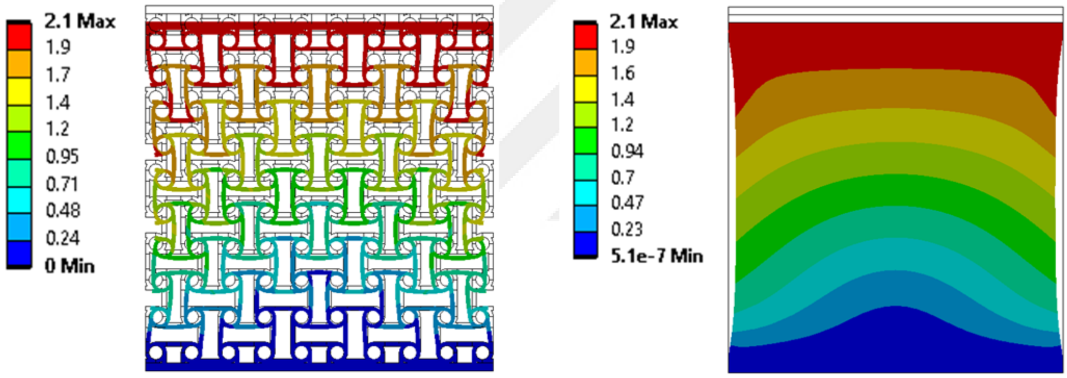

Figure 4.24: Total Deformation Distribution for the Anti-tetrachiral Structure under Compression Load: Full-Scale and Simplified FE Models.

These findings highlight a key trade-off: while the full-scale models offer detailed geometric representation, they tend to slightly overestimate the compressive stiffness of the auxetic structures compared to experimental data, with differences reaching 12.3% for the re-entrant and 14.6% for the anti-tetrachiral structures. The simplified homogenized models, although less detailed, achieve a closer match to the experimental results, with differences generally below 12% for the re-entrant and 4% for the anti-tetrachiral structures.

Overall, these results indicate that for compressive loading simulations, simplified homogenized models provide an acceptable approximation of experimental behavior, offering a practical balance between accuracy and computational efficiency.

The analysis demonstrates that while full-scale models remain the most accurate choice for final validation and high-fidelity compression studies, homogenized models provide a computationally efficient alternative with acceptable accuracy for early-stage design, parametric exploration, and iterative optimization tasks. These results reinforce the viability of the homogenization approach for representing the compression behavior of complex auxetic structures.

4.4.Tensile Load Static Structural FE Analysis Results and Comparison Against

This section presents the results of the static structural finite element analyses (FEA) performed to investigate the tensile behavior of the re-entrant and anti-tetrachiral auxetic structures under uniaxial loading. The analyses were conducted using both full-scale and simplified FE models. The primary aim was to compare the structural responses of these models under tensile loads applied along two principal directions, X and Y, and to evaluate the accuracy and computational efficiency of the homogenization approach in representing the tensile behavior of complex auxetic lattices.

All results discussed in this section are based on the finite element models described previously in Section 3.4 (Tensile Load Static Structural FEM).

As no experimental tensile tests were conducted for this study, the comparison focuses solely on the numerical predictions obtained from the full-scale and simplified FE models. The following subsections present a detailed analysis of the tensile simulation results for each loading direction.

4.4.1.Tensile load in y direction only

For the re-entrant structure, the force-deflection results obtained from the full-scale FEA and simplified FEA and the corresponding percentage differences among these results are presented in Table 4.17.

At a displacement of 1.0 mm, the full-scale FEA predicts a reaction force of 7569 N, while the simplified model predicts 6898 N. As the displacement increases to 2.0 mm, the full-scale model yields 15,137 N, and the simplified model predicts 13,797 N. The results show that the simplified model consistently underestimates the reaction force compared to the full-scale model, with an approximate difference of 8.9% across the displacement range.

The visual comparison of the deformation patterns, as shown in Figure 4.25 for the re-entrant structure, further supports these observations. The simplified model captures the global tensile behavior and overall deformation trends effectively, despite lacking the detailed local geometric features resolved in the full-scale model. Both models, however, predict comparable global responses under tensile loading along the Y direction.

From a computational perspective, the full-scale re-entrant model consists of 897,600 elements and 1,185,500 nodes, whereas the simplified model is composed of 311,808 elements and 337,125 nodes. The full-scale model also requires approximately three times longer computational solve time than its simplified counterpart, highlighting the significant efficiency advantage offered by the homogenization approach.

Table 4.17: Tensile Load in Y Direction FEA Results for Re-entrant Structure.

Deflection of Load Cell (mm)	Full-Scale FEM Force Reaction (N)	Simplified-Scale FEM Force Reaction (N)	Simplified FEA vs. Full-Scale FEA (%)
1.0	7569	6898	-8.9%
1.5	11353	10348	-8.9%
2.0	15137	13797	-8.9%

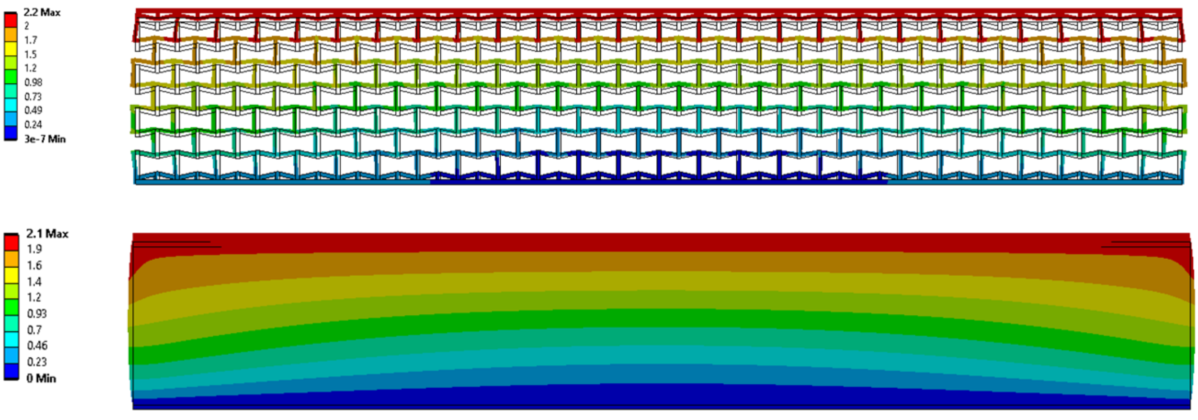

Figure 4.25: Total Deformation Distribution for the Re-entrant Structure under Tensile Load in Y Direction: Full-Scale and Simplified FE Models.

For the anti-tetrachiral structure, the results exhibit a similar trend. As detailed in Table 4.18 and visually presented in Figure 4.26, the full-scale FEA predicts a reaction force of 13,870 N at a displacement of 1.0 mm, while the simplified model predicts 11,136 N. At 2.0 mm displacement, these values increase to 27,740 N for the full-scale model and 22,272 N for the simplified model. The simplified model underestimates the reaction force relative to the full-scale model by approximately 19.7% across the range of displacements.

The visual comparison of the deformation patterns, shown in Figure 4.26 for the anti-tetrachiral structure, reinforces these findings. The simplified model effectively captures the overall tensile behavior, mirroring the global deformation trends observed in the full-scale model, although it does not resolve the finer geometric details. Both models, however, yield comparable predictions for the global tensile response.

In terms of computational efficiency, the full-scale anti-tetrachiral model comprises 2,928,720 elements and 3,722,325 nodes, while the simplified model contains 283,296 elements and 307,125 nodes. The full-scale model required approximately eight times longer computational solve time than the simplified model, underscoring the substantial efficiency gains offered by the homogenization approach.

Table 4.18: Tensile Load in Y Direction FEA Results for Anti-tetrachiral Structure.

Deflection of Load Cell (mm)	Simplified FEA vs. Full-Scale FEA (%)	Full-Scale FEA vs. Test Results (%)	Simplified FEA vs. Test Results (%)
1.0	13870	11136	-19.7%
1.5	20805	16704	-19.7%
2.0	27740	22272	-19.7%

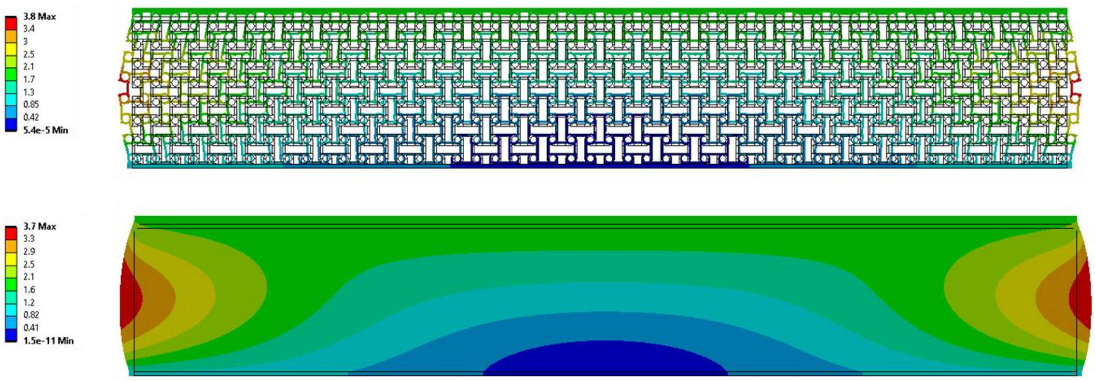

Figure 4.26: Total Deformation Distribution for the Anti-tetrachiral Structure under Tensile Load in Y Direction: Full-Scale and Simplified FE Models.

4.4.2.Tensile load in x direction only

For the re-entrant structure, the force-deflection results obtained from the full-scale FEA and simplified FEA models, along with the corresponding percentage differences, are presented in Table 4.19.

At a displacement of 1.0 mm, the full-scale FEA predicts a reaction force of 2268 N, while the simplified model predicts 2103 N. As the displacement increases to 2.0 mm, the full-scale model yields 4536 N, and the simplified model predicts 4206 N. The results show that the simplified model consistently underestimates the reaction force compared to the full-scale model, with an approximate difference of 7.3% across the displacement range.

The visual comparison of the deformation patterns, as shown in Figure 4.27 for the re-entrant structure, further supports these observations. The simplified model captures the global tensile behavior and overall deformation trends, despite lacking the detailed local geometric features resolved in the full-scale model. Both models, however, predict comparable global responses when subjected to loading along the X direction.

From a computational perspective, the full-scale re-entrant model consists of 897,600 elements and 1,185,500 nodes, whereas the simplified model is composed of 311,808 elements and 337,125 nodes. The computational solve time for the full-scale model is approximately three times longer than that of the simplified model, underscoring the substantial efficiency advantage of the homogenization approach.

Table 4.19: Tensile Load in X Direction FEA Results for Re-entrant Structure.

Deflection of Load Cell (mm)	Full-Scale FEM Force Reaction (N)	Simplified-Scale FEM Force Reaction (N)	Simplified FEA vs. Full-Scale FEA (%)
1.0	2268	2103	-7.3%
1.5	3402	3155	-7.3%
2.0	4536	4206	-7.3%

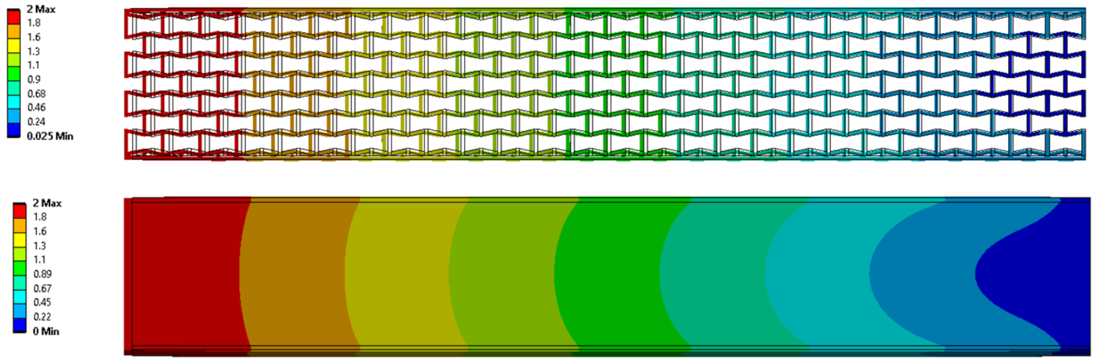

Figure 4.27: Total Deformation Distribution for the Re-entrant Structure under Tensile Load in X Direction: Full-Scale and Simplified FE Models.

For the anti-tetrachiral structure, the results exhibit a similar trend. As shown in Table 4.20 and illustrated in Figure 4.28, the full-scale FEA predicts a reaction force of 1007 N at a displacement of 1.0 mm, while the simplified model predicts 846 N. At 2.0 mm displacement, these values increase to 2014 N for the full-scale model and 1693 N for the simplified model. The simplified model underestimates the reaction force relative to the full-scale model by approximately 16.0% across the displacement range.

The visual comparison of the deformation patterns, presented in Figure 4.28 for the anti-tetrachiral structure, confirms these observations. The simplified model accurately captures the overall tensile behavior and global deformation trends of the structure, although it does not resolve the finer geometric features captured by the full-scale model. Nevertheless, both models provide comparable predictions for the global tensile response under X-direction loading.

In terms of computational efficiency, the full-scale anti-tetrachiral model comprises 2,928,720 elements and 3,722,325 nodes, whereas the simplified model contains 283,296 elements and 307,125 nodes. The full-scale model requires approximately eight times longer computational solve time than the simplified model, emphasizing the significant computational savings achieved through the homogenization approach.

Table 4.20: Tensile Load in X Direction FEA Results for Anti-tetrachiral Structure.

Deflection of Load Cell (mm)	Simplified FEA vs. Full-Scale FEA (%)	Full-Scale FEA vs. Test Results (%)	Simplified FEA vs. Test Results (%)
1.0	1007	846	-16.0%
1.5	1511	1270	-16.0%
2.0	2014	1693	-16.0%

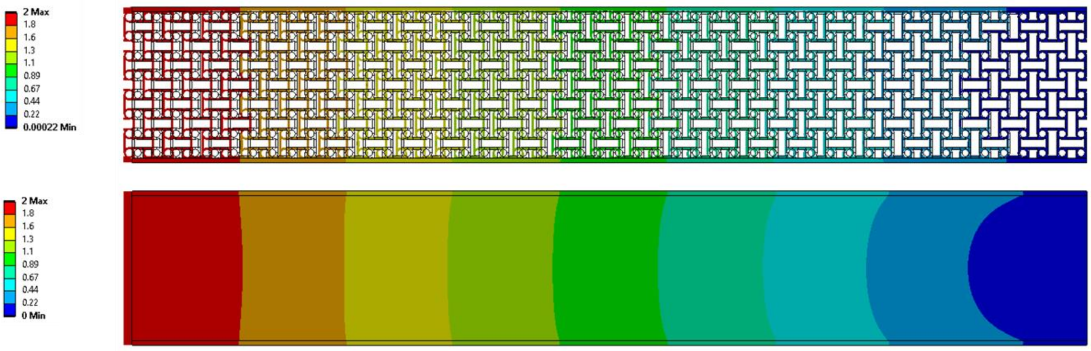

Figure 4.28: Total Deformation Distribution for the Anti-tetrachiral Structure under Tensile Load in X Direction: Full-Scale and Simplified FE Models.

5.CONCLUSIONS AND RECCOMENDATIONS

This thesis has presented a comprehensive investigation of the mechanical behavior of sandwich structures featuring re-entrant and anti-tetrachiral auxetic cores, employing both experimental testing and numerical analyses. The primary objective was to assess the accuracy, computational efficiency, and practical applicability of homogenized finite element models in comparison to detailed full-scale models across a range of loading scenarios, including modal response analysis, static compression, three-point bending, and tensile simulations. Experimental tests, encompassing modal analysis, compression, and three-point bending, were also conducted to provide a benchmark for evaluating the numerical predictions and to examine the performance of the homogenization approach.

The findings from the modal response analyses demonstrated that full-scale finite element models predicted natural frequencies and mode shapes with a high degree of accuracy, showing maximum differences of 7.3% for the re-entrant and 8.0% for the anti-tetrachiral structures when compared to experimental modal test data. The simplified homogenized models, despite their geometric simplifications, produced natural frequency predictions with maximum deviations of 9.7% for the re-entrant and 15.5% for the anti-tetrachiral structures relative to the experimental results. Notably, the computational efficiency improvements were substantial: the homogenized models reduced node counts by approximately 73% for the re-entrant FE models and 92% for the anti-tetrachiral FE models, while also achieving solve times up to 44 times faster for the re-entrant analyses and 70 times faster for the anti-tetrachiral cases compared to the full-scale models. These results highlight that while full-scale models remain essential for high-fidelity modal analyses, homogenized models provide sufficiently accurate approximations for early-stage design, parametric studies, and optimization tasks.

The findings from the static compression analyses indicate that the full-scale finite element models overestimated the experimental results by up to 12.3% for the re-entrant structure and 14.6% for the anti-tetrachiral structure. In contrast, the homogenized models demonstrated closer agreement with experimental data, with differences within 12% for the re-entrant and 4% for the anti-tetrachiral structures. Furthermore, the homogenized FE results for the re-entrant structure aligned closely with the corresponding full-scale FE model, showing a negligible difference of 0.2%, while for the anti-tetrachiral structure, the homogenized results deviated from the full-scale FE predictions by approximately 12%. The computational efficiency gains achieved through homogenization were significant: node counts were reduced by up to 97% for the re-entrant FE models and 95% for the anti-tetrachiral FE models, while solve times improved by factors of up to 10 and 50, respectively. These findings reinforce the practical value of homogenized models for simulating the compressive behavior of auxetic structures, particularly in scenarios where computational resources are limited.

The three-point bending analyses revealed that the load–displacement behavior of the re-entrant and anti-tetrachiral structures was strongly influenced by manufacturing factors, including dimensional deviations and the layer-induced anisotropy inherent to the Material Jetting process. These effects, combined with microstructural phenomena such as localized buckling, geometric imperfections, and anisotropic variations, contributed to discrepancies between numerical predictions and experimental results. Among all loading cases studied in this thesis, three-point bending initially showed the largest differences when material models were based solely on tensile test data, with full-scale FE predictions overestimating experimental forces by up to 42% for the re-entrant structure and 67% for the anti-tetrachiral design. However, when the averaged Young's modulus obtained from both tensile and compression tests was applied, the correlation improved significantly, reducing differences to within 7% for the re-entrant and approximately 15% for the anti-tetrachiral structure. The refined modeling strategy that incorporated separate tensile and compressive modulus with neutral axis consideration yielded the best results, limiting differences to 2–4% for the re-entrant and 5–9% for the anti-tetrachiral. These findings emphasize the importance of accounting for the mixed stress state in bending and demonstrate that improved material modeling substantially enhances predictive reliability. The homogenized models, although geometrically simplified and defined solely using tensile test data, demonstrated improved alignment with experimental data, with differences typically within 19% for the re-entrant structure and 26% for the anti-tetrachiral. These outcomes highlight the continued value of homogenization in approximating global bending behavior. Relative to full-scale models, the homogenized bending results deviated by approximately 15.7% for the re-entrant and 24.6% for the anti-tetrachiral. The computational efficiency benefits of homogenization were significant: node counts were reduced by up to 65% for the re-entrant FE models and 90% for the anti-tetrachiral, with solve times improved by factors of up to 3 and 6, respectively. These findings suggest that the homogenization approach provides a practical trade-off between computational efficiency and predictive accuracy for preliminary bending analyses. When combined with the improved material definitions, homogenized models would achive results that not only aligned closely with experimental force–deflection curves but also maintained significant efficiency benefits, making them highly attractive for preliminary design and optimization studies. Overall, these results confirm that homogenization remains a practical trade-off between accuracy and efficiency, but they also emphasize that careful material calibration is essential for bending-dominated problems. While the homogenized models successfully approximate global structural behavior, they cannot fully capture localized nonlinearities, failure mechanisms, or micro-buckling effects.

The FEA results obtained using the averaged Young’s modulus derived from both tensile and compression tests (Section 4.2.1), as well as the results obtained using separate tensile and compressive modulus with neutral-axis consideration (Section 4.2.2), further emphasize the critical importance of defining material properties accurately when modeling auxetic geometries with polymer-based materials, and particularly for polymer-based applications in general. Accurate representation of the material response under both tensile and compressive loading is essential for achieving realistic and physically consistent simulation outcomes. Three-point bending and general flexural analyses can only capture the true mechanical behavior of the specimens when the model correctly reflects the distinct stiffness characteristics in tension and compression. Collectively, these two approaches substantially reduce discrepancies between numerical predictions and experimental measurements, ensuring that the bending response of auxetic sandwich structures is modeled in a manner that more closely reproduces the actual material behavior.

In the tensile loading simulations, conducted solely through numerical analyses due to the absence of experimental validation in this study, the homogenized models exhibited a consistent underestimation of reaction forces. Specifically, for tensile loading in the Y direction, the homogenized models predicted reaction forces 8.9% lower than the full-scale finite element models for the re-entrant structure and 19.7% lower for the anti-tetrachiral. When the tensile loading was applied in the X direction, the differences were 7.3% and 16.0% for the re-entrant and anti-tetrachiral structures, respectively. The computational efficiency improvements achieved through homogenization were notable, homogenized models reduced node counts by up to 73% for the re-entrant FE models and 92% for the anti-tetrachiral models, with solve times improving by factors of up to 3 and 8, respectively. These findings indicate that the homogenization approach provides a practical and efficient modeling strategy for conceptual evaluations and early-stage design phases. However, the observed differences also highlight the limitations of homogenized models in capturing localized distributions and detailed mechanical responses under tensile loading.

These findings highlight the fundamental trade-off between accuracy and computational efficiency in finite element modeling of complex auxetic lattice structures. Full-scale models deliver highly accurate predictions and capture detailed local behavior, but at the cost of significantly higher computational demands. In contrast, homogenized models provide a practical and computationally efficient alternative for early-stage design, parametric studies, multi-variable optimization studies, and system-level analyses. While homogenized models effectively predict global response characteristics, they inherently lack the resolution needed to capture localized details, geometric discontinuities, and fine-scale deformation mechanisms.

Experimental validation further revealed the critical influence of manufacturing-induced imperfections, such as dimensional deviations, anisotropy, and variability introduced by the Material Jetting process, on the mechanical behavior of fabricated structures. The results confirm that even the highest-fidelity numerical models cannot fully account for these imperfections, highlighting the importance of incorporating manufacturing tolerances and detailed material characterization into future modeling and simulations efforts.

The practical implications of this study are valuable for engineering designs and applications where rapid prototyping, iterative optimization, and system-level analyses are required. This is especially relevant in cases such as heat exchangers and lightweight panels, where full-scale finite element modeling becomes computationally prohibitive due to the sheer number of repeating unit cells, often reaching into the millions in industrial-scale applications.

In conclusion, this thesis confirms that homogenized models provide a viable, practical, efficient and reliable solution for analyzing auxetic lattice structures with complex geometries, or components comprising numerous repeating substructures. Homogenized models offer a compelling balance between accuracy and computational efficiency, making them highly effective for broader structural analyses where detailed, fine-scale accuracy is not a primary concern. However, for applications requiring precise local stress distributions, failure mechanisms, or nonlinear deformation analysis, such as aerospace components, biomedical implants, or load-bearing structural elements, full-scale models remain essential. The choice between homogenized and full-scale models should be guided by the specific design objectives, the required level of accuracy, and the available computational resources.

5.1.Recommendations for Further Studies

Building upon the findings of this thesis, several key directions are recommended for future research to further enhance the accuracy, reliability, and practical utility of homogenized finite element models for complex auxetic structures.

First, the refinement of homogenization techniques remains an essential research avenue, particularly through the integration of nonlinear and anisotropic effects that are inherent to auxetic geometries and additive manufacturing processes. Incorporating these factors would enable more realistic and physically consistent predictions of structural responses under complex and multiaxial loading scenarios.

Second, the development of hybrid finite element modeling strategies presents a promising direction. By combining homogenized global representations with localized full-scale analyses in critical regions, such hybrid frameworks can achieve a balanced compromise between computational efficiency and detailed accuracy. This approach is particularly advantageous for large-scale engineering systems that require both global performance evaluation and local stress analysis.

Third, conducting comprehensive experimental tensile and compressive material tests is essential to close the current validation gap and to refine the constitutive modeling of auxetic lattice structures. The absence of detailed experimental data for polymer-based auxetic cores currently limits the accuracy of numerical simulations, particularly in capturing the distinct mechanical responses that occur under tensile and compressive loading conditions. Obtaining reliable stress–strain data from well-controlled tests would enable the identification of accurate elastic and inelastic regions, provide a better understanding of nonlinear deformation mechanisms, and allow for the calibration of tension–compression-dependent material models. This enhanced material characterization would, in turn, improve the predictive fidelity of finite element analyses for bending, compression, and dynamic simulations, ensuring that the numerical models more closely replicate the real mechanical performance of the printed auxetic structures. Moreover, such experimental efforts would establish a stronger foundation for developing future homogenized and multi-scale models that more effectively represent the anisotropic and nonlinear nature of polymer-based auxetic materials.

Fourth, the establishment of a comprehensive experimental database encompassing diverse loading conditions, deformation modes, and auxetic topologies would significantly enhance both material characterization and numerical modeling accuracy. Beyond conducting individual tensile or compressive tests, such a database should systematically compile mechanical properties obtained from multiple test types—tension, compression, bending, and dynamic loading—across various auxetic configurations. Furthermore, an organized and well-documented database would facilitate the development of data-driven constitutive formulations, support the standardization of material parameters for polymer-based auxetic structures, and accelerate progress toward predictive, multi-scale modeling frameworks that are grounded in experimental evidence.

Pursuing these research directions will bridge the present limitations of homogenized finite element analysis and foster the development of robust, validated, and computationally efficient modeling approaches. These advancements will not only enhance the predictive capability of auxetic sandwich structures but also support their implementation in a broader range of aerospace, mechanical, and structural engineering applications.

REFERENCES

[1] **K. Günaydın. Z. Eren, Z. Kazancı** (2022). Additive Manufacturing of Tunable Metamaterials, Nanotechnology-Based Additive Manufacturing: Product Design, Properties and Applications, Volume 2, Chapter 6.

[2] **H. M. A. Kolken, A. A. Zadpoor** (2017). Auxetic mechanical metamaterials, RSC Advances, 2017, 7, 5111-5129.

[3] **A. Seyfi, A. Teimouri, F. Ebrahimi** (2021). Scale-dependent torsional vibration response of non-circular nanoscale auxetic rods, Waves in Random and Complex Media Volume 34, 2024 - Issue 5, Pages 4425-4441.

[4] G. Mchale, A. Alderson, S. Armstrong, S. Mandhani, M. Meyari, G. G. Wells, E. Carter, R. L. Aguilar, C. Semprebon, K. E. Evans (2023). Superhydrophobicity of auxetic metamaterials, Cornell University Archive.

[5] **Q. Hu, X. Zhang, J. Zhang, G. Lu, K. M. Tse.** (2024). A review on energy absorption performance of auxetic composites with fillings, Thin-Walled Structures Volume 205, Part A, December 2024, 112348.

[6] **V. A. Lvov, F. S. Senatov, A. A. Veveris, V. A. Skrybykina, A. D. Lantada** (2022). Auxetic Metamaterials for Biomedical Devices: Current Situation, Main Challenges, and Research Trends, Materials 2022, 15(4), 1439.

[7] **K. Günaydın, Z. Eren, Z. Kazancı, F. Scarpa, A. M. Grande, H. S. Türkmen** (2019). In-plane compression behavior of anti-tetrachiral and re-entrant lattices, Smart Materials and Structures, Volume 28, Number 11, 1-14, Article 115028.

[8] **O. Günel, M. Ranjbar** (2019). REVIEW ON AUXETIC MATERIALS, 1 st International Conference on Advances in Mechanical and Mechatronics Engineering ICAMMEN2018.

[9] **Y. Kim, K. H. Son, J. W. Lee** (2021). Auxetic Structures for Tissue Engineering Scaffolds and Biomedical Devices,Materials 2021, *14*(22), 6821.

[10] **M. Arredondo-Soto, E. Cuan-Urquizo, A. Gómez-Espinosa** (2021). A Review on Tailoring Stiffness in Compliant Systems, via Removing Material: Cellular Materials and Topology Optimization, Applied Sciences 2021, 11(8), 3538.

[11] **M. S. Rad, H. Hatami, Z. Ahmad, A. K. Yasuri** (2019). Analytical solution and finite element approach to the dense re-entrant unit cells of auxetic structures, Acta Mechanica, Volume 230, pages 2171–2185, (2019).

[12] **Z. D. Ma** (2016). HOMOGENIZATION METHOD FOR DESIGNING NOVEL ARCHITECTURED CELLULAR MATERIALS, ECCOMAS Congress 2016 VII European Congress on Computational Methods in Applied Sciences and Engineering.

[13] **J. Somnic and B. W. Jo** (2022). Homogenization Methods of Lattice Materials, Encyclopedia 2022, 2(2), 1091-1102.

[14] **H. Deng, J. Zhao, C. Wang** (2021). Leaf Vein-Inspired Bionic Design Method for Heat Exchanger Infilled with Graded Lattice Structure, Aerospace 2021, 8(9), 237.

[15] **D. Jiang, H. Thissen, T. C. Hughes, K. Yang, R. Wilson, A. B. Murphy, V. Nguyen** (2024). Advances in additive manufacturing of auxetic structures for biomedical applications, Materials Today Communications Volume 40, August 2024, 110045.

[16] **K. Günaydın, C. Rea, Z. Kazancı** (2022). Energy absorption enhancement of additively manufactured hexagonal and re-entrant (auxetic) lattice structures by using multi-material reinforcements, Additive Manufacturing, Volume 59, Part A, November 2022, 103076.

[17] **G. Imbalzano, P. Tran, T. D. Ngo, P. V. S. Lee** (2015). Three-dimensional modelling of auxetic sandwich panels for localised impact resistance, Journal of Sandwich Structures & Materials, 2015, Volume 19, Issue 3, 291-316.

[18] **Q. Hu, X. Zhang, J. Zhang, G. Lu, and K. M. Tse (2024).** A review on energy absorption performance of auxetic composites with fillings, Thin-Walled Structures Volume 205, Part A, December 2024, 112348.

[19] **M. Najafi, H. Ahmadi, and M. Liaghat** (2022). Evaluation of the mechanical properties of fully integrated 3D printed polymeric sandwich structures with auxetic cores: experimental and numerical assessment, The International Journal of Advanced Manufacturing Technology 122(9-10):1-20.

[20] **K. Terada, N. Kikuchi** (2001). A class of general algorithms for multi-scale analyses of heterogeneous media, Computer Methods in Applied Mechanics and Engineering Volume 190, Issues 40–41, 20 July 2001, Pages 5427-5464.

[21]**Url-1**<https://support.stratasys.com/en/Materials/PolyJet/Vero-Family> , Data Retrieved May, 2025.

[22]**Url-2**<https://www.gluespec.com/Materials/prototyping/stratasys/veroblue-rgd840> Data Retrieved May, 2025.

[23]**Url-3**<https://www.3ds.com/make/guide/process/material-jetting>Data Retrieved May, 2025.

[24]**Url-4**< https://www.matweb.com/search/DataSheet.aspx?MatGUID=be2de6867bad431a8a0264b30d095bed&ckck=1 > Data Retrieved May, 2025.

[25]**Url-5** < https://www.buildparts.com/materials/veroblue/> Data Retrieved May, 2025.

[26]**Url-6** < https://www.wehl-partner.de/wp-content/uploads/Datenblatt-VeroBlue-FullCure840.pdf> Data Retrieved May, 2025.

[27] **S. Nemat-Nasser and M. Hori** (1993). Micromechanics: Overall Properties of Heterogeneous Materials, North-Holland Series in Applied Mathematics and Mechanics Volume 37.

[28] **T. Belytschko, W. K. Liu, B. Moran and K. Elkhodary** (2014). Nonlinear Finite Elements for Continua and Structures, Chichester, UK: Wiley.

[29] **U. Simsek, A. Akbulut, C. E. Gayir, C. Basaran, and P. Sendur** (2020). Modal characterization of additively manufactured TPMS structures: Comparison between different modeling methods, The International Journal of Advanced Manufacturing Technology, Volume 115, pages 657–674, (2021).

CURRICULUM VITAE

Name Surname: Özgür DEĞİRMENCİ

EDUCATION:

- **B.Sc.:** 2012, Eskisehir Osmangazi University, Department of Mechanical Engineering, Mechanical Engineering Programme

PROFESSIONAL EXPERIENCE AND REWARDS:

- 2016-2020 : General Electric Aerospace at Türkiye Technology Center (TTC), Design Engineer
- 2020-2023 : General Electric Aerospace at TTC, Lead Design Engineer
- 2023-2024 : General Electric Aerospace at TTC, Advanced Lead Design Engineer
- 2024-2025 : General Electric Aerospace at TTC, Module Systems Integration Leader for Mechanical Systems

PUBLICATIONS, PRESENTATIONS AND PATENTS ON THE THESIS:

- **Ö. Değirmenci,** K. Günaydın, H. S. Türkmen and Ş. Yılmaz (2025). A Comparative Modal Analysis of Homogenized and Full-Scale FE Models of Sandwich Composite Structures with Re-entrant Auxetic Core. 4th International Graduate Research Symposium IGRS'25, May 12-14, 2025 Istanbul, Turkey.